Reversible Redox Reactions for High Temperature Thermochemical Energy Storage

A doctoral thesis accepted by the Faculty of
Energy-, Process- and Bio-Engineering of the University of Stuttgart
in fulfillment of the requirements for the degree of
Doctor of Engineering Sciences (Dr.-Ing.)

presented by

Michael Christian WOKON

born August 23rd 1984 in Treuchtlingen

Main reviewer: Prof. Dr. rer. nat. habil. André Dietrich THESS
Co-reviewer: Prof. Dr. rer. nat. habil. Martin SCHMÜCKER

Date of oral examination: July 20th 2020

Institute for Building Energetics, Thermotechnology and Energy Storage
of the University of Stuttgart

2020

For my Parents

Acknowledgments

The research for this thesis was conducted at the Institute of Engineering Thermodynamics of the German Aerospace Center (Deutsches Zentrum für Luft- und Raumfahrt, DLR e.V.) in Cologne, during the period between March 2012 and February 2017. First of all I would like to thank the main reviewer Prof. Dr. André Thess for supervising my thesis. I further wish to thank the co-reviewer Prof. Dr. Martin Schmücker for his support of my work as well as in depth discussions regarding all aspects of storage material characteristics.

I am especially grateful to Dr. Marc Linder for the excellent supervision as well as unrestricted encouragement, patience and motivation in all phases of my thesis. His personal effort and valuable advice was an important building block in my individual development from a scientific as well as personal perspective. He provided far-ranging possibilities to freely unfold ideas and gave me the freedom to decide on the conceptual orientation of the thesis. Furthermore, I highly appreciate the expertise and support of Dr. Thomas Bauer in the course of numerous fruitful discussions on thermochemical energy storage.

Moreover, I am also indebted to Dr. Tina Block (Institute of Materials Research, DLR) for performing scanning electron microscopy and X-ray powder diffractometry. Her help with all aspects of material specific questions was very valuable for my research. Sincere thanks is also given to the aid of Sven Nicolai (VITO Flemish Institute for Technological Research, Mol, Belgium) for the preparation of the manganese-iron oxide granulate.

I would like to express a special thanks to all my colleagues in Stuttgart and Cologne for their great support and in depth encouraged discussions, in particular to Dr. Margarethe Richter and Dr. Inga Bürger for their helpful suggestions in reaction kinetics and material analyses, but also to Dr. Matthias Schmidt, Dr. Christian Roßkopf, Marie Gollsch, Nicole Neumann and Dr. Jan Felinks for the day-to-day mutual collaboration as well as for always listening to and helping each other in all kinds of challenges which came along with daily research life. I also owe a huge debt of gratitude to Andreas Kohzer for his technical support and collaboration at the experimental test rig. Furthermore, the strong commitment and contribution of my former students Nadine Kaczmarkiewicz, Anes Benzarti, Elise Sarrault and Dena Kartouzian is also gratefully acknowledged. It has been a great pleasure for me to work with the research group of *Thermochemical Systems*, which has left many lasting memories.

Most importantly, the realization and completion of this thesis would not have been possible without the continuous encouragement by my parents, who always motivated me and believed in me throughout the entire period of the preparation of the thesis.

Thermochemical energy storage, gas-solid reaction, redox reaction, manganese-iron oxide, thermodynamic equilibrium, thermal hysteresis, gas-solid reaction kinetics, packed bed reactor, direct contact heat transfer, thermal charging and discharging

Abstract

Thermochemical energy storage (TCS) constitutes a promising concept to exploit reaction enthalpies for the storage of thermal energy, which offers great potential for the development of more efficient storage solutions with higher energy densities compared to sensible and latent thermal energy storage. Reversible redox reactions of multivalent metal oxides with oxygen allow the use of ambient air simultaneously as heat transfer fluid (HTF) and source of the reactant O_2.

Based on a literature review regarding decisive TCS properties such as thermodynamic equilibrium, energy storage density, reactivity as well as material availability and a general health & safety rating, manganese-iron oxide with a Fe/Mn molar ratio of 1:3, prepared in granular form using low-cost, technical grade raw materials, has been selected as a suitable reference material for detailed examinations in this thesis. Redox cycles of $(Mn_{0.75}Fe_{0.25})_2O_3/(Mn_{0.75}Fe_{0.25})_3O_4$ performed by means of thermal analyses (TG-DSC) in the temperature range between 750 °C and 1060 °C in air showed, that the material exhibits a narrowed thermal hysteresis, a higher reaction enthalpy, enhanced reaction rates, as well as a better long-term cycling stability than the corresponding redox transition Mn_2O_3/Mn_3O_4 of pure manganese oxide, which served as underlying base material for comparison. Thereupon the thermodynamic characteristics including the thermal hysteresis behavior of the redox reaction as well as thermophysical material properties of the Mn-Fe oxide were characterized in detail. Effective reaction rate equations for the reduction and oxidation step have been derived, describing the dependence of the reaction rate not only on temperature but for the first time also on the prevalent oxygen partial pressure.

A lab-scale test rig with a packed bed storage reactor for about 470 g of Mn-Fe oxide filling (128 kJ chemical storage capacity, energy density of 102 kWh/m^3) has been developed and operated with ambient air as HTF and reaction gas carrier using direct contact heat transfer between the two phases. The redox reaction based storage concept could be demonstrated over consecutive storage cycles between 400 °C and 1040 °C. The proceeding redox reactions disclosed the development of distinct temperature profiles with a plateau formation, characteristic for exploiting the heat effect of reversible reactions for TCS. Parametric studies regarding the influence of essential operating parameters revealed the main limitations affecting the reaction progress. At higher HTF flow rates the observed charging and discharging rate (reaction rate of packed bed) was limited by the present rate of heat input and rate of heat dissipation by the HTF. At low HTF flow rates the discharging performance was dominated by a reduced packed bed reaction rate due to a shortened availability of O_2 as well as by diminished heat transfer and heat transport capabilities of the HTF.

Owing to the high operating temperatures of a redox reaction based TCS reactor, a high proportion of thermal energy is stored as sensible energy, particularly in the case of the comparatively low chemical storage density of manganese-based oxides. This circumstance equally necessitates the utilization of the sensible thermal energy in the overall storage concept, in order to increase the total storage capacity and exploit the energy storage system efficiently.

Thermochemische Energiespeicherung, Gas-Feststoff-Reaktion, Redoxreaktion, Manganeisenoxid, thermodynamisches Gleichgewicht, thermische Hysterese, Reaktionskinetik von Gas-Feststoff-Reaktionen, Festbettreaktor, direkte Wärmeübertragung, thermische Be- und Entladung

Zusammenfassung

Thermochemische Energiespeicherung (TCS) stellt ein vielversprechendes Konzept dar, Reaktionsenthalpien zur Speicherung thermischer Energie zu nutzen, wodurch sich im Vergleich zu sensiblen und latenten thermischen Energiespeichern eine höhere Speicherdichte erreichen lässt. Reversible Redoxreaktionen mehrwertiger Metalloxide mit O_2 ermöglichen dabei die Nutzung von Umgebungsluft sowohl als Wärmeträgerfluid (WTF) als auch Quelle des Reaktanten O_2.

Ausgehend von einer Literaturrecherche bezüglich potentieller Speichermaterialien wurde Manganeisenoxid mit einem molaren Fe/Mn-Verhältnis von 1:3 als geeignetes Referenzmaterial für detaillierte Untersuchungen in dieser Arbeit ausgewählt. Die Herstellung als Granulat erfolgte aus kostengünstigen Ausgangsstoffen technischer Qualität. Über Thermische Analyse (TG-DSC) durchgeführte Redoxzyklen von $(Mn_{0.75}Fe_{0.25})_2O_3/(Mn_{0.75}Fe_{0.25})_3O_4$ im Temperaturbereich zwischen 750 °C und 1060 °C in Luft zeigten eine kleinere thermische Hysterese, eine höhere Reaktionsenthalpie, schnellere Reaktionsraten, sowie eine bessere Langzeit-Zyklenstabilität als der entsprechende Redoxübergang Mn_2O_3/Mn_3O_4 von reinem Manganoxid, welches als zugrundeliegendes Basismaterial vergleichend herangezogen wurde. Daraufhin wurden die thermodynamischen Eigenschaften einschließlich des Hystereseverhaltens der Redoxreaktion sowie die thermophysikalischen Stoffeigenschaften von Manganeisenoxid eingehend charakterisiert. Zudem wurden Gleichungen für die effektiven Reaktionsraten des Reduktions- und Oxidationsschrittes hergeleitet, welche zum ersten Mal nicht nur die Abhängigkeit der Reaktionsrate von der Temperatur, sondern auch von dem vorliegenden Sauerstoffpartialdruck beschreiben.

Für reaktionstechnische Untersuchungen wurde ein Festbettreaktor für eine Schüttung von etwa 470 g Mn-Fe-Oxid (128 kJ chemische Speicherkapazität, Energiedichte von 102 kWh/m^3) entwickelt und mit Umgebungsluft als WTF sowie Träger des Reaktionsgases betrieben. Wärmeübertragung erfolgte somit durch direkten Kontakt zwischen den beiden Phasen. Das Speicherkonzept konnte über mehrere aufeinanderfolgende Speicherzyklen zwischen 400 °C und 1040 °C experimentell dargestellt werden. Parameterstudien bezüglich des Einflusses der entscheidenden Betriebsparameter offenbarten die wesentlichen Limitierungen im Rahmen der Laborexperimente. Bei hohen WTF-Volumenströmen wurde die beobachtete Be- und Entladungsrate des Speicherreaktors durch die jeweils vorliegende Wärmezufuhr- und Wärmeabfuhrrate des WTF limitiert. Bei niedrigen Strömen wurde die Entladeleistung von einer verringerten Reaktionsrate der Speichermaterialschüttung beherrscht, welche durch eine verminderte Verfügbarkeit an O_2 sowie niedrigere Wärmeübertragung und reduzierte Wärmetransportfähigkeit des WTF hervorgerufen wurde.

Aufgrund der hohen Betriebstemperaturen eines metalloxidbasierten TCS-Reaktors ist ein großer Anteil der thermischen Energie als sensible Energie gespeichert, insbesondere im Fall der verhältnismäßig niedrigen, chemischen Energiespeicherdichte von manganbasierten Oxiden. Zur Erhöhung der Gesamtspeicherkapazität und effizienten Ausnutzung des Speichersystems erfordert das Speicherkonzept folglich die Nutzung der sensibel gespeicherten Energie gleichermaßen.

Contents

List of Figures

List of Tables

Nomenclature

Roman Characters

A	area	m^2
A	pre-exponential factor	1/s
a	thermal diffusivity	m^2/s
C_{HTF}	heat capacity rate of HTF	W/K
c_p	specific heat capacity at constant pressure	J/(kg·K)
D	reactor tube diameter	m
$d_{p,m}$	mean particle diameter/size	m
$d_{p,pr}$	equivalent particle diameter (sphere diameter of equal projected area)	m
$\Delta_R G$	Gibbs free energy of reaction, free enthalpy	kJ/mol
$\Delta H_{g,max}$	maximum possible enthalpy change of HTF flow	J
$\Delta_F H^{\ominus}$	molar standard enthalpy of formation	kJ/mol
$\Delta_{Fus} h$	specific enthalpy of fusion, (latent) heat of fusion	kJ/kg
$\Delta_R H$	molar reaction enthalpy	kJ/mol
$\Delta_R h$	specific reaction enthalpy	kJ/kg
$\Delta_R S$	molar reaction entropy	J/(mol·K)
E_a	activation energy	kJ/mol
$f(X)$	reaction model (mechanism), dependence on extent of conversion	–
$g(X)$	integral form of the reaction model	–
H	filling height of packed bed	m
h	heat transfer coefficient	$W/(m^2 \cdot K)$
$h(p)$	pressure-dependent function, pressure term	–
K_{eq}	equilibrium constant	–
$k(T)$	Arrhenius term, rate constant	1/s
M	molecular weight	g/mol
m	mass	kg
m	exponent of pressure term	–
$\dot{m}$	mass flow rate	kg/s
n	molar amount	mol
n	parameter of reaction model, coefficient of reaction mechanism	–
$\dot{n}$	molar reaction rate, molar flow rate	mol/s
p	pressure	Pa
p_i	partial pressure of gas i	Pa

pO_2	oxygen partial pressure	Pa
$pO_{2,eq}$	oxygen partial pressure at equilibrium	Pa
Q	quantity of thermal energy, storage capacity	kJ
$\dot{Q}$ (and P)	heat flow, thermal power	W
Q_i	volume fraction of i^{th} particle size fraction	–
T	thermodynamic temperature	K
T_{eq}	equilibrium temperature	K
t	time	s
t_0	delay period	s
t	thickness	m
$\vec{u}$	superficial gas velocity vector	m/s
V	volume	m^3
$\dot{V}$	volume flow rate	m^3/s
V_m	molar volume	m^3/mol
w_i	mass fraction of solid i	–
X	reaction conversion	g/g, mol/mol
x_i	molar fraction of solid i	–
y_i	molar fraction of gas i	–
y_{O_2}	molar fraction of oxygen	–

Greek Characters

β	heating rate or cooling rate	K/min
Δ	difference	–
ε_{bed}	porosity of packed bed, without consideration of intraparticle porosity	–
ε_p	inner porosity of particles, fraction of pore volume	–
ε_{tot}	total void percentage, total porosity	–
η	dynamic viscosity	kg/(m·s)
λ	thermal conductivity	W/(m·K)
μ	chemical potential	kJ/mol
ν	kinematic viscosity	m^2/s
ν	stoichiometric coefficient	–
ρ	density	kg/m^3
ρ_{app}	apparent density of solid	kg/m^3
ρ_{bulk}	bulk density of packed bed	kg/m^3
$\rho_{en,m}$	gravimetric energy storage density	kWh/kg
$\rho_{en,v}$	volumetric energy storage density	kWh/m^3
ρ_{true}	true density of solid	kg/m^3
σ	volume concentration of gas	%

ϑ	temperature, thermocouple position	°C

Indices

0	initial value
50	at 50 %
ambient	ambient conditions
av	average
bed	packed bed
c	charging
chem	chemical
d	discharging
eff	effective
eq	equilibrium
exp	experimental
final	final state
g	gaseous, gas phase
HTF	heat transfer fluid
i ... n	index of summation
in	inlet
initial	initial state
insu	insulation
lam	laminar
m	mean
max	maximum
min	minimum
$\ominus$	standard conditions according to IUPAC (1982): 273.15 K = 0 °C and 100 kPa
oo	onset-offset
out	outlet
Ox	oxidation
ox	oxidized
p	pressure
p	particle(s)
pr	projected area
Red	reduction
red	reduced
rxn	reaction
s	solid, solid phase
std	standardized

t	current state
theo	theoretical
tot	total
turb	turbulent
w	wall

Dimensionsless Numbers

Nusselt Number $\mathrm{Nu} = (h_{\text{s-g}} \cdot d_{\text{p,m}})/\lambda_{\text{g}}$

Prandtl Number $\mathrm{Pr} = \nu_{\text{g}}/a = (\nu_{\text{g}} \cdot \rho_{\text{g}} \cdot c_{\text{p,g}})/\lambda_{\text{g}} = (\eta_{\text{g}} \cdot c_{\text{p,g}})/\lambda_{\text{g}}$

Particle Reynolds Number $\mathrm{Re_p} = (|\vec{u}| \cdot d_{\text{p,m}})/\nu_{\text{g}} = (\rho_{\text{g}} \cdot |\vec{u}| \cdot d_{\text{p,m}})/\eta_{\text{g}}$

Particle Reynolds Number (altern. def.) $\mathrm{Re}_{\text{p},\varepsilon_{\text{bed}}} = (|\vec{u}| \cdot d_{\text{p,m}})/(\nu_{\text{g}} \cdot \varepsilon_{\text{bed}}) = (\rho_{\text{g}} \cdot |\vec{u}| \cdot d_{\text{p,m}})/(\eta_{\text{g}} \cdot \varepsilon_{\text{bed}})$

Tube Reynolds Number $\mathrm{Re} = (|\vec{u}| \cdot D)/\nu_{\text{g}} = (\rho_{\text{g}} \cdot |\vec{u}| \cdot D)/\eta_{\text{g}}$

Constant

$\mathbb{R}$	molar gas constant, universal gas constant	8.31446	J/(mol·K)

Abbreviations

a	absolute (pressure)
B	cubic bixbyite phase $(\mathrm{Mn,Fe})_2\mathrm{O}_3$
BET	BET method developed by Brunauer, Emmett and Teller
CLC	chemical-looping combustion
CLOU	chemical-looping with oxygen uncoupling
CSP	concentrated solar power
DSC	differential scanning calorimetry
EtOH	ethanol
g	gauge (pressure)
HT	high temperature
HTF	heat transfer fluid
HTM	heat transfer medium
LT	low temperature
LTES	latent thermal energy storage
Me	metal
MFC	mass flow controller
N_2	nitrogen
NL	liter at standard conditions of 273.15 K and 101325 Pa absolute
NmL	milliliter at standard conditions of 273.15 K and 101325 Pa absolute
O_2	oxygen

PCM	phase change material
PSD	particle size distribution
redox	reduction-oxidation
RT	room temperature
S	cubic spinel phase β-$(Mn,Fe)_3O_4$
SEM	scanning electron microscopy
STA	simultaneous thermal analysis
STC	sample temperature control
STES	sensible thermal energy storage
T	tetragonal spinel phase α-$(Mn,Fe)_3O_4$ – hausmannite Mn_3O_4
TC	thermochemical
TCS	thermochemical energy storage
TES	thermal energy storage
TG	thermogravimetry
TGA	thermogravimetric analysis
WTF	Wärmeträgerfluid
XRD	X-ray diffraction
XRF	X-ray fluorescence

1 Introduction and Motivation

The reduction of CO_2 emissions and dependence on fossil fuels – essentially the carbon-based raw materials crude oil, coal and natural gas – belong to the key targets of international energy and climate policies [36]. An alternative, carbon-free energy supply can be achieved by means of an expansion of renewable energy sources, such as solar, wind and hydropower, potentially in combination with a continued use of nuclear energy. Germany is putting the main emphasis on the transformation of its current energy system towards the development of a sustainable energy system based on renewable energy. Owing to the inherent fluctuations in the energy supply of renewables the integration of energy storage technologies into the energy system network is crucial to match the energy supply and demand [17]. In this context, innovative solutions for the storage of thermal energy at high temperatures, applying storage materials with high energy densities, will be required, which is the focus of the present thesis.

Since more than 50 % of the final energy consumption in Germany is spent on the utilization of thermal energy, the widely discussed transformation of the electricity sector is closely related to a turnaround in the heating sector, which is therefore just as important to achieve the long-term climate protection targets. The heating sector accounts for roughly 26 % (share in 2015) of the total German greenhouse gas emissions per year. In industrial processes the supply of process heat accounts for over 65 % of the final energy demand, thus accounting for the most energy-intensive field in the industrial sector [32, 17].

Therefore, alongside sophisticated heat integration concepts, which are in part already existing, appropriate thermal energy storage (TES) solutions are required to enhance the energy efficiency of established high temperature (HT) industrial processes and save the use of primary energy carriers. Such storage solutions are decisive in energy-intensive sectors, such as the metal and steel production, the cement industry as well as in glass and ceramic manufacturing, to recover discontinuous waste heat for reutilization on demand and hence reduce thermal energy losses.

Moreover, thermal energy storage in HT applications also becomes increasingly important with the expansion of concentrated solar power (CSP) plants, which represent a promising, alternative and sustainable technology for electricity generation in regions with high solar irradiation [113]. The integration of a large-scale HT-TES system into a CSP plant is one of the most important aspects to facilitate the dispatchability of power generation and increase the efficiency of the plant. The unfavorable intermittency of solar energy can only be overcome by a temporal decoupling of the solar energy supply during sunshine hours and the demand for electricity generation, in order to mitigate short fluctuations in solar irradiation, bridge short-term deficiencies during cloud passage and extend electricity production into the nighttime hours, overall ensuring a base load capacity of such solar thermal power plants [66, 92, 164].

The focus of this thesis will be particularly directed to potential TES solutions for HT applications. The technology of so-called regenerator-type storage (e.g., a *Cowper stove* as part of a blast

furnace for iron production, or a glass furnace regenerator in glass manufacturing), which is solely based on sensible thermal energy storage (STES), represents the state of the art in the high temperature operating range above 500 °C. Those storage systems, classified as *passive dual media TES systems*, are characterized by a gaseous heat transfer medium, only passing through a stationary solid storage medium for charging and discharging of the system [66]. Oxide ceramics typically arranged in the form of a stack of regularly shaped checker bricks or even a packed bed of natural stones can be employed as solid storage materials [91]. For example, packed bed regenerators are part of the so-called *Advanced Adiabatic Compressed Air Energy Storage* technology (AA-CAES), a novel concept proposed to store excess electricity by compression of air, which can subsequently be stored in a tank or cavern. The implementation of regenerators is envisaged for the storage of the thermal energy generated in the compression step. In the discharging step, the thermal energy can be used again to reheat the air prior to expansion [26].

Since the principle of STES is merely based on a change in temperature of the solid storage medium, the energy storage density is primarily dependent on the maximum attainable temperature lift between the discharged and charged state of the storage system. Besides the maximum temperature difference, the energy storage density which can be reached is confined by the specific heat capacity of the respective solid storage medium and the bulk porosity of its structure.

For HT storage applications the novel field of thermochemical energy storage (TCS), exploiting the reaction enthalpies of reversible chemical reactions for the storage of thermal energy, offers promising storage opportunities. A TCS system has the potential to enhance the achievable energy storage density and thereby lower the storage costs for a required storage capacity compared to conventional sensible and latent energy storage systems. In particular reversible gas-solid reactions have attracted an increasing degree of interest [111, 117]. Multivalent metal oxides pose practical storage materials for the targeted HT operating range, as some materials are capable of reacting reversibly with oxygen at high temperatures above 500 °C. The underlying storage concept based on *redox reactions* (*red*uction-*ox*idation *reactions*) facilitates the utilization of ambient air as HTF as well as source of the gaseous reactant oxygen, which renders this concept especially attractive from a process technological point of view.

In addition, the use of air as HTF allows to work with higher HTF temperatures even beyond 1000 °C, which makes redox reactions particularly interesting for TCS applications in central receiver CSP plants, e.g., with a future generation of volumetric (open-loop atmospheric system for a Rankine cycle) or pressurized, windowed (closed-loop system for a Brayton cycle) air receiver technology [144, 77].

However, due to the constant reaction temperature, metal oxides can only be applied appropriately on a technical scale, if the influencing factors on the redox reaction during thermal charging and discharging under various operating conditions using air as HTF, which is simultaneously providing the reactant O_2, have been fully comprehended. This is the main reason why TCS systems for this HT operating range are still at an early stage of development [111]. Even though growing research efforts have been devoted to the development of suitable metal oxide materials and

initial reactor concepts over the past few years, there has not yet been sufficient research carried out into the determining relationships (e.g., pO_2-T operating conditions) of this novel storage concept, which is why diverse phenomena associated with redox reaction based TCS have not yet been understood. On this account this work focuses on systematic, fundamental examinations of redox reactions applying air as HTF. Those studies are essential for an application-oriented storage material and storage reactor development to enable efficient storage of thermal energy on a high temperature level.

Structure and Methodology of the Thesis At first a literature overview on potential metal oxides will be given in this work to further narrow down the range of suitable storage materials, putting emphasis on aspects such as thermodynamic equilibrium and TCS performance of the corresponding redox reactions as well as raw material availability, costs and environmental safety. On the basis of those broad considerations, a promising material will be selected as reference TCS material to be characterized and examined in granular form, prepared from technical grade raw material(s).

The storage material will be experimentally assessed by means of thermal analysis regarding fundamental TCS requirements, specifically focusing on the temperature level of the proceeding redox reaction, reaction reversibility, cycling stability as well as the specific reaction enthalpy. Subsequently, the material will be characterized in detail with respect to thermodynamic, kinetic and thermophysical material properties, yielding all relevant material properties to gain a comprehensive understanding of the redox reaction over a wide range of temperatures and oxygen partial pressures.

The chosen redox reaction will be further investigated on an appropriate, larger scale by means of a directly permeated reactive bed with *direct contact heat transfer* between the HTF air and the storage material, in order to understand the storage concept and identify the determining aspects for this novel metal oxide based TCS technology. Based on the results the technologically relevant directions for further storage material and storage system development can be provided. As all investigations in this work are plain fundamental and not oriented towards a specific case of application, this thesis will conclude with different application possibilities derived and pointed out on the basis of the main findings obtained throughout the experiments.

The detailed methodological approach followed in this work is depicted in Fig. 1.1.

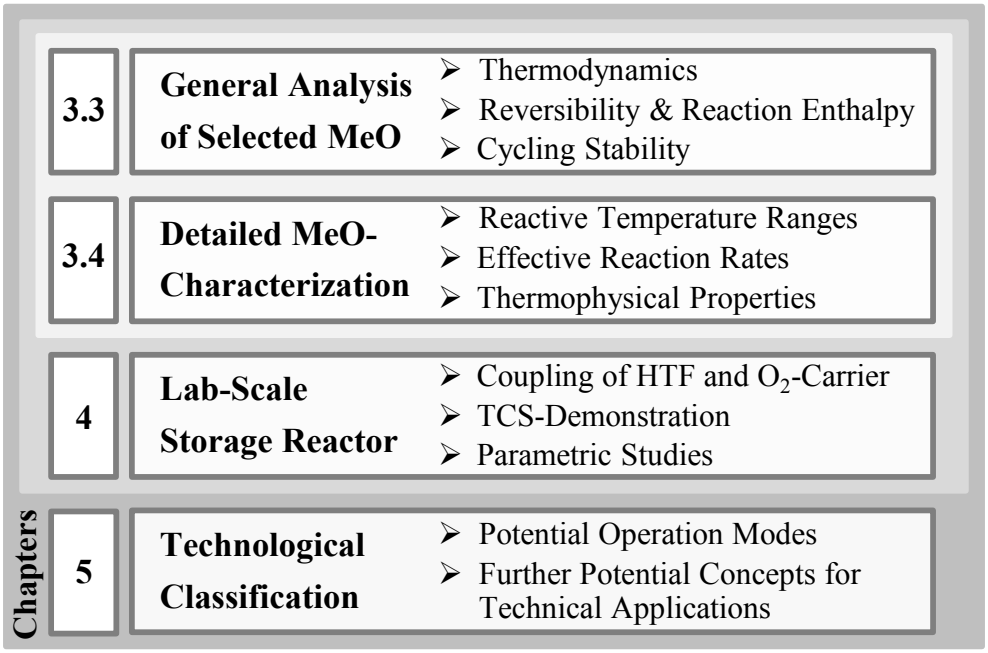

Figure 1.1: Research methodology pursued in this thesis.

2 Fundamentals and State of the Art

2.1 Thermal Energy Storage

2.1.1 Introduction and General Definitions

Energy storage constitutes a generic term, which applies to various forms of energy storage technologies, comprising electrical, mechanical, thermal and chemical storage systems, depending on the form of energy. The consistent efforts to expand the utilization of renewable energy resources with their intrinsic character of fluctuating power generation and the development of novel mobility concepts, for example, illustrate the importance of further development and implementation of energy storage solutions in the present energy supply system [17]. Moreover, cross-sectoral energy storage systems, such as power-to-gas, power-to-heat or power-to-liquid facilities, can also contribute considerably to the system and market integration of renewable energies by transferring energy from the electricity sector to the gas, heating or fuel sector [141].

According to their functions and applications, *energy storage systems* describe technical facilities, which can absorb a certain amount of energy by means of a storage medium in a controlled manner (*charging phase*), store the energy for the required period of time (*storage phase*), and release/provide the energy – e.g., in form of electricity, thermal energy for heating/cooling, or a gas – in a likewise controlled manner within a certain period as desired (*discharging phase*) [141, 17].

Focusing on *thermal energy storage* in the context of the thesis, the term has several meanings as well and may describe the storage technology in general, the storage tank, the entire storage system including the periphery, as well as the storage medium itself.

The storage capacity Q, expressed in kJ or kWh, describes the amount of thermal energy stored in the material. This capacity can be referred to the mass or volume of the storage material, which yields the so-called gravimetric $\rho_{\mathrm{en,m}}$ or volumetric energy storage density $\rho_{\mathrm{en,v}}$ expressed in kJ/kg or kWh/m^3, the latter being typically used to compare different TES technologies and define the required size of a storage tank. For solids it is important to note, which volume the storage capacity is referred to: plain material volume without pores (true density), material volume with pores (apparent density), bulk volume of a packed bed of solid (bulk density) [111].

2.1.2 Thermal Energy Storage Technologies – An Overview

The following section presents a brief comparative overview of the different types of TES technologies, which can be classified into sensible, latent and thermochemical storage systems based on the exploited physical or chemical mechanism for the storage of thermal energy [66, 90].

Sensible Thermal Energy Storage (STES) In STES systems thermal energy is stored in thermal form as sensible heat (no phase change of storage medium). The storage capacity is defined by the amount of storage medium, its temperature dependent specific heat capacity and the rise in temperature of the material. In the charging step thermal energy is stored by enhancing the temperature of the storage medium without the occurrence of a phase change, raising its energy content. After the actual storage period, thermal energy is released in the discharging step, which is accompanied by a decline of the temperature of the storage medium correspondingly [111, 164].

The energetic storage density

$$\rho_{\mathrm{en,v}} = \frac{m}{V} \int_{T_{\mathrm{LT}}}^{T_{\mathrm{HT}}} c_p \, \mathrm{d}T \tag{2.1}$$

of a STES system therefore depends on the temperature difference $\Delta T = T_{\mathrm{HT}} - T_{\mathrm{LT}}$ which can be achieved between the charged and discharged state. Both solids and liquids can be applied as storage media. STES represents the most established storage technology, which has already been applied on an industrial scale since the 19$^{\mathrm{th}}$ century and covers a wide operating temperature range depending on the individual application and the thermal stability of the storage material.

Regenerator-type storage systems constitute well established HT storage systems based on STES, employing directly heated solid storage media such as ceramic materials or natural rocks. During charging the heat transfer fluid on a high temperature level, e.g., hot air from the solar receiver in a CSP plant, enters the storage tank at the top and flows downward, forming a characteristic transient temperature profile along the axis of the solid inventory. The direction of the flow is subsequently reversed in the discharging stage, cold fluid entering at the bottom of the storage tank. In this way an axial thermal stratification inside the bed can be maintained, when thermal energy is transferred to and extracted from the storage [163, 167].

Latent Thermal Energy Storage (LTES) Latent heat describes the amount of thermal energy absorbed or released during a first-order phase transition, during which process the subject matter does not undergo a change in temperature (origin of the term "latent" heat). The storage of thermal energy is accomplished by either vaporization of a liquid or melting of a solid. Typically, materials which undergo a solid-liquid phase transition are used as storage media in LTES systems. The materials are also known as *phase change materials "PCMs"* (e.g., $NaNO_3/KNO_3$ [66]). The release of thermal energy during condensation of the vapor or solidification of the liquid also takes place at a constant temperature level.

The energetic storage density of LTES systems based on solid-liquid phase transitions is determined as follows:

$$\rho_{\mathrm{en,v}} = \Delta_{\mathrm{Fus}} h \cdot \rho \tag{2.2}$$

with $\Delta_{\mathrm{Fus}} h$ being the specific enthalpy of fusion of the phase transformation and ρ the density of the storage material. The density of PCMs usually changes from solid to liquid state (lower ρ applied in Eq. (2.2)), leading to volume changes during phase transformation.

Those materials allow to store a large quantity of thermal energy in a narrow temperature range around the phase transition. Due to their higher energy storage density compared to sensible heat storage media, PCMs offer the decisive advantage of lower storage volumes for the same storage capacity and thus lower storage media costs [66].

Sorption Thermal Energy Storage Sorption storage is considered a subcategory of thermochemical energy storage (see next paragraph). Charging the storage material (e.g., using a zeolite as adsorbent) is performed by the desorption of adsorbed molecules (e.g., water vapor) under the supply of thermal energy, followed by a spatial separation from the adsorbent. The storage unit can be discharged on demand by bringing the solid adsorbent and the gaseous component (e.g., water vapor or humid air) together again, releasing thermal energy by means of the adsorption process [17].

Thermochemical Energy Storage (TCS) First activities on thermochemical energy storage (TCS) date back to the 1970s, looking into various reversible decomposition reactions to be applied for solar thermal energy storage [149, 131, 56, 151]. Scientific research in this novel field was mainly motivated by the search for alternative energy sources as a response to the first oil crisis in 1973, with the focus being on electrical power generation by means of solar energy in this case. However, investigations on TCS were not further pursued after this short peak until new interest has been stimulated in the beginning of the 2010s. Research on the identification and improvement of TCS materials as well as on the design of reactor concepts for TCS is hence still at an early stage [111, 49].

The comparatively new concept of TCS is based on the utilization of the reaction enthalpy ($\Delta_R H$) of reversible chemical reactions to convert thermal energy to chemical bond energy, which enables the achievement of storage solutions with high energy storage densities and higher temperature levels. While thermal energy is supplied a chemical compound A is dissociated into the substances B and C (endothermic decomposition), which process represents the thermal charging step:

$$\nu_A A + \Delta_R H \rightleftharpoons \nu_B B + \nu_C C \tag{2.3}$$

The separation of the products B and C basically facilitates a long-term storage of thermal energy, in principle without energy losses, if the products are cooled down to room temperature (RT) and the extracted sensible heat is used efficiently. A recombination of the reactants B and C upon demand leads to the reverse reaction (exothermic) back to the starting material A, releasing the stored thermal energy entirely if full reaction conversion can be reached. This process is termed the thermal discharging step. The products of the individual reaction step can be stored at either ambient temperature or at the operating temperature of the storage process. It is even conceivable to transport the charged storage material to a different location, where the thermal energy can be released on demand [56].

Although the potential of using reversible gas-gas and gas-liquid reactions for TCS was discussed [149, 162], essentially gas-solid reactions have been in the focus of investigations with regard to TCS. Gas-solid reactions are predestined for TCS applications, attributed to their large entropy change which arises from the change of a solid reactant to a solid and gaseous product (accompanied by a large enthalpy change), as well as to the feasibility of a facile separation of the gaseous reactant from the solid product in the course of the decomposition step.

Depending on the operating conditions of the TCS reactor thermal energy can essentially be stored and released at a constant temperature level (at $p = \text{constant}$). In the discharging phase for example, constant temperature levels are attainable, if the released thermal energy is removed at a rate which prevents self-heating [90]. The reaction temperature can be adjusted to the affiliated technical process within certain limits. On the one hand, a reaction system needs to be selected, which exhibits appropriate thermodynamic properties (equilibrium relationship) to match the process conditions. On the other hand, the partial pressure of the gaseous reactant (e.g., by variation of the total pressure) can be adjusted to reach a certain reaction temperature in the charging as well as discharging step (p_{eq}-T_{eq}-correlation). These influencing factors also offer the possibility to apply a thermochemical reaction system for heat transformation (upgrade of thermal energy). Various gas-solid reaction systems which can be classified according to their reaction family – distinguished by different gaseous reactants (H_2, SO_3, H_2O, CO_2 and O_2) – have been investigated to identify potential storage materials, among them metal hydrides, sulfates, hydroxides, carbonates and oxides [66, 111, 15].

The volumetric energy storage density $\rho_{en,v}$ (kJ/m^3 or kWh/m^3) of a TCS system depends on the molar enthalpy of the chemical reaction $\Delta_R H$, the bulk density ρ_{bulk} (effective density) as well as the molecular weight M_A of the starting material:

$$\rho_{en,v} = \frac{\Delta_R H \cdot \rho_{bulk}}{\nu_A \cdot M_A} \quad \text{and} \quad \rho_{en,m} = \Delta_R h = \frac{\Delta_R H}{\nu_A \cdot M_A} \tag{2.4}$$

The corresponding gravimetric energy storage density $\rho_{en,m}$ (kJ/kg or kWh/kg) is defined likewise. The bulk density is usually referred to the educt A. In the case of solid storage materials, ρ_{bulk} is calculated from the true solid density ρ_{true} and the total void percentage ε_{tot} (porosity) of a corresponding packed bed of the solid:

$$\rho_{bulk} = \rho_{true} \cdot (1 - \varepsilon_{tot}) \tag{2.5}$$

Furthermore, the total amount of energy which can be stored in a TCS reactor is dependent on the degree of conversion of the storage material. TCS offers great potential for the development of efficient storage solutions with higher energy storage densities – typically five to ten times higher – compared to more established and mature sensible and latent TES systems [90, 111]. This leads to smaller-sized storage tanks and thus to more efficient and cost-effective TES systems [56].

Table 2.1 summarizes the main characteristics of the introduced TES systems [66, 111, 2, 15, 59, 17].

Table 2.1: Main characteristics and comparison of different types of TES technologies based on various performance parameters.

Performance Characteristics	Type of Thermal Energy Storage System		
	Sensible	**Latent**	**Thermochemical**
Temperature Range and Upper Limit	limited by thermal material stability (concrete < 400 °C [17], $NaNO_3/KNO_3$ molten salt < 600 °C [17], solid ceramics < 1400 °C [164])	T defined by sharp transition [17], broad range of melting temperatures between < 0 °C up to 900 °C [66]	broad range between < 0 °C up to 1400 °C [17]
Attainable Energy Storage Density (Guide Values)	up to ≈50–600 kWh/m^3 of material [66][a], up to ≈0.1–0.3 kWh/kg of material[a]	up to ≈150 kWh/m^3 of material, up to ≈0.05–0.1 kWh/kg of material	up to ≈700 kWh/m^3 of reactant (solid-gas reaction), up to ≈0.5–1 kWh/kg of reactant [111]
Storage Period	limited (thermal losses)	limited (thermal losses)	theoretically unlimited (if gaseous reactant is completely separated)
Lifetime	long	often limited owing to cycling of storage material	depending on reactant degradation and side reactions
Transport	over short distance feasible	over short distance feasible	over long distance feasible
Advantages	low-cost, reliable, simple application using available materials	medium storage density, small storage volumes, constant temperature level at charging and discharging, primarily easy to use	high storage density, low heat losses (storage at $T_{ambient}$ possible), long storage period, highly compact storage, heat transformation possible
Disadvantages	heat losses over time (depending on level of insulation), large storage volume necessary, T is a function of load	heat losses over time (depending on level of insulation), corrosion problems, flammability, low thermal conductivity	high investment costs, possible degradation of storage materials with cycling, technically complex, handling of gas under pressure
Complexity	simple	medium	complex
Technology Status	industrial scale, commercially available (e.g., regenerators, STES in CSP plants, etc.)	pilot scale, commercially available for a few materials at low temperatures	laboratory to pilot scale

[a] Attainable volumetric and gravimetric energy storage densities dependent on the maximum change in temperature of the storage medium; high energy densities achievable with high temperature stable molten salts and high temperature stable solid storage materials such as ceramics and fire clay bricks.

2.2 Gas-Solid Reactions

In this section the physico-chemical background of gas-solid reactions will be addressed, which knowledge is essential for a mathematical description of the proceeding reactions in a TCS reactor. The understanding of the conditions where the reaction takes place from a thermodynamic point of view and the conditions where high reaction rates occur is fundamental for a controlled operation of the reactor. Therefore, the underlying principles of chemical thermodynamics and reaction kinetics of gas-solid reactions, which are closely interlinked, are introduced.

2.2.1 Definitions

Applying the general reaction equation Eq. (2.3) to reversible gas-solid reactions, characterized by different stoichiometric coefficients dependent on the chosen reaction system and participating components, gives the equation

$$\nu_{AB}\mathrm{AB}_{(s)} + Q \rightleftharpoons \nu_{A}\mathrm{A}_{(s)} + \nu_{B}\mathrm{B}_{(g)} \tag{2.6}$$

which is used for the subsequent thermodynamic and kinetic derivations. Supplying sufficient thermal energy Q to drive the reaction – Q equals the product of the number of moles of the reactant n_{AB} and the enthalpy of reaction $\Delta_R H$ in case of complete conversion – the solid compound AB is dissociated into the components A (solid) and B (gaseous). In this thesis heterogeneous redox reactions of pure and binary mixed oxides have been investigated, releasing and absorbing oxygen as reaction gas in the forward and reverse reaction step, respectively.

Hess's Law defines the principle of the energy conservation for a chemical reaction. As the standard enthalpy of reaction $\Delta_R H^{\ominus}$ is independent of the reaction pathway, it can be calculated by the summation of the standard enthalpies of formation $\Delta_F H^{\ominus}$ of all products and reactants at the temperature specified for the reaction [147].

$$\Delta_R H^{\ominus} = \sum_{\text{j products}} \nu_j \Delta_F H_j^{\ominus} - \sum_{\text{i educts}} \nu_i \Delta_F H_i^{\ominus} \tag{2.7}$$

The same approach can also be applied to determine the molar standard entropy $\Delta_R S^{\ominus}$ and standard Gibbs free energy $\Delta_R G^{\ominus}$ of the reaction.

The extent of conversion X describes the progress of the reaction and indicates if the reaction runs to completion, adopting values between 0 and 1. In the case of gas-solid reactions the conversion can be conveniently determined by means of the mass change of the solid reactant, which can be monitored via thermogravimetric analysis. The equation for X is defined separately for the forward and reverse reaction, giving

$$X = \frac{\Delta m}{\Delta m_{\text{theo}} \cdot m_{\text{initial}}} = \frac{m_{\text{final}} - m_{\text{initial}}}{m_{AB} - m_{A}} \tag{2.8}$$

for the forward reaction. Δm represents the observed mass change in the course of the reaction. The term $\Delta m_{\text{theo}} \cdot m_{\text{initial}}$ with the relative theoretical mass change Δm_{theo} according to the stoichiometry of the considered reaction stands for the maximal possible mass change in the case of a

fully completed reaction. The first derivative of X with respect to time t constitutes the reaction rate $\mathrm{d}X/\mathrm{d}t$.

2.2.2 Thermodynamics

The knowledge of the chemical equilibrium state of the proceeding chemical reaction is fundamental for the determination of the relevant process parameters of the TCS system. Thermodynamic fundamentals are exemplarily described for a reversible gas-solid reaction – specified in Eq. (2.6) – with oxygen as gaseous reactant ($\mathrm{B} = \mathrm{O_2}$), the reaction being *reversible* from a chemical point of view.

The equilibrium constant $K_{\mathrm{eq}}(T)$ of a chemical reaction represents the reaction quotient $(a_{\mathrm{A}}^{\nu_{\mathrm{A}}}\, a_{\mathrm{B}}^{\nu_{\mathrm{B}}})/a_{\mathrm{AB}}^{\nu_{\mathrm{AB}}}$ at chemical equilibrium (K_{eq} is a function of the activities a of the chemical species involved in the reaction). The activity of pure condensed phases (solids in this case) can be set to 1. Presuming the gaseous reactant to behave like an ideal gas, its activity can be replaced by its partial pressure. Consequently, the equilibrium constant

$$K_{\mathrm{eq}}(T) = \left(\frac{p\mathrm{O_2}}{p^{\ominus}}\right)^{\nu_{\mathrm{O_2}}} \tag{2.9}$$

for a gas-solid reaction such as in Eq. (2.6) is equivalent to the equilibrium partial pressure of oxygen (decomposition vapor pressure of solid AB), which is referred to the reference pressure $p^{\ominus}$ of 100 kPa at standard conditions, at which oxygen behaves like an ideal gas [27].

The equilibrium constant is linked to the change in the standard Gibbs free energy $\Delta_{\mathrm{R}}G^{\ominus}$ and the standard chemical potential $\Delta_{\mathrm{R}}\mu^{\ominus}$ of the reaction at a given temperature via the reaction isotherm equation:

$$\Delta_{\mathrm{R}}G^{\ominus} = \Delta_{\mathrm{R}}\mu^{\ominus} = \sum \nu_{\mathrm{i}}\mu_{\mathrm{i}}^{\ominus} = -\mathbb{R}T \cdot \ln(K_{\mathrm{eq}}) \tag{2.10}$$

with the chemical potentials $\mu_{\mathrm{i}}^{\ominus}$ of the pure substances i (pure condensed phases and hypothetical ideal gas in Eq. (2.6)) in their standard state. This relation enables the calculation of the equilibrium constant of a reaction based on tabulated thermodynamic data, and therefore the prediction of the equilibrium composition of the considered reaction mixture [27, 16].

The standard Gibbs free energy can also be expressed through the standard enthalpy and entropy changes of the reaction at a given temperature T:

$$\Delta_{\mathrm{R}}G^{\ominus} = \Delta_{\mathrm{R}}H^{\ominus} - T\Delta_{\mathrm{R}}S^{\ominus} \tag{2.11}$$

A transformation of this equation yields the *Gibbs–Helmholtz equation* (see [16], eq. not shown here).

Substituting $\Delta_{\mathrm{R}}G^{\ominus}$ in Eq. (2.10) with Eq. (2.11) yields

$$-\mathbb{R}T \cdot \ln(K_{\mathrm{eq}}) = \Delta_{\mathrm{R}}H^{\ominus} - T\Delta_{\mathrm{R}}S^{\ominus} \tag{2.12}$$

Insertion of Eq. (2.9) in Eq. (2.12) results in the term

$$\ln(K_{\mathrm{eq}}) = \ln\left(\frac{p\mathrm{O_2}}{p^{\ominus}}\right) = -\frac{\Delta_{\mathrm{R}}H^{\ominus}}{\nu_{\mathrm{O_2}}\mathbb{R}T_{\mathrm{eq}}} + \frac{\Delta_{\mathrm{R}}S^{\ominus}}{\nu_{\mathrm{O_2}}\mathbb{R}} \tag{2.13}$$

which describes the correlation between the oxygen partial pressure (pO_2) and the temperature at thermodynamic equilibrium (T_{eq}). It becomes apparent, that in the storage process both charging and discharging temperatures depend on the partial pressure of the gaseous reactant. The standard reaction enthalpy and entropy are commonly approximated as independent of temperature over the range of interest. Plotting the logarithm of different partial pressures versus the corresponding reciprocal temperatures at thermodynamic equilibrium yields a linear slope, which is proportional the standard reaction enthalpy $\Delta_R H^{\ominus}$. The standard reaction entropy $\Delta_R S^{\ominus}$ can be obtained from the constant ordinate intercept.

The derivative of expression Eq. (2.13) with respect to the variable T_{eq} at constant pressure yields the *van't Hoff equation*, also known as the *van't Hoff reaction isobar*, which describes the dependence of the equilibrium constant on the temperature:

$$\left(\frac{\mathrm{d}\ln K_{eq}}{\mathrm{d}T}\right)_p = \frac{\Delta_R H^{\ominus}}{\mathbb{R}T^2} \tag{2.14}$$

To simplify the denotations throughout the thermodynamic analyses in this thesis, terms such as *van't Hoff equation* or *van't Hoff plot* refer to the expression in Eq. (2.13).

If the temperature dependence of the standard reaction enthalpy – described in Appendix A – is neglected ($\Delta_R C_p^{\ominus} = 0$) and the equilibrium constant equals unity ($K_{eq} = 1$ is applied), Eq. (2.12) can be transformed to the so-called *turning temperature* T^*:

$$T^* = \frac{\Delta_R H^{\ominus}}{\Delta_R S^{\ominus}} \tag{2.15}$$

(2.15) states the relationship between the reaction enthalpy $\Delta_R H^{\ominus}$ and the reaction entropy change $\Delta_R S^{\ominus}$ at thermodynamic equilibrium. Temperature T^* defines the turning point of the reaction at the partial pressure of the gaseous reactant corresponding to $K_{eq} = 1$, where the reaction turns to the respective favorable side of the equilibrium. The ratio $\Delta_R H^{\ominus}/\Delta_R S^{\ominus}$ can thus be used as an approximation to screen potential reactions with respect to the equilibrium temperature [149].

From an economical point of view a large enthalpy change $\Delta_R H^{\ominus}$ of the endothermic reaction is essential for achieving high storage densities in relation to the volume of the reaction products. This requirement needs to be accompanied by a large positive entropy change $\Delta_R S^{\ominus}$ for the forward reaction, which magnitude depends on the magnitude of $\Delta_R H^{\ominus}$ [149]. A reaction involving an increase in moles of gases accompanied by a change from a solid phase to the gas phase implicates a large positive entropy change, which is typically the case in dissociation reactions with gaseous reaction products (thermodynamically irreversible process). Consequently, the achievement of higher energy storage densities with gas-solid reactions compared to other chemical reactions can be substantiated based on thermodynamics. In principal, the amount of gas exchanged ($\equiv \Delta m$) – e.g., O_2 released in the forward reaction and taken up in the back reaction – is proportional to the amount of energy converted (corresponding to the reaction enthalpy of the redox reaction).

The *Gibbs' Phase Rule* can be applied to specify the number of possible degrees of freedom (number of system variables which can be chosen independently) of the thermodynamic system:

$$\mathrm{F} = \mathrm{C} - \mathrm{P} - \mathrm{R} + 2 \tag{2.16}$$

where F indicates the number of degrees of freedom (variances), C the number of components, P the number of phases present and R the number of independent reactions. For example, the dissociation equilibrium of the pure oxide Mn_2O_3 to Mn_3O_4 and O_2 according to Eq. (2.6) can be described by three components (Mn_2O_3, Mn_3O_4 and O_2), three phases (Mn_2O_3 (s), Mn_3O_4 (s), O_2 (g)) and one independent reaction. Thus the phase rule yields the degree of freedom F = 1, so that the system can be specified as monovariant. The phase stability diagram of a monovariant system exhibits only a single equilibrium line, as the pressure of the gaseous component is directly correlated to the prevailing temperature (intensive state variables T or pO_2 can be freely chosen) [27]. It has to be noted, though, that redox reactions of mixed oxides have to be distinguished from the behavior of pure oxides. According to the Gibbs' Phase Rule the degree of freedom may increase owing to the occurrence of two-phase regions in the course of the considered redox reaction, where two solid phases coexist in a broader temperature and composition range (molar quantities) [14].

2.2.3 Kinetics of Gas-Solid Reactions – Kinetic Modeling Procedure

The determination of the respective reaction rate equations for the forward and reverse reaction is crucial, in order to describe the influence of the process parameters – pressure of the gaseous reactant and temperature – on the temporal change of the reaction rate of the storage material in the dynamic charging and discharging process of a storage reactor. Moreover, the amount of thermal energy absorbed or released over a specified cycle time can be calculated and controlled. Thermogravimetric measurements constitute the most widespread means to determine the reaction rate and deduce the required kinetic parameters of gas-solid reactions, as those are generally accompanied by mass changes. Owing to the high available sensitivity of the TG-DSC instruments in the microgram range only small sample masses are necessary, which minimizes the effects of heat and mass transfer on the reaction rate with this technique [146].

According to the recommendations of the ICTAC Kinetics Committee the conversion rate of gas-solid reactions (see Eq. (2.6)) can be parameterized in terms of three major variables, namely temperature, extent of reaction conversion and pressure, whose influences on the reaction rate need to be determined independently from each other [145]. The general differential form of the reaction rate equation of a single-step process represents a widely accepted empirical expression for heterogeneous gas-solid reactions [145]:

$$\frac{\mathrm{d}X}{\mathrm{d}t} = k(T) \cdot f(X) \cdot h(p, p_{\mathrm{eq}}(T)) \tag{2.17}$$

The deduced differential form of the reaction rate Eq. (2.17) eventually allows the calculation of the overall conversion curve of the reaction. As real processes commonly take place in more than a single reaction step, Eq. (2.17) represents a rather large simplification of the reality [146]. Nevertheless its application is absolutely adequate for a simplified description of the reaction rate. It may be noted, though, that the application of the reaction rate equation Eq. (2.17) is also critically discussed, e.g., Pijolat *et al.* proposed an alternative approach with a more general

equation based on assumptions related to the nucleation and growth processes of the new solid phase [114].

The direct influence of the temperature on the reaction rate – represented by the rate constant $k(T)$ – can be empirically described based on the exponential Arrhenius equation:

$$k(T) = A \cdot \exp\left(-\frac{E_a}{\mathbb{R} \cdot T}\right) \tag{2.18}$$

The Arrhenius temperature dependence includes the pre-exponential factor A as a measure for the collision rate of the reactants, the activation energy E_a and the universal gas constant $\mathbb{R}$.

The dependence of the reaction rate on the extent of conversion can be described by a variety of available kinetic models $f(X)$, generally representing different reaction mechanisms [63, 145]. Those reaction models can be divided into three major groups (see X-t-plot in Fig. 2.1): Reactions whose rate increases continuously with rising extent of conversion (accelerating models; e.g., power law model), reactions whose rate exhibits a maximum at the beginning and decreases continuously with rising extent of conversion (decelerating models; e.g., diffusion models), and reactions possessing an initial accelerating stage, a maximum reaction rate at an intermediate extent of conversion and a decelerating final stage (sigmoidal models, showing an autocatalytic kinetic behavior; e.g., Avrami-Erofeev models [18, 19, 20]). A detailed mathematical description of the most common reaction mechanism models is specified in Table B.6 [63, 145].

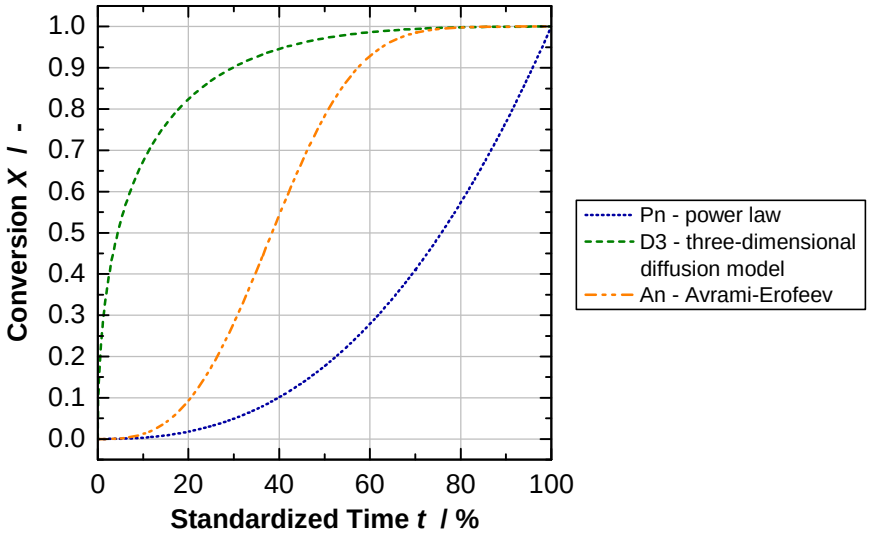

Figure 2.1: Characteristic isothermal conversion curves illustrating three major types of "reaction profiles": Accelerating, decelerating and sigmoidal kinetic models.

Using isothermal measurement data is a convenient way to get a first indication of the relevant reaction types $f(X)$, which is illustrated in Fig. 2.1. Plotting the reaction conversion against time yields characteristic reaction profiles with a distinctive curve shape, as the term $k(T) \cdot h(p, p_{eq}(T))$ in Eq. (2.17) is constant and the shape of the curve is determined by the reaction model alone. However, in the case of non-isothermal measurement conditions both $k(T) \cdot h(p, p_{eq}(T))$ and $f(X)$ vary simultaneously with the temperature, giving rise to sigmoidal curves (X plotted versus T),

which makes it difficult to recognize the type of reaction model by simple inspection and therefore requires other methods of identification [145].

The pre-exponential factor A, the activation energy E_a and the reaction mechanism $f(X)$ represent the so-called *kinetic triplet* of the investigated process step [145].

Although the pressure term $h(p, p_{eq}(T))$ is often neglected in kinetic computations, it can exert a strong influence on kinetic processes [145, 108]. Especially in reversible gas-solid reactions the pressure dependence gains importance, typically specifying the dependence of the reaction rate on the applied partial pressure of the gaseous reactant and the corresponding pressure of the gas at thermodynamic equilibrium. The pressure term can also be referred to as the "driving force" for the reaction and reflects its reversible character. Accordingly, the effect of the pressure term on the reaction rate correlates with the so-called *driving force approach* reported by Obermeier *et al.* [106]. The conversion rate of reduction and oxidation reactions is typically controlled by the oxygen partial pressure p_{O_2} as well as the equilibrium pressure $pO_{2,eq}(T)$ of the reaction, whereas the latter is again affected by arising temperature changes. Thus, the influence of the pressure dependence cannot by neglected in this case. $h(pO_2, pO_{2,eq}(T))$ can potentially adopt different mathematical expressions [122, 145], such as the following, illustrated for the reduction step (oxygen evolution) of a metal oxide redox reaction:

$$\left[1-\frac{pO_2}{pO_{2,eq}(T)}\right]^m \quad \text{or} \quad \left[pO_{2,eq}(T)-pO_2\right]^m \quad \text{or} \quad \left[\ln\frac{pO_{2,eq}(T)}{pO_2}\right]^m \quad \text{or} \quad {pO_2}^m \tag{2.19}$$

The exponent m constitutes the order of the pressure dependence, which is used to adapt the suitable pressure term to the experimental data (see also [122]). The term on the left hand side stands for the most common approach describing reversible solid-state decomposition reactions [145]. Expressions for the corresponding oxidation step can be phrased vice versa.

The mathematical equations of the reaction rates in the form of Eq. (2.17), describing the temperature and pressure dependence of the respective reaction, form the basis for transient reactor models used for the simulation of thermochemical storage reactors. It has to be noted, that the mathematical models evolved in this thesis reflect an approximation of empirical data without claiming a profound interpretation of the underlying physical processes of the reaction. In contrast to the term "reaction kinetics", which describes the intrinsic kinetic parameters of the individual reaction steps based on the actual underlying physical phenomena (e.g., diffusion through a boundary layer or limitation by nucleation processes), the experimentally determined models in this work represent "effective" or "apparent" reaction rates for the reduction and oxidation, comprising apparent values for the pre-exponential factor, the activation energy and the reaction mechanism. Consequently, the parameterized model based on Eq. (2.17) summarizes superimposed physical effects [145].

2.3 Reversible Redox Reactions of Metal Oxides – Literature Review

2.3.1 Fields of Application at Advanced State of Research – Overview

Current investigations for HT applications from 500 °C up to 1100 °C and even beyond are focused on redox cycles employing multivalent metal oxides, which have the potential to undergo reversible redox reactions. Those can be used for various kind of applications, each exploiting different beneficial characteristics of this reaction system. In the following section important functional principles of HT cyclic processes using metal oxides and their respective stage of development are briefly introduced. Thereby a distinction has to be made between the focus on the material utilization of O_2 on the one hand, and the thermal use of the redox cycle on the other hand.

Air Separation – Oxygen Production

In the so-called *Brin Process* the thermal reversibility of the redox reaction between barium oxide (BaO) and barium peroxide (BaO_2) was used for the production of oxygen on an industrial scale. The discovery of this process dates already back to the year 1811 [83]. In the first step, favored at low temperatures and/or high pressure, BaO is oxidized by means of the O_2 in ambient air. As the reaction step is exothermic, it is accompanied by heat release. In the second step, the resulting peroxide BaO_2 is decomposed under heat absorption at high temperature and/or low pressure to generate O_2. Repeating the cycling thus allowed to separate O_2 from air. However, due to the high sensitivity of BaO towards carbon dioxide to form $BaCO_3$, the CO_2 in air had to be removed prior to the application of the described process. This finding by the brothers Quentin and Arthur Brin paved the way for the industrial production between 1886 and 1906, performing the process by shifting only the pressure at a constant temperature of about 700 °C [83]. Around 1900 the more economically liquefaction of air (*Linde Process*) to produce O_2 by cryogenic distillation replaced the Brin Process.

$$2\,BaO\,(s) + O_2\,(g) \rightleftharpoons 2\,BaO_2\,(s) \tag{2.20}$$

The BaO/BaO_2 redox system was reconsidered for a more practical and effective oxygen production by Jin *et al.* in 2001. The authors prepared an oxygen acceptor by pelletizing a mixture of barium peroxide and magnesium oxide. They studied the reaction under isothermal and isobaric conditions with regard to chemical equilibrium and reaction rate to identify appropriate operating conditions. Based on their findings the reaction was found to be potentially applicable to industrial O_2 production [84].

Later on Hutchings *et al.* investigated the role of kinetic and thermodynamic factors on the oxygen absorption and desorption of cobalt oxide. A temperature/pressure-swing absorption/desorption assessment of the Co_3O_4/CoO redox couple for the generation of O_2 showed, that on the one hand high-purity O_2 delivery (> 99 %) is possible by a repetitive HT cycling process.

On the other hand – due to existing drawbacks in terms of heat transfer and oxygen diffusion considerations – this method of O_2 supply for industrial use was rated not economically attractive compared to present methods for delivering pure oxygen, such as *pressure swing adsorption* (PSA) or *vacuum swing adsorption* (VSA) methods, which are applied when lower O_2 volumes are required [78].

Furthermore, redox reactions are also employed in the concept *Chemical-Looping Air Separation* (CLAS), which represents a new method for the production of O_2 by separation from air to be applied in advanced clean coal technologies, such as *oxy-fuel combustion* and *integrated gasification combined cycles* (IGCC) [100, 133].

Oxygen Carriers in Chemical-Looping

In the context of CO_2 capture and storage technologies the so-called *Chemical-Looping Combustion* (CLC) and *Chemical-Looping with Oxygen Uncoupling* (CLOU) are novel combustion technologies for power plants, which enable facile separation and capture of CO_2 as well as a diminution of nitric oxides in the exhaust gas. In those concepts direct contact between combustion air and fuel (gaseous, liquid or solid) is avoided [96, 80]. Instead, a metal oxide is used as oxygen carrier material to transfer O_2 from the combustion air to the fuel. The redox reaction hence provides the oxygen for the process. CLC and CLOU differ in the mechanism of combustion in the so-called *fuel reactor*: In CLC on the one hand, the solid oxygen carrier directly reacts with fuel to CO_2 and water vapor (Eq. (2.21)). As only lattice oxygen is available for the combustion of gaseous fuel, solid fuels have to be gasified in situ or via an external process. In CLOU on the other hand, only oxygen carriers are utilized, which can release molecular oxygen into the gas phase via the reduction of the oxide, reacting with the fuel in a similar way as in conventional combustion processes (Eq. (2.22)). In both cases the exhaust stream of the fuel reactor consists only of CO_2 and H_2O. After condensation of water vapor, pure CO_2 can be obtained and separated for subsequent treatment. The reduced form of the oxygen carrier is re-oxidized by combustion air in the so-called *air reactor* to close the reaction cycle. Primarily two interconnected continuously operated fluidized bed reactors are utilized for this combustion technology, the oxygen carrier being the solid fraction. Numerous monometallic and combined metal oxide systems have been studied for CLC and CLOU regarding their oxygen carrier properties [96, 80].

$$(2n+m)\,Me_xO_y + C_nH_{2m} \rightarrow (2n+m)\,Me_xO_{y-1} + n\,CO_2 + m\,H_2O \tag{2.21}$$

$$C_nH_{2m} + \left(n+\frac{m}{2}\right)O_2 \rightarrow n\,CO_2 + m\,H_2O \tag{2.22}$$

Thermochemical Cycles – Water and Carbon Dioxide Splitting for Solar Fuel Production

Solar-driven thermochemical cycles based on metal oxide redox materials facilitate the solar production of fuels (synthesis gas: hydrogen and carbon monoxide) exclusively from the regenerative

resources water and carbon dioxide [1]. The concept is also known as *water and/or carbon dioxide splitting*, which can also proceed simultaneously. In general, two-step redox reaction processes are considered most efficient for H_2O and CO_2 splitting, providing H_2 and CO. In the first step, the HT endothermic activation step, the metal oxide is reduced to the lower valence metal oxide releasing lattice oxygen using concentrated solar radiation (Eq. (2.23)).

$$2\,Me_xO_y\,(s) \rightleftharpoons 2\,Me_xO_{y-1}\,(s) + O_2\,(g) \tag{2.23}$$

$$2\,Me_xO_{y-1}\,(s) + 2\,H_2O\,|\,CO_2\,(g) \rightleftharpoons 2\,Me_xO_y\,(s) + 2\,H_2\,|\,CO\,(g) \tag{2.24}$$

In the reverse step, the water and/or carbon dioxide splitting step, the reduced metal oxide reacts with water vapor and/or carbon dioxide and incorporates the oxygen from those molecules in its crystal lattice. H_2 and/or CO are formed according to Eq. (2.24) and the redox cycle is completed again. This exothermic oxidation step to regenerate the higher valence metal oxide proceeds at a lower temperature level than the reduction step. Overall, two-step thermochemical cycles can be conducted at significantly lower temperatures compared to the direct thermal dissociation of water vapor into H_2 and O_2.

2.3.2 Thermochemical Energy Storage – Introduction and Technological Opportunities of Redox Reactions

In contrast to the utilization of the oxygen carrier properties of metal oxides, the concept of TCS is targeted on the exploitation of the reaction enthalpies of reversible redox reactions for the storage of thermal energy. The enthalpy change ($\Delta_R H$) in the course of the chemical transformation from the reactant(s) to the product(s) can be utilized to store (reduction to the lower valence metal oxide) and release (oxidation to the higher valence metal oxide) thermal energy according to the following pathway:

$$\text{Thermal Charging} \qquad 2\,Me_xO_y\,(s) + \Delta_R H \rightleftharpoons 2\,Me_xO_{y-1}\,(s) + O_2\,(g) \tag{2.25}$$

$$\text{Thermal Discharging} \qquad 2\,Me_xO_{y-1}\,(s) + O_2\,(g) \rightleftharpoons 2\,Me_xO_y\,(s) + \Delta_R H \tag{2.26}$$

The endothermic reduction step under the release of O_2, driven by the supply of thermal energy, accounts for the thermal charging process (Eq. (2.25)), which can be either performed directly by means of thermal radiation, e.g., in a solar central receiver, or indirectly in a TCS reactor by means of the HTF air. This step is accompanied by the advantage of a facile separation of the gaseous product O_2 from the reduced solid, preventing a re-oxidation for the period of storage. Thus, the energy can be stored basically loss-free over an indefinite period of time. The recombination of the reduced metal oxide and O_2 (from ambient air) leads to the exothermic oxidation step, representing the thermal discharging process by the complete recovery of thermal energy via the release of the heat of reaction (Eq. (2.26)). A schematic illustration of the storage principle is shown in Fig. 2.2.

Some promising metal oxides exhibit this intrinsic advantage to react reversibly with oxygen at high temperatures. A detailed overview of potentially applicable materials is given in Section 2.3.3.

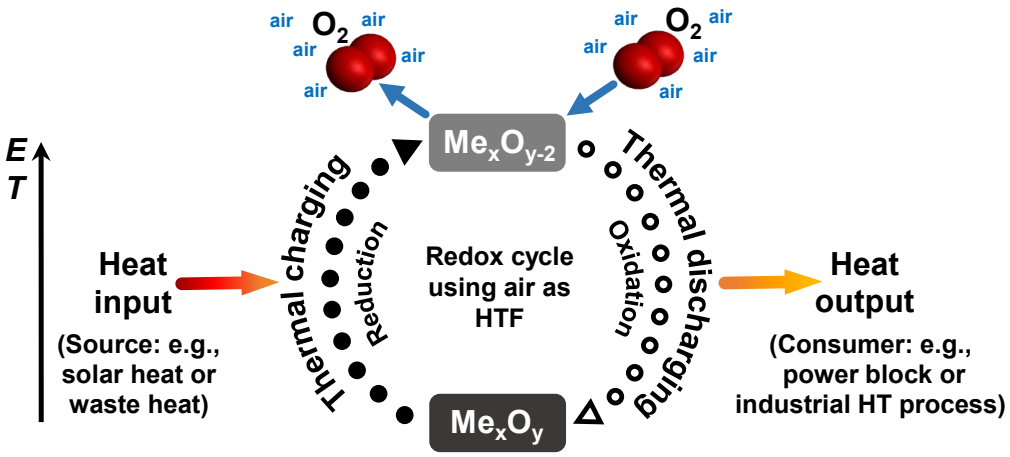

Figure 2.2: Schematic description of the underlying principle of thermochemical energy storage based on reversible redox reactions using air as HTF (E = chemical potential energy).

The metal oxide based TCS concept allows to employ ambient air simultaneously as carrier of the reaction gas O_2 and HTF, which constitutes a nonhazardous heat transfer medium free of charge. Air acts as sink and source of the reaction gas. This approach facilitates a reactor concept with input and extraction of thermal energy by means of a direct contact heat exchange between the gas (air) and the surface of the solid storage material (metal oxide). The concept does not require an additional HT heat exchanger. Consequently, there is no need for intermediate storage of the reactant gas O_2, which offers process-technological advantages and is highly beneficial for future system integration concepts compared to other TCS materials. Otherwise, in case of gaseous products noncondensable at RT, the volumetric energy storage capacity $\Delta_R H^{\ominus}/V_m$ (in kJ/L) would be small due to the large molar volume V_m of the gas [149]. The implementation of a metal oxide storage reactor into a technical system could potentially be realized in the form of an open-loop storage operation using ambient air. Moreover, the great advantage of the infinite O_2 availability – without involving energy consumption for compression of the gaseous reactant – theoretically allows to reach energy cycle efficiencies close to 100 %, if thermal losses to the surroundings are minimized. However, as the HTF outlet temperatures during discharging are generally lower than the HTF inlet temperatures during charging, owing to the temperature gradient necessary for heat transfer, a loss of exergetic storage efficiency has to be taken into account.

2.3.3 Metal Oxides as TCS Materials – Thermal Analysis

Metal oxides reacting according to the specified pathway in Eqs. (2.25) and (2.26) to store thermal energy in form of the reaction enthalpy are the focus of this thesis. The current state of the scientific knowledge on redox reaction based TCS reveals, that the majority of examinations have been carried out by means of thermal analysis using small sample masses mostly on the mg-scale, to identify and improve prospective storage materials. The potential of different pure and mixed metal oxides has been assessed regarding their applicability for TCS by means of thermodynamic and economic analyses as well as thermal analysis measurements in various publications, which

are introduced in the following subsection.

Pure Oxides

Metal oxide storage materials – as well as TCS materials in general – are assessed and selected according to certain material requirements [149, 126, 29, 111], which include both thermodynamic principles and chemical reaction properties, as well as the physical properties of the reactants:

- Reduction and oxidation reactions need to be thermodynamically favored in the temperature and pressure range relevant for the storage operation considered (dependent on prevailing process parameters)
- High specific reaction enthalpies $\Delta_R h$, implicating a high specific storage capacity Q_{chem} of the material
- Complete chemical reversibility of the redox reaction without side reactions and by-products
- High reaction rates of reduction (charging) and oxidation (discharging)
- Small thermal hysteresis between the onset temperatures of the forward and reverse reaction (no kinetic limitations)
- Long-term cycling stability without reactivity degradation allowing constant thermochemical storage performance over innumerable cycles, while maintaining the initial thermophysical and mechanical properties of the solid
- Facile separation of the gaseous reaction product (O_2) prior to the actual storage period, preventing the reverse reaction (stable products)
- Abundant, low-cost, mechanically stable, environmentally friendly and non-toxic materials
- No requirement for high equipment complexity

A practical storage material should meet as many of the above mentioned criteria as possible. It is obvious that the exploitation of the specific reaction enthalpy is not the only decisive factor for an applicability of the metal oxide based TCS concept, to increase the energy storage density of a HT-TES system. Naturally, the concept is highly dependent on the thermodynamic characteristics as well as the kinetic behavior of the redox reaction under the applied operating conditions. Generally various metal oxides are available, exhibiting redox transitions at different temperature levels. Those oxides are introduced in the following. Moreover, a variation of the oxygen partial pressure also facilitates an adjustment of the reaction temperature in a certain range according to the $pO_{2,eq}$-T_{eq} correlation (see Section 2.2.2 and comments in Section 2.1.2).

Several research groups focused on the screening of diverse redox couples regarding their TCS applicability, narrowing down the selection to BaO_2/BaO, Co_3O_4/CoO, Mn_2O_3/Mn_3O_4 and CuO/Cu_2O as the most promising in the temperature range of 500-1100 °C at ambient pressure in air, i.a. [6, 5, 15, 29, 159, 158].

The redox transition BaO_2/BaO, with a specific enthalpy of 474 J/g BaO_2, was first analyzed for TCS regarding kinetics and cyclability around 1980. However, the material lacked in reversibility and the reactivity decreased on repeated cycling [31, 58]. In contrast, a recent paper reported

the potential feasibility of commercially available BaO_2 for TCS, as the reaction system showed redox reversibility over 30 cycles with stable reduction and oxidation rates [38]. However, BaO exhibits a high sensitivity towards moisture and CO_2, forming the corresponding hydroxides and carbonates upon exposure [5].

Among the selection of redox couples specified above, cobalt oxide – reacting from the mixed-valence cubic spinel structure Co_3O_4 to the cubic rock salt structure CoO – can be considered as the most outstanding material due to complete reversibility, high reaction rates (both forward and reverse), a high reaction enthalpy (a theoretical value of ≈844 J/g Co_3O_4 has been reported in the literature) as well as a reasonable cycling stability. This is why it has already been comprehensively analyzed for TCS [6, 37, 29, 78]. However, in spite of the benefits compared to the other storage materials described in this subsection, cobalt oxide is the costliest raw material of the above mentioned, which also entails health and safety issues, as Co_3O_4 is suspected to be carcinogenic (inhalation of cobalt compounds increases risk of developing lung carcinoma [53]).

Pure manganese oxide, possessing a theoretical enthalpy value of ≈202 J/g Mn_2O_3, has been suggested as a promising TCS material by several authors, as it particularly fulfills the essential requirements on a storage material for large-scale applications to be nonhazardous, abundant in nature as well as low-priced [158, 39, 37, 86, 29]. The redox reaction of Mn_2O_3/Mn_3O_4 exhibits a pronounced thermal hysteresis, though, which is characteristic for manganese oxide [40] and implies a strong, highly disadvantageous decoupling of the forward and reverse reaction. Furthermore, re-oxidation rates are slow and appear to decrease continuously in the course of consecutive cycles, which illustrates the poor cyclability of the material [39, 158, 60]. According to André *et al.* the present slow re-oxidation rates can be attributed to the formation of the tetragonal spinel phase Mn_3O_4 (hausmannite), which displays only a poor re-oxidation capability back to the bixbyite phase [13]. It has been found that the Mn_3O_4 oxidation reactivity is highly affected by the synthesis method and resulting morphology [39, 15]. Carrillo *et al.* disclosed, that the reversibility of the Mn_2O_3/Mn_3O_4 redox reaction is strongly influenced by the initial particle size of the sample, giving rise to different irreversible sintering mechanisms and possible degradation of the reactivity. Complete cyclability could be proven for larger particles (127 to 266 nm) over 30 charge-discharge cycles, whereas small-sized particles (65 to 88 nm) suffered from incomplete re-oxidation at some point in the course of cycling, which process further deteriorated from cycle to cycle [39].

Various investigations on the redox reaction of copper oxide concluded, that the material suffers from pronounced sintering effects due to a reduction temperature close to the melting point of the reduced phase Cu_2O (1235 °C), subsequently resulting in slow re-oxidation rates [158, 75, 5, 29, 15]. By contrast, the reduction step of CuO occurs rapidly (reaction enthalpy of approx. 650 J/g [29]). Deutsch *et al.* were able to demonstrate good cycling stability over the course of 20 CuO/Cu_2O redox cycles at 950 °C, performing the reduction step in N_2, the oxidation step in air [52].

(Binary) Mixed Oxides

The diverse drawbacks of pure oxides noted above require the development of improved materials in the form of binary or even ternary mixed oxides, which can be achieved via different synthesis routes (e.g., modified sol-gel based *Pechini method*, or mixing of pure oxides followed by solid-state reaction during heat treatment). In contrast to pure oxides, mixed metal oxides have only scarcely been examined for TCS applications so far. In recent studies some binary metal oxides offered improved material properties in comparison to pure oxides [158, 28, 41, 40, 29, 13], which potential improvements can essentially be classified into the following aspects:

- Enhanced and more stable re-oxidation rates, resulting in lower reaction times
- Increased microstructural stability – hindrance of material sintering – by means of the addition of non-reactive components (incorporation of inert cations)
- Improved long-term cycling stability without degradation of the reaction rates
- Possibility of tuning the reaction temperatures by modifying the composition in terms of the stoichiometric metal cation ratio, essentially facilitating a shift of the redox transition temperature
- Narrowed thermal hysteresis, thus increasing the storage efficiency of metal oxides
- Cost reduction due to a combination of low-cost and high-priced raw materials

Those possible improvements of material properties via the incorporation of secondary cations of different oxidation states and radii, replacing primary cations, could mainly be attributed to the formation of charge imbalances, disorders or increase of anion vacancies, which promote an enhanced anionic oxygen diffusion through the lattice [40, 15]. However, Block and Schmücker reported that the benefit of binary metal oxides is often accompanied by a loss of reaction enthalpy compared to the corresponding pure oxides, which can be attributed to the dilution of the reactive species with a non-reactive component [28, 29]. For an implementation of a TCS storage into different technical processes, a certain flexibility to adjust the temperature level of the reaction is essential. The possibility that mixed metal oxides containing different metal cations allow to adjust the oxide composition and therefore modulate the reaction temperature within a certain temperature range to some extent, makes mixed oxides substantially superior to pure oxides.

Some binary metal oxide systems have been analyzed and evaluated to identify potential storage materials with improved properties compared to the pure oxides. Discovering oxide compositions with different redox transition temperatures, but still appropriate storage material properties, mixed oxides also facilitate to broaden the range of available storage materials in general. The examined systems include, for example, copper oxide/cobalt oxide [29, 13], cobalt oxide/iron oxide [28, 29, 12], manganese oxide/copper oxide [29, 13], manganese oxide/iron oxide [159, 40, 29, 12].

For example, cobalt oxide with around 13 mol-% Fe exhibits enhanced microstructural stability accompanied by improved cyclability (40 cycles studied) in comparison to pure cobalt oxide, however with somewhat lower reaction enthalpy [28]. Furthermore, doping cobalt oxide with copper

has demonstrated the potential to significantly modulate the material characteristics. Especially oxides of cobalt-rich compositions (mole fraction of copper cations between 10 and 30 mol-%) are considered promising TCS materials. It was found, that the amount of the CuO component has to be kept low, since the reaction enthalpy and therefore the possible energy storage density declines with increasing fraction of the secondary Cu cation [29, 13]. Block and Schmücker identified a composition with a Cu/Co molar ratio of 1:9 as the most promising, determining a reduction onset temperature of 865.8 °C and an enthalpy of 457 J/g. Remarkably, the binary oxide exhibits a lower transformation temperature than the phase transition of Co_3O_4/CoO. Enhanced as well as more stable re-oxidation rates could be revealed compared to pure cobalt oxide, which were assumed to be attributed to a stabilization of the microstructure by the non-reactive CuO component against sintering [29].

A major focus of several studies was on the improvement of the downsides associated with the redox cycle Mn_2O_3/Mn_3O_4, namely slow re-oxidation rates, deficient durability over innumerous cycles and a detrimental, large thermal hysteresis. Mixed oxides of the copper oxide/manganese oxide system with Cu in the range between 40 and 80 mol-% feature improved reaction reversibility with equal or even higher reaction enthalpies [13]. Carrillo *et al.* even examined metal co-doping of manganese oxide with Fe and Cu. The best cycling performance along with the highest reduction enthalpy of 165 J/g of all mixed oxides investigated in this study was found for the ternary oxide composed of 79 mol-% Mn, 20 mol-% Fe and 1 mol-% Cu. Significantly higher oxidation rates and a reduced thermal hysteresis compared to pure manganese oxide could be observed [42].

Arising interest has been attracted by manganese oxide/iron oxide, as recent studies have shown, that the above-mentioned drawbacks can be overcome by the incorporation of iron as secondary transition metal into manganese oxide. Significantly higher re-oxidation rates, better long-term cycling stability (75 redox cycles carried out with molar ratio Fe/Mn of 1:4 [43]) as well as a narrowed thermal hysteresis of the redox couple Mn_2O_3/Mn_3O_4 have been reported, overall maintaining the energy storage density [158, 40, 29, 43, 14]. In part, even higher reaction enthalpy values were measured for Fe-doped manganese oxides (e.g., for molar ratio Fe/Mn of 1:4 [40, 14]) compared to undoped Mn_2O_3, thus improving the energy storage capacity. Generally, the manganese-based oxide must contain a certain amount of Fe dopant (at least 20 mol-%, see also Fig. B.2) in order to avoid the appearance of the tetragonal spinel phase (*hausmannite*) during cycling in air (statement equally valid for Cu dopant), owing to the poor reversibility of this phase transition during oxidation (discharging) [14].

Moreover, metal oxides with a perovskite structure $La_xSr_{1-x}Co_yM_{1-y}O_{3-\delta}$ (M = Mn, Fe), in general characterized by a continuous increase of thermal energy stored in the system with rising oxygen non-stoichiometry (δ) according to $ABO_3 + \Delta_R H \rightleftharpoons ABO_{3-\delta} + \delta/2\,O_2$ (perovskite family with metal cation sites A and B), have been screened as TCS media via equilibrium thermogravimetric experiments over a range of temperatures and oxygen partial pressures [23]. The experiments revealed the highest specific reaction enthalpy of 250 J/g ABO_3 for the composition of $La_{0.3}Sr_{0.7}Co_{0.9}Mn_{0.1}O_{3-\delta}$. Even higher reaction enthalpy capacities of up to 370 J/g and

390 J/g have been reached for the $CaB_{0.2}Mn_{0.8}O_{3-\delta}$ (B = Al, Ti) perovskite family, along with an absorption/release of reaction enthalpy up to 1250 °C and reduced material cost owing to higher mass-specific sensible enthalpy storage capacity [24]. Further, Ba and/or Sr perovskite materials with Fe, Co and/or Mn incorporated have been recently evaluated regarding their oxygen exchange capacity and reaction reversibility for solar energy storage (up to 292 J/g reached with $BaCoO_{3-\delta}$) [165].

2.3.4 Reaction Kinetics of Metal Oxide Redox Reactions with Focus on TCS

The kinetic analysis of metal oxide reactions has been reported by several authors within the scope of various applications, including TCS, thermochemical cycles or merely fundamental investigations on material characteristics. In this section a brief literature overview of kinetic modeling approaches for redox reactions of mainly pure metal oxides with regard to TCS is given. Up to date only few approaches have been reported, which cover the modeling of the effective reaction rates of binary oxides. It is especially noticeable, that the influence of the pressure term $h(pO_2, pO_{2,eq}(T))$ is ignored in most of the reported reaction rate models, even though this term specifies the dependence of the reaction rate of gas-solid reactions on the prevailing gas pressure and equilibrium pressure of the gaseous reactant/product and thus affects the process rate significantly.

Pure Oxides In the 1980s Fahim and Ford studied the reaction kinetics of the redox cycle BaO_2/BaO based on isothermal and non-isothermal thermogravimetric techniques in air to evaluate their potential use for TCS, respectively. Chadda and Ford pursued a similar approach to study the kinetics of the CuO/Cu_2O redox transition. Forward and reverse reactions were identified to follow first-order kinetics, respectively [58, 44]. It was assumed, that the reactions are controlled by surface intrinsic kinetics and that the total pO_2 remains unchanged, neglecting the pressure dependence of the reaction rates. The redox couple BaO_2/BaO was also investigated by Carrillo *et al.*, who derived the kinetic triplet for the oxidation of BaO in air and identified a zero-order reaction model for $X < 0.8$ in this case. However, the group solely focused on the temperature range, where the Arrhenius term dominates the reaction rate ($T \leq 450$ °C, further away from the equilibrium). On this account the pressure term in Eq. (2.17) had been neglected as well [38].

Recently, an alternative *model-free* approach, called *non-parametric kinetic (NPK) analysis*, has been applied for a kinetic analysis of the CuO/Cu_2O redox cycle with respect to TCS [52]. According to Jahromy *et al.* this method is based on the discretization of the general kinetic equation (Eq. (2.17)), which results in a rank-one matrix, when only the terms $f(X)$ and $k(T)$ are accounted for. Experimental data are arranged in a matrix to derive the kinetic model by means of tensor rank-one approximation methods to separate the contribution of each variable [82]. As the temperature dependence of the NPK method is limited, though, the Arrhenius equation was introduced to extend the applicable temperature range of the derived kinetic model. However, the

authors did not look into the pressure dependence of the reaction rate [52]. Further studies on copper oxide kinetics were performed with an extended NPK method, which allows the derivation of kinetic models with more than two variables to take the pressure term of Eq. (2.17) into account as well. Based on isothermal runs between 800 °C and 930 °C at different oxygen partial pressures (0.1, 0.2, 0.5, and 1.0 bar), the pressure term could be incorporated into the kinetic model, considering the distance from the equilibrium state. It was clarified that the impact of the pO_2 on the oxidation rate must not be neglected. A suitable reaction model fit was achieved with a 2D nucleation model (Avrami-Erofeev A2) [82].

Muroyama *et al.* conducted a kinetic analysis of the redox reaction of Co_3O_4/CoO with respect to a potential storage application in an Air Brayton Cycle for solar electricity generation, where the reduction step of the integrated two-step thermochemical cycle based on cobalt oxide is intended to be driven by concentrated solar irradiation. The process rates are parameterized through Eq. (2.17) in terms of the variables temperature, extent of conversion and pO_2. A weighted non-linear regression method was applied to fit appropriate reaction rate laws to the experimental TG data. The reduction rate was represented by an Avrami-Erofeev model with a power rate term to capture the dependence on the prevailing pO_2 as well as $pO_{2,eq}$ (T-range 840-940 °C). Remarkably, no evident dependence on pO_2 could be discovered within the scope of non-isothermal oxidation measurements in O_2 atmospheres between 5% and 100% (in Ar), analyzing the oxidation during heating at 10 K/min up to ≈600 °C. This observation was attributed to ionic diffusion of Co and O trough the oxide to be the limiting mechanism in the range between ≈180 °C and ≈480 °C, which is why the reaction could be described by the 3D diffusion model in this range [103].

Pestalozzi investigated the reaction kinetics of the redox couple Mn_2O_3/Mn_3O_4 with respect to TCS by means of a small differential packed bed reactor, as potential diffusion limitations were assumed to be reduced in contrast to a thermogravimetry setup. A kinetic rate law based on the combined Šesták model was derived for the redox reaction as a function of temperature only. The author states that, while keeping the O_2 mole fraction constant (air), the pressure term $h(p, p_{eq}(T))$ in Eq. (2.17) is also considered constant and is therefore incorporated into $k(T)$. However, as the oxidation rate increases up to ≈725 °C and decreases at temperatures closer to the equilibrium, two separate kinetic parameter sets had to be calculated [112].

Several studies on the reduction kinetics of Mn_2O_3 to Mn_3O_4 have been reported within the scope of thermochemical cycles for solar hydrogen production by water splitting (e.g., see [30, 9]). As the experiments were generally carried out in an inert atmosphere (N_2 or Ar), the released O_2 and therefore the pressure term in Eq. (2.17) was not considered. Botas *et al.* determined the activation energy based on a *model-free isoconversional method*, the kinetic model and pre-exponential factor based on a multivariate non-linear regression method. The reduction process was found to follow a first order kinetic model [30]. Alonso *et al.* exposed the oxide to high-flux thermal irradiation under Ar to derive the kinetic rate law parameters under similar process conditions as existing in highly concentrating solar systems, using a methodology combining master plots and model fitting by means of Eq. (2.17). Similarly, the authors also described the

reaction to follow an nth-order mechanism ($n = 0.93$) [9].

Mixed Oxides Carrillo *et al.* targeted a detailed understanding of the redox kinetics of iron-doped manganese oxide with a molar ratio Fe/Mn of 1:4 for a future deployment in CSP plants. Rate law models based on the general kinetic equation (Eq. (2.17)) have been determined for the reduction and oxidation reactions (the latter valid between 650 °C and 725 °C). Both reactions could be described by a nucleation and growth mechanism, applying the empirical Šesták-Berggren formula for a more accurate description for $f(X)$ in their work. However, the dependence of those reaction rates on the pO_2, accounted for by the pressure term in Eq. (2.17), which inclusion would be important for reactor modeling and future reactor development, has not been taken into account. As the oxidation rates were expectedly decreasing in the temperature range closer to the equilibrium (725-800 °C), the reported Arrhenius plot gave negative E_a values in this range, which have no physical meaning. This is why the authors excluded the data in this temperature range from the calculation of E_a and A [43].

A shrinking core model was applied by Hamidi *et al.* to fit the reaction rate expression to non-isothermal experimental data of the reduction of an iron-manganese oxide with a molar ratio Fe/Mn of 2:1 (spherical particles of 0.5-1.0 mm). The authors presumed that the reduction rate in air is controlled by internal diffusion of O_2 followed by external diffusion of O_2 through the boundary layer between the particles and surrounding air atmosphere [71]. Al-Shankiti *et al.* identified two different reaction mechanisms for the oxidation of the reduced phase $MnFe_2O_4$, as the reaction proceeded by a diffusion-controlled mechanism without a phase change at first, followed by a nucleation and growth mechanism [8].

2.3.5 Metal Oxides as TCS Materials – Thermochemical Storage Reactors

Investigations on Laboratory-Scale

In contrast to examinations by thermal analysis on mg-scale, a larger experiment is able to provide information about the superimposed effects of heat and mass transport processes coupled with the chemical reaction. Up to date only few experimental studies on reactor types and storage concepts for HT-TCS have been described in the literature, where air utilized as HTF directly flows through the bulk of the reactive metal oxide material both in the thermal charging and discharging stage. The main focus was generally on a principal demonstration of the storage feasibility on lab-scale.

The TCS concept based on metal oxides has been verified for the first time by Wong *et al.* using a packed bed (Ø = 25 mm, about 76 mm in height) of Co_3O_4 as well as MnO_2-10 % Fe_2O_3 powder in a small quartz tube reactor, respectively. The peak bed temperature illustrated the release of thermal energy due to the proceeding oxidation in air, indicating a reaction front traveling down the bed [159, 158].

Our previous experiments performed with a packed bed of manganese oxide in powder form (≈206 g Mn_2O_3) indicated channeling, such that a homogeneous flow of the HTF air through

the powder bed (Ø = 54 mm, about 140 mm in height) was hampered [155]. We also concluded, that the oxidation reaction posed the limiting step in the storage cycle, whereas the rate of the reduction reaction could be considered sufficient with respect to heat input and achievable power level. Thereupon, use of granular manganese oxide (≈422 g Mn_2O_3) implicated an improved gas flow through the packed bed (Ø = 54 mm, about 136 mm in height), but a degradation of the oxidation rate as well as particle agglomeration – both caused by severe sintering – could not be averted [153].

Furthermore, Deutsch *et al.* performed cycling tests with a fixed bed of 50 g CuO granulate (Ø = 40 mm) in the scope of a kinetic analysis, where the reduction was performed in N_2, the oxidation in synthetic air. However, heavy sintering occurred over the course of 20 cycles, blocking the reaction after a few cycles [52].

Directly irradiated rotary kilns – operated in batch mode in air atmosphere – were investigated with regard to on-sun reduction under absorption of direct radiation and off-sun oxidation, respectively, applying the redox pairs Co_3O_4/CoO (30 cycles conducted by Neises *et al.* [104]) and CuO/Cu_2O (3 cycles conducted by Alonso *et al.* [10]). Figure 2.3 (left) shows a picture of the first-mentioned rotary kiln, operated with Co_3O_4/CoO and installed at a solar furnace in Cologne, Germany. It was concluded, that a measurement of the actual reaction temperature of the sample inside the reaction chamber turns out to be difficult with rotary kilns and could not be accomplished by means of the presented setups. This is why fundamental relationships between the reaction temperature and oxygen release/uptake under the prevailing conditions could not be assessed. In order to increase the reactor efficiency by means of an operation at constant temperature (heating up the reactor only once during ramp-up), Tescari *et al.* designed a continuously operated rotary kiln with improved mixing for powder material. Subsequent storage discharging in terms of the oxidation was planned to be carried out in a separate reactor [139].

The design and construction of an irradiation independent TCS particle reactor ($Ø_{inner}$ = 142 mm; 650 mm in total height) for a larger scale storage capacity of up to 100 Wh Mn_2O_3/Mn_3O_4 has been reported by Álvarez *et al.*, which can be operated flexibly as fixed bed or fluidized bed depending on the chosen experimental conditions (HTF gas velocity). The lab-scale setup is illustrated in Fig. 2.3 (middle) [94, 93].

Furthermore, small structured perforated monolithic bodies made entirely of pure cobalt or manganese oxide, shaped as dense, flow-through pellets (Ø = 28.5 mm, about 4.4 mm in height) with a mass of 9-10 g, have been given consideration for TCS utilization by Karagiannakis *et al.*. Oxygen evolution profiles were measured during thermochemical cycling experiments in air (up to 10 cycles) employing a single pellet placed in a tube reactor. Due to better heat transfer characteristics between the HTF and the storage medium the structured bodies demonstrated improved redox kinetics compared to powder samples [86]. Pagkoura *et al.* evaluated advanced cobalt oxide–alumina and cobalt oxide–iron oxide composites, also shaped as flow-through pellets, which showed improved thermomechanical stability while reasonably keeping up the redox performance [110].

Figure 2.3: Selection of experimental setups of thermochemical energy storage reactors reported in the literature: Solar-heated rotary kiln (left), reprinted from [104], copyright 2012, with permission from Elsevier; packed bed TCS reactor (middle), reprinted from [93], copyright 2016, with permission from AIP Publishing; pilot-scale TCS unit consisting of Co_3O_4 coated cordierite honeycomb structures (right), reprinted from [140], copyright 2017, with permission from Elsevier.

Further studies focused on extruded monolithic honeycomb structures based on cobalt oxide compositions with a mass of 14.0-14.8 g (Ø = 30 mm, about 28 mm in height) as well as inert cordierite honeycomb substrates coated with Co_3O_4 to be applied as active redox reactors/heat exchangers [109]. Karagiannakis *et al.* continued the evaluation of small-scale extruded honeycomb structures of pure Co_3O_4 and cobalt oxide–alumina composites (Ø = 28.5 mm, about 30 mm in height, 16-31.6 g) for an application as monolithic TCS reactors. Thermal cycling of the reactive honeycombs in air (up to 116 cycles) was conducted in a FeCrAl alloy tube enclosed by an electrical furnace with ceramic insulation, measuring the O_2 release/consumption as well as gas inlet and outlet temperatures. Composite materials turned out to reduce swelling intensity – observed with honeycombs made of pure Co_3O_4 – and to substantially improve macro-structural stability upon thermal/redox cycling [85].

Tescari *et al.* described the setup of a first pilot-scale thermochemical storage unit based on Co_3O_4/CoO coated cordierite honeycomb structures as storage medium. The prototype reactor consists of two chambers (see Fig. 2.3, right), each containing a stack of inert honeycomb supports coated with 44 kg of redox active material, giving an overall reactor storage capacity of 47 kWh (sensible and chemical storage). In total 22 thermochemical charge-discharge cycles have been carried out during the campaign to demonstrate the concept at pilot-scale. However, the measurement of the O_2 concentration turned out to be unreliable in the pilot-scale system, which is why the reaction conversion could only be calculated based on the estimated thermal energy stored in the system [140].

Hybrid Sensible-Thermochemical Energy Storage Concepts

The concept of high temperature TCS implicates a high degree of thermal energy stored as sensible heat due to the elevated working temperatures of the system, typically temperatures above the reduction temperature in the charging stage. Correspondingly, this amount of thermal energy constitutes one of the most important intrinsic aspects and also challenges of this TCS technology based on metal oxides, which cannot be neglected in the storage process and overall system examination.

On this account, the first "hybrid" or "combined" storage concepts using sensible and thermochemical energy storage simultaneously in one single storage unit have been proposed to enhance the overall energy storage density of the unit [139, 7, 136], ranging from concepts with completely reactive material, to combined and even cascaded storage concepts to integrate sensible heat.

A cascaded thermochemical storage concept for CSP plants operated with air as HTF, which is based on the idea to employ a cascade of porous structures with different reactive metal oxide materials incorporated, has been proposed by Agrafiotis *et al.*. Those structures could be spatially arranged along the height of the storage module in such a way, that their characteristic redox reactions cover complementary temperature ranges [5]. The authors performed experimental tests with a lab-scale cascaded configuration of cordierite honeycombs and foams ($\varnothing = 25$ mm) coated with Co_3O_4 and Mn_2O_3, employing redox oxide quantities in the range of 15-150 g. Although thermal effects of the redox reaction could be demonstrated for Co_3O_4-coated honeycombs and foams, any beneficial thermal effects of the Mn_2O_3/Mn_3O_4 pair system were not evident, attributed to the unfavorable redox properties of pure manganese oxide [3].

2.4 Objectives

In the search for a practical TCS material, which exhibits a high specific storage capacity for applications at elevated operating temperatures between 500 °C and 1100 °C, the reversible reaction of metal oxides offers the possibility to enhance the storage capacity at high temperatures compared to established inert materials used up to date for the storage of sensible heat. The basic idea of this novel storage concept is to utilize ambient air both as HTF for direct input/extraction of thermal energy and as source of the reaction gas oxygen. This – at first glance – simple concept implicates several potential benefits, which have been elucidated in Section 2.3.2.

The current state of scientific knowledge in the field of TCS based on redox reactions is still at an early stage, which is why relevant literature data on material properties and thermochemical behavior of metal oxides with respect to TCS are scarce. On this account the thesis is aimed at gaining a substantiated understanding of the reaction behavior as well as identifying the determining aspects for this metal oxide based TCS technology. Starting with promising metal oxides emerged from a literature research on TCS materials (Sections 2.3.3 and 3.2), a suitable storage material has to be selected as reference material for more profound investigations. As

the choice of pure oxides potentially eligible for TCS applications is only limited, the material screening in this work will also focus on binary mixed oxides. Those offer several advantages compared to pure oxides (Section 2.3.3), but have only been scarcely characterized in view of TCS with only few material properties available up to now. The potential materials will be examined by means of thermal analysis and compared with respect to different criteria, such as reversibility of the reaction, cycling stability and specific reaction enthalpy. Subsequently, the selected material has to be characterized regarding thermodynamic aspects, kinetic behavior and thermophysical material properties. Based on this characterization, model equations for the reaction rate as well as for prospective heat and mass transfer kinetics of the storage material can be derived (essential for mass and energy balance equations in storage reactor modeling).

In contrast to measurements by means of thermal analysis, the oxygen concentration and temperatures in a storage reactor vary depending on the prevailing conditions, both along the height of the reactor and over the course of the corresponding charging/discharging period (redox reaction step). Up to date generic fundamental investigations on the understanding of the redox reaction behavior during dynamic thermal charging and discharging under different operating conditions in air have received only little attention, taking the arising change of the O_2 concentration in the gas phase (HTF) and prevailing temperature levels in the reactive bed into account. Hence, fundamental correlations with respect to the temperature and pressure dependence of the redox reaction have not been reported on a larger scale so far. For this purpose a test rig with a direct-flow storage reactor for a larger amount of storage material needs to be designed on an appropriate scale. A systematic examination on a larger scale is highly essential, as the redox reaction taking place in a storage reactor is superimposed by heat and mass transfer phenomena compared to the reaction studied by thermal analysis methods on mg-scale. On the one hand the experiments serve to demonstrate the general feasibility of the storage concept. On the other hand the determining influencing factors on the reversible redox reaction can be derived from variations of the operating parameters. It should be noted that the studies presented in this thesis have a generic approach and are therefore independent of any assumed source of the HTF air (e.g., solar air receiver, industrial waste heat) or the operation principle (e.g., regenerator-type storage system, fixed bed or moving bed).

All investigations are in fact technology-oriented. However, specific prospective technical applications for TCS based on redox reactions are yet to be defined. Based on the findings obtained from the experimental campaign, promising potential fields of future technical application for this TCS technology are deduced in the last part of this work.

3 Metal Oxides for TCS – Material Characterization

Prior to the preselection of potential storage materials and eventually the characterization of the most promising storage material candidate, the method of thermal analysis is introduced, which represents the main tool for the investigation of the reactivity in this work. As only milligram quantities of the metal oxides are applied, this method allows to study thermodynamic and kinetic aspects of the redox reaction, widely excluding heat and mass transport limitations. All other methods for the characterization of the physical and thermophysical material properties – applied throughout this chapter – are briefly described in Appendix B.1.

3.1 Analytical Method of Choice: Thermal Analysis

Generally, the term *thermal analysis* denotes a variety of measuring methods to study one or more sample properties, while the sample is subjected to a controlled temperature program. The program may be isothermal ($T = \text{const.}$) or non-isothermal with linear temperature changes ($T = T(t)$) [70, 34]. For the thermodynamic and kinetic analyses of redox reactions the conversion of the reaction can be determined as a function of time (or temperature) at predefined temperatures and gas compositions. As the process variables temperature and partial pressure of the reactant can be chosen freely by the operator, *thermogravimetric analysis* (TGA) – or simply denoted *thermogravimetry* (TG) – and *differential scanning calorimetry* (DSC) represent the methods of choice for the investigations in this work. The term *calorimetry* stands for the measurement of the heat changes occurring during a process [70]. Both measuring methods facilitate an exact determination of the reaction rate and conversion at defined process conditions. Therefore, all measurements are carried out with a simultaneous thermal analyzer (device STA 449 *F3 Jupiter*® from NETZSCH Gerätebau GmbH), coupling TGA and DSC. The instrument is equipped with a silicon carbide furnace, which allows measurements in a temperature range from RT to 1550 °C. A TG-DSC sample carrier (Pt/Rh) with type S thermocouples is employed. The schematic setup of the instrument is illustrated in Fig. 3.1.

3.1.1 Thermogravimetry

Thermogravimetric analysis represents an analytical technique, which measures the mass change of a sample subjected to a preset temperature program under a defined gas atmosphere in the sample chamber [34]. As shown in the setup of the thermobalance in Fig. 3.1, the entire TG-DSC sample carrier – equipped with a thermocouple – is positioned on a balance. In this way both mass change obtained from the gravimetric signal and sample temperature can be measured continuously. The

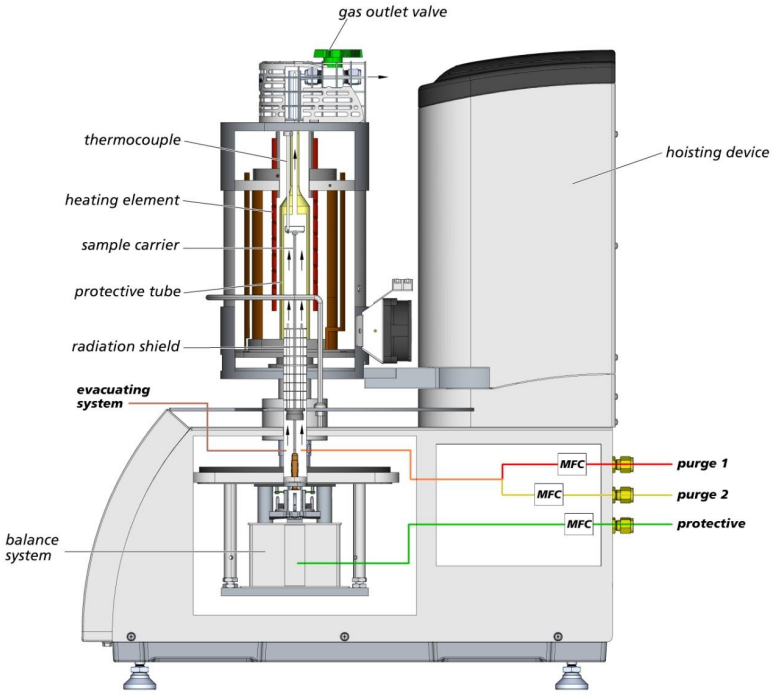

Figure 3.1: Setup of the measuring apparatus STA 449 *F3 Jupiter*® for simultaneous thermal analysis from Netzsch Gerätebau GmbH [105].

mass change is used for the determination of the reaction conversion (see Section 3.1.3). For the mass signal a measuring error of $\pm 1\ \mu$g is specified based on the data sheet of the instrument.

3.1.2 Differential Scanning Calorimetry

DSC is used to obtain information on thermal changes in a sample by measuring the difference in the amount of thermal energy required to increase the temperature of a sample and an inert reference as a function of the temperature. The term "differential" emphasizes the setup of the sample carrier, which consists of two identical temperature sensors, one used for the sample and one for the reference. The signal from a differential scanning calorimeter depends on the difference between the response of the two sensors owing to the thermal changes to be examined [70]. If the sample undergoes a phase transformation, more or less heat needs to flow to the sample compared to the reference in order to maintain both at the same temperature, depending on the endothermic or exothermic nature of the process. In the case of the *heat flux operating principle* – which the applied instrument is based on – the temperature difference between the sample and the reference is recorded as a direct measure of the difference in the heat flow rates (thermal power) to the sample and the reference. The heat flow rate difference is assigned by a suitable sensitivity calibration based on the heat of fusion of known salt standards or metals, preceding the actual heat flux measurement of the unknown sample [34]. Thereupon, the amount of thermal energy absorbed or released in the course of a physical phase transformation or chemical reaction can be calculated. Integration of the heat flux curve allows the determination of the specific enthalpy of the redox reaction, which is, e.g., crucial to determine the energetic storage density of the TCS material (see

Eq. (2.4)).

3.1.3 General Information on Experimental Procedure and Data Analysis

Measurement Conditions and Experimental Procedure In the experiments a dry flow of nitrogen 5.0 is used as purge (purge 2) and protective gas. A flow of oxygen 5.0 is utilized as purge gas (purge 1), which is mixed with nitrogen to adjust the desired oxygen volume fractions at ambient pressure. The overall gas flow rate surrounding the sample is set to 100 NmL/min, with the balance being protected by a nitrogen flow of 30 NmL/min at all times. Hereinafter a gas composition of 20 NmL/min O_2 and 80 NmL/min N_2 is referred to as air. The built-in mass flow controllers have an accuracy of ± 1 % within the applied flow range. The absolute pressure inside the reaction chamber is equal to the atmospheric pressure p_{ambient}, which is measured with a hand-held measuring device (Co. Lufft, XA1000 with integrated air pressure sensor, accuracy of 0.05 kPa at 25 °C and 101.325 kPa) prior to each measurement.

Pt/Rh-crucibles with a volume of 85 µL are used throughout all measurement series, leaving the reference crucible empty. A general temperature and sensitivity (heat flow) calibration of the TG-DSC sample carrier is conducted on the basis of the phase transition of salt standards prior to the beginning of the measurement series. A separate blank measurement with an empty sample crucible is carried out for the baseline correction of each single sample measurement, applying the same temperature program and gas atmosphere. The measurements described in this thesis have been conducted in *sample temperature control* (STC) mode, controlling the sample temperature – in fact the reference temperature is measured and controlled – instead of the furnace temperature. On this account it is assumed, that the temperature of the sample corresponds to the controlled temperature of the reference thermocouple below the DSC cell.

The crucibles are used without a pierced lid, in order to ensure optimal O_2 exchange between the metal oxide sample and the surrounding gas atmosphere, which is crucial for the thermodynamic and kinetic analyses conducted in this work. Crucibles equipped with pierced lids are known to accomplish more accurate results for caloric measurements to visualize and account for even small thermal effects. This is why the reference and sample crucible are used with a pierced lid exclusively in the calibration and measurement runs conducted for a study of the specific reaction enthalpies by DSC in air (see Section 3.3.3). It has to be noted, though, that using a pierced lid can potentially lead to a shift of the onset temperature due to limited gas transport through the pinhole, especially in the case of the oxidation reaction. A detailed description of the experimental procedure for each specific measurement series is given in the result sections 3.3.2 and 3.4.1 to 3.4.3.

Two different measuring methods are employed to study the redox reactions in this chapter: The most frequent temperature program employs a linear temperature change with respect to time, so that $\beta = \mathrm{d}T/\mathrm{d}t = \mathrm{const.}$ [145], the magnitude of the heating rate β generally having a large influence on the measurement results [70]. As illustrated in Fig. 3.2a, the reactions are carried out in the

course of a continuous change in temperature, while the pO_2 is kept constant. Alternatively, the sample may be held isothermally ($\beta = 0$), so that reactions can be initiated by an abrupt change in the pO_2 (see Fig. 3.2b). On the one hand, dynamic measurements constitute an appropriate method to analyze the cycling stability of different materials in air (see Section 3.3.4) as well as to examine the reaction rate of the reduction step. On the other hand, the abrupt pressure change in isothermal measurements results in a step response of the reaction, which offers the possibility to study the influence of pressure and temperature on the reaction independently from each other. This method is especially convenient to examine the reaction rate of the oxidation step.

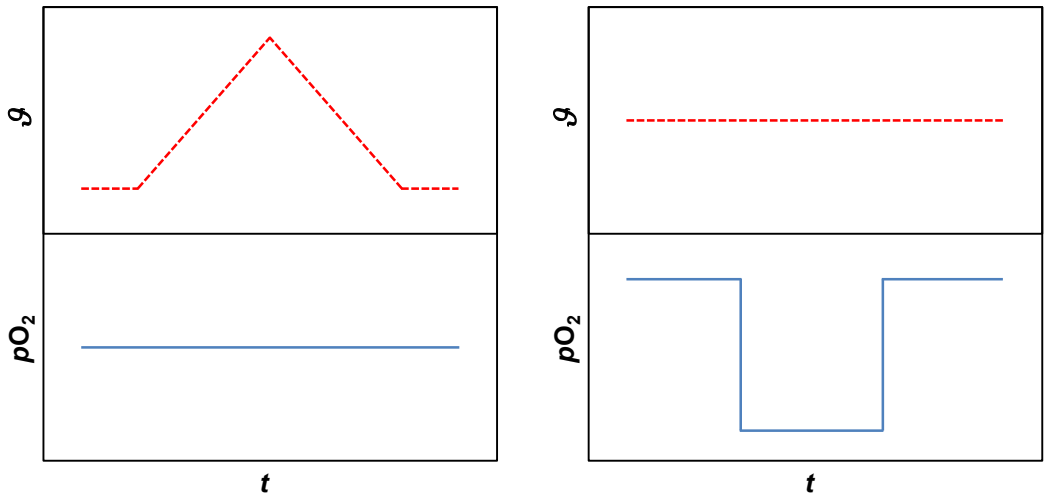

(a) Non-isothermal measurement at a constant heating and cooling rate.

(b) Isothermal measurement.

Figure 3.2: Schematic illustration of typical measuring programs applied in thermal analysis measurements throughout this work, varying either temperature (ϑ) or oxygen partial pressure (pO_2) to initiate the corresponding redox reaction.

Data Analysis Methods The calorimetric signal is chosen for the calculation of the extrapolated peak onset temperatures of the redox reaction in the scope of measurements at different heating and cooling rates [70, 73, 34]. Data evaluation is performed using the software Netzsch Proteus® 6.1. A detailed description of the procedure is given in Appendix B.3.2. It is important to note that the approach to determine extrapolated peak onset temperatures for the assessment of the reactive temperature ranges of the reaction (see Section 3.4.1) represents an approximation, as those temperatures per se do not reflect the actual beginning of the reaction, which is apparently registered prior to that. The actual reaction start turns out to be quite difficult to assess in a reproducible way. On this account the chosen approach stands for a reproducible evaluation methodology. Hereinafter the abbreviated term *onset temperature* always refers to the *extrapolated peak onset temperature*. It is defined as the beginning of the reaction. In this work the term t_{oo} denotes the period between the extrapolated onset and offset temperature, determined by means of the DSC signal at all times. More significant is the actual reaction time t_{rxn}, which can be

estimated according to the changes of the first derivative of the thermogravimetric curve, indicating the beginning and the end of the mass change owing to the respective redox reaction process.

Moreover, specific reaction enthalpies are analyzed according to the following procedure (crucibles with pierced lids applied for DSC measurements, see comments above): Determining the peak area of the reduction step, the baseline is constructed using a tangential function due to a small offset of the signal between the oxidized and reduced state of the material (boundaries are set at the visible change of the first derivative of the DSC curve). The peak area of the oxidation step is determined likewise, applying a tangential function for the baseline construction. The calculated specific enthalpy is referred to the weighted sample in the oxidized state, respectively.

The largest error in the procedure of determining the reaction enthalpy of the redox reaction derives from the conducted sensitivity calibration of the sample carrier. Salt standards for sensitivity calibration are only available up to 808 °C ($BaCO_3$). Thus, the calibration curve is extrapolated for the temperature range above, which causes a larger error for higher temperatures. Moreover, the method for the baseline construction is crucial for the determination of the specific enthalpy and needs to be carefully chosen. Accurate setting of the boundaries for the baseline construction is also important. Considering those potential sources of error an uncertainty of the determined values of approximately ±8 % can be estimated.

Thermogravimetric measurements provide the basis for kinetic analyses of redox reactions [146], allowing a facile determination of the conversion of the corresponding reaction step by means of the measured mass change of the storage material. The relative experimental mass change (in %) is calculated as follows:

$$\Delta m_{\mathrm{exp,Red}} = 100\left(1-\frac{m_{\mathrm{final}}}{m_{\mathrm{initial}}}\right) \quad \text{and} \quad \Delta m_{\mathrm{exp,Ox}} = 100\left(\frac{m_{\mathrm{final}}}{m_{\mathrm{initial}}}-1\right) \tag{3.1}$$

with m_{initial} being the initial weight prior to the reaction and m_{final} being the final weight after the reaction of the corresponding redox step.

The non-normalized extent of conversion – as applied in Section 3.3.4 – is referred to the relative theoretical mass change $\Delta m_{\mathrm{theo,Red}}$ and $\Delta m_{\mathrm{theo,Ox}}$ (in %) according to the stoichiometry of the reaction (see Eqs. (B.2) and (B.3) in Appendix B.3.3):

$$X_{\mathrm{Red}} = \frac{m_{\mathrm{initial}}-m_{\mathrm{t}}}{(\Delta m_{\mathrm{theo,Red}}/100)\cdot m_{\mathrm{initial}}} \quad \text{and} \quad X_{\mathrm{Ox}} = \frac{m_{\mathrm{t}}-m_{\mathrm{initial}}}{(\Delta m_{\mathrm{theo,Ox}}/100)\cdot m_{\mathrm{initial}}} \tag{3.2}$$

m_{t} denotes the current sample weight at time t. The normalized extent of conversion for the reduction X'_{Red} and oxidation X'_{Ox}, ranging from 0 to 1, is defined as:

$$X'_{\mathrm{Red}} = \frac{m_{\mathrm{initial}}-m_{\mathrm{t}}}{m_{\mathrm{initial}}-m_{\mathrm{final}}} \quad \text{and} \quad X'_{\mathrm{Ox}} = \frac{m_{\mathrm{t}}-m_{\mathrm{initial}}}{m_{\mathrm{final}}-m_{\mathrm{initial}}} \tag{3.3}$$

Equation (3.3) is applied for the kinetic analyses in Section 3.4.2 and Section 3.4.3.

The pO_2 – relevant for thermodynamic estimations and kinetic analyses – is determined based on the product of the employed oxygen volume fraction of the gas flow (which equals the molar fraction y_{O_2}) and p_{ambient} in the laboratory, to account for natural fluctuations (see Eq. (B.1)).

3.2 Preselection of Potential Storage Materials Based on a Literature Review

Thermodynamic Equilibrium Data As mentioned in Section 2.3.3, the choice of pure metal oxide systems suitable for TCS is rather limited. Only few metal oxides are potentially applicable for TCS based on their thermodynamic properties. Candidates are primarily oxides of the metals Mn, Fe, Co and Cu, which can be assigned to the first transition metal period in the periodic table. Table 3.1 specifies the temperatures of chemical equilibrium for relevant redox couples in the range between 500 °C and 1400 °C. Chemical equilibria have been determined for a pO_2 of 21.228 kPa in atmospheric air by means of the calculation of the corresponding equilibrium constants $K_{eq}(T)$ in the temperature range of interest, using Eq. (2.10) along with Eq. (2.9) and $\Delta_R G^{\ominus}$ according to Eq. (2.7) (Hess's Law with values of $\Delta_F G^{\ominus}$ tabulated in [27]).

Table 3.1: Preliminary selection of potential metal oxide redox couples for TCS: Equilibrium temperatures and reaction enthalpies calculated for a pO_2 of 21.228 kPa (atmospheric air with $y_{O_2} = 0.2095$ at total pressure of 101.325 kPa), calculated based on available thermochemical property data listed by Barin [27].

Metal Oxide Redox Couple	ϑ_{eq} °C	$\Delta_R H^{\ominus}$ kJ/mol educt	$\Delta_R h$ kJ/kg educt	$\rho_{en,v}$ kWh/m³	$\rho_{en,v,eff}$ [a] kWh/m³
BaO_2/BaO	697	76	447	616	185
Co_3O_4/CoO	894	198	823	1387	416
Mn_2O_3/Mn_3O_4	903	32	204	255	76
CuO/Cu_2O	1033	65	817	1471	441
Fe_2O_3/Fe_3O_4	1342	78	488	711	213

[a] Effective storage density referred to solid in oxidized state with a packed bed total porosity of 70 % (average, empirical value) according to Eq. (2.5).

The enthalpies of reaction $\Delta_R H^{\ominus}$ are calculated on the basis of the standard enthalpies of formation at the corresponding temperatures T_{eq} according to Eq. (2.7), the theoretical storage densities $\rho_{en,v}$ are based on Eq. (2.4). Energetic storage densities in the range between 255 kWh/m³ and 1471 kWh/m³ – referred to the true density of the solid matter in the oxidized state – can be achieved, respectively. Overall, the redox reactions of CuO and Co_3O_4 yield the highest storage densities of the selected oxides. Owing to the typically high total porosity of a loose packed bed of storage material (in the order of ≈70 %), the effective storage densities $\rho_{en,v,eff}$ are hence significantly lower, ranging between 76 kWh/m³ and 441 kWh/m³.

Plotting the equilibrium partial pressure of O_2 on a logarithmic scale as a function of temperature (see also correlation of Eq. (2.13)) gives the theoretical equilibrium lines of the selected redox reactions in Fig. 3.3. The diagram indicates the regions of stability of the corresponding oxidized and reduced phases under a gas atmosphere comprising the reactant gas oxygen and inert nitrogen.

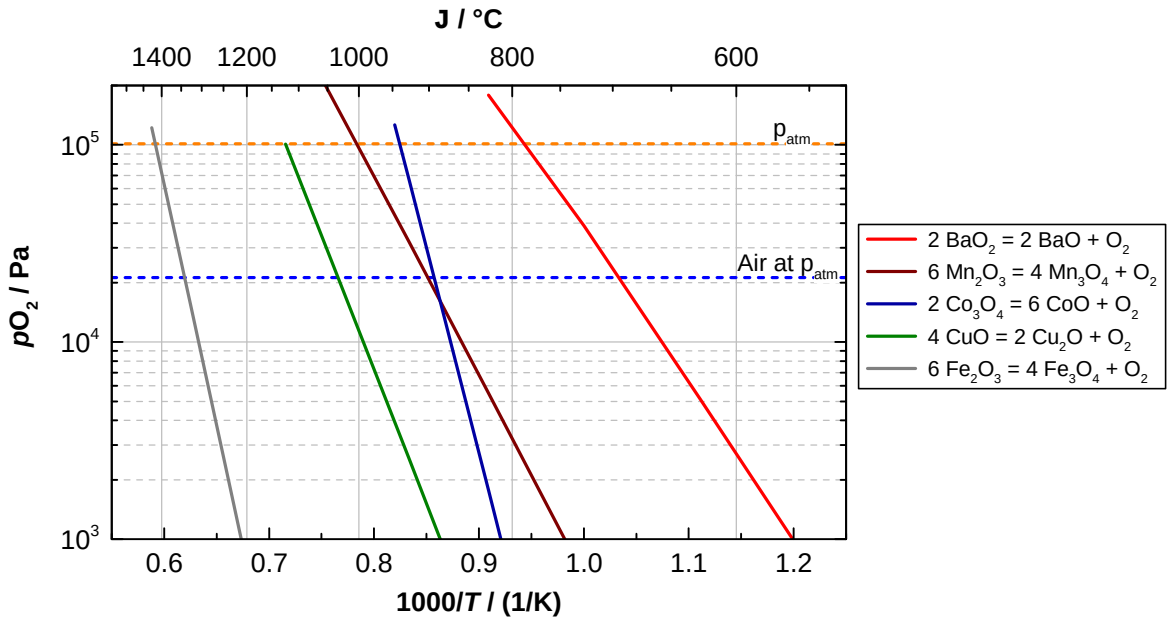

Figure 3.3: Temperature dependence of the equilibrium partial pressure of O_2 along the phase boundaries of different redox couples (calculated based on thermochemical property data by Barin [27]): BaO_2/BaO, Co_3O_4/CoO, Mn_2O_3/Mn_3O_4, CuO/Cu_2O and Fe_2O_3/Fe_3O_4.

Suitable process conditions have to be chosen in order to exceed the respective equilibrium line and allow the desired redox reaction to take place from a thermodynamic point of view. For the reduction of the storage material (*charging step*) the temperature has to be increased and/or the pO_2 has to be decreased to reach process conditions to the left of the van't Hoff line, where the reduced phase represents the stable phase. For the oxidation of the material (*discharging step*) relevant process conditions to the right of the van't Hoff line have to be selected, where the oxidized phase constitutes the stable phase. This can be achieved by lowering the temperature and/or increasing the pO_2. Each redox reaction is characterized by an ideal temperature range, though. On the one hand, excessive temperatures lead to enhanced sintering processes, which may be detrimental to the reaction reversibility and redox kinetics. If temperatures are too low, on the other hand, kinetic restraints may occur.

Raw Material Reserves & General Health and Safety Assessment Besides performance characteristics like reaction enthalpy, reaction reversibility, sufficient reactivity in both directions as well as cycling stability, additional criteria play a decisive role in the selection process, such as abundance of mineral resources, mining potential to win minerals containing the respective transition metals (Mn, Fe, Co, Cu) cost-effectively, as well as subsequent ore processing to obtain the desired oxides. Since commodity prices generally depend strongly on those factors, it can be supposed that costs of TCS raw materials correlate with the availability of mineral resources, besides the worldwide demand for the raw material. Last but not least the synthesis of mixed oxide compounds (binary, ternary, ...) also constitute an important factor for a future material

scale-up. However, solid state reactions represent common sintering processes in the ceramic industry, which allow a facile and convenient preparation of mixed oxides.

The worldwide mining output (data from 2014) of the mineral raw materials in Table 3.2 clarifies the abundance and vast availability of manganese and iron compounds [118]. Iron represents one of the most abundant elements in the earth's crust, turning it into a low-cost raw material. It becomes apparent that doping cobalt oxide and manganese oxide with low-priced Cu and Fe (see also Section 2.3.3), respectively, both yield more attractive binary oxides at reduced (Co-Cu oxides, Mn-Fe oxides) or similar (Mn-Cu oxides) material costs (apart from additional costs for the required mixing and sintering process).

Table B.1 in the appendix provides an overview of the hazard statements and pictograms for the relevant pure oxides and potential mixed oxide components. Both cobalt oxides [53] and copper oxides [120] attract special attention, as those materials are exceedingly harmful to human health and the environment, requiring strict safety regulations. On the contrary, manganese oxides are considered less critical and easier to handle, iron oxides are completely nonhazardous.

TCS Material Performance versus Health and Safety Issues In the literature particularly cobalt oxide and manganese oxide have been in the focus of interest, both exhibiting different characteristics, which are each on its own fundamental for a potential application as TCS material. The corresponding temperature levels of the redox transition in air, 894 °C for Co_3O_4/CoO and 903 °C for Mn_2O_3/Mn_3O_4 according to the thermodynamic equilibrium [27], are within the relevant temperature range between 500 °C and 1100 °C, which has been specified in this thesis. Thus, both materials offer promising opportunities for HT-TES applications. While cobalt oxide is regarded as the most promising pure oxide with respect to energy density, reaction kinetics and cycling stability, manganese oxide stands out due to its high availability at low cost as well as as its relatively low harmfulness to health, in turn allowing a facile handling of the material (see also Section 2.3.3).

In spite of the high attainable reaction enthalpy, rapid reaction rates and the relatively small thermal hysteresis [37], cobalt oxide based storage materials cannot be qualified as a reference system for lab-scale experiments in this thesis as well as large-scale technical applications owing to the high expenses and potential health threat. Proven to provoke pulmonary diseases and suspected of causing cancer [53], a utilization as TCS material is out of question, especially in an open-loop storage system. However, the use of cobalt oxide compounds might be reasonable for special small-scale applications, where high reaction performance is required and the material can be handled safely by means of a self-contained storage.

Consequently, hereinafter the main focus in this thesis will be put on manganese-based oxides.

General Material Characteristics of Manganese-Based Oxides Pure manganese oxide is characterized by the potential to occur in multiple oxidation states depending on the prevailing conditions. The following transition constitutes the most attractive one in terms of reversibility

Table 3.2: Information about occurrence and mining of the mineral resources from which the relevant TCS materials are extracted.

World production of mineral raw materials in in the year 2014, output in metric t [118]			
Mineral resource	**Total production output**	**Main mining countries**	**Occurrence of transition metals in nature**
Cobalt	130.222	Congo D.R. (76.475), China (8.500), Canada (6.574)	Co occurs in a widespread but dispersed form in trace quantities in many rocks, soils and plants; largest Co concentrations are found in mafic (45-52 wt-% SiO_2) and ultramafic (< 45 wt-% SiO_2) volcanic rocks, rocks which are rich in magnesium and iron; overall Co is a major constituent of about 70 minerals [53]
Copper	18.435.342	Chile (5.749.600), China (1.635.000), Peru (1.379.626)	Cu primarily occurs in elementary form as metallic copper (so-called *native copper*); CuO occurs as the black minerals tenorite and paramelaconite; Cu_2O occurs as the red or reddish brown mineral cuprite [120]
Manganese	19.323.994	South Africa (6.182.550), China (3.310.000), Australia (3.049.987)	Mn predominantly occurs in the form of MnO_2-containing mineral pyrolusite (German: *Braunstein*) and can be recovered from low-grade (Mn content < 20 wt-%) and high-grade manganese ores (Mn content > 40 wt-%); Mn_3O_4 occurs naturally as the mineral hausmannite, the manganese salt $MnCO_3$ as the mineral rhodochrosite [119]
Iron	1.554.479.681	China (484.556.800), Australia (423.669.000), Brazil (200.567.480)	Fe_2O_3 is naturally found in abundant iron ore deposits as the mineral hematite; Fe_3O_4 occurs naturally as the mineral magnetite, the magnetite-containing iron ore constitutes the most important and widespread deposit; Fe can also be recovered from the abundant carbonate mineral $FeCO_3$ [107]

and appropriate temperature range for TCS:

$$6\,Mn_2O_3 + \Delta_R H \rightleftharpoons 4\,Mn_3O_4 + O_2 \tag{3.4}$$

While β-Mn_2O_3 adopts a cubic bixbyite structure, α-Mn_3O_4 (*hausmannite*) crystallizes in a spinel structure, which is tetragonally distorted due to the so-called "Jahn-Teller effect" [69, 81].

As already mentioned in Section 2.3.3, inherent drawbacks of pure manganese oxide such

as slow re-oxidation rates and a large thermal hysteresis between the reduction and oxidation temperature can be overcome by the incorporation of secondary iron cations into manganese oxide. Previous works have focused on the preparation of high-purity manganese-iron oxides (hereinafter generally denoted by Mn-Fe oxides) with different Fe contents by means of a modified sol-gel based Pechini method (in the form of fine powders), accompanied by a general assessment of the reactivity and its overall potential as TCS material [29, 40].

Based on thermal analysis Carrillo *et al.* suggested a molar ratio Fe/Mn of 1:4 with a reduction onset temperature of 995 °C and an enthalpy of 219 J/g, measured at a heating rate of 5 K/min in air. This composition stands out due to high oxidation rates as well as a significantly improved stability over 75 redox cycles [40, 43]. Carrillo *et al.* also focused on scrutinizing the arising crystallographic transformations and the role of Fe incorporation on the oxidation rate improvement. The latter was hypothesized to be attributed to an enlargement of Mn-O bond lengths of Mn^{2+} cations induced by the Fe incorporation, facilitating an easier mobility of Mn cations and oxygen anions through the lattice during oxidation [43]. Block and Schmücker highlighted a molar ratio Fe/Mn of 1:2 with a reduction onset temperature of ≈999 °C and an enthalpy of ≈233 J/g, measured at a heating rate of 10 K/min in air [29]. Remarkably, re-oxidation rates of such Fe-doped manganese oxides can be significantly increased in comparison to the corresponding transition from pure Mn_3O_4 to Mn_2O_3.

On the basis of these literature data, a Mn-Fe oxide with a Fe/Mn molar ratio of 1:3 has been selected as a potentially suitable storage material to be further investigated as TCS reference material in this work. A spray-dried material of the same composition has previously been analyzed regarding oxygen carrier properties in CLOU processes by Azimi *et al.* [22].

Diverse literature studies have concentrated on the thermodynamic assessment of the manganese oxide - iron oxide system, which comprise experimental determinations of the phase evolution as well as calculations of the prevailing phase equilibria [50, 87, 150]. Considering the selected composition with a Fe/Mn molar ratio of 1:3, reported phase diagrams for air indicate the cubic bixbyite $(Mn,Fe)_2O_3$ (B) to be the thermodynamically stable structure at low temperatures (e.g., at 750 °C) and the cubic spinel β-$(Mn,Fe)_3O_4$ (S) to be the stable structure at high temperatures (e.g., at 1060 °C). Hence, the following redox reaction is expected, when the temperature is increased (and/or the pO_2 is lowered):

$$6\,(Mn_{0.75}Fe_{0.25})_2O_3 + \Delta_R H \rightleftharpoons 4\,(Mn_{0.75}Fe_{0.25})_3O_4 + O_2 \tag{3.5}$$

The reaction proceeds via one or several two-phase regions at intermediate temperatures in air, where several phases coexist due to a miscibility gap. Inconsistent results have been published regarding the nature of these two-phase regions. This might be attributed to the complexity of the Mn-Fe-O system, as manganese and iron occur in multiple oxidation states, and sample preparation as well as examination methods vary. Some reports illustrate that the tetragonal spinel α-$(Mn,Fe)_3O_4$ (T), also known as *hausmannite* phase, forms as intermediate. In this case the reaction Eq. (3.5) proceeds via the two-phase fields "T + B" and "S + T" with rising temperature in

air [50, 102]. In other phase diagrams, though, the phase boundaries of those two-phase regions are shifted further towards Mn-rich compositions, such that the contemplated reaction proceeds via the two-phase region "B + S" [87, 148, 150]. Generally, the presence of a two-phase region inherently leads to an overlap of the reduction and oxidation step, so that the ratio of reduced to oxidized phase varies within this region depending on the prevailing temperature and corresponding dwell time.

In the present thesis an analysis of a granular Mn-Fe oxide with a Fe/Mn molar ratio of 1:3 prepared from technical grade raw materials will provide new, detailed insights on the redox transformation of $(Mn_{0.75}Fe_{0.25})_2O_3/(Mn_{0.75}Fe_{0.25})_3O_4$ in view of a potential TCS application.

3.3 General Analysis of Selected Manganese-Iron Oxide Regarding Decisive TCS Properties

3.3.1 Origin of Technical Grade Storage Materials: Base Material Mn_2O_3 and Mixed Oxide $(Mn_{0.75}Fe_{0.25})_2O_3$

Commercially available, technical grade Mn_3O_4 (manganese(II,III) oxide, powder, LH grade, Co. Erachem Comilog) is employed as pure oxide sample for comparative measurements in this work. This pure oxide is subsequently referred to as underlying "base material". The sample has been calcined for 3 h at 700 °C in air prior to use, in order to remove any impurities and oxidize Mn_3O_4 to Mn_2O_3 (see X-ray diffraction pattern in Fig. B.5).

Granular Mn-Fe oxide with a Fe/Mn molar ratio of 1:3 is prepared by means of a build-up granulation technique in the particle size range of approximately 1 mm to 3.5 mm (see particle size distribution in Section 3.4.4, Fig. 3.19a, calculated based on an image analysis method), using technical grade powders of Fe_2O_3 and Mn_3O_4. The preparation has been performed by VITO (Mol, Belgium). The detailed preparation method can be found in Appendix B.5 and [154]. The total elemental composition of the granular material analyzed by XRF spectroscopy is summarized in Table B.3 in the appendix. A Fe/Mn molar ratio of 1:3 could be verified. Consequently, for the sake of simplicity the oxidized form will be denoted $(Mn_{0.75}Fe_{0.25})_2O_3$ throughout this work.

As fine powders potentially lead to channeling effects, larger pressure losses and sever particle agglomeration due to sintering [127, 121, 155], which characteristics render a storage operation with a solid storage material and HTF in direct contact impractical, Mn-Fe oxide has been prepared in granular form. The minimum particle size of ≈1 mm has been chosen to prevent fluidization under relevant operating conditions on lab-scale as well as to minimize parasitic losses due to the occurrence of lower pressure drops over a packed bed in contrast to powder material. Maximum particle sizes have been restricted to ≈3.5 mm in order to minimize the influence of potential boundary effects on the fluid flow at the tube wall of a storage reactor as well as to ensure comparable reactivity between small and large particles (exclusion of internal diffusion resistance

within larger particles).

The calculation of the relative theoretical mass change of the respective metal oxides Mn_2O_3 and $(Mn_{0.75}Fe_{0.25})_2O_3$ is elaborated in Appendix B.3.3. Thermogravimetric analyses conducted throughout this work have revealed an average weight loss of approx. 3.181 % in the reduction step ($\Delta m_{exp,Red}$ according to Eq. (3.1)). This value is lower than the expected weight loss of 3.368 % given by the stoichiometry of the reaction in Eq. (3.5) ($\Delta m_{theo,Red}$ according to Eq. (B.2) in Appendix B.3.3), for which calculation the Fe fraction of the compound has been taken into account. Based on this observation only about 94.4 % of the technical grade redox material is considered reactive, the remaining 5.6 % inert. Hence, a weight loss of 3.181 % is adopted as complete reaction conversion for subsequent examinations in this work (approximatively viewed as $\Delta m_{theo,Red}$ hereinafter). Previous studies with high-purity mixed oxides reported a weight loss of ≈3.4 % measured for Fe/Mn molar ratio of 1:2 [29] and 1:4 [43] though.

3.3.2 Experimental Procedure

The sample crucible is typically charged with ≈30 mg of Mn_2O_3 and $(Mn_{0.75}Fe_{0.25})_2O_3$, respectively. Fresh starting material (apart from TG measurement of already cycled material, indicated in Fig. C.5) in the oxidized form is used for each single measurement. Powder samples are weighted down carefully with the dead load of a small crucible forming tool to ensure effective heat transfer and provide identical starting conditions for each measurement. In the case of Mn-Fe oxide two granules of nearly equal size with an average overall weight of typically ≈30 mg are placed in the middle of the crucible throughout all measurement series. Two granules of approximately the same weight are chosen to ensure comparability.

A comparison of three samples with different granule sizes – one, two and eight granules with a respective total mass of ≈30 mg placed in the crucible – in the course of an isothermal oxidation at 855.8 °C in air proved, that the reactivity of the material is independent of the granule size within the investigated size range, as only insignificant changes could be observed (see Fig. B.4). Mass transfer effects due to intra-particle gas diffusion cannot be excluded with the application of those rather large particle sizes and may therefore be limiting the reaction to a certain extend. However, this study is targeted on the characterization of a storage material in the size and shape intended for application on a larger scale, in order to derive apparent values for the material.

As DSC measurements have to be conducted with metal oxides in powder form to ensure adequate contact of the material to the bottom of the crucible, some $(Mn_{0.75}Fe_{0.25})_2O_3$ granules have been pestled with EtOH prior to this measurement. Lower weighted samples of ≈15 mg Mn_2O_3 and ≈20 mg $(Mn_{0.75}Fe_{0.25})_2O_3$ have been applied for those calorimetric measurements.

At all times a reference cycle in air (gas flow of 20 NmL/min O_2 and 80 NmL/min N_2) is conducted as a material pre-treatment step prior to the actual redox cycle used for data evaluation (2^{nd} cycle), so that equal starting conditions can be provided for each sample measurement. The temperature program of the reference and subsequent measuring cycle is exemplarily described

for Mn-Fe oxide hereinafter, the temperature program for the comparative measurements with manganese oxide is given in Table B.2, summarizing all programs.

Initially the sample is heated up to 200 °C and held for 30 min, in order to remove moisture and any impurities. Then the material undergoes a redox cycle during heating at a rate of 10 K/min up to 1060 °C (reduction) and cooling at a rate of 10 K/min down to 750 °C (oxidation), followed by an isothermal period of 30 min. Within the scope of subsequent dynamic experiments performed at different oxygen atmospheres the gas flow is switched to the desired oxygen fraction in the middle (after 15 min) of this isothermal period at 750 °C (see Section 3.4.1). The detailed procedure for the subsequent redox cycles which are taken for analysis is explained in Section 3.4.

For a cycling stability study described in Section 3.3.4 the sample is subjected to 100 thermal cycles of heating up to 1060 °C and subsequent cooling down to 750 °C at heating/cooling rates of 10 K/min under air (no isothermal period). Based on reported phase diagrams the maximum applied temperature of 1060 °C in air should be adequate for the formation of the cubic spinel phase β-$(Mn,Fe)_3O_4$ [50, 87, 150].

3.3.3 Reversibility and Specific Reaction Enthalpy

This section focuses on a deeper analysis of the general reaction behavior of the selected Mn-Fe oxide as well as the arising reaction enthalpy of the $(Mn_{0.75}Fe_{0.25})_2O_3/(Mn_{0.75}Fe_{0.25})_3O_4$ redox transition, comparing both properties to the Mn_2O_3/Mn_3O_4 redox transition of the underlying pure oxide (outlined in Appendix B.6.2). As those properties define the energy storage density and attainable thermal power output, both are central criteria for the potential suitability of a metal oxide as TCS material. Parts of this section have been published in [154].

Manganese Oxide The general reaction behavior of pure manganese oxide is described in Appendix B.6.2, along with a DSC measurement for the determination of the specific reaction enthalpy of the corresponding redox transition Mn_2O_3/Mn_3O_4 (see Fig. B.7). An average value of 201.1 J/g Mn_2O_3 has been measured for the specific reaction enthalpy of the reduction step, which is consistent with values reported in the literature [27, 40, 29].

Manganese-Iron Oxide Figure 3.4 illustrates a dynamic redox cycle for the Fe-doped manganese oxide (Fe/Mn molar ratio of 1:3) in air. The change of the DSC signal corresponds to the absorption and release of thermal energy, it thus correlates with the reaction enthalpy of the endothermic reduction and exothermic oxidation step. Complete reversibility of the redox reaction is given. Generally, higher onset temperatures were measured for the transition of $(Mn_{0.75}Fe_{0.25})_2O_3/(Mn_{0.75}Fe_{0.25})_3O_4$ compared to the Mn_2O_3/Mn_3O_4 transition of pure manganese oxide, which is in accordance with reported phase diagrams for air as well as previous findings for similar compositions of Mn-Fe oxide [29, 40, 50, 87, 150]. The onset temperature of the reduction in the heating step is registered at about 988.6 °C, whereas the onset temperature of

the oxidation in the subsequent cooling step is identified at approximately 895.0 °C. Thermodynamic properties of the binary oxide have changed compared to pure manganese oxide, shifting the reduction onset by about 47 °C to higher temperatures (see also Table B.4).

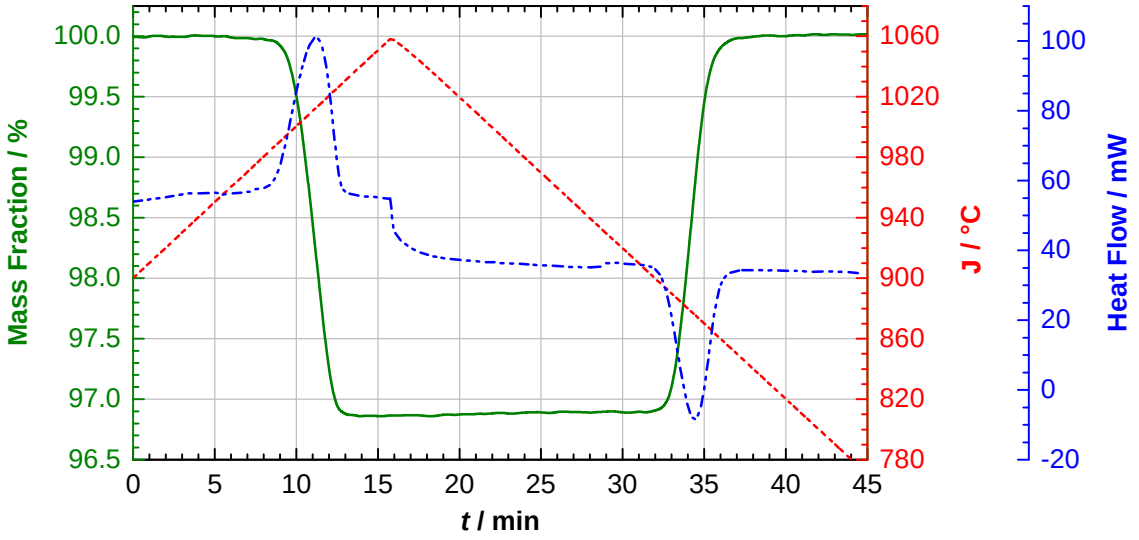

Figure 3.4: Excerpt of dynamic redox cycle of Mn-Fe oxide with a Fe/Mn molar ratio of 1:3 according to reaction equation $6\,(Mn_{0.75}Fe_{0.25})_2O_3 + \Delta_R H \rightleftharpoons 4\,(Mn_{0.75}Fe_{0.25})_3O_4 + O_2$, applying a heating rate of 10 K/min up to 1060 °C and a cooling rate of 10 K/min down to 750 °C in air.

Further, the pronounced thermal hysteresis measured for the redox pair Mn_2O_3/Mn_3O_4 (Appendix B.6.2) could be narrowed by means of iron doping (see also [29, 40]), mainly caused by a significant increase of the oxidation onset and therefore the storage discharging temperature. Storage charging and discharging in a closer temperature range is highly beneficial for a technical storage operation, as the energy efficiency of the storage cycle can be improved. The maximum temperature chosen for the redox cycle does not seem to be a crucial factor in the case of Mn-Fe oxide. In contrast to pure manganese oxide, the reaction time for complete oxidation amounts to only ≈6.4 min and is therefore in the same range as the period of ≈6.2 min for complete reduction. Thus, doping with Fe leads to a significant enhancement of the oxidation rate. The current observations when applying technical grade material confirm the findings of previous studies on hysteresis [40] as well as on enhanced oxidation rates of Mn-Fe oxides with similar composition [159, 40, 29, 4, 12].

Additional measurements have been conducted for the determination of the specific reaction enthalpy of the redox reaction, utilizing sample and reference crucibles with a pierced lid, respectively, to allow for the detection of even small thermal effects. In this work a specific reaction enthalpy of 272.4 J/g $(Mn_{0.75}Fe_{0.25})_2O_3$ has been measured for the reduction step, illustrated in Fig. 3.5.

The enthalpy value corresponds to about 273 kJ/mol O_2 (calculation based on average value of 271.4 J/g $(Mn_{0.75}Fe_{0.25})_2O_3$ of two measurements, listed in Table 3.3), which has been calculated based on assumed full stoichiometric reaction conversion. A similar value (254 kJ/mol O_2) was specified for the redox reaction of a binary oxide with a Fe/Mn molar ratio of 1:4 [123]. The

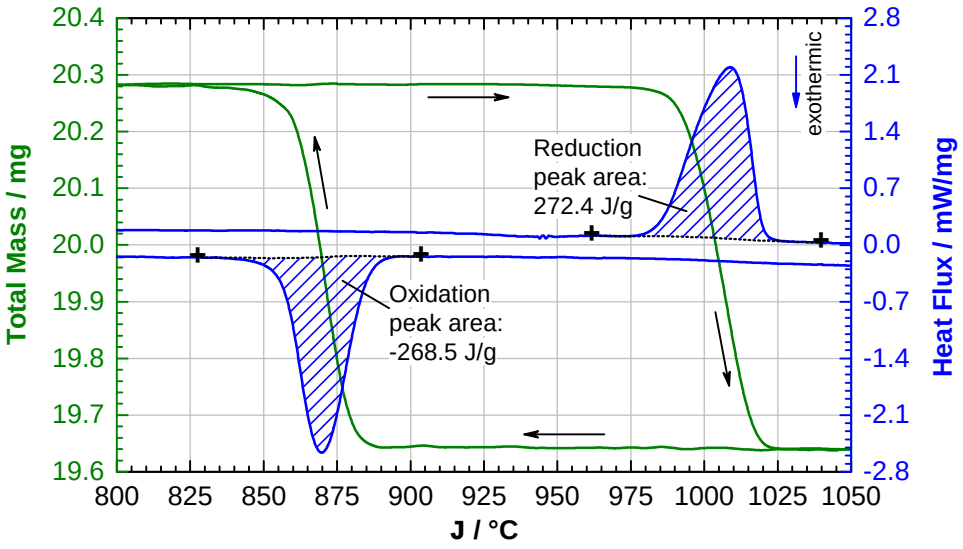

Figure 3.5: DSC measurement (excerpt): Evaluation of the specific reaction enthalpy of the $(Mn_{0.75}Fe_{0.25})_2O_3/(Mn_{0.75}Fe_{0.25})_3O_4$ transformation in air (20 mL/min O_2, 80 mL/min N_2), applying a heating and cooling rate of 10 K/min (crucible covered with pierced lid); 2nd cycle taken for analysis.

determined enthalpy of reaction in the current work turns out to be somewhat higher than the previously reported values experimentally obtained for the reduction step of similar compositions, yielding 219 J/g [40] and 193.3 J/g [11] for a Fe/Mn molar ratio of 1:4, and 233 J/g for a molar ratio of 1:2 [29]. This may be explained by the circumstances, that other authors employed open crucibles even for the measurement of enthalpy changes by DSC, giving rise to considerable heat losses. Overall, the measured reaction enthalpy of the $(Mn_{0.75}Fe_{0.25})_2O_3/(Mn_{0.75}Fe_{0.25})_3O_4$ transition turns out to be higher than the respective reaction enthalpy of the Mn_2O_3/Mn_3O_4 transition (see average value of 201.1 J/g Mn_2O_3 in Table B.4).

Table 3.3 summarizes the evaluated data for the analyzed redox transition $(Mn_{0.75}Fe_{0.25})_2O_3/(Mn_{0.75}Fe_{0.25})_3O_4$ of Mn-Fe oxide:

Table 3.3: Thermal analysis of the redox couple $(Mn_{0.75}Fe_{0.25})_2O_3/(Mn_{0.75}Fe_{0.25})_3O_4$: Onset temperatures (determined on the basis of the DSC signal), reaction times, mass changes (assessed by TG) and specific reaction enthalpies (assessed by DSC) of reduction and oxidation step.

Crucible	Reduction						Oxidation						Hyst.
	ϑ_{Onset} °C	t_{oo} min	t_{rxn} min	Δm_{exp} %	Δm_{theo} %	Δh J/g	ϑ_{Onset} °C	t_{oo} min	t_{rxn} min	Δm_{exp} %	Δm_{theo} %	Δh J/g	ΔT K
w/o lid [a]	988.6	3.9	6.2	–3.14	–3.37	-	895.0	3.5	6.4	+3.23	+3.49	-	93.6
w/ lid [b]	985.0	-	-	-	-	271.4	884.9	-	-	-	-	–266.4	100.1

[a] Weighted sample of ≈30 mg $(Mn_{0.75}Fe_{0.25})_2O_3$ for measurement without lid.

[b] Weighted sample of ≈20 mg $(Mn_{0.75}Fe_{0.25})_2O_3$ for measurement with covering lid (determination of the specific reaction enthalpy Δh by DSC).

The onset temperatures and enthalpies determined by means of the DSC measurements using pierced lids for the sample and reference crucible, listed in Table 3.3, represent the average of

two individual measurements, respectively. Always the 2nd cycle has been considered for data evaluation. The observed shift of the onset temperature of the oxidation step to lower values can be attributed exclusively to an oxygen transport resistance evoked by using pierced lids for the caloric measurements.

Following the progress of the redox reaction, the shape of the DSC peaks in Fig. 3.5 does not indicate the existence of a two-phase region and therefore two-stage reaction progress (in the form of a kink in the TG curve or double peak in the DSC curve), which would be expected according to various reports on the phase diagram of the manganese oxide/iron oxide system [87, 150, 50]. However, the absence of such an indication might be attributed to the relatively small temperature range of the two-phase region for the chosen composition (see also Fig. B.2 in the appendix) along with the dynamic measuring conditions.

3.3.4 Test of Cycling Stability

Long-term cycling stability of the redox reaction refers to a complete reversibility of the reaction with constant conversion rates – and steady reaction times accordingly – for the forward and reverse reaction over innumerous cycles. Thus, it represents a crucial requirement on a suitable TCS material. A potential degradation of the reaction rates could be caused by phase changes or sintering phenomena, resulting in a reduced energy storage capacity of the material. Therefore, XRD patterns and SEM images of the raw material and cycled sample are compared regarding possible changes of the microstructural morphology to draw conclusions about the observed redox reactivity, respectively. To receive an impression of the trend in reactivity, performing 100 cycles is considered sufficient in this work. Parts of this section have been published in [154].

Manganese-Iron Oxide Figure 3.6a illustrates the cycling performance of the granular Mn-Fe oxide in air. The reduction step proceeds sufficiently fast within about 6 min and reveals an advantageous stability with only minor changes over the progression of 100 cycles. Hence, the reduction is basically unaffected by cycling. As the reaction rate is expected to increase with enhanced heating rate and temperature (see also [40]), this is a sign of a merely heat transfer limited character of the reduction step.

The cycles further indicate stable onset temperatures for the subsequent oxidation step, respectively. Only a small increase of the reaction time from ≈5.6 min to ≈7.2 min is observed over the first 40 cycles, which is why the reactivity can be considered fairly stable in this range. In the course of consecutive cycling, though, the oxidation rate decreases slightly, indicated by a shift of the end of reaction towards lower temperatures during cooling. An elongated total reaction time (≈10.6 min) is registered for the 100th cycle. Overall, the oxidation proceeds to completion during all cycles until the preset lower temperature limit of 750 °C is reached.

It has to be noted, however, that the granular particles exhibit a so-called “swelling effect” over the course of 100 redox cycles, such that the particle density decreased and particles gained

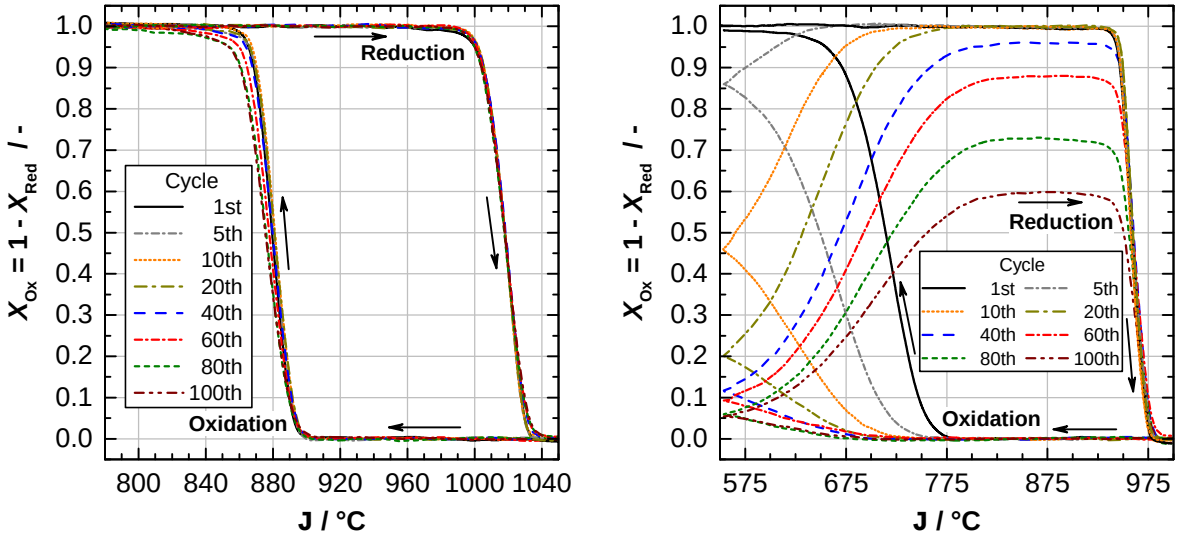

(a) $(Mn_{0.75}Fe_{0.25})_2O_3/(Mn_{0.75}Fe_{0.25})_3O_4$ transformation (excerpt).

(b) Mn_2O_3/Mn_3O_4 transformation.

Figure 3.6: Non-normalized conversion curves of 100 redox cycles of manganese-iron oxide and manganese oxide in air (20 mL/min O_2, 80 mL/min N_2), applying a heating and cooling rate of 10 K/min.

approximately double the initial size. The macro-structural integrity of the material could not be maintained. Images of the granular raw material in comparison to the swollen granules after 100 cycles are presented as insets in Fig. 3.8 (b) and (d), respectively. Indications for such a "swelling" have also been found in a recent study by Preisner *et al.*, who performed 30 redox cycles of Mn-Fe oxide granules with a Fe/Mn molar ratio of 1:2.33 in air [116]. A similar swelling behavior has been described previously for pure iron oxide particles (400-600 μm in size) over the course of repeated Fe_2O_3-Fe_3O_4 cycling in the field of CLC. The authors pointed out that the increased porosity results in more fragile particles, unable to withstand impacts and more susceptible to fragmentation [35]. An increase in the porosity over the course of 41 consecutive reduction-oxidation cycles has also been reported for Mn-Fe oxide particles of 125-180 μm in size (80/20 wt-% Mn_3O_4/Fe_2O_3) in the field of CLOU [130].

Thus, it can be assumed that the "swelling effect" of iron-doped manganese oxide observed over consecutive cycles in the current work might follow a similar mechanism, potentially arising from iron cation doping. This effect as well as the slight decline of the re-oxidation rate certainly need to be tackled and inhibited in potential future large-scale applications. The addition of inert additives during the preparation process of the mixed oxide could be a potential solution, which in turn reduces the specific energy density of the material though. For instance, Azimi *et al.* added inert ZrO_2 as a promising support material for a Mn-Fe oxide used in CLOU, also utilizing a Fe/Mn molar ratio of 1:3. The authors were able to prove an increase of the mechanical stability of the material [21]. Preisner *et al.* studied granular $(Mn_{0.7}Fe_{0.3})_2O_3$ with respect to the effect of chemical, thermal and mechanical stress – which the material is typically subjected to in a TCS reactor (e.g., moving bed) – on the reactivity, agglomeration and attrition behavior under

TCS-relevant conditions (packed bed of storage material in the order of 10-25 g). The modification of the material by the addition of 20 wt-% ZrO_2 or CeO_2, respectively, proved to decrease particle agglomeration and to enhance the particle strength in comparison to pure $(Mn_{0.7}Fe_{0.3})_2O_3$. It could be confirmed, that especially ZrO_2 allows for a higher resistance to attrition [116].

XRD phase analyses of the oxidized material prior to cycling and after 100 cycles are presented in Fig. 3.7. The background subtracted diffraction patterns indicate a cubic Mn_2O_3 crystal phase (bixbyite phase B; ICDD PDF-2, #41-1442), crystallizing in the space group $Ia\bar{3}$ with a lattice parameter a = 9.4091, which are consistent with phase diagrams in the literature [50, 87, 150], discussed in Section 3.2.

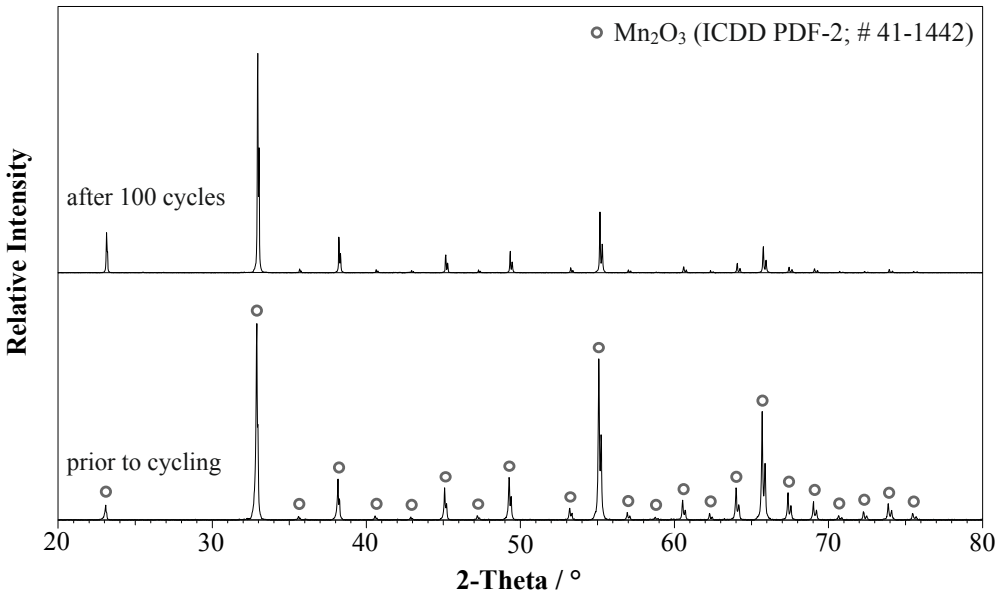

Figure 3.7: X-ray diffraction patterns of Mn-Fe oxide raw material and material cycled 100 times in air, both being in the oxidized state (XRD analysis performed by Institute of Materials Research, DLR).

A hematite phase, which would still indicate the presence of the raw material Fe_2O_3 (space group $Ia\bar{3}$ with a lattice parameter a = 9.404), cannot be observed. The subtraction of the background does not distort the data, as the raw data without background subtraction gave no indication of the presence of an amorphous fraction. Moreover, a $K\alpha_2$ correction was not conducted, which is why the peak width in Fig. 3.7 has not been altered. It has to be mentioned, that the cubic $FeMnO_3$ crystal structure (bimetallic bixbyite phase B; ICDD PDF-2, #75-0894; space group $Ia\bar{3}$) exhibits virtually the same peak positions with a peak displacement by only about 0.02° (2θ). Thus, a differentiation between the bixbyite phase Mn_2O_3 and bixbyite structure $(Mn,Fe)_2O_3$ merely based on the lattice parameters is not feasible. It can be concluded, that the diffraction patterns of the samples do not differ from each other, both disclosing a single phase crystal structure corresponding to $(Mn,Fe)_2O_3$.

The microstructure of the starting material and cycled material – both in the oxidized state – is illustrated in Fig. 3.8, with SEM images (a) and (c) showing the top view of a granule, respectively. While the starting material (a) features irregularly shaped grains of various sizes with an angular

and sharp structure to some extent, the SEM image of the material cycled 100 times (c) clearly reveals larger, coherent bulk structures with sinter neck formation between individual grains. Those sintering processes are evoked by the severe HT conditions up to 1060 °C, which given fact might be responsible for the slight decline in the re-oxidation rate discovered over continuous cycling, slowing down oxygen diffusion. It is remarkable, though, that despite sintering effects (along with the associated decrement of the specific surface area) a degradation of the oxidation rate in the way observed for pure manganese oxide can be overcome by means of Fe doping. Thus it can be excluded, that the observed increase in the oxidation rate could be ascribed to an enhancement of the contact area between the reactive oxide and O_2 (see also findings by [40, 43]).

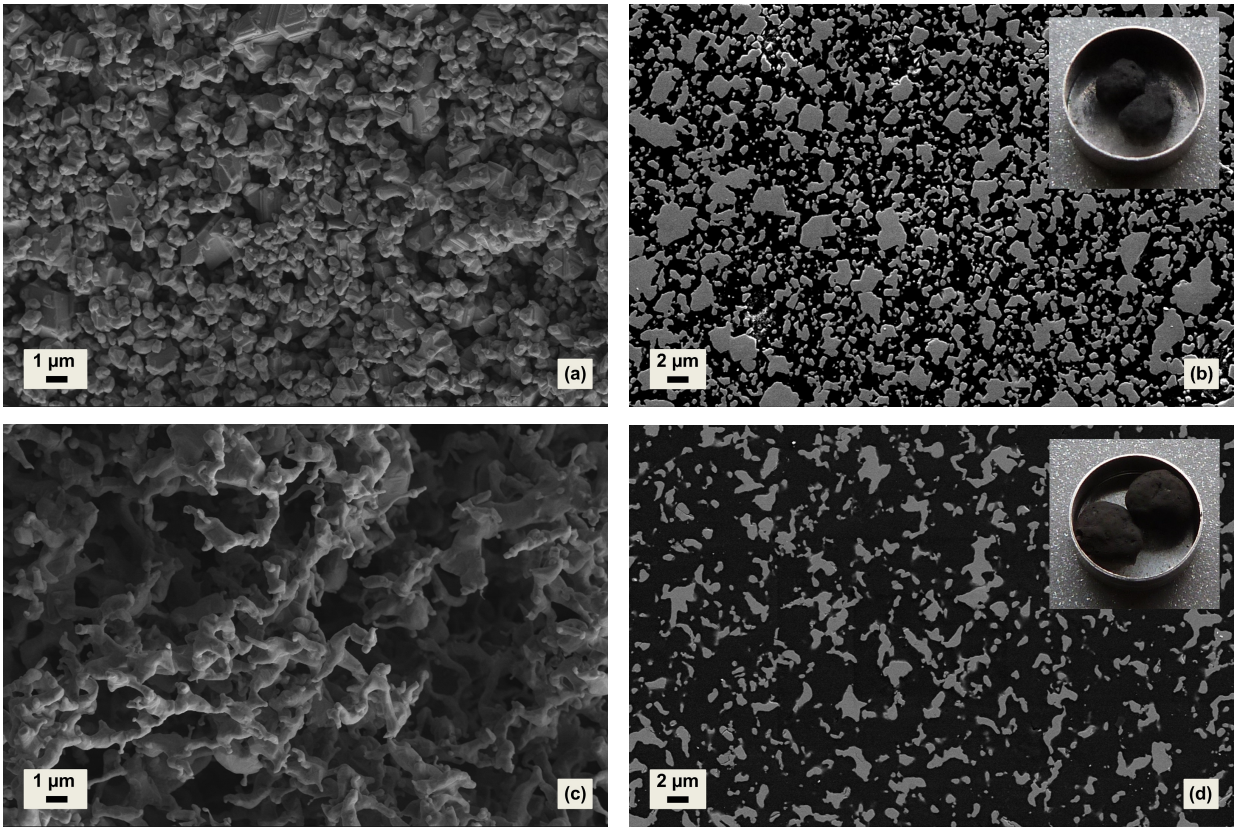

Figure 3.8: Scanning electron micrographs: Granulate surface and microsection of Mn-Fe oxide as prepared (a and b) as well as after 100 redox cycles in air conducted by means of TGA (c and d), both samples being in the oxidized state; SEM images (b) and (d) show polished cross sections of granules with epoxy glue (dark areas) and solid particle fraction (grey areas); conditions of SEM measurements: magnification images (a) and (c) 10.000 x, images (b) and (d) 5.000 x; working distance 8.0 mm; acceleration voltage 5.0 kV; SEM images recorded by Institute of Materials Research, DLR; pictures of the granules are shown as insets (b and d).

Representative SEM images of polished granule cross sections are also shown in Fig. 3.8 to compare the porosity of the raw material (b) and cycled material (d). The granular particles were infiltrated with epoxy glue to stabilize the structure. Dark areas (epoxy glue) represent the voidage of the particles. The SEM image of the cycled material clearly shows less solid fraction (grey areas) per image section. Although the material was affected by sintering phenomena due to the

exposition to temperature up to 1060 °C, pore sizes and total pore volume of the structure increased significantly over the period of cycling in comparison to the raw material. The particle density decreased accordingly. This can be attributed to the swelling of the granules and is therefore in accordance with the visual observation of the immense growth in granule size, presented as insets in Fig. 3.8 (b) and (d). Due to those structural alterations of the material, the mechanical properties and structural integrity of the granules could not be thoroughly sustained. Future work comprises cycling experiments in a furnace with a larger quantity of storage material in order to allow more comprehensive material characterizations, e.g., determining the specific surface area by means of the BET method.

Manganese Oxide as Base Material for Comparison Although the redox reaction of Mn_2O_3/Mn_3O_4 has been widely explored as reported in the literature, a detailed study with data for the redox behavior over 100 redox cycles is not available so far. Figure 3.6b illustrates the cycling behavior of pure manganese oxide. Poor oxidation kinetics have already been specified as a critical issue for this material (see redox cycle in Appendix B.6.2). Isothermal oxidations of Mn_3O_4, displayed in Fig. B.8, point out that the highest reaction rates in air occur in the range between ≈700 °C and ≈730 °C, which has also been previously reported [5, 155]. At lower temperatures the reaction rate appears to be very slow.

With each further cycle in Fig. 3.6b the oxidation tends to become slower at such a rate, that the reaction is not completed in the cooling step down to 550 °C any more, already obvious in the 5^{th} cycle. The oxidation continues in the subsequent heating step in the range between 550 °C and 850 °C. Full conversion is still reached within the primary 20 cycles though. Between cycle 20 and 40 the oxidation in the cooling step becomes so slow and even more incomplete, that full re-oxidation in the heating step cannot take place any more. This implicates a decrement of reactive material and consequently loss of energy storage capacity. The reduction rate, however, turns out to be unaffected by the number of cycles conducted. This finding is in accordance with the observation made by Carrillo *et al.*, who concluded that the reduction rate is controlled by heat transfer [39]. The two-stage oxidation process during thermal cycling has also been reported previously for 6 cycles performed with manganese oxide flow-through pellets [86].

A comparison of the microstructure of the material prior to cycling and after 100 cycles in Fig. B.9 (Appendix B.6.4) sheds light on the degradation of the oxidation rate in the course of thermal cycling. The morphology of manganese oxide changed significantly. The raw material exhibits a fine-textured morphology (Fig. B.9 (a)). Owing to the periodic exposition to thermal conditions up to 1000 °C, severe sintering effects led to an immense grain growth and the formation of sinter necks between adjacent particles (Fig. B.9 (b)). Particle sizes changed in an order of magnitude from nanoscale to microscale, leading to a considerable reduction of the specific surface area with advancing cycles. The material has a coral-like structure with an open macroporosity. This appearance has been described as well by Carrillo *et al.*, who attributed the driving force for sintering phenomena to the reduction of surface energy [39, 45]. Similarly, the slowdown

of the oxidation rate in the current study can thus be ascribed to a physical barrier to oxygen diffusion [39].

Overall, pure manganese oxide of technical grade examined in the current study suffers severely from a lack of redox cyclability in air. The comparison with pure manganese oxide clearly emphasizes the advantageous effect of Fe doping and the resulting superior cycling performance of the binary Mn-Fe oxide.

3.3.5 Findings Derived from General Analysis of Redox Transformation $(Mn_{0.75}Fe_{0.25})_2O_3/(Mn_{0.75}Fe_{0.25})_3O_4$

Taking the selection criteria for TCS materials described in Section 2.3.3 into account, the selected Mn-Fe oxide with a Fe/Mn molar ratio of 1:3 has been proven to be a suitable reference TCS material to be applied for a detailed characterization as well as lab-scale experiments in the current work. The results obtained in Section 3.3 can be summarized as follows:

- The Mn-Fe oxide examined in this work was prepared in granular form from technical grade raw materials. It therefore meets the material requirements to be economical and non-toxic in handling, rendering the binary oxide a cost-efficient storage material. A specific reaction enthalpy of 271 J/g $(Mn_{0.75}Fe_{0.25})_2O_3$ was obtained for the redox transition of $(Mn_{0.75}Fe_{0.25})_2O_3/(Mn_{0.75}Fe_{0.25})_3O_4$, which value is higher than the energy density of the system Mn_2O_3-Mn_3O_4-O_2 (measured value of 201 J/g Mn_2O_3).
- The redox reaction of Mn-Fe oxide exhibits a smaller thermal hysteresis ($T_{ox} < \approx 895$ °C & $T_{red} > \approx 989$ °C) than the corresponding redox reaction of pure manganese oxide ($T_{ox} < \approx 773$ °C & $T_{red} > \approx 941$ °C), which is highly advantageous for storage discharging to enable the release of thermal energy at a high temperature level.
- Experimental examinations of $(Mn_{0.75}Fe_{0.25})_2O_3$ and Mn_2O_3 have pointed out, that the sintering behavior of metal oxides defines the upper temperature limit for the application conditions (charging stage), which limit is particularly critical for pure manganese oxide. The lower temperature limit is in turn dictated by oxidation kinetics, as reactions proceed only slowly at low temperatures, according to the temperature dependence of the reaction rate (kinetic limitation). Generally, oxidation kinetics constitute the critical step in the storage cycle (discharging stage), with fast oxidation rates at a temperature level as high as possible being crucial for a suitable TCS material. The examined Mn-Fe oxide disclosed a high overall reactivity, which equally applies to the reduction and oxidation step.
- The cycling stability of the material could be sufficiently maintained in terms of the reversibility and reactivity throughout 100 dynamic redox cycles in air, verifying its potential for the use as TCS material. However, the morphology of the granular particles changed in the course of 100 cycles, mainly attributed to the observation of a “swelling effect” of the granules, already known for iron-doped manganese oxide.

The durability of the selected Mn-Fe oxide to keep up the redox reactivity over numerous consecutive cycles (see Fig. 3.6a) can be considered sufficient for fundamental examinations of thermodynamics and reaction kinetics (Section 3.4) as well as subsequent upscaling to lab-scale (Chapter 4), in order to derive the main influencing factors on the TCS concept based on metal oxide redox reactions in general. Since mainly high purity storage materials have been reported in the literature up to now, this technical grade material constitutes the next important step forward in the development of competitive storage materials and reactor concepts.

3.4 Detailed Characterization of Technical Grade $(Mn_{0.75}Fe_{0.25})_2O_3/(Mn_{0.75}Fe_{0.25})_3O_4$

Although Mn-Fe based mixed oxides prepared from technical grade raw material have been investigated in the field of CLOU, the operating methods of TCS-reactors differ significantly from the methods relevant for CLOU-reactors. Consequently, the redox reaction of the TCS material has to fulfill different requirements in comparison to CLOU. Even though the reaction enthalpy defines the achievable increase in energy storage density, a comprehensive understanding of the reactivity behavior is crucial for the operation of a TCS reactor based on a metal oxide storage material.

In the first part of this section, dynamic experiments are performed by means of simultaneous thermal analysis in order to derive the pO_2-dependent reaction temperatures of the reduction and oxidation step. Special emphasis is placed on the technically relevant material reactivity in the temperature range nearby equilibrium, taking the presence of a thermal hysteresis into account. The knowledge of the pO_2-T dependence is fundamental, as a rise/drop of the pO_2 owing to the release/uptake of O_2 during the charging/discharging step or even due to storage operating methods using pressurization/pressure reduction directly affects the reaction temperature.

In the second part, a parameterization of the reaction rate is applied within the scope of kinetic analyses, in order to establish a mathematical relationship between the conversion rate and temperature, extent of conversion, pressure of the reaction gas as well as thermodynamic equilibrium for the respective reaction steps. Simplified kinetic equations for the reduction and oxidation – valid for different oxygen partial pressures – are derived from thermogravimetric measurement data. For Mn-Fe oxide such equations have not been reported so far. The approach to separate and identify the temperature-, conversion- and pressure-dependent terms of the expression in Eq. (2.17) varies for the reduction and oxidation, depending on the chosen measurement methodology [145]. All approximations are carried out by means of the minimization of the sum of error squares using the program OriginPro®, which is furthermore used for all data processing in this chapter.

In the third part, the characterization will be completed with the determination of the physical and thermophysical properties of the binary oxide.

Even though it is important to keep in mind, that thermodynamic and kinetic material characteristics will be further superimposed with heat and mass transfer phenomena in an actual working storage reactor, the material specific investigations in Section 3.4 form the basis for any further analysis. Parts of this section have been published in [154].

3.4.1 Thermodynamic Equilibrium and Hysteresis Behavior

Methodology According to the described passive dual media storage concept (see Section 2.1.2), the envisaged TCS reactor will be operated using air as HTF in direct contact with the storage material during charging and discharging. The coupling of the HTF and reaction gas supply has a direct influence on the reaction temperature due to the correlation between pO_2 and temperature, as oxygen is released and taken up during a storage cycle. Consequently, the knowledge of the position of the thermodynamic equilibrium for different oxygen partial pressures is essential to identify the relevant temperature ranges for reduction and oxidation as well as to specify the operating boundary conditions of the reactor. In this work simultaneous thermal analysis measurements were carried out to identify experimental pO_2-T conditions for the redox process (reduction and oxidation step) and reveal potentially occurring limitations, which knowledge is highly relevant from a technical point of view.

In general the difference between the measured onset temperature and the equilibrium temperature of a phase transition decreases with diminishing heating and cooling rates. The *German Society for Thermal Analysis* (GEFTA) has suggested a procedure to approach the thermodynamic equilibrium temperature by an extrapolation of determined onset temperatures for different temperature ramps to a heating and cooling rate of zero [73, 74]. Its use has already been reported in the thermodynamic characterization of TCS materials [101].

In order to study the temperature ramp dependence of the reaction onset and test this procedure in the present examination of Mn-Fe oxide, dynamic measurements at different heating and cooling ramps were performed in various O_2 atmospheres. In this way experimental pO_2-T conditions for the reaction onsets can be identified and temperature regions determined, where the material still exhibits a technically relevant reactivity. Heating and cooling rates of 0.5, 1, 2, 5 and 10 K/min were chosen for the reduction and corresponding oxidation step. The lowest temperature ramps applied (0.5 K/min) are considered sufficient for the current characterization with respect to a technical application of the material. Average oxygen partial pressures of 5.1 ± 0.017 kPa, 10.1 ± 0.106 kPa, 20.4 ± 0.271 kPa, 40.4 ± 0.132 kPa and 71.1 ± 0.114 kPa were realized for the respective series of dynamic measurements. The adjustment of a $pO_2 > \approx 70$ kPa is not possible due to the experimental setup, as the balance is flushed with 30 NmL/min N_2 at all times. The pO_2 is assumed to be constant throughout each experimental run owing to the small amount of sample as well as relatively low heating and cooling rates.

Experimental Results Figure 3.9 shows the dependence of the onset temperatures at various oxygen fractions under atmospheric pressure on different heating rates for the reduction (positive x-coordinate) as well as on the respective cooling rates for the oxidation (negative x-coordinate).

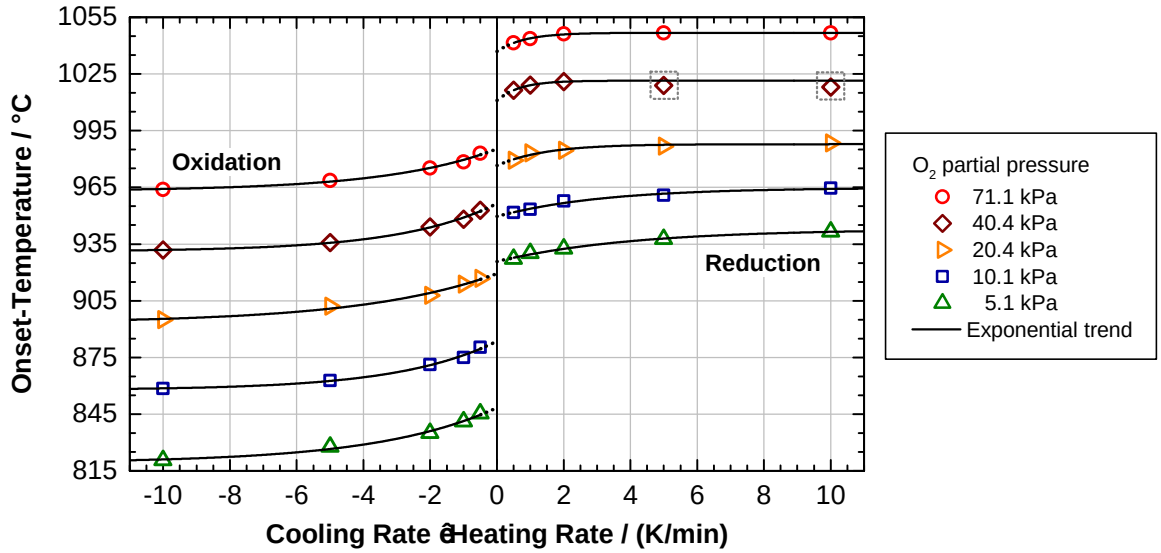

Figure 3.9: Extrapolated peak onset temperatures of the $(Mn_{0.75}Fe_{0.25})_2O_3$ reduction and $(Mn_{0.75}Fe_{0.25})_3O_4$ oxidation for various oxygen partial pressures plotted against different heating (positive x-coordinate) and cooling (negative x-coordinate) rates; onset temperatures determined on the basis of the measured DSC signal.

The progress of the determined onset temperatures of the reduction and oxidation can be represented adequately by means of an exponential function. Reduction onset temperatures for 5 K/min and 10 K/min at a pO_2 of 40.4 kPa differed from the exponential trend and were not included in the respective exponential fit for the sake of simplicity (points marked by boxes). An extrapolation of the onset temperatures to a heating and cooling rate of 0 K/min would generally lead to the equilibrium state of the reaction. This is clearly not the case for the illustrated trend in Fig. 3.9, as the determined onset temperatures are still far away from the actual equilibrium, even for the lowest temperature ramp of 0.5 K/min. At least for the oxidation step the thermodynamic equilibrium could not even nearly be approached (e.g., compare $\vartheta_{Onset,DSC}$ of 916.8 °C, determined at a cooling rate of 0.5 K/min and a pO_2 of 20.4 kPa, with ϑ_{eq} of 972.1 °C, calculated for a pO_2 of 20.4 kPa according to the phase boundary line eqII in Table 3.4), which characteristic oxidation behavior will be elaborately discussed below (see Fig. 3.10 and Fig. 3.11).

It is important to note, that the progress of the exponential trend towards the thermodynamic equilibrium cannot be discovered by means of the available data, as the trend is presumed to be more pronounced for heating and cooling rates lower than the adjusted 0.5 K/min. As will be shown later, the oxidation proceeds extremely slow closer to the equilibrium (Fig. 3.11), which is why considerably lower temperature ramps would be necessary. The setting of lower temperature ramps, however, is limited due to a loss of instrument sensitivity, rendering the analysis of the DSC signal difficult. Furthermore, lower ramps are not relevant from an application-oriented point of view. On this account the prolongation of the exponential trend for heating and cooling rates lower

than 0.5 K/min is only displayed by a dotted curve, respectively (Fig. 3.9). The temperature values obtained for heating and cooling rates of 0 K/min at different oxygen partial pressures (summary in Table B.5) do not represent equilibrium conditions in the current work and are therefore defined as technically relevant temperature threshold values, beyond which the reactions do not become visually evident in the presented dynamic measurements.

The experimentally determined temperature thresholds and corresponding oxygen partial pressures are transferred to a linearized van't Hoff plot (Fig. 3.10), plotting the average pO_2 on a logarithmic scale versus the reciprocal temperature threshold, respectively. A linear correlation (pO_2-T) between the pO_2 and the temperature thresholds can be derived for the reduction and oxidation step, as marked in the diagram.

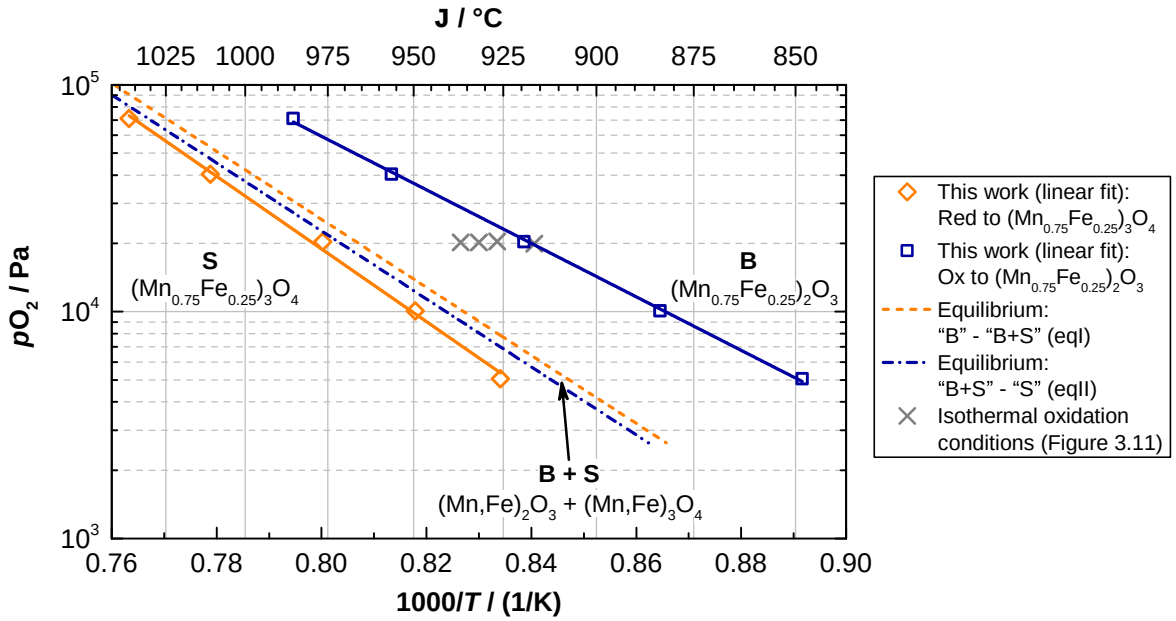

Figure 3.10: Correlation between oxygen partial pressures and temperature threshold values (derived from Fig. 3.9) for the reduction of $(Mn_{0.75}Fe_{0.25})_2O_3$ to $(Mn_{0.75}Fe_{0.25})_3O_4$ and oxidation of $(Mn_{0.75}Fe_{0.25})_3O_4$ to $(Mn_{0.75}Fe_{0.25})_2O_3$; equilibrium conditions for Mn-Fe oxide with a Fe/Mn molar ratio of 1:3 calculated by means of the thermochemical software FactSage™ is displayed for comparison (dashed lines); predominant phases: "B" = cubic bixbyite, "S" = cubic spinel and "B + S" = two-phase area of bixbyite and spinel.

The linear correlations for the experimentally determined data and equilibrium data in Fig. 3.10 can be rearranged to yield expressions according to Eq. (2.13), derived from the van't Hoff equation. The corresponding linear approximations with the slope (S) and y-intercept (Y) are summarized in Table 3.4:

$$\ln\left(\frac{pO_2}{10^5\,\mathrm{Pa}}\right) = \mathrm{S}\cdot\frac{1000}{T_{\mathrm{Red|Ox}}/\mathrm{K}} + \mathrm{Y} \tag{3.6}$$

In addition, Fig. 3.10 also illustrates the equilibrium partial pressure of oxygen ($pO_{2,eq}$) as a function of the temperature, calculated with the thermochemical software FactSage™ using the FToxid database [25]. Due to the presence of the small two-phase field, where the bixbyite and spinel phase coexist, two equilibrium conditions are deduced according to Eq. (2.13), referred to as phase boundary lines below. Only the partial pressure range which exhibits a linear relationship

between partial pressure and temperature is represented in the van't Hoff plot (from ≈2.6 kPa to 100 kPa). Below ≈2.6 kPa the additional two-phase field "T + B" begins, which is out of the envisaged operating range of a TCS reactor and will therefore not be addressed in this work. The presence of the illustrated two-phase field "B + S" is in accordance with phase diagrams reported in the literature [87, 148, 150]. As expected, the intrinsic thermodynamic equilibria are located between the experimentally determined pO_2-T conditions. However, the deviation of the oxidation conditions from equilibrium is clearly larger. The crosses marked in the diagram indicate the measurement conditions for isothermal oxidations, which are explained below (see Fig. 3.11).

For atmospheric air at 101.325 kPa with a pO_2 of 21.228 kPa a temperature threshold of ≈981.8 °C can be calculated for the reduction and ≈920.4 °C for the oxidation based on the experimentally determined pO_2-T correlations, respectively. The equilibrium correlations $pO_{2,eq}$-T_{eq} derived from FactSage™ data yield temperatures of 968.6 °C (phase boundary line of "B" - "B + S") and 973.9 °C (phase boundary line of "B + S" - "S") in air. Based on the average of both equilibrium lines (eqI and eqII in Table 3.4) for the phase boundaries, a molar standard reaction enthalpy of 287.1 kJ/mol O_2 can be evaluated for the redox reaction from the linear slope according to Eq. (2.13). The measured enthalpy value based on DSC deviates by around 5 % (273 kJ/mol O_2).

Table 3.4: Experimentally determined correlations between pO_2 and temperature threshold value for the reduction and oxidation onset of the considered redox reaction $(Mn_{0.75}Fe_{0.25})_2O_3/(Mn_{0.75}Fe_{0.25})_3O_4$ as well as pO_2 as a function of the temperature at equilibrium (see phase boundary lines eqI and eqII, calculated on the basis of FactSage™ data for an oxide composition with a Fe/Mn molar ratio of 1:3) according to Eq. (3.6).

Reaction Step | Phase Boundary Lines (FactSage™)	**S (slope)**	**Y (y-intercept)**
pO_2-T correlation for reduction threshold (this work)	–36.874	27.833
pO_2-T correlation for oxidation threshold (this work)	–27.159	21.205
Phase boundary line of "bixbyite" - "bixbyite + spinel" (eqI)	–34.538	26.265
Phase boundary line of "bixbyite + spinel" - "spinel" (eqII)	–34.522	26.134

Figure 3.10 accentuates the presence of a large thermal hysteresis under the prevailing experimental conditions, thermally decoupling the reduction and oxidation step. The thermal hysteresis implies the occurrence of a "passive" temperature range close to equilibrium, where the driving force of the reaction is low and hence the reaction – especially the oxidation step, showing an asymmetrical behavior – takes a longer time to be initiated and to proceed. This is why this range has no technical relevance and cannot be exploited for a TCS operation in this Mn-Fe oxide reaction system. It can be ascertained from Fig. 3.9 and Fig. 3.10 that the hysteresis extends over a broader temperature range at lower oxygen partial pressures, whereas the region becomes smaller at higher oxygen partial pressures (despite the inverse plotting of the temperature). Moreover, Carrillo *et al.* reported a narrowing of the thermal hysteresis loop of Mn-Fe oxide with increasing degree of Fe doping compared to pure manganese oxide [40], which allows to accomplish higher

discharging temperatures. This finding could be confirmed for the composition in the current study.

The redox reaction cannot proceed at the equilibrium temperature. A comparison of the experimentally determined pO_2-T dependencies (thresholds) and the calculated equilibrium conditions in Fig. 3.10 reveals, that different degrees of overheating and undercooling (ΔT) are required to initiate the corresponding phase transition of the reduction or oxidation. Only a low degree of overheating (ΔT) is necessary for the reduction to set in, as the increase of the thermodynamic driving force ΔG as well as the general increase of the reaction rate with rising temperature both favor the reduction. In contrast, the initiation of the oxidation requires a large degree of undercooling (ΔT) to overcome the activation energy barrier ΔG^* for the formation of a cluster (nuclei) with a critical radius by statistical thermal fluctuations. Hence, the oxidation step is primarily subjected to kinetic limitations during cooling.

A similar overheating phenomenon was reported for the reduction of pure Mn_2O_3 to Mn_3O_4 by Marugán *et al.*, who ascribed the observed phenomenon to reaction kinetics and O_2 diffusion effects, neglected in equilibrium calculations but generally dominating solid-state reactions [95]. Moreover, Carrillo *et al.* highlighted that experimentally determined phase diagrams reported in the literature are generally constructed by means of data of the reduction step and therefore do not account for the reverse oxidation step [40], which is why the presence of a thermal hysteresis also does not become obvious just by the analysis of available phase diagrams.

Isothermal oxidation measurements within the experimentally determined thermal hysteresis loop are illustrated in Fig. 3.11. These clearly demonstrate, why the methodology to extrapolate the onset temperatures for different temperature ramps to a respective rate of 0 K/min does not necessarily lead to the identification of the thermodynamic equilibrium on the basis of the underlying data set (lowest ramp of merely 0.5 K/min, compare Fig. 3.9) – especially in the case of the present severe kinetic limitations.

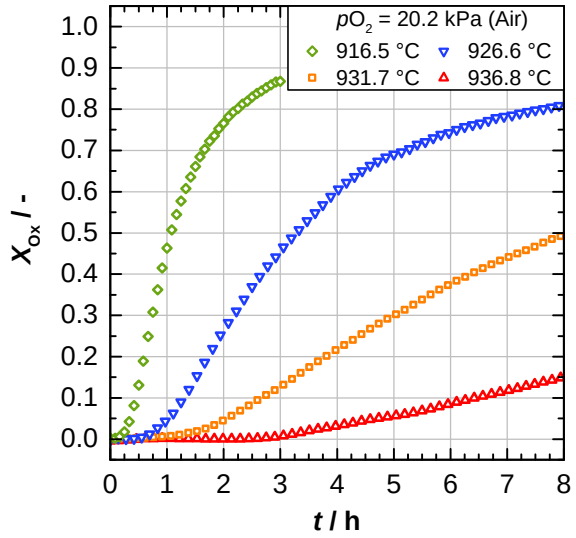

Figure 3.11: Isothermal oxidation of $(Mn_{0.75}Fe_{0.25})_3O_4$ in air over a period of 8 h at different temperatures within the experimentally determined thermal hysteresis range (apart from the measurement at 916.5 °C).

The graph reveals that the oxidation reaction actually proceeds at temperatures within the experimentally determined hysteresis range, verifying the assumption of underlying kinetic limitations closer to the equilibrium in the oxidation step. While at a temperature of 916.5 °C – below the aforesaid temperature threshold of ≈920.4 °C in air – only a short induction period could be observed, a long induction period of over 30 min is discovered for a temperature of 926.6 °C exceeding the temperature threshold marked in Fig. 3.10. Overall, it has to be differentiated between the temperature range below and above the experimentally determined pO_2-T threshold condition for the oxidation step, as for the latter the reaction progress changes drastically. Even though the required reaction rate might depend on the application, this temperature range can be excluded as potential operating condition, if a complete conversion cannot even be reached within a period of 8 h of oxidation.

Overall it can be concluded, that the knowledge of the actual equilibrium state is not sufficient for the description of the reactive temperature range. The presented dynamic measurement methodology, however, allows a valid approximation of the technically relevant operating conditions by determining the temperature thresholds at different oxygen partial pressures. From a technical point of view, beyond those thresholds the redox reactions proceed in a reasonable period of time upon further heating in the reduction or cooling in the oxidation step. While the pO_2-T threshold conditions for the reduction are closer to the equilibrium conditions, the corresponding pO_2-T threshold conditions for the oxidation are far-off, mainly attributed to prevailing kinetic limitations.

3.4.2 Effective Reaction Rate of Reduction

General Methodology and Experimental Procedure This section describes the parameterization of the reaction rate for the reduction step to model its dependence on the prevailing pressure and temperature. According to the general approach for the reaction rate of reversible decomposition reactions (Eq. (2.17)) described in Section 2.2.3, the effective kinetic parameters A, E_a, $f(X)$ and $h(pO_2, pO_{2,eq}(T))$ need to be determined. Owing to the constant protective gas flow of 30 NmL/min, the oxygen flow can only be adjusted to a maximum of 70 NmL/min, which in turn accounts for a maximum pO_2 of ≈70 kPa. The equilibrium conditions would therefore only allow a rather limited temperature window for the study of the reduction under isothermal conditions, where the reaction would be initiated by means of a partial pressure drop from 70 kPa O_2 to the desired pO_2 for the reaction. For this reason dynamic measurements at different heating rates are carried out for the reduction step. Moreover, lab-scale experiments (see Section 4.2 and Section 4.3.1) as well as the designated storage operation for technical applications are aimed at dynamic modes of operation, preferentially in ambient air. The utilization of air as HTF makes especially the temperature range closer to the equilibrium relevant for the modeling approach.

Within the scope of the determination of the reaction rate constant $k(T_{Red})$ the pressure term $h(pO_2, pO_{2,eqII}(T_{Red}))$ in Eq. (2.17) generally exerts an influence on the reaction rate, which is due to the temperature dependence of the equilibrium pressure $pO_{2,eqII}(T_{Red})$. On this account the

Arrhenius term cannot be readily identified. Consequently, dynamic measurements at different heating rates (0.5, 1.0, 2.0, 5.0 and 10.0 K/min) are performed in pure N_2 atmosphere at first, in order to exclude the influence of the pressure term on the reaction. In the process the partial pressure of O_2 released during the reaction is neglected. This allows to derive the kinetic triplet – values of apparent A, E_a and $f(X_{Red})$ – solely from measurements of the reduction in pure N_2. The pressure dependence of the reaction is subsequently identified based on dynamic measurements in different O_2 atmospheres, which temperature profiles are schematically illustrated in the van't Hoff diagram (Fig. 3.12).

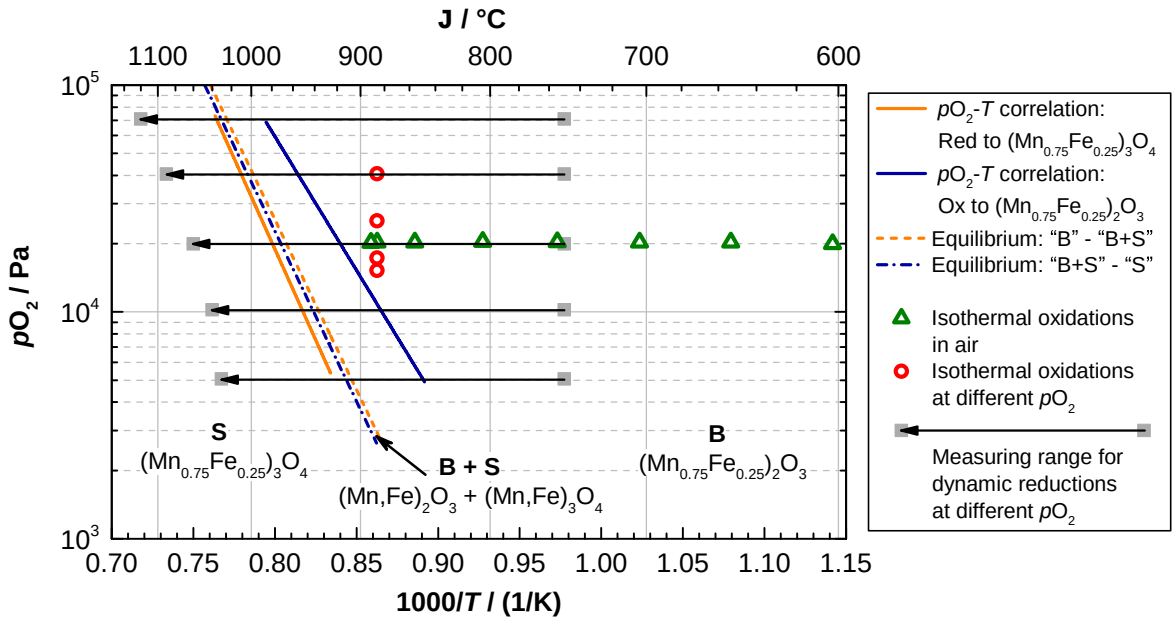

Figure 3.12: Temperature ranges for the determination of the effective reaction rates: Dynamic reduction and isothermal oxidation measurements.

Results – Discussion and Validation Figure 3.13a illustrates the corresponding experimental conversion curves in N_2, which show a strong dependence of the onset and offset temperatures of the reaction on the applied heating rate. The onset temperatures of the reaction shift to higher values with increasing heating rate. All curves reveal a rather long drawn-out progress of the reaction onset. This characteristic curve progression has also been observed in the reduction of pure Mn_2O_3 to Mn_3O_4 in N_2 or Ar [9, 30].

Owing to the prevailing N_2 atmosphere the reduction onset temperatures can be significantly decreased, as Fig. 3.13a indicates. The experiments illustrate the heat transfer limited nature of the reduction step, implying that an enhancement of the heating rate entails higher reaction rates, which has also been stated by Carrillo *et al.* [39, 40]. Thus, the reaction rate obeys the temperature dependence described by the Arrhenius term in Eq. (2.18). An *in situ* XRD analysis of the reduction of Mn-Fe oxide with a similar composition (molar ratio Fe/Mn of 1:4) at 10 K/min in argon by Carrillo *et al.* revealed the presence of two polymorphic spinel phases at a temperature of 900 °C, namely the cubic spinel β-$(Mn,Fe)_3O_4$ as the main phase and the tetragonal spinel

α-$(Mn,Fe)_3O_4$ to a minor extent. It was found, that in the absence of O_2 several reactions seem to proceed successively with increasing temperature. The formation of the tetragonal spinel took place at lower temperatures, whereas the prevailing formation of the cubic spinel was identified at higher temperatures, where higher reaction conversions ($X_{Red} > 0.5$) have been reached [43].

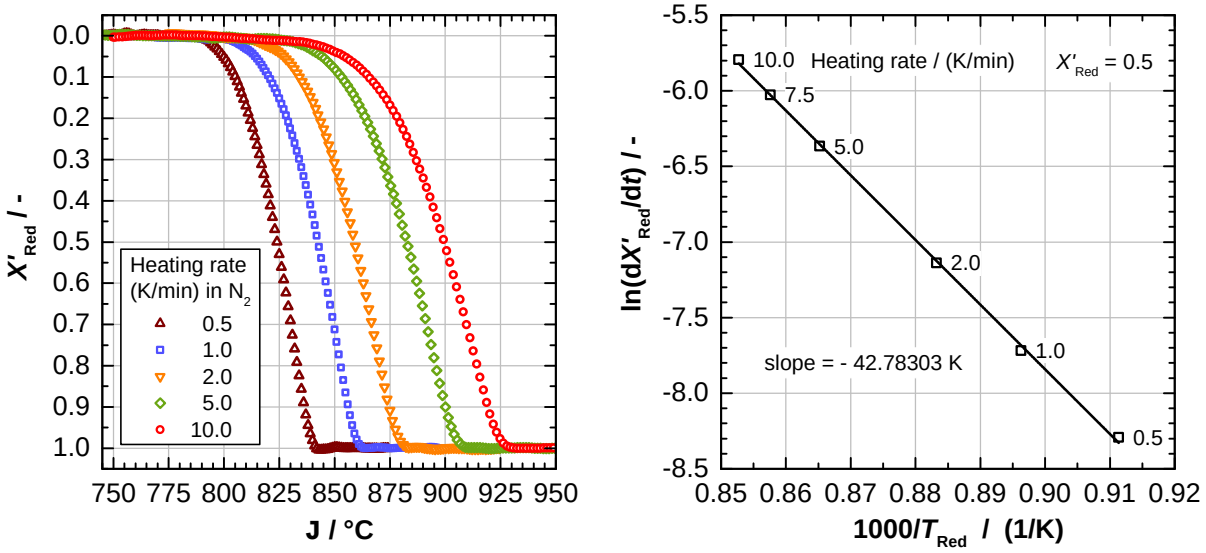

(a) Conversion over temperature. **(b)** Arrhenius plot for the determination of E_a.

Figure 3.13: Reduction of $(Mn_{0.75}Fe_{0.25})_2O_3$ to $(Mn_{0.75}Fe_{0.25})_3O_4$ in N_2 at different heating rates (thermogravimetric measurements).

The evaluation procedure for the derivation of the different dependencies of the reaction model, described by Eq. (2.17), involves three steps:

1. The identification of the kinetic triplet A, E_a and $f(X_{Red})$ poses an interlinked problem in dynamic measurements, as the reaction rate depends on $k(T_{Red})$ and $f(X_{Red})$ at any given time. Consequently, in the first step the effective activation energy E_a of the reduction step in pure N_2 is evaluated by means of the so-called *differential isoconversional method* according to Friedman [62]. The method is based on the isoconversional principle, which states that the reaction rate at constant extent of conversion is only a function of temperature [145]. Preliminary assumptions regarding the underlying kinetic model $f(X_{Red})$ are not required, which is why it is also referred to as a *model-free method*. As the van't Hoff correlation (eqII) according to Table 3.4 is not valid in the case of measurements in pure N_2 atmosphere, the pressure term is not required and has been set equal to one for the determination of the kinetic triplet: $h(pO_2, pO_{2,eqII}(T)) = 1$. Taking the logarithm of Eq. (2.17) gives $\ln[(dX'_{Red}/dt)_{X'_{Red},i}] = \ln[\beta_i (dX'_{Red}/dT)_{X'_{Red},i}] = \ln[f(X'_{Red}) \cdot A_{X'_{Red}}] - [E_{a,X'_{Red}}/(\mathbb{R}T_{X'_{Red},i})]$. Plotting $\ln(dX'_{Red}/dt)$ at constant extent of conversion X'_{Red} over the corresponding reciprocal temperature $1000/T_{X'_{Red},i}$ for different heating rates β_i, respectively, yields an Arrhenius-type plot. The slope $-E_{a,X'_{Red}}/(1000\mathbb{R})$ of the linear regression is proportional to the apparent activation energy $E_{a,X'_{Red}}$. For a constant conversion of 50 % an apparent activation energy $E_{a,50}$ of 355.72 kJ/mol is found (Fig. 3.13b). Similarly, Carrillo *et al.* carried out the reduction of $(Mn_{0.8}Fe_{0.2})_2O_3$ at different heating rates in Ar and reported an average value of

371.2 kJ/mol, also determined based on the *Friedman method* [43].

Furthermore, the principle of the isoconversional method is applied to the conversion range between 7.5 % and 92.5 % with a step size of 2.5 %. The apparent activation energies determined by means of the Friedman method are subsequently plotted against the respective reaction conversion X'_{Red} in order to identify a possible dependence of the isoconversional $E_{\mathrm{a},X'_{\mathrm{Red}}}$ on the extent of conversion, which would be an indication of a multi-stage reaction. If the variation of the activation energy (difference between the maximum and minimum values) over the extent of conversion accounts for more than 20 to 30 % in relation to the average E_{a}-value, a simple single-step reaction cannot be taken as basis for further calculations [145]. In the case of the $(Mn_{0.75}Fe_{0.25})_2O_3$ reduction the trend of the apparent activation energy values reveals a slight but constant decrease with advancing reaction conversion (and temperature), which observation is typical for decomposition reactions such as the present reduction step [145]. However, the difference between $E_{\mathrm{a,max}}$ and $E_{\mathrm{a,min}}$ in the above-mentioned conversion range amounts to ≈17 % of the average E_{a}-value. On that account the approach to treat the reduction as a single-step process (using a single-step rate equation hereinafter) can be considered adequate. Correspondingly, the chosen procedure applying the isoconversional method, which is based on the assumption that the activation energy does not vary significantly with conversion, is legitimated.

2. Subsequently, the reaction mechanism $f(X_{\mathrm{Red}})$ and the pre-exponential factor A are simultaneously quantified by plotting the product of the experimental conversion rate and the exponential part of the Arrhenius term $y(X'_{\mathrm{Red}}) = (\mathrm{d}X'_{\mathrm{Red}}/\mathrm{d}t)_{X'_{\mathrm{Red}}} \cdot \exp[E_{\mathrm{a}}/(\mathbb{R}T_{X'_{\mathrm{Red}}})] = A \cdot f(X'_{\mathrm{Red}})$ against the conversion X'_{Red} for each different heating rate β_{i}, respectively, following a common master plot approach [145]. For each plot a conversion step size of 1 % is selected. The resulting curve progression is characteristic for a certain reaction mechanism model $f(X_{\mathrm{Red}})$, as the pre-exponential factor is a constant. A comparison of the experimental with theoretical master plots for different kinetic models used in solid-state kinetics (see also Table B.6) leads to the most appropriate kinetic model. By means of this approach the empirical kinetic model $f(X_{\mathrm{Red}})$ of Avrami-Erofeev, indicating a nucleation and growth mechanism, is identified as an adequate match, as shown in Fig. 3.14a. The parameter n of the corresponding model function along with the pre-exponential factor A are determined by numerical curve fitting based on a minimization of the sum of error squares, which yield the values of 1.95 for n and $2.74 \cdot 10^{13}$ 1/s for A.

3. In the final step dynamic measurements at 10 K/min in different oxygen atmospheres (pO_2 between ≈5 kPa and ≈70 kPa) are used to identify the dependence of the reaction rate on the gas pressure. In the reduction step the gas pressure is lower than the equilibrium pressure at a given temperature. The calculation is based on the logarithm of Eq. (2.17), $\ln(\mathrm{d}X'_{\mathrm{Red}}/\mathrm{d}t) - \ln(A) + [E_{\mathrm{a}}/(\mathbb{R}T_{X'_{\mathrm{Red}}})] - \ln[f(X'_{\mathrm{Red}})] = \ln[h(pO_2, pO_{2,\mathrm{eqII}}(T_{X'_{\mathrm{Red}}}))]$, applying the isoconversional method ($X'_{\mathrm{Red}} = 0.5$). The phase boundary line "bixbyite + spinel" - "spinel" – denoted "eqII" in Table 3.4 – is applied as the equilibrium pressure $pO_{2,\mathrm{eqII}}(T_{X'_{\mathrm{Red}}})$ in the model equation of the reduction step, with the equilibrium partial pressure of oxygen being calculated according to the respective

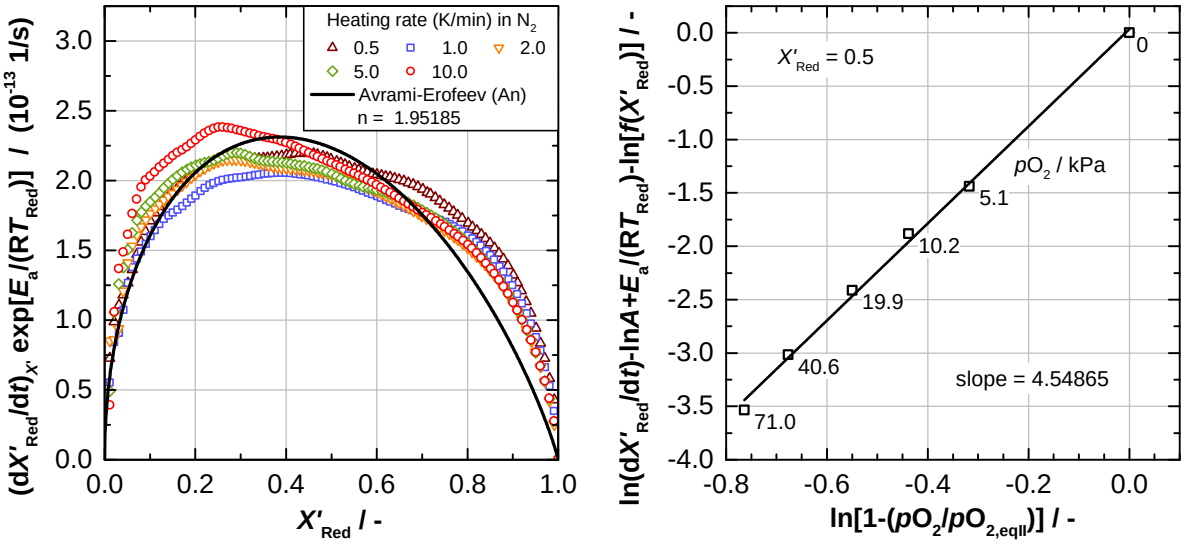

(a) Approximation of an empirical kinetic model $f(X_{\mathrm{Red}})$.

(b) Determination of the exponent m of the pressure term (measurements at 10 K/min).

Figure 3.14: Approximation of an empirical reaction mechanism based on reduction measurements in N_2 and influence of different pO_2 on the reaction rate of the reduction.

temperature $T_{X'_{\mathrm{Red}}}$ at 50 % conversion. A suitable pressure term can be identified, if the left hand side of the expression at 50 % conversion plotted against the logarithm of a potential pressure term results in a linear relationship. Experimental data are suitably represented by the pressure expression $[1-(pO_2/(pO_{2,\mathrm{eqII}}(T_{X'_{\mathrm{Red}}})))]^m$, as illustrated in Fig. 3.14b. The slope of the linear correlation in the double-logarithmic plot corresponds to the empirical exponent m of the pressure term, giving a value of 4.55.

Based on the reaction rate in terms of the time derivative of experimental conversion data, a parameterization according to Eq. (2.17) yields the following effective reaction rate for the reduction step:

$$\begin{aligned}\frac{\mathrm{d}X_{\mathrm{Red}}}{\mathrm{d}t} = 2.74\cdot 10^{13}\,\frac{1}{\mathrm{s}}\exp\left(-\frac{355.72\,\frac{\mathrm{kJ}}{\mathrm{mol}}}{\mathbb{R}T_{\mathrm{Red}}}\right)\\ \cdot 1.95(1-X_{\mathrm{Red}})[-\ln(1-X_{\mathrm{Red}})]^{\left(1-\frac{1}{1.95}\right)}\cdot\left(1-\frac{pO_2}{pO_{2,\mathrm{eqII}}(T_{\mathrm{Red}})}\right)^{4.55}\end{aligned} \tag{3.7}$$

The developed model for the effective reaction rate is valid for temperatures up to about 1085 °C and oxygen partial pressures between ≈5 kPa and ≈70 kPa. For the reactivity beyond the given ranges the model serves only as a rough estimation. Figure 3.15a shows the model prediction for the reaction rate in pure N_2 (dashed lines), with the pressure term equal to unity.

Figure 3.15b displays the comparison of the model prediction against the experimental conversion profiles of the reduction at various O_2 atmospheres and a heating rate of 2 K/min, which can be considered as a realistic condition in the envisaged technical application. All conversion curves point out a similar progress of reaction, with a shift of the curves according to the experimentally determined pO_2-T dependence. Overall, in comparison to the measurement at 2 K/min in N_2, the

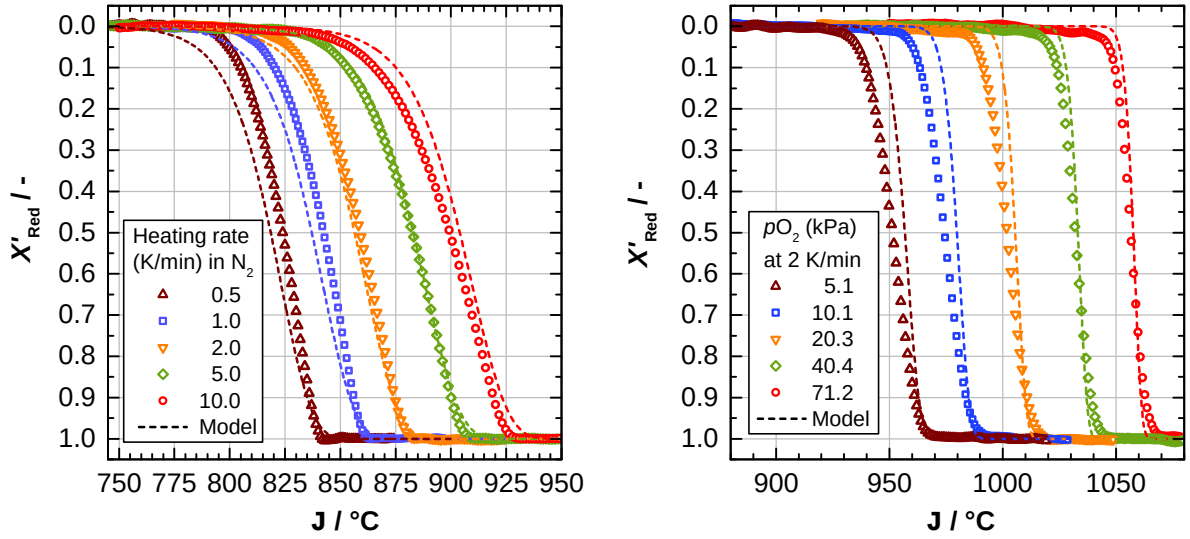

(a) Reduction of $(Mn_{0.75}Fe_{0.25})_2O_3$ in N_2 at different heating rates, the pressure term equals unity in this case.

(b) Reduction of $(Mn_{0.75}Fe_{0.25})_2O_3$ in different O_2 atmospheres at a heating rate of 2 K/min.

Figure 3.15: Comparison of measurements and determined model for the reduction step: Symbols correspond to experimental data, dashed lines to the prediction by the model for the effective reaction rate according to Eq. (3.7).

onset of the reactions becomes sharper and the reaction progress turns out to be steeper in different O_2 atmospheres at 2 K/min, indicating higher reaction rates. These are essentially evoked by higher reaction temperatures with rising pO_2.

It has to be taken into account, that the two-phase fields in the phase diagram of Mn-Fe oxide (Fig. B.2 in the appendix illustrates the phase diagram in air) are shifted in the absence of O_2 or atmospheres at significantly reduced pO_2, such that the tetragonal spinel α-$(Mn,Fe)_3O_4$ (T) forms at intermediate temperatures (see also results from *in situ* XRD analysis of Mn-Fe oxide with Fe/Mn molar ratio of 1:4 in the range from 700 °C to 900 °C in Ar [43]). In this case the phase transition from the cubic bixbyite $(Mn,Fe)_2O_3$ (B) to the cubic spinel β-$(Mn,Fe)_3O_4$ (S) proceeds via the two-phase fields "T + B" and "S + T" with rising temperature. Considering that a systematic approach to determine the kinetic triplet by means of measurements in pure N_2 has been applied (*isoconversional method*), while the mixed oxide may have been subjected to a shift of the two-phase fields under these conditions though, the model predictions and the experimental curves in Figs. 3.15a and 3.15b show good agreement.

The occurrence of sequential transformations in pure N_2 may also explain the slight variation of the isoconversional activation energy with conversion, as described above, since the formation of each phase might follow a different kinetic model of nucleation and growth (see also [43]). Consequently, the reaction mechanism of the reduction in O_2 atmosphere may deviate somewhat from the mechanism in pure N_2. Furthermore, it should be noted that the small deviation of model curves from experimental curves may also be attributed to the fact, that the isolation of the pressure

term is generally more complex in the case of mixed oxides compared to pure oxides.

In summary, the reaction rate of the reduction increases with rising temperature and falling pO_2, which corresponds to an increment of the temperature driving force $T_{Red} - T_{eqII}(pO_2)$ as well as an increment of the pressure driving force $pO_{2,eqII}(T_{Red}) - pO_2$ for the reaction. From a technical point of view it can be suggested, that the HTF air – e.g., from the solar field – needs to have a temperature of up to ≈1050 °C in order to provide a temperature difference sufficient to drive the reaction.

3.4.3 Effective Reaction Rate of Oxidation

General Methodology and Experimental Procedure For the oxidation step isothermal measurements are performed at different temperatures and oxygen partial pressures to extract effective kinetic parameters. Measurements at nearly isothermal conditions conveniently enable to demonstrate the temperature and partial pressure dependence of the reaction rate as well as to overcome the kinetic limitations revealed in Section 3.4.1. All reactions are initiated by switching the gas atmosphere from pure nitrogen to the desired oxygen content, imposing a sudden change of the pO_2. Therefore conversion and conversion rate of the transformation to cubic bixbyite can be clearly attributed to the chosen temperature and pO_2 as a function of time, respectively. The detailed evaluation procedure for the evolution of a reaction model for the effective oxidation rate is given below. Considering the utilization of air as HTF, measurements in the temperature region closer to the equilibrium are chosen for the modeling approach, similar to the reduction step.

For isothermal measurements in different O_2 atmospheres the material is again (after reduction in the reference cycle) reduced at a heating rate of 10 K/min up to 1060 °C and subsequently cooled down to 980 °C in air. Further cooling down to the desired temperature for oxidation is performed in pure N_2 in order to prevent a premature re-oxidation. After a holding time of 10 min to wait for a steady sample temperature, the oxidation is initiated by switching to the desired O_2 atmosphere. The latter is adjusted by means of the required fractions of the corresponding O_2 and N_2 volume flow rate at an overall flow of 100 NmL/min. Figure 3.12 in Section 3.4.2 depicts the measurement range for the isothermal oxidation runs in air as well as atmospheres with different O_2 partial pressures.

Results – Discussion and Validation Carrillo *et al.* analyzed the oxidation of $(Mn_{0.8}Fe_{0.2})_3O_4$ at 700 °C under air by means of *in situ* XRD. The authors identified a phase mixture of mainly cubic spinel β-$(Mn,Fe)_3O_4$ and in a lower proportion tetragonal spinel α-$(Mn,Fe)_3O_4$ for the reduced phase upon reduction up to 900 °C in Ar (1 h holding time) and subsequent cooling to 700 °C in Ar. They were able to prove the transformation of the phase mixture into cubic bixbyite $(Mn,Fe)_2O_3$ in the presence of air [43]. In the current studies a similar phase composition can be assumed for the reduced phase $(Mn_{0.75}Fe_{0.25})_3O_4$ upon cooling-down in pure N_2 from 980 °C to the respective isothermal oxidation temperature, followed by the transformation into bixbyite

under atmospheres at different pO_2. The varied dependencies of the reaction model described by Eq. (2.17) are derived in three steps:

1. At first the pO_2 is varied at an isothermal temperature of 886.2 °C in order to identify the pressure dependence of the oxidation rate. The temperature is chosen from a technological point of view in close-range of the determined temperature threshold value for the oxidation in atmospheric air (≈920.4 °C at pO_2 of 21.228 kPa). The current measurements indicate, that the onset of the dominant rate process is deferred by a delay period t_0, which originates from the latency caused by switching from N_2 to the desired O_2 atmosphere as well as from an induction period required for the generation of growth nuclei prior to the onset of the accelerating period [63, 103]. This induction period is highly dependent on the prevailing temperature.

The magnitude of t_0 can be obtained from the intercept on the t-axis of a $g(X_{Ox})$-time plot [63, 145], $g(X_{Ox}) = k(T_{Ox})t$ being the integral form of the suitable reaction model (determination of $f(X_{Ox})$ see below). In Fig. 3.18a, the dependence of the oxidation rate on the prevalent pO_2 – and on the state of equilibrium accordingly – is shown (symbols). An increment of the pO_2 from ≈15 kPa to ≈40 kPa at constant temperature, respectively, induces a significant increase of the reaction rate, emphasizing a strong impact of the pO_2. A rise of the pO_2 in this region implicates a stronger driving pressure difference $pO_2 - pO_{2,eqI}(T_{Ox})$ as well as driving temperature difference $T_{eqI}(pO_2) - T_{Ox}$ to the equilibrium state at a constant temperature T_{Ox} of 886.2 °C, shifting the reaction towards the oxidized phase more rapidly.

The mathematical form of the pressure term is derived from plotting the logarithm of the conversion rate $\ln(dX'_{Ox}/dt)$ at 50 % conversion (according to the isoconversional method [62, 145]) against the logarithm of various pressure terms (see also Eq. (2.19)), respectively, taking all measurements at different oxygen partial pressures but constant temperature of 886.2 °C into account. In this plot the conversion- and temperature-depending terms in Eq. (2.17) are assumed to be constant. The pressure dependence of the reaction is expressed in the best possible way by the mathematical form of the pressure term, which gives a linear relationship. Among different forms of the pressure term, the logarithmic function $[\ln(pO_2/pO_{2,eqI}(T_{Ox}))]^m$ yields an appropriate linear approximation, displayed in Fig. 3.16a.

The slope of the line with a value of 7.06 corresponds to the empirical exponent m of this pressure term. The phase boundary line “bixbyite” - “bixbyite + spinel” – denoted “eqI” in Table 3.4 – has been applied as the equilibrium oxygen partial pressure $pO_{2,eqI}(T_{Ox})$ in the model equation of the oxidation step.

2. A typical master plot method based on the differential form of the kinetic equation Eq. (2.17) is applied for the determination of the kinetic model. In contrast to experimental data obtained under non-isothermal conditions at linear heating rates, in which case the assumed kinetic model and calculated kinetic parameters are interdependent, the knowledge of the E_a is not required for the construction of the master plots in the case of isothermal conditions [68]. Using a conversion of 50 % as a reference point, the following expression for the experimental conversion rate, referred

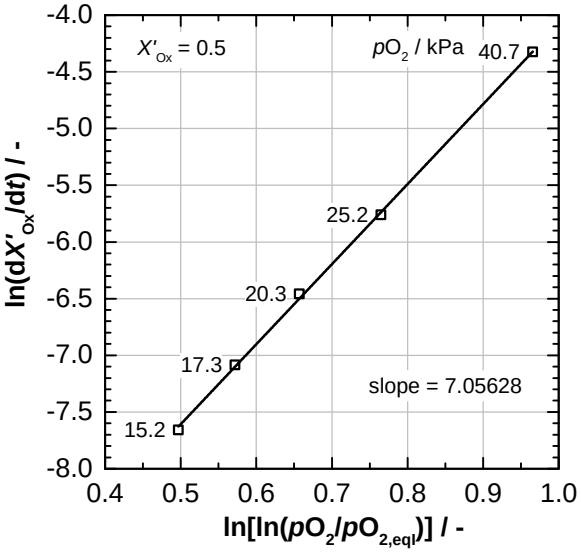

(a) Determination of the exponent m of the pressure term at 886.2 °C.

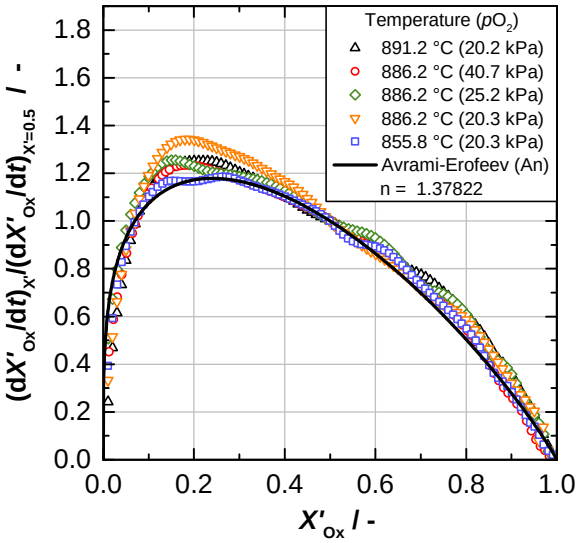

(b) Approximation of an empirical kinetic model $f(X_{Ox})$.

Figure 3.16: Influence of different pO_2 on the reaction rate of isothermal $(Mn_{0.75}Fe_{0.25})_3O_4$ oxidation to $(Mn_{0.75}Fe_{0.25})_2O_3$ and approximation of an empirical reaction mechanism.

to the respective rate at $X'_{Ox} = 0.5$, can be derived for the reactions under isothermal conditions:

$$\frac{\left(\frac{dX'_{Ox}}{dt}\right)_{X'_{Ox}}}{\left(\frac{dX'_{Ox}}{dt}\right)_{X'_{Ox}=0.5}} = \frac{f(X'_{Ox})}{f(0.5)} \tag{3.8}$$

A comparison of the standardized conversion rates (plotted against the respective conversions X'_{Ox}) with theoretically calculated plots of $f(X'_{Ox})/f(0.5)$ against X'_{Ox}, drawn by assuming various possible $f(X_{Ox})$ functions (see also Table B.6) [63], provides indications of the potential reaction mechanism. Due to the sigmoidal progress of the oxidation reaction, a sigmoidal function on the basis of the Avrami-Erofeev mechanism $f(X_{Ox}) = n(1-X_{Ox})[-\ln(1-X_{Ox})]^{(n-1)/n}$ has been chosen for the measurements at 855.8 °C, 886.2 °C and 891.2 °C in air, as well as for 886.2 °C at 25.2 kPa and 40.7 kPa O_2. The corresponding parameter n of the kinetic model is fitted to the experimental data by means of non-linear curve fitting as shown in Fig. 3.16b. The evaluation results in a value of 1.38. It can also be asserted that the reaction follows different mechanisms depending on the temperature and pressure region, as the reaction progress at lower temperature (805.2 °C in air) as well as lower partial pressure (pO_2 of 15.2 kPa and 17.3 kPa at 886.2 °C) cannot be reflected by an Avrami-Erofeev model.

3. In the final step the temperature dependent term of the reaction rate is derived from an Arrhenius-type plot at a conversion X'_{Ox} of 50 % (Fig. 3.17a). Therefor $\ln(dX'_{Ox}/dt) - \ln[f(X'_{Ox})] - \ln[h(pO_2, pO_{2,eqI}(T_{Ox}))]$ is plotted versus the reciprocal temperature $1000/T_{Ox}$ for different isothermal measurements, taking the already identified parameters of the pressure term and kinetic model into account. The modified Arrhenius plot reveals a linear relationship for the temperature range between 805.2 °C and 891.2 °C, with the slope $-E_a/(1000\mathbb{R})$ giving an apparent E_a of 463.53 kJ/mol.

A pre-exponential factor A of $1.78 \cdot 10^{16}$ 1/s is calculated based on the y-intercept. In the range below 805.2 °C the apparent E_a appears to vary somewhat with temperature, as the slope and thus the apparent activation energy slightly decreases (temperature range not considered in the calculation in Fig. 3.17a). Carrillo *et al.* deduced an average E_a of 74 ± 7 kJ/mol for the oxidation of $(Mn_{0.8}Fe_{0.2})_3O_4$ based on isothermal TGA runs merely conducted in air. However, this comparatively low value can be ascribed to the fact, that the dependence of the process rate on the partial and equilibrium pressure of the gaseous product O_2 has not been regarded in this case. The kinetic triplet was only determined for the low temperature oxidation range, dominated by the increase of the reaction rate with temperature [43].

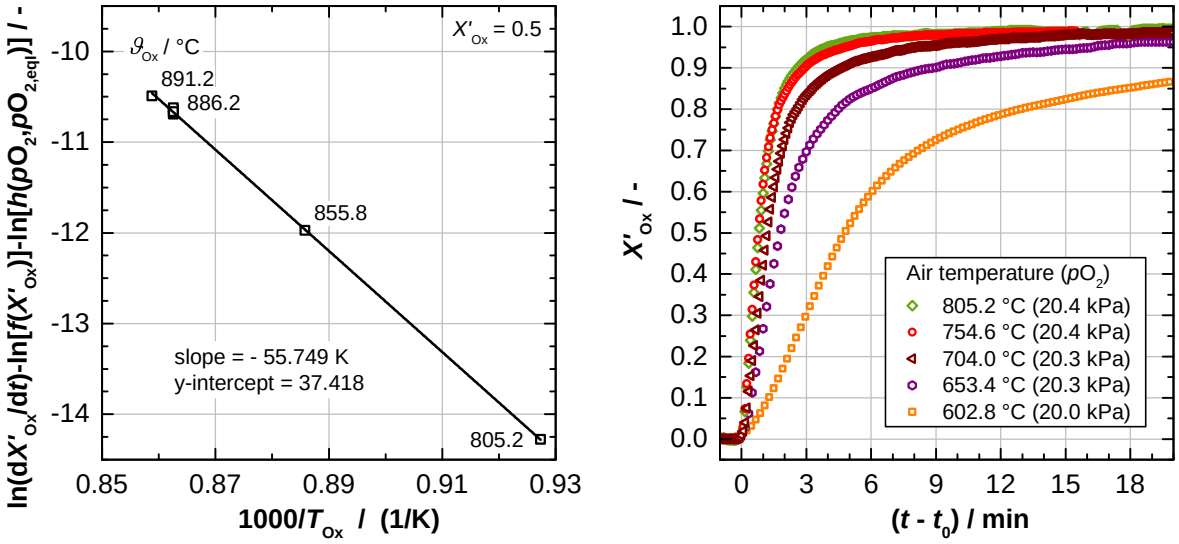

(a) Modified Arrhenius plot for the determination of E_a.

(b) Time evolution of $(Mn_{0.75}Fe_{0.25})_3O_4$ oxidation conversion in air at different temperatures far from equilibrium.

Figure 3.17: Isothermal oxidation of $(Mn_{0.75}Fe_{0.25})_3O_4$ to $(Mn_{0.75}Fe_{0.25})_2O_3$.

Figure 3.17b presents the conversion curves for temperatures far from equilibrium. In this region the reaction rate clearly rises with increasing temperature, as the temperature dependence of the reaction rate according to the Arrhenius term (Eq. (2.18)) constitutes the dominating factor on the rate. The influence of the pressure driving force is only of minor importance in this temperature region. At temperatures far from equilibrium ($T \leq \approx 800$ °C) the shape of the conversion curves reveal distinctively, that the reaction proceeds via a different mechanism. This is also the reason why it takes a comparatively long time for the reactions to reach full conversion. In order to derive the effective reaction rate far from equilibrium, a different kinetic model, a relevant apparent activation energy and pre-exponential factor as well as a suitable pressure term – which requires to measure the dependence of the reaction rate on the pO_2 in this temperature range – would have to be deduced along the modeling procedure. In summary it can be stated, that varying reaction mechanisms and dependencies on temperature and partial pressure make it difficult to evolve a single reaction rate expression valid for a broad temperature and pressure range.

In contrast, examining the oxidation reactivity of $(Mn_{0.8}Fe_{0.2})_3O_4$ in air Carrillo *et al.* identified somewhat different temperature ranges. While the reaction followed an Arrhenius behavior from 650 °C to 725 °C, exhibiting higher oxidation rates with rising temperature, a deceleration of the reaction rate was observed from 725 °C to 800 °C. The maximum rate occurred at 725 °C with a total conversion reached in ≈8 min. It has to be noted, though, that the preceding reduction step was carried out entirely in Ar atmosphere [43]. The deviations between the current findings and the results obtained by Carrillo *et al.* might be attributed to various differences, such as the modified composition of the binary oxide, different measurement conditions and a comparatively long exposure to inert Ar atmosphere prior to $(Mn_{0.8}Fe_{0.2})_3O_4$ oxidation according to the reported study [43].

As a result of the systematic parameterization of the oxidation rate using Eq. (2.17), the following effective reaction rate has been deduced:

$$\begin{aligned}\frac{\mathrm{d}X_{\mathrm{Ox}}}{\mathrm{d}t} = 1.78 \cdot 10^{16} \frac{1}{\mathrm{s}} \exp\left(-\frac{463.53\,\frac{\mathrm{kJ}}{\mathrm{mol}}}{\mathbb{R}T_{\mathrm{Ox}}}\right) \\ \cdot 1.38(1-X_{\mathrm{Ox}})[-\ln(1-X_{\mathrm{Ox}})]^{\left(1-\frac{1}{1.38}\right)} \cdot \left(\ln\frac{pO_2}{pO_{2,\mathrm{eqI}}(T_{\mathrm{Ox}})}\right)^{7.06}\end{aligned} \tag{3.9}$$

The developed model for the effective reaction rate is specifically valid for temperatures above 800 °C and oxygen partial pressures between ≈15 kPa and ≈40 kPa. For the reactivity beyond the given ranges the model serves only as a rough estimation. Figure 3.18a illustrates the model predictions (dashed lines) based on expression Eq. (3.9) in comparison to measurements at different pO_2 (symbols), taking the corresponding delay periods t_0 into account. The model clearly represents the effect of the pressure dependence of the reaction.

Good agreement between the evolved model and experimental curves is also obtained for the variation of the isothermal oxidation temperature in air. Figure 3.18b demonstrates the dependence of the reaction rate on the equilibrium state, similar to the pressure dependence described above. As expected, the lowest reaction rates emerge closer to the thermodynamic equilibrium. Therefore, a temperature decrease down to about 800 °C results in an increase of the reaction rate due to an enhancement of the driving temperature difference $T_{\mathrm{eqI}}(pO_2) - T_{\mathrm{Ox}}$ as well as driving pressure difference $pO_2 - pO_{2,\mathrm{eqI}}(T_{\mathrm{Ox}})$ to the equilibrium state.

Generally, compared to pure manganese oxide (see Fig. B.8), rates of $(Mn_{0.75}Fe_{0.25})_3O_4$ oxidation are considerably higher. The highest reaction rate in air is achieved between 750 °C and 800 °C, as indicated in Fig. 3.17b and Fig. 3.18b. The ***T**ime-**T**emperature-**T**ransformation* (TTT) diagram for the oxidation of $(Mn_{0.75}Fe_{0.25})_3O_4$ at 50 % conversion – illustrated in Fig. B.10 – accentuates the transformation times at different isothermal temperatures in air.

The most rapid overall reaction takes place at temperatures close to 850 °C, reaching complete conversion within 10 min upon switching from N_2 to air (see Fig. 3.18b).

The observed deceleration of the reaction rate with rising temperature closer to the equilibrium – $T \geq$ ≈800 °C in the present case – has also been reported for other metal oxide oxidations, such as for the redox couples CuO/Cu_2O [48] as well as BaO_2/BaO [38], and is characteristic not only for

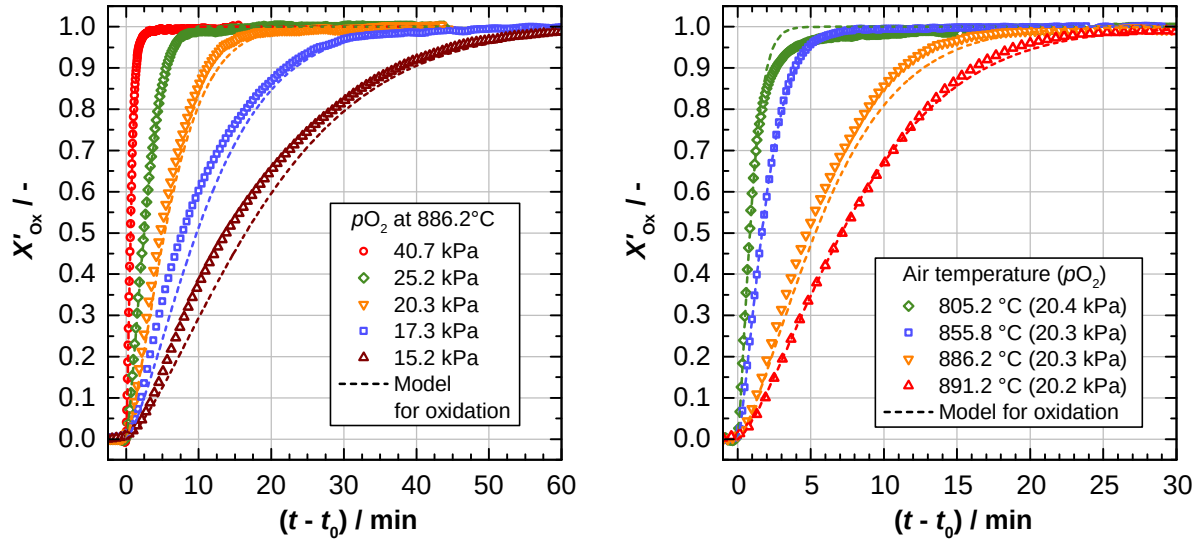

(a) Dependence of isothermal $(Mn_{0.75}Fe_{0.25})_3O_4$ oxidation on different oxygen partial pressures at 886.2 °C.

(b) Time evolution of isothermal oxidation conversion in air at different temperatures.

Figure 3.18: Comparison of measurements and determined model for the oxidation step of $(Mn_{0.75}Fe_{0.25})_3O_4$ closer to equilibrium: Symbols correspond to experimental data, dashed lines to the prediction by the model according to Eq. (3.9) for the effective reaction rate.

reversible gas-solid reactions. The decrease in oxidation rate at higher temperatures might not only be attributed to the decline in the driving force caused by an increase in the equilibrium partial pressure of oxygen with temperature. For instance, Carrillo *et al.* supposed that the deviation of BaO oxidation from Arrhenius behavior at temperatures closer to equilibrium might also be due to possible hindrances of anionic oxygen diffusion caused by the formation of an external layer of BaO_2 in this case [38].

3.4.4 Physical and Thermophysical Material Properties

Material Density and Particle Porosity From the standard atomic weights of the elements Mn, Fe and O [99] follows an average molecular weight of 158.328 g/mol for $(Mn_{0.75}Fe_{0.25})_2O_3$ and 229.492 g/mol for $(Mn_{0.75}Fe_{0.25})_3O_4$. The theoretical solid density $\rho_{true,th}$ of $(Mn_{0.75}Fe_{0.25})_2O_3$ can be roughly estimated based on the true densities of the single oxides Mn_2O_3 (4.5 g/cm^3, GESTIS database) and Fe_2O_3 (5.25 g/cm^3, GESTIS database) and their respective mass fractions w_i in the binary oxide according to Eq. (3.10) [160]:

$$\rho_{true,th} = \left(\frac{w_{Mn_2O_3}}{\rho_{Mn_2O_3}} + \frac{w_{Fe_2O_3}}{\rho_{Fe_2O_3}} \right)^{-1} \tag{3.10}$$

Since $(Mn_{0.75}Fe_{0.25})_2O_3$ represents a new compound, the calculated theoretical value of 4.668 g/cm^3 is only an estimate. On this account the true solid density ρ_{true} of $(Mn_{0.75}Fe_{0.25})_2O_3$ – excluding open and closed pores – is measured with a helium pycnometer based on the method of

gas displacement.[1] At first the granules are ground to a fine powder with an agate mortar to make even closed pores accessible to the measurement and thereby eliminate internal voids, followed by drying the sample at 110 °C overnight. The instrument has been tested using a silica reference prior to the sample measurement. Helium pycnometry yields an average of 5.125 ±0.012 g/cm^3 for the true density of $(Mn_{0.75}Fe_{0.25})_2O_3$ (fivefold measurement), which value is somewhat higher than the calculated one. Owing to the high accuracy of the measuring technique, the measured value is used for further calculations in this work.

Hg porosimetry measurements of the $(Mn_{0.75}Fe_{0.25})_2O_3$ granules yield a high average intraparticle porosity ε_p of 60.0 %, which value reflects all accessible inner pores. A repeat determination with a sample mass of ≈1.1 g has been performed, respectively. The average median pore diameter by volume is 0.81 μm, which diameter corresponds to 50 % of the total Hg volume intruded. The instrument-specific measurement uncertainty amounts to < 2.5 %, which has been determined using a silica-alumina reference material. Taking the true density of the solid into account gives a value of 2.050 g/cm^3 for the apparent particle density of the granules according to the following relation $\rho_{app} = \rho_{true}(1-\varepsilon_p)$.

Mean Granular Particle Size and Particle Size Distribution As described in Section 3.3.1 granular particles were prepared in the size range of approximately 1 mm to 3.5 mm. However, the employed particles are irregularly shaped due to the preparation process, which can be clearly seen in Fig. B.3 (right). An image analysis is performed in order to determine a mean representative particle diameter, which influences the evaluation of the heat transfer coefficient (see Eq. (C.21)) and the permeability of a packed bed. Furthermore, the solid surface available for heat transfer also depends on the mean representative diameter of the granules. At first granules are evenly spread onto an adhesive foil and scanned by means of a flat bed scanner (Perfection V750 Pro, Epson). The recorded two-dimensional particle images are then refined and analyzed with the aid of the software ImageJ [79, 128]. In the process the projected area A_{pr} of each single particle is identified and the corresponding diameter $d_{p,pr}$ of a sphere of equal projected area is calculated according to the following equation:

$$d_{p,pr} = \sqrt{\frac{4 \cdot A_{pr}}{\pi}} \tag{3.11}$$

A total of ≈4700 particles are analyzed. The average value of all equivalent particle diameters $d_{p,pr}$ results in a mean particle diameter $\bar{d}_{p,pr}$ of 2.13±0.56 mm. It has to be noted, that this value serves only as a rough estimate for the mean particle size, since the shape and hence a shape factor could not be taken into account.[2] Consequently, for calculations throughout this work a spherical

[1] He pycnometry as well as Hg porosimetry measurements of $(Mn_{0.75}Fe_{0.25})_2O_3$ were carried out by the Research Institute for Inorganic Materials - Glass/Ceramics - GmbH (FGK) in Höhr-Grenzhausen, Germany.

[2] The perimeter of the particles, which would have been required for the determination of the sphericity, could not be specified. The outline of the projected areas turned out to be too pixelated due to reflections of the foil covering the affixed particles.

particle shape is considered. The resulting particle size distribution (histogram) of the equivalent particle diameter $d_{p,pr}$ is displayed in Fig. 3.19a.

In case of the present broad particle size distribution, monodisperse particles with a characteristic particle diameter $d_{p,m}$ (so-called *Sauter mean diameter*) can be approximated by

$$d_{p,m} = \left(\sum_{i=1}^{n} \frac{Q_i}{d_{p,pr,i}} \right)^{-1} = \left[\sum_{i=1}^{n} \left(\frac{V_i}{V} \frac{1}{d_{p,pr,i}} \right) \right]^{-1} \tag{3.12}$$

with Q_i being the i^{th} volume fraction, which is the volume V_i of the i^{th} particle size fraction referred to the total analyzed particle volume V, and $d_{p,pr,i}$ being the average particle diameter of fraction i [142, 152]. A value of 2.42 mm is obtained for $d_{p,m}$, which is used as mean diameter for calculations in this work.

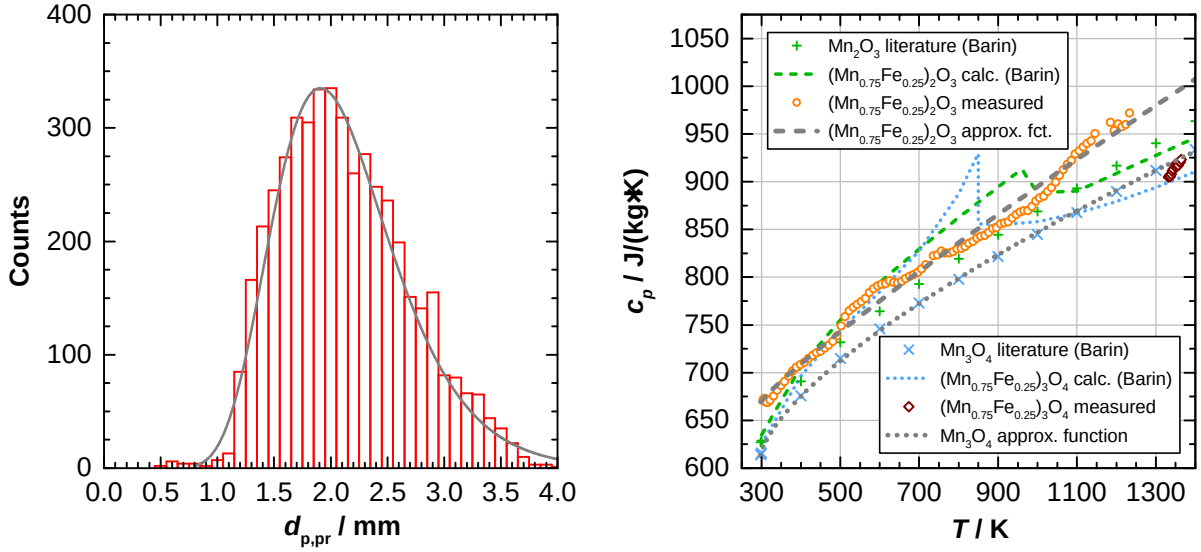

(a) Particle size distribution showing the calculated equivalent particle diameter $d_{p,pr}$ (Eq. (3.11)).

(b) Specific heat capacity of Mn-Fe oxide: Comparison of measured values and literature data.

Figure 3.19: Particle size distribution of the $(Mn_{0.75}Fe_{0.25})_2O_3$ raw material and specific heat capacity of Mn-Fe oxide.

Specific Heat Capacity The specific heat capacity of the mixed oxide constitutes an important thermophysical property, which determines the amount of thermal energy which can be stored by changing the temperature of the storage material (principle of STES). Temperature dependent specific heat capacities of the pure oxides can be taken from tabulated values [27], which are exemplarily illustrated for Mn_2O_3 and Mn_3O_4 in Fig. 3.19b. Generally, specific heat capacities of mixed oxides can be calculated from the specific heat capacities of the respective single oxides according to $c_{p,mixed} = \sum w_i \cdot c_{p,i}(T)$, with w_i being the mass fraction and $c_{p,i}(T)$ the specific heat capacity of the component i [57]. This has been carried out with the values of Mn_2O_3 ($w = 0.74785$) and Fe_2O_3 ($w = 0.25215$) for the oxidized as well as Mn_3O_4 ($w = 0.74778$) and

Fe_3O_4 ($w = 0.25222$) for the reduced phase of Mn-Fe oxide. The results of this approximation are displayed in Fig. 3.19b.

However, this calculation method does not seem to be suited for an exact c_p determination, especially since the Mn-Fe oxide represents a novel compound with a different lattice structure in comparison to iron oxide. The iron oxides exhibit anomalies of magnetic nature. Magnetic transitions occur at ≈960 K (*Néel temperature*) with α-Fe_2O_3 and ≈850 K (*Curie temperature*) with Fe_3O_4, involving maxima in the respective heat capacity curves [27, 54]. Hence, those are also reflected in the curve progressions of the calculated c_p-values in Fig. 3.19b. On this account measurements of the c_p-values of Mn-Fe oxide need to be performed by means of DSC (for description see also Appendix B.1).

For this purpose $(Mn_{0.75}Fe_{0.25})_2O_3$ granules are pestled to powder with the aid of EtOH, then compressed to pellets (85.0 mg and 91.3 mg, Ø of 5 mm) with a powder compacting tool, followed by calcination for 10 h at 950 °C in air (below the transition temperature). In the measurement run a pellet – placed in a Pt/Rh-crucible with pierced lid for accurate measuring conditions – was then heated from 30 °C up to 1200 °C with a heating rate of 10 K/min in air at 50 NmL/min. Using a baseline measurement, a sensitivity calibration measurement with a sapphire disc of known c_p-values and the actual sample measurement, the unknown c_p-values of Mn-Fe oxide can be evaluated based on a comparative method. The average c_p-values from two experimental runs are depicted in Fig. 3.19b. Between approx. 400 K and 1000 K the measured values for $(Mn_{0.75}Fe_{0.25})_2O_3$ are roughly in the range of the Mn_2O_3 and calculated $(Mn_{0.75}Fe_{0.25})_2O_3$ values, beyond ≈1050 K the measured values are clearly above. It becomes obvious that the magnetic anomaly described for iron oxides does not seem to occur in the mixed oxide. Using a regression analysis the curve progression can be well approximated with a power equation (Eq. (3.13)).

$$c_{p,\mathrm{ox}}(T) = \left(669.28596 + 0.62604 \left|\frac{T}{K} - 298\right|^{0.8982}\right) \mathrm{J/(kg \cdot K)} \tag{3.13}$$

$$c_{p,\mathrm{red}}(T) = \left(613.07996 + 2.58034 \left|\frac{T}{K} - 298\right|^{0.68764}\right) \mathrm{J/(kg \cdot K)} \tag{3.14}$$

As only one heating-up phase was conducted with a $(Mn_{0.75}Fe_{0.25})_2O_3$ sample per measurement, merely a few c_p-values have been obtained for $(Mn_{0.75}Fe_{0.25})_3O_4$ at high temperatures after completion of the reduction step (step not shown in Fig. 3.19b). Figure 3.19b indicates a reasonable agreement of those values with the literature data of pure Mn_3O_4 [27]. As a future numerical reactor model requires c_p-data in the full temperature range to allow the simulation of different storage operation modes, the power equation is fitted to the c_p-values of Mn_3O_4 (Eq. (3.14)). This estimated equation is considered adequate for $(Mn_{0.75}Fe_{0.25})_3O_4$ and is therefore adopted for further calculations in this work (see specific enthalpy values h illustrated in Fig. 4.5).

3.4.5 Findings Derived from Detailed Material Characterization

In Section 3.4 the reversible redox reaction of a granular Mn-Fe oxide with a Fe/Mn molar ratio of 1:3 has been systematically investigated by simultaneous thermal analysis with regard to thermodynamics and effective reaction rates, arriving at the following conclusions:

- Based on thermodynamic equilibrium data obtained from reported phase diagrams the redox reaction proceeds via a two-phase region in the examined pO_2-range from ≈2.6 kPa to 100 kPa. Since the reduction and oxidation step are, however, thermally decoupled owing to the presence of a thermal hysteresis under the chosen, practical dynamic measuring conditions, the sole information regarding the state of thermodynamic equilibrium is eventually not sufficient for the identification of the reactive operating temperature range of a TCS reactor.
- Corresponding pO_2-T correlations for the reduction and oxidation step, specifying technically relevant temperature threshold conditions for the reactivity of the storage material at different oxygen partial pressures, have been experimentally derived. Specifically, temperature threshold values of ≈981.8 °C and ≈920.4 °C have been determined for the reduction and oxidation onset in atmospheric air, respectively. It has to be noted, that particularly the oxidation step is subject to severe kinetic limitations, inhibiting the reaction in a temperature range nearby the equilibrium state.
- A comparison of the actual equilibria and the temperature threshold values for the reduction and oxidation – experimentally determined at different oxygen partial pressures – reveals that only a low degree of overheating ΔT is necessary for the reduction to set in. In contrast, the initiation of the oxidation requires a large degree of undercooling ΔT, essentially evoked by the occurrence of the described kinetic limitations during cooling. For this reason the oxidation constitutes the critical reaction step within the redox cycle.
- The redox reactivity of the reduction and oxidation has been examined in a wide temperature and partial pressure range to get a better understanding of the material behavior, which is crucial for the operation of a TCS reactor. Overall, kinetic and thermodynamic influences on the reaction rates have been derived. The effective reaction rate models developed for the reduction and oxidation step (oxidation model valid for $T \geq 800$ °C, closer to equilibrium) adequately describe the experimental data.
- While the reduction step can be considered mainly heat transfer limited, implying an enhancement of the reaction rates with higher heating rates, the oxidation step can be divided into two temperature ranges. On the one hand, at temperatures lower than 750-800 °C – far from equilibrium – the reaction rate rises with increasing temperature. On the other hand, at temperatures higher than ≈800 °C the reaction rate slows down closer to the equilibrium, showing a non-Arrhenius behavior due to strong thermodynamic influences. Overall, the pO_2 and therefore pressure driving force plays a significant role in the oxidation of Mn-Fe oxide.

The general scientific findings obtained as well as the general methodology pursued in the current study can be equally applied to similar cases of metal oxide characterizations and corresponding TCS applications. Additionally, the characterization data and expressions derived in this section can be incorporated into a future transient reactor model in order to gain a deeper understanding of the processes occurring in a reactive packed bed of Mn-Fe oxide (Chapter 4) by means of numerical simulation. Furthermore, such a reactor model allows to design a technical scale storage reactor and simulate its charging/discharging behavior.

4 Experimental Setup and Examination of TCS-Concept on Lab-Scale

4.1 Reactor Concept and Design – Granular Packed Bed

A packed bed configuration has been chosen for the storage reactor, in order to analyze the main influencing facets and demonstrate the heat effect of the TCS concept based on redox reactions. In comparison to continuous concepts with moving storage material, a large impact of mechanical stress on the behavior and integrity of the reactive particles can be widely excluded. The technical grade granules characterized in Section 3.4 are applied for the lab-scale experiments, as the utilization of fine powders on a larger scale potentially causes sintering, particle agglomeration as well as enhanced pressure losses and would therefore not allow a storage operation with direct contact heat exchange between the gas and solid phase. Nevertheless, the granular material will also be assessed regarding its susceptibility to sintering and breakage upon cycling.

Thus, a tube reactor for a directly permeated packed bed of granules has been designed and implemented in lab-scale. Air simultaneously serves as HTF and carrier of the reactant O_2. In this regard a direct contact heat transfer between the gas phase and the solid metal oxide storage material is facilitated. This can be referred to as a directly heated (*charging*) and cooled (*discharging*) reactor concept for TCS. An additional HT heat exchanger is therefore not necessary.

Typically, in the charging stage of a technical scale regenerator-type storage system the HTF flow enters the storage from the top, whereas the direction of the flow is reversed in the discharging stage. It has to be noted, though, that the lab-scale operating conditions in the current work have been chosen for simplification: Charging as well as discharging in the lab-scale setup is realized by means of an air flow passing through the reactor solely from the bottom to the top, so that a fairly uniform initial bed temperature serves as starting point and final point of each experiment, respectively. Consequently, the formation of an axial temperature distribution along the bed height, typical for regenerator-type storage operation on a technical scale (e.g., see [98, 163]), is not feasible and was also not in the focus of this study. Parts of Chapter 4 have been published in [156].

4.1.1 Lab-Scale Storage Reactor

A metallic reactor tube made of nickel-based alloy 2.4856 (Inconel® 625) with an inner diameter D of 54.3 mm and a wall thickness t of 3.0 mm is applied. The actual reaction chamber containing the reactive packed bed of metal oxide granules, as shown in Fig. 4.1 (left), has a total height of 195 mm. Sheath thermocouples (Nicrobell® sheath alloy) of type N with an insulated measuring point are implemented for all temperature measurements in the experimental setup. The tolerance

of the class 1 thermocouples amounts to $\pm 0.004 \cdot |\vartheta|$ in the range of 375-1000 °C. A testing of the thermocouples with a temperature block calibrator (Pegasus^{PLUS} 1200, Isotech) showed deviations in the range of ±2.5 K at 1000 °C, which are within the given tolerance. Thus, an additional calibration of the thermocouples was not carried out.

The radial heat flows have the lowest influence on the reaction temperatures along the axis of the tube, owing to the intrinsically low thermal conductivity of the granular metal oxide bed. Therefore, four thermocouples (Ø = 1 mm) are positioned in the center along the axis of the packed bed (Fig. 4.1, left) with a height of 10 mm (ϑ_1), 50 mm (ϑ_2), 90 mm (ϑ_3) and 130 mm (ϑ_4) above a gas distribution disc (fused silica frit, porosity P1), in order to measure the reaction progress in terms of a temperature front along the bed height. The gas distribution disc rests on a perforated plate, which was welded into the tube to hold the packed bed. Two thermocouples (Ø = 1 mm) are placed between the axis and the tube wall – even with ϑ_2 and ϑ_4 – to measure the temperature of the packed bed in the radial direction ($\vartheta_{2,r}$ and $\vartheta_{4,r}$). Moreover, the temperature of the reactor tube wall is also measured at four positions ($\vartheta_{1,w}$, $\vartheta_{2,w}$, $\vartheta_{3,w}$ and $\vartheta_{4,w}$; thermocouple-Ø = 1.5 mm) on the outer surface.

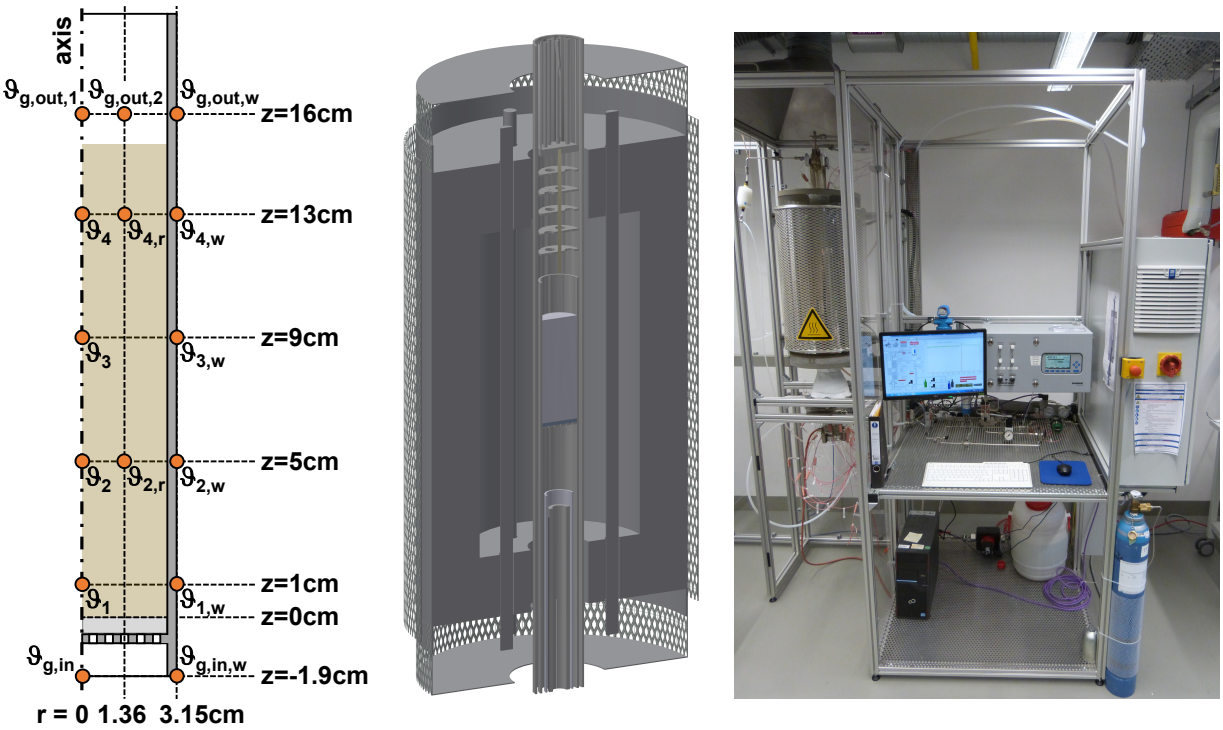

Figure 4.1: Geometry of the reaction chamber with locations of the thermocouples placed in the packed bed of metal oxide (left); position of the packed bed storage reactor integrated in a tube furnace with additional gas/air heater below the bed (middle); experimental setup of the test rig (right).

In order to measure and control the gas temperature – according to the chosen setpoint throughout the experiments – at the inlet of the reactor ($\vartheta_{g,in}$), a thermocouple (Ø = 1.5 mm) is installed about 10 mm below the perforated plate. For the measurement of the gas temperature at the outlet two thermocouples (Ø = 1 mm) are positioned approximately 10 mm above the packed bed ($\vartheta_{g,out,1}$ along the axis and $\vartheta_{g,out,2}$ radially offset). The reaction chamber is capped with a filter (fused

silica frit, porosity P1) to retain possibly abraded metal oxide particles inside the chamber, sealing the gap between filter and tube with insulation paper (Contherm BTP 1300, CaMg-silicate fiber paper, 1 mm thick). The position of the reaction chamber within the experimental setup is shown in Fig. 4.1 (middle). The *reactor tube* is encased by a second tube with an inner diameter of 70.1 mm and a wall thickness of 3.0 mm made of nickel-based alloy 2.4633 (Inconel® 602 CA), which is referred to as *casing tube* thereafter. Reactor tube and casing tube are connected by a flange connection at the bottom, which enables pulling out the reactor tube and accessing the reaction chamber for the storage material filling and emptying.

4.1.2 Lab-Scale Test Rig

Figure 4.2 illustrates the process flowsheet of the test rig, which has been designed to survey a TCS reactor based on metal oxides. An in-house developed electrical gas heater (2) is integrated into the reactor unit below the reaction chamber (1) in order to heat air or other compositions of O_2 and N_2 to the desired temperature for the experiments. The casing tube is encased by a vertically arranged tube furnace (3), which is used to assist the gas heater and heat up the reaction bed as well as to minimize thermal losses to the ambience. In a future large-scale TCS system this electric trace heating system will be replaced by thick insulating material. The annular gap of 4.9 mm between the reactor tube and casing tube is filled with an insulation layer (Contherm BTM 1300, CaMg-silicate fiber mat, 6 mm thickness), which had to be slightly compressed to fit into the gap. Additionally, the casing tube is also insulated by a layer of 9 mm thick CaMg-silicate fiber mat (Contherm BTM 1300, see properties data in Table C.4). Both layers serve to further minimize heat losses during oxidation and to thermally uncouple the reactor tube from the tube furnace during reduction to the greatest possible extent.

According to the prospective application oil-free, dry and filtered ambient air is used, which is provided by a bundle of compressed air (DIN EN 12021). Gas flow rates and the composition of N_2 5.0 and O_2 4.8 mixtures are adjusted by means of (4) three mass flow controllers (MFCs for Air/N_2 in the range of 0.8-40 NL/min, MFC for O_2 in the range of 0.1-5 NL/min, all exhibiting an accuracy of ± 0.5 % of reading plus ± 0.1 % of full scale, Bronkhorst HI-TEC). A gas mixing chamber (5) provides homogeneous mixing of O_2 and N_2 for the cooling phases in atmospheres of reduced oxygen content. The maximum gas flow rate is restricted to 15 NL/min in the current experimental setup to ensure the attainment of the desired gas temperatures at the inlet of the packed bed.

Above the reactor tube the off-gas is cooled to about RT with an integrated water cooler (7). Subsequently, the gas is filtered by means of a HEPA filter (Whatman HEPA-CAP 150, 6702-9500). Five thermal shields consisting of nickel-based alloy 2.4856 (Inconel 625) disks are arranged between the reactor unit and the water cooler to reduce the radiation of heat from the upper filter of the reaction chamber towards the cooler (see Fig. 4.1, middle). An insulation layer (Maftec® blanket) between each thermal shield enhances the protective effect, respectively.

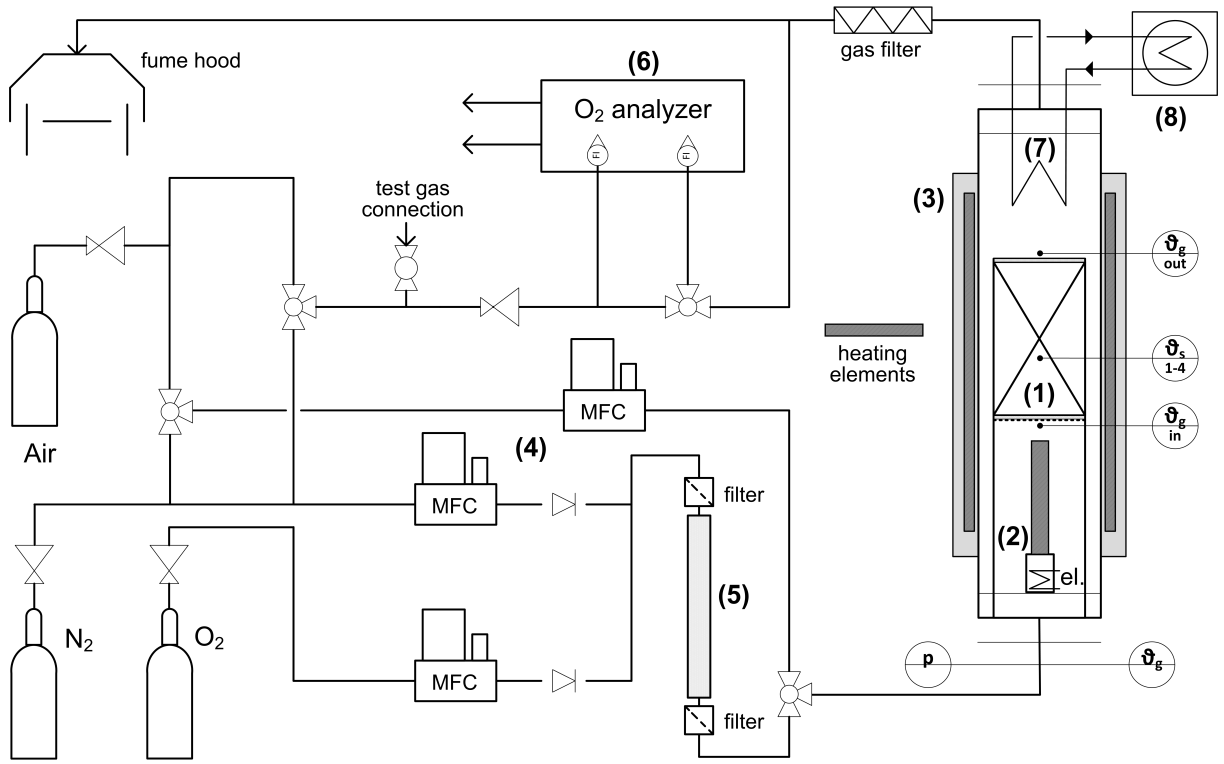

Figure 4.2: Process flowsheet of the laboratory-scale test rig: Packed bed tube reactor (1), electrical gas/air heater (2), tube furnace (3), gas supply (4), gas mixing chamber (5), oxygen gas analyzer (6), gas cooler (7) and laboratory heat exchanger (8).

A gas analysis (6) with a paramagnetic oxygen measurement principle (NGA-2000 MLT-2 multi-component gas analyzer with built-in pressure and temperature compensation, range of fluctuation of measured O_2 values in the course of a single redox cycle over the period of several hours is $<0.03\,\%\ O_2$; Co. Emerson Process Management | Rosemount Analytical) is used to record the O_2 concentration upstream ($\sigma_{O_2,in}$) and downstream the reactor unit ($\sigma_{O_2,out}$), in order to track the reaction progress and determine the reaction conversion. A two-point calibration of the gas analyzer is conducted prior to every single redox cycle. N_2 5.0 is taken as zero reference gas and a distinct test gas (25 % O_2, 1000 ppm CO_2, residual gas N_2) is used as calibration gas for sensitivity calibration. The test rig is open to the fume hood dismissing the off-gas stream, which is why all measurement series are conducted at atmospheric pressure.

The installation of a pressure transducer (Siemens SITRANS P200, 0-2.5 bar*g*) downstream the MFCs enables the determination of the pressure drop across the packed bed of metal oxide particles at RT or the entire setup during the experiments by indicating the present overpressure with a typical error of ±6.25 mbar (±12.5 mbar max). In addition, the absolute ambient pressure (Siemens SITRANS P200, 0–4 bar*a*) is monitored to determine the corresponding pO_2 at the gas outlet of the setup, calculated based on the product of the measured volume fraction of O_2 in the air flow (which equals the molar fraction of O_2 in air) and the ambient pressure in the laboratory (see Eq. (C.9)). The entire test rig (Fig. 4.1, right) is controlled and regulated by the implementation of a programmable logic controller (PLC).

4.1.3 Packed Bed Characteristics and General Experimental Procedure

Packed Bed Characteristics The reaction chamber is filled with 471.2 g of granulated material in the oxidized state $(Mn_{0.75}Fe_{0.25})_2O_3$ (weighted sample m), resulting in a bed height H of approximately 152 mm prior to gas flow and chemical reaction. The ratio of bed height over diameter H/D amounts to 2.8. the highest positioned thermocouple in the packed bed (ϑ_4) is located roughly 20 mm below the top layer of particles. Although the granulated material can be assigned to Geldart group D, the possibility of fluidization can be excluded under the applied measurement conditions working with granule sizes larger than 1 mm [65].

The total porosity ε_{tot} of the packed bed, which defines the entire volume fraction of the gas including intraparticle pores (accessible and inaccessible), can be calculated according to Eq. (2.5) based on the true solid density of $(Mn_{0.75}Fe_{0.25})_2O_3$ (ρ_{true}) and the bulk density of the packed bed (ρ_{bulk}):

$$\varepsilon_{tot} = 1 - \frac{\rho_{bulk}}{\rho_{true}} = 1 - \frac{m}{A_{bed} H \rho_{true}} \tag{4.1}$$

In the calculation of the cross-sectional area of the bed (A_{bed}) the slight reduction of the inner reactor tube diameter owing to the installation of four metal bars (profile of 2x3 mm), which hold the terminal filter frit, is taken into account. The bulk density of the loose $(Mn_{0.75}Fe_{0.25})_2O_3$ granule bed amounts to about 1.353 g/cm^3. Thus a value of 0.736 is obtained for ε_{tot}.

However, a differentiation must be made between the intraparticle porosity ε_p of the granules (pore volume fraction) and the interparticle porosity ε_{bed} of the packed bed. The latter constitutes the porosity between single particles, which is relevant for the free HTF flow through the packed bed as well as the available heat transfer surface. The following relation

$$\varepsilon_{tot} = \varepsilon_{bed} + \varepsilon_p(1 - \varepsilon_{bed}) \tag{4.2}$$

between the prevailing porosities [135] can therefore be solved for $\varepsilon_{bed} = (\varepsilon_{tot} - \varepsilon_p)/(1 - \varepsilon_p)$, yielding a value of 0.340. This value is in the range of bed porosities reported for packings of polydisperse, irregularly shaped particles [135].

The chemical storage capacity of the packed bed (Q_{chem}) amounts to ≈35.5 Wh (128 kJ). The effective energetic storage density ($\rho_{en,v,eff}$) is approximately 101.8 kWh/m^3, ≈385.8 kWh/m^3 ($\rho_{en,v}$) in relation to the absolute density of $(Mn_{0.75}Fe_{0.25})_2O_3$. Considering a hypothetical weight change of 3.368 % (value expected based on the stoichiometry of the reaction), all values would be ≈5.9 % higher.

The reaction conversion is determined based on the measured O_2 concentration. A description of the calculation method for the corresponding reaction conversions X_{Red} and X_{Ox} can be found in detail in Appendix C.2.

Experimental Procedure Overall, 17 cycles are performed with a single batch of storage material. A complete redox cycle consists of the endothermic reduction of $(Mn_{0.75}Fe_{0.25})_2O_3$ to $(Mn_{0.75}Fe_{0.25})_3O_4$ and the reverse exothermic oxidation step, also referred to as *thermal charging*

and discharging of the storage thereinafter. One redox cycle is carried out per day, cooling down the packed bed to RT under a flow of air after the performance of each cycle. The detailed experimental procedure is described prior to the presentation of the results of each measurement series. An overview of the experimental campaign is specified in Fig. 4.3 as well as more detailed in Table C.1.

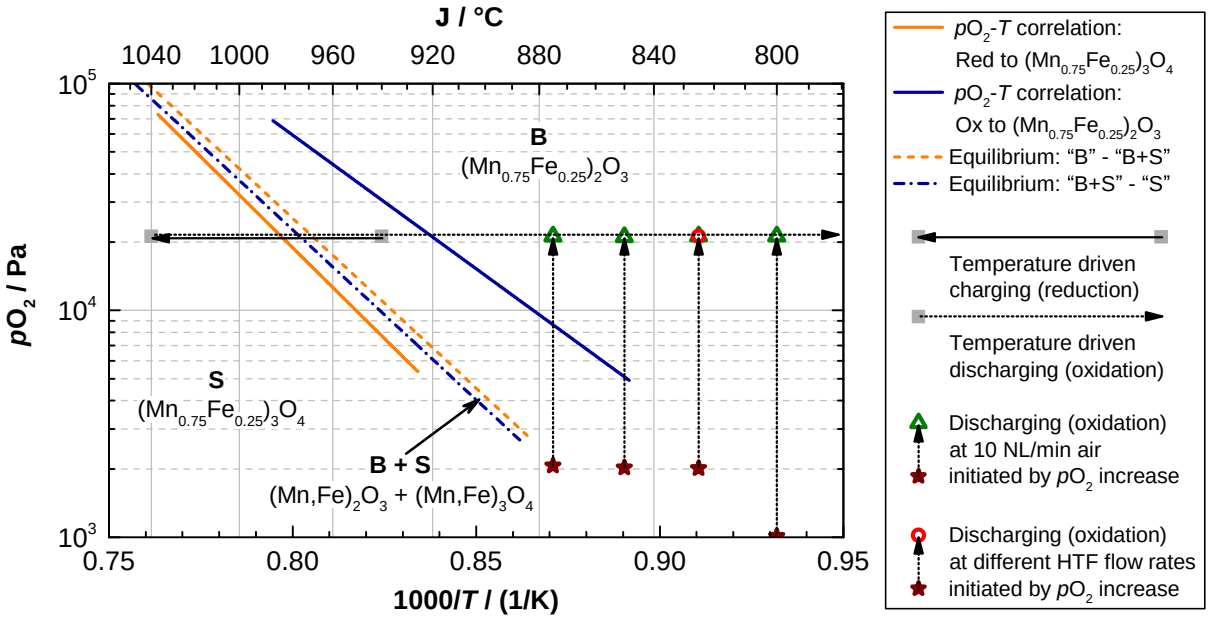

Figure 4.3: Operating parameters for storage charging and discharging in lab-scale packed bed reactor: Temperature driven charging and discharging in air (horizontal lines), as well as thermal discharging initiated by a change of the oxygen partial pressure (vertical lines).

In order to test the storage material regarding its cycling stability on a larger scale and to ensure the comparability of the results obtained from parameter variations, experimental conditions for a reference redox cycle (2^{nd}, 6^{th}, 9^{th} and 17^{th}) – denoted *reference experiment* thereinafter – have been defined (see Section 4.2 for charging step, Appendix C.6 for discharging step). This cycle is performed in between the individual series of measurements studying different parameter variations. Prior to the presentation of the parametric studies, in the following section the evolution of characteristic temperature profiles along the bed height is outlined and interpreted for a typical charging and discharging process of the storage reactor.

While the charging step is typically carried out by raising the temperature of the packed bed in air (solid horizontal line in Fig. 4.3), two modes of operation can be distinguished for the discharging step: The first mode resembles the operating method of a regenerator-type storage system, characterized by simply cooling down the packed bed via the flowing HTF air to extract the sensible and thermochemical energy stored in the system (dotted horizontal line in Fig. 4.3). The second operation mode with constant boundary conditions at the inlet of the packed bed is well suited for an examination of the impact of different HTF mass flow rates as well as different gas inlet and initial bed temperatures on the reaction kinetics along with heat and mass transfer phenomena (dotted vertical lines in Fig. 4.3). In the second mode of operation, thermal discharging

is initiated by an abrupt enhancement of the oxygen partial pressure.

4.2 Characteristics of Temperature Driven Thermal Charging and Discharging

Thermal Charging is performed by means of a temperature change to initiate the reduction. The reaction can be considered temperature driven in this case. At first the packed bed of granules is heated up to an initial temperature (ϑ_0) of 940 °C, using a constant air flow rate of 10 NL/min. The initial conditions of the experiment – prevalent pO_2 and temperature of the packed bed – do not allow the reduction reaction to take place. As soon as thermal equilibrium has been maintained for at least 20 min, the air temperature at the inlet of the reaction chamber ($\vartheta_{g,in}$) as well as the tube furnace temperature ($\vartheta_{furnace}$) are simultaneously raised to 1040 °C. The left part of Fig. 4.4 illustrates the reference experiment for thermal charging, showing the air inlet temperature, the temperature profiles along the height of the packed bed ($\vartheta_1 - \vartheta_4$) and the O_2 concentration profile downstream the reaction chamber ($\sigma_{O_2,out}$). Point zero indicates the assignment of the temperature increase by 100 K.

In the beginning the solid storage material is heated up along the entire bed height reflecting the storage of sensible heat. Faster rates of heating in the lower part of the bed can be explained by a higher heat input via the HTF entering at the bottom, in comparison to the thermal energy which is introduced via the tube furnace across the tube wall along the entire height of the bed. Approximately 5 min after assigning the temperature increase, the endothermic reduction of $(Mn_{0.75}Fe_{0.25})_2O_3$ particles is triggered in the lowest part of the bed, indicated by the beginning of oxygen release. As soon as the reaction zone has reached the position of the first thermocouple (ϑ_1) after about 12 min, a temperature drop (by 0.5 K in this experiment) down to a level of about 983.5 °C could be detected for a brief period of around 4 min due to the absorption of thermal energy. The short reaction time and comparatively high reaction temperature level in this region is due to the proximity of ϑ_1 to the bottom of the bed, where heat input by the entering air is more intense. As soon as $(Mn_{0.75}Fe_{0.25})_2O_3$ has been converted to $(Mn_{0.75}Fe_{0.25})_3O_4$ in the lower part, temperature ϑ_1 begins to rise up to 1040 °C, again reflecting the storage of sensible heat. It may be noted that all bed temperatures reveal small signs of an initial overheating effect (typically in the order of about 1 K) prior to the beginning of the reduction reaction (see also Fig. 4.6a).

In contrast to the region of thermocouple ϑ_1 in the lower part, the storage material in the middle and upper part of the bed exhibits the formation of widely constant temperature plateaus for longer periods. In the process thermal energy is absorbed due to the advancement of the endothermic reduction, preventing the granules from further heating up. The lowest temperature plateaus with ≈978.5 °C are observed in the middle part for ϑ_2 and ϑ_3. This value is in good accordance with the experimentally determined (STA) temperature threshold for the reduction onset in air, as described above (see Section 3.4.1). Overall, the reaction proceeds at temperature levels close to

the equilibrium, where only slow reaction rates can be attained. Based on those low temperature levels and long duration of the reaction in this region, it can be assumed, that the reduction step is mainly limited by heat transfer into the packed bed.

Input of thermal energy by means of the HTF entering at the bottom leads to the development of a pronounced temperature front gradually traveling in flow direction through the packed bed. The front indicates the termination of the reaction in a certain part of the bed, followed by sensible heating up to 1040 °C. The charging stage is completed after a total time of 124.7 min, once the O_2 concentration at the outlet has returned to the baseline level and temperatures along the bed height have reached constant values close to 1040 °C. The period of O_2 release accounts for only 120.9 min. The reaction reaches nearly complete conversion of about 99.5 % within the possible accuracy of evaluation (Fig. 4.4, bottom left). As heat losses appear to be higher in the upper region of the bed, ϑ_4 has only reached a value somewhat lower than 1040 °C at the end of the experiment.

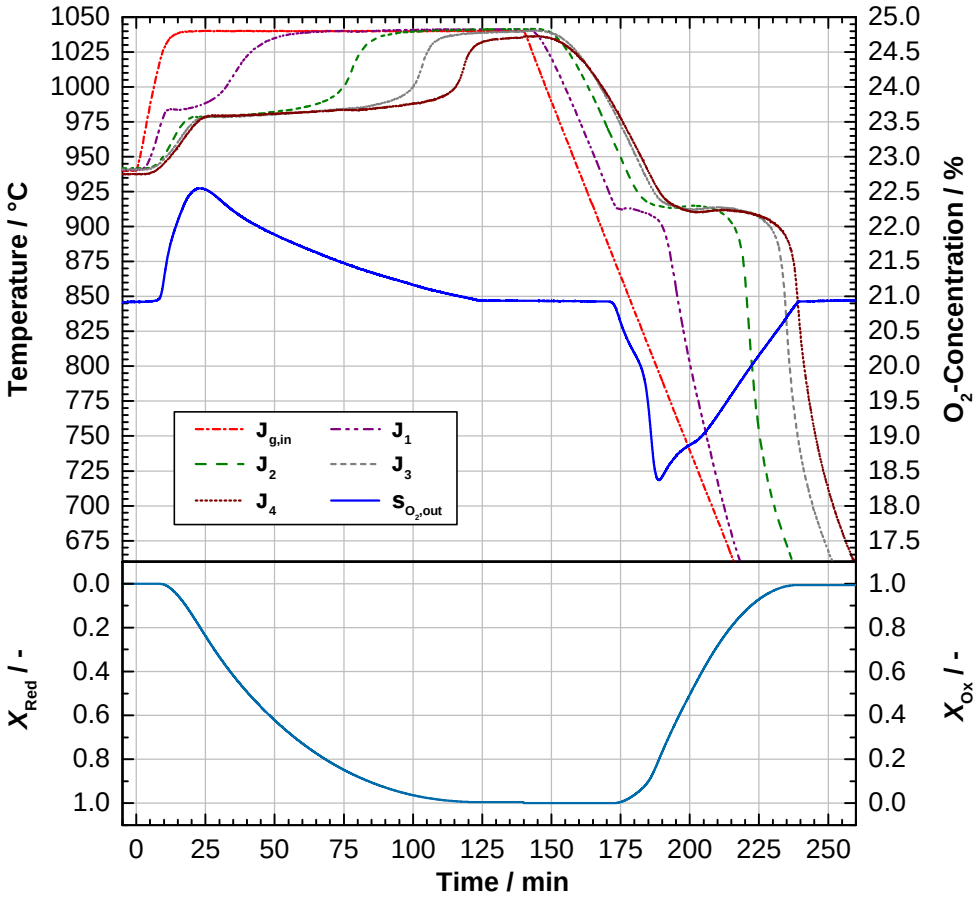

Figure 4.4: Progress of the charging stage 6 $(Mn_{0.75}Fe_{0.25})_2O_3 \rightarrow 4\ (Mn_{0.75}Fe_{0.25})_3O_4 + O_2$ upon increase of air inlet $\vartheta_{g,in}$ and tube furnace temperature $\vartheta_{furnace}$ from 940 °C to 1040 °C (reference experiment) and excerpt of the discharging stage 4 $(Mn_{0.75}Fe_{0.25})_3O_4 + O_2 \rightarrow 6\ (Mn_{0.75}Fe_{0.25})_2O_3$ with a cooling rate of the air inlet and tube furnace temperature of 5 K/min, both at 10 NL/min air (11^{th} redox cycle).

A typical **Thermal Discharging** experiment of the storage conducted with decreasing temperature is illustrated on the right hand side of Fig. 4.4. The packed bed is cooled down with a constant cooling rate of the gas inlet temperature of 5 K/min at 10 NL/min air. This mode is subsequently

denoted *dynamic operation mode for thermal discharging* and allows to study the redox reactivity under controlled conditions. In order to ascertain that consistent boundary conditions can be achieved, equal cooling rates are adjusted for the air inlet and tube furnace temperature. A rate of 5 K/min constitutes the maximum possible cooling rate to challenge the material appropriately, but still control the HTF inlet temperature at a constant rate in this work. The setpoints are adjusted to 400 °C, an arbitrarily chosen value in this case. If the tube furnace was turned off for the cooling procedure, the packed bed would experience a more rapid cooling due to large heat losses across the tube wall (uncontrolled conditions).

At first the sensible part of stored energy is extracted, as the packed bed is cooled down along the bed height. The reaction onset in the lowest part of the bed is indicated by the recorded oxygen uptake. It can be observed, that the $(Mn_{0.75}Fe_{0.25})_3O_4$ oxidation is initiated in sequence along the axis throughout the discharging period, a distinct reaction front moving from the bottom to the top of the packed bed can be traced. All bed temperatures show small signs of initial undercooling prior to the beginning of the oxidation, followed by a small temperature increase of 1.5–2 °C. This phenomenon can be ascribed to the energy necessary to overcome the activation energy barrier for nucleation, hence initiating nucleation and subsequent crystal growth. The rather short temperature plateau of ϑ_1 is again a consequence of the high cooling capacity of the entering HTF at this stage, while the granular particles above are still subject to sensible heat extraction. All temperature profiles exhibit steady temperatures over periods of up to 15 min. This clearly accentuates the possibility to stabilize bed temperatures due to the release of the heat of reaction, while the gas inlet and tube furnace temperature are constantly declining at 5 K/min. The levels of the "self-adjusted" temperature plateaus are in the range of 912–915 °C, which are also consistent with the experimentally determined (STA) temperature threshold for the oxidation onset in air (see Section 3.4.1).

The oxidation reaction is completed after about 69.3 min, once the O_2 concentration at the outlet has risen to the baseline level. A total conversion of about 99.4 % was identified based on the absorbed amount of O_2 (Fig. 4.4, bottom right), which is in line with the reduction reaction. Overall, the duration of the oxidation step is significantly shorter than the corresponding reduction step. This can be explained by the continuously increasing ΔT between the solid temperatures in the progress of the oxidation reaction and the HTF at the inlet, eventually increasing the rate of heat removal. In comparison to the cooling curves prior to the respective reaction onset it can be stated, that the temperature profiles along the bed height spread further apart after the redox reaction.

Figure 4.4 discloses the appearance of the above-mentioned thermal hysteresis, which amounts to roughly 63.5 °C in this case, thermally decoupling the reduction and oxidation step under prospective technically relevant operating conditions. Further assessment of the oxidation step via TGA measurements revealed, that the oxidation is primarily subject to kinetic limitations closer to the equilibrium, which behavior – distinctive for manganese-based oxides – has been further addressed in Section 3.4 on the thermodynamic and kinetic characteristics of this technical grade

material.

The total gravimetric energy storage density of the Mn-Fe oxide, combining sensible heat and chemical energy, is depicted in Fig. 4.5 as a function of temperature for thermal charging and discharging, respectively. For the calculation of the specific enthalpy values h the experimentally determined values of the specific heat capacity c_p have been taken into account (see Eqs. (3.13) and (3.14)). A lower temperature limit of 100 °C is assumed, which can be regarded as HTF inlet temperature within a temperature range technically relevant for storage discharging [136, 167, 166]. Taking the granular filling material of 471.2 g in the oxidized state $(Mn_{0.75}Fe_{0.25})_2O_3$ and 456.2 g in the reduced state $(Mn_{0.75}Fe_{0.25})_3O_4$ into account, an overall storage capacity of 139 Wh can theoretically be provided with the lab-scale packed bed reactor, if the entire temperature range between 100 °C and the final temperature of 1040 °C would be exploited for storage (idealized assumption) and complete reaction conversion is reached. This value is made up of 25.6 % of chemically stored energy (enthalpy $\Delta_R h$ of the phase transition) and 74.4 % of energy stored as sensible heat (charging stage).

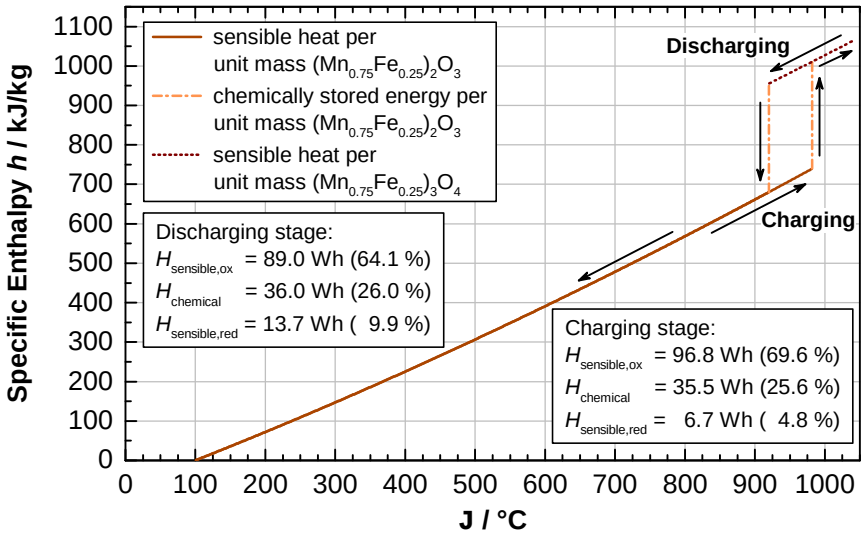

Figure 4.5: Specific energy storage capacity of Mn-Fe oxide between 100 °C and the maximum operation temperature of 1040 °C in the lab-scale experiments: Graphical illustration of the chemically stored energy and energy stored as sensible heat.

The diagram also represents the presence of the thermal hysteresis in the storage process (due to kinetic limitations, see also Section 3.4.1), applying the temperature threshold values of ≈982 °C (reduction) and ≈920 °C (oxidation) – experimentally determined in Section 3.4.1 – as an approximation for the respective phase transitions.[1] It can be concluded, that owing to the high working temperatures of a TCS reactor based on Mn-Fe oxide and metal oxides in general, the large amount of sensible thermal energy cannot be neglected in the storage process and process integration overall.

[1] According to Kirchhoff's Law (see Appendix A) the reaction enthalpy increases slightly with falling temperature, giving a value of ≈275.3 kJ/kg at ≈920 °C in contrast to ≈271.4 kJ/kg at ≈982 °C. This accounts for a slightly larger proportion of thermal energy released by the chemical reaction in the discharging stage.

4.3 Parametric Studies

Three parametric studies are conducted to examine different operating parameters influencing the behavior of a reactor with direct heat transfer, including the mass flow rate directed through the reactor as well as the gas inlet and initial bed temperature $\vartheta_{g,in} = \vartheta_0$. It is exemplarily referred to the bed temperatures ϑ_1 and ϑ_3, located axially 1 cm and 9 cm above the gas distribution disc, for the representation of the temperature profiles in the granular packed bed.

4.3.1 Temperature Driven Thermal Charging and Discharging: Flow Rate Variation

Temperature Driven Thermal Charging The utilization of air as HTF and purge gas to take up oxygen during the reduction has a strong impact on the chemical reaction in a directly permeated storage reactor. The heat capacity rate $C_{HTF} = c_{p,g} \cdot \mathrm{d}m_g/\mathrm{d}t$ resulting from the adjusted HTF flow rate generally constitutes the most significant parameter to regulate the heat input and attainable thermal power level of a storage reactor. Therefore, the influence of different air flow rates on the reactor behavior is examined more closely.

The packed bed is heated up to a 940 °C at an air flow rate of 5 NL/min ($1.08 \cdot 10^{-4}$ kg/s), 10 NL/min ($2.16 \cdot 10^{-4}$ kg/s) and 15 NL/min ($3.23 \cdot 10^{-4}$ kg/s), respectively. As soon as thermal equilibrium has been held for at least 20 min, the setpoints of the air inlet temperature ($\vartheta_{g,in}$) as well as the tube furnace temperature are simultaneously increased to 1040 °C. The pO_2 at ambient conditions amounts to ≈21.2 kPa. Figure 4.6a illustrates the experimental results of the charging experiments. Point zero marks the assignment of the temperature increase by 100 K. Generally, the rate of sensible heating turns out to be somewhat slower in the case of the lowest flow rate. About 4–6 min after assigning the temperature increase, the equilibrium condition of the redox reaction in air has already been exceeded for particles in the lowest part of the bed. Oxygen is released due to the initiation of the $(Mn_{0.75}Fe_{0.25})_2O_3$ reduction. According to the adjusted gas flow rates, the O_2 concentration profiles reflect the expected changes owing to the evolution of O_2. The highest change with a maximum of ≈23.8 % O_2 was detected for 5 NL/min, whereas the flow rate of 15 NL/min yields the lowest change with a maximum of ≈22.0 % O_2.

Temperatures ϑ_1 in the lower part of the bed are generally higher, as the incoming air flow at high temperature leads to a stronger heating effect. Since part of the thermal energy transported by the fluid flow has already been utilized to dissociate $(Mn_{0.75}Fe_{0.25})_2O_3$ and heat up the reduced material in the bottom part, only a lower temperature difference between fluid and solid is available in the upper part of the bed. Consequently, heat transfer in the upper part is lower, leading to longer reaction times and therefore longer periods of, to a certain extent, constant temperature plateaus, clarified by ϑ_3 in Fig. 4.6a. With rising air flow rate this plateau becomes shorter, as higher gas velocities entail an enhancement of the heat transfer coefficient between gas and solid phase (as well as between the packed bed and the tube wall). Moreover, the adjustment

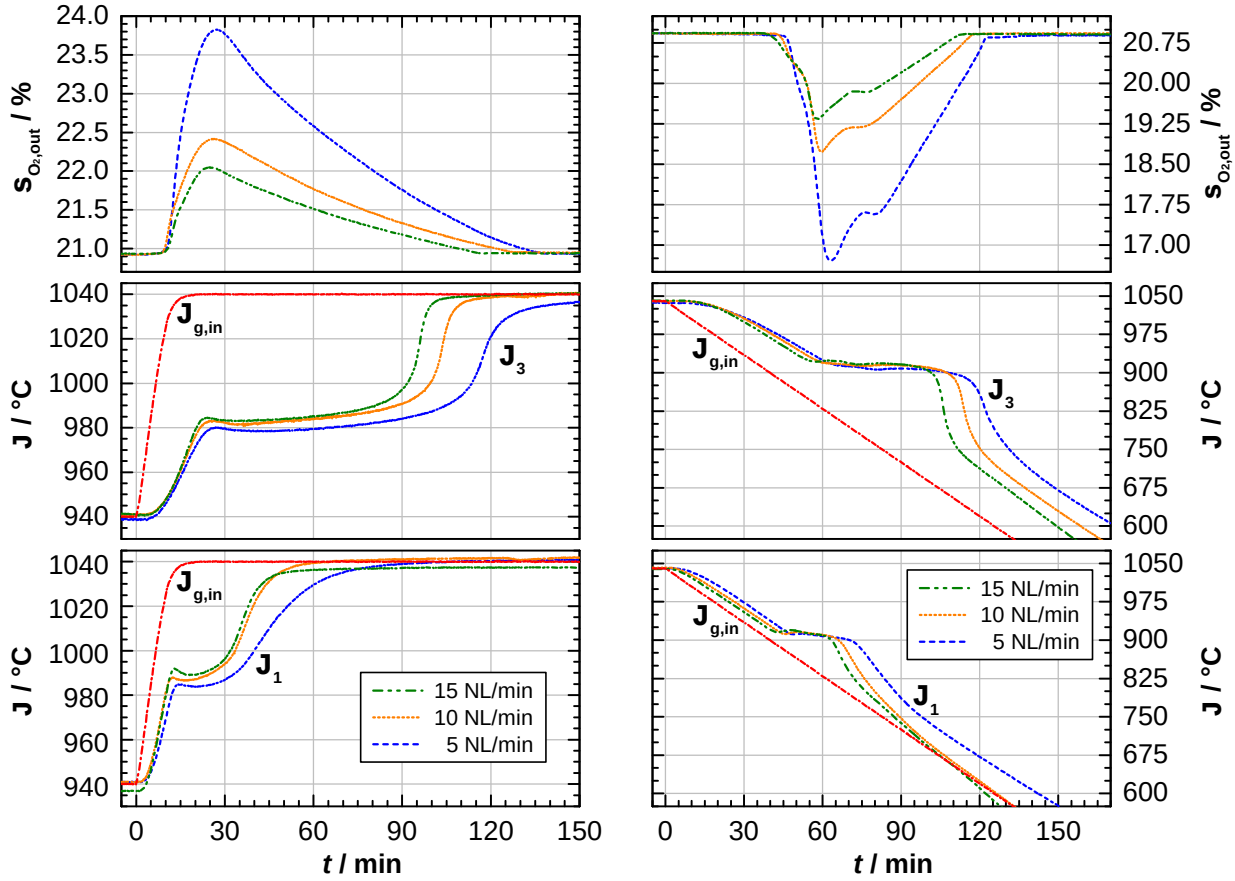

(a) Storage charging step 6 $(Mn_{0.75}Fe_{0.25})_2O_3 \rightarrow 4\ (Mn_{0.75}Fe_{0.25})_3O_4 + O_2$ performed by increasing the air inlet $\vartheta_{g,in}$ and tube furnace temperature $\vartheta_{furnace}$ from 940 °C to 1040 °C.

(b) Storage discharging step 4 $(Mn_{0.75}Fe_{0.25})_3O_4 + O_2 \rightarrow 6\ (Mn_{0.75}Fe_{0.25})_2O_3$ at a cooling rate of the air inlet $\vartheta_{g,in}$ and tube furnace temperature $\vartheta_{furnace}$ of 3.5 K/min.

Figure 4.6: Flow rate variation in temperature driven charging and discharging experiments: 5 NL/min, 10 NL/min and 15 NL/min air.

of higher mass flow rates also implies higher heat capacity rates C_{HTF}, causing higher thermal power input. The transfer of thermal energy from the HTF to the solid hence increases, which provokes an accelerated reaction progress. All registered temperature levels (minima reached between ≈977.5 °C at 5 NL/min and ≈983.0 °C at 15 NL/min) during the proceeding reaction are in the range of the technically relevant temperature threshold of ≈981.7 °C for the reduction onset, calculated at a pO_2 of 21.2 kPa based on the experimentally determined pO_2-T correlation (see Section 3.4.1). It should be noted that, on the one hand, somewhat increased reaction temperatures would be expected for the run at 5 NL/min based on the higher O_2 concentrations reached in the gas flow as a result of the O_2 release, therefore elevating the local pO_2. On the other hand, higher pressure drops together with enhanced heat input ascribed to higher heat capacity rates C_{HTF} in the runs with 10 and 15 NL/min seem to compensate the locally lower O_2 concentrations correspondingly. Generally, a balance between the heat supply rate (by the HTF) and the heat absorption rate (by the endothermic reaction) is established at a certain temperature level.

In summary, the variation of the adjusted mass flow rate has a significant impact on the charging time. This can be well distinguished by means of the O_2 evolution curves as well as the length of the temperature plateaus, also reflected in the offset of the respective sensible heating curves after completion of the reaction at position of sensor ϑ_3. In all experiments complete conversion was achieved within the feasible accuracy of the evaluation. The charging time from the beginning of the temperature increase until the end of O_2 release amounts to ≈138.0 min (5 NL/min), ≈128.1 min (10 NL/min) and ≈116.3 min (15 NL/min). As expected, the highest maximum reaction rate has been reached in the case of 15 NL/min. Correspondingly, the experiments at 10 NL/min and 5 NL/min yielded lower maximum reaction rates. For the charging stage the conclusion can be drawn, that thermal power input by means of the HTF as well as heat transferred from the tube wall to the solid storage material can be regarded as the limiting factors under the applied operating conditions, the latter also attributed to the intrinsically poor thermal conductivity of metal oxides. Besides higher HTF mass flow rates, demonstrated in this section, a raise of the HTF charging temperature provokes a larger temperature driving force for the reaction (larger distance to the equilibrium state) and therefore leads to higher reaction rates and enhanced charging performance as well. However, due to the experimental setup the maximum operating temperature is generally restricted to 1040 °C in this case.

Thermal Discharging with Decreasing Temperature The influence of different air flow rates is also investigated on the discharging performance with decreasing temperature. In order to simulate the reaction behavior along with the extraction of sensible thermal energy, the gas inlet temperature ($\vartheta_{g,in}$) is decreased at a constant rate of 3.5 K/min, setting the air flow rate through the reactor to 5 NL/min, 10 NL/min and 15 NL/min, respectively. The preceding reduction step has invariably been performed by means of a temperature increase from 940 °C to 1040 °C with equal flow rates. The experimental results of the discharging experiments are shown in Fig. 4.6b.

In general, as the reaction rate of the material and therefore the rate of heat release increases with further distance from the equilibrium, the temperature plateau settles down at a stable temperature level according to the locally prevailing pO_2, where a balance between the rate of heat release due to the chemical reaction and the rate of heat removal by the HTF is reached. Higher mass flow rates of air implicate enhanced heat transfer between the solid and gas phase along with elevated heat capacity rates C_{HTF}, which eventually lead to an accelerated extraction of the sensible heat and heat of reaction from the particle bed. The evolution of the cooling curves of ϑ_1 and ϑ_3 indicate this trend.

The onset of the oxidation reaction is first observed for the experiment at 15 NL/min. However, somewhat higher onset temperatures of the reaction as well as the attainment of higher temperature levels during the proceeding exothermic reaction were monitored in this run, which are on average about 7–10 °C higher at 15 NL/min compared to the experiment at 5 NL/min. These phenomena can be directly ascribed to a superimposed effect caused by an increase of the HTF mass flow rate: On the one hand, a lower decline of the O_2 concentration appears in the process of the oxidation,

as a minimum of 19.3 % was recorded for 15 NL/min versus 18.7 % for 10 NL/min and 16.7 % for 5 NL/min. On the other hand, the total pressure loss over the experimental setup turns out to be higher. Average values of 15.9 kPa at 15 NL/min, 9.9 kPa at 10 NL/min and 4.8 kPa at 5 NL/min could be measured for the total pressure loss over the period of the O_2 uptake, respectively.[2] Both effects give rise to locally higher oxygen partial pressures, which induce an elevation of the corresponding reaction temperatures. To give an indication for the influence of the varied pressure drops on the reaction temperature: Leaving the prevalent pO_2 drop in the packed bed (owing to the O_2 uptake in the course of the proceeding reaction) entirely out of consideration, the increase of the average total pressure drop by ≈5.1 kPa from the run at 5 NL/min to 10 NL/min ambient air would lead to a rise in the oxidation temperature by ≈2.5 K, the increase of the average total pressure drop by ≈6.0 kPa from the run at 10 NL/min to 15 NL/min ambient air would lead to a rise in the oxidation temperature by ≈2.8 K, according to the experimentally determined pO_2-T dependence of the oxidation temperature threshold in Table 3.4. However, this consideration serves only as an estimation, since the actual pressure drop solely across the packed bed is smaller and the varying drop of the pO_2 in the course of the reaction is assumed to constitute the main reason for the observed difference in the attained temperature levels between the three experiments at different air flow rates, respectively.

As the oxidation of Mn-Fe oxide is subject to the above-mentioned kinetic limitations (Section 3.4.1), the observed temperature levels are far from thermodynamic equilibrium. All registered temperature levels (maxima reached reached between ≈914.0 °C at 5 NL/min and ≈923.5 °C at 15 NL/min) during the proceeding reaction are in the range of the technically relevant temperature threshold of ≈920.3 °C for the oxidation onset, calculated at a pO_2 of 21.2 kPa based on the experimentally determined pO_2-T correlation (see Section 3.4.1).

In all three cases the proceeding oxidation reaction leads to a stabilization of the solid and gas temperatures, while the gas inlet ($\vartheta_{g,in}$) and tube furnace temperature constantly decline at a fixed rate, further enhancing the cooling effect. The highest cooling effect is achieved at a flow rate of 15 NL/min. Reaction times t_{rxn} (period of O_2 uptake) amount to ≈75.6 min for 15 NL/min and ≈81.1 min for 5 NL/min, which is why the impact of different flow rates on the extraction of the heat of reaction can be clearly distinguished. In consequence of varied heat capacity rates C_{HTF}, which in turn induce different reaction rates, the temperature profiles spread further apart after completion of the redox reaction in comparison to the cooling curves prior to the reaction (see ϑ_3 in Fig. 4.6b). A clear shift of over 15 min can be identified between the cooling curves of 5 NL/min and 15 NL/min owing to the enhanced extraction of thermal energy at 15 NL/min.

[2] According to the experimental setup illustrated in Fig. 4.2, a direct measurement of the prevalent absolute pressure and corresponding pO_2 in the packed bed has not been possible throughout the storage experiments. As the pressure transducer had to be installed downstream the MFCs, only the pressure drop over the entire setup composed of piping, gas heater, welded perforated plate, gas distribution disc, packed bed, filter frit, water cooler and gas filter could be assessed in the scope of the experiments.

4.3.2 Thermal Discharging at Constant Gas Inlet Temperature

Significant factors determining the reactor discharging behavior comprise the particle reaction rate, heat transfer, availability and mass transport of O_2 as well as the maximum possible enthalpy difference $\Delta H_{g,max}$ of the HTF flow between reactor inlet and outlet. Compared to the dynamic mode of operation for thermal discharging, described in Section 4.2, an alternative approach enables to study the *release of thermal energy at a constant gas inlet temperature* (defined boundary condition), *inducing the reaction by means of a sudden change of the* pO_2. In this case the reaction can be considered pressure driven.

On the one hand, an *operation mode with constant boundary conditions at the inlet of the packed bed* – along with a uniform initial bed temperature as starting point – constitutes an effective way to investigate the influence of various gas inlet $\vartheta_{g,in}$ and initial bed temperatures ϑ_0 as well as different HTF mass flow rates on the specified macroscopic parameters. On the other hand, the experiments illustrated in this section point out the possibility towards operating methods, which can be adapted to the corresponding temperature level of individual, envisaged technical applications. For instance, the charging step could alternatively be performed at reduced atmospheric pressure – thereby reducing the pO_2 – to substantially lower the reduction temperature (e.g., thermal charging could also potentially be performed solely by means of indirect heat input through the reactor tube walls). The subsequent discharging step in air could then be utilized to upgrade thermal energy by lifting the HTF process temperature in this case.

A detailed description of all temperature profiles along the bed height and their interpretation is given in Appendix C.6 (see Fig. C.2) for a thermal discharging experiment at a constant gas inlet and initial bed temperature of 850 °C and a gas flow of 10 NL/min (reference experiment), the temperature of 850 °C being arbitrarily chosen. It is worthwhile noting that the sensible heat between the upper temperature limit of the charging stage and the targeted bed temperature for discharging could as well be recovered by means of a practical process integration strategy in absence of air, so that the sole heat of reaction can be provided for discharging on demand.

Flow Rate Variation

At first the influence of different heat capacity rates C_{HTF} on the reaction performance along with heat and mass transfer effects is surveyed, adjusting the air flow rate through the reactor to 5 NL/min, 10 NL/min and 15 NL/min, respectively. After completion of the preceding reduction step the packed bed of granular $(Mn_{0.75}Fe_{0.25})_3O_4$ is cooled down to an arbitrarily chosen gas inlet and initial bed temperature of 825 °C under a flow of 2 % O_2 in N_2 at the respective flow rate to be examined, since the atmosphere with reduced O_2 concentration inhibits an early initiation of the oxidation during cooling. It has been verified by means of thermogravimetric measurements in an atmosphere of 2 % O_2 over an isothermal period of 8 h, that – within this time period – an oxidation does not take place at temperatures $\geq \approx$825 °C (see Fig. C.1 in Appendix C.3).

Once thermal equilibrium has been reached and maintained in the packed bed over a period of

at least 20 min, the experiments are triggered by switching the gas flow to air, which corresponds to an abrupt elevation of the pO_2 from ≈2.0 kPa to ≈21.2 kPa (referred to ambient conditions at the gas outlet). The air inlet ($\vartheta_{g,in}$, not shown) as well as the tube furnace temperature are held at 825 °C throughout the entire period of each experiment. Results of the thermal discharging are illustrated in Fig. 4.7a, the gas change indicated by the point of origin. The experiments clearly reveal the superimposition of different phenomena in terms of the particle reaction rate as well as heat and mass transfer effects. In the following the impact of individual phenomena on the discharging progression will be discussed.

When switching the gas flow to air, the O_2 concentration at the outlet rises within the primary 25 s, indicated by the peak in Fig. 4.7a (top) at $t = 0$ min. In this period flushing of the reaction chamber is superimposed by O_2 uptake due to the abrupt initiation of the oxidation reaction, since the prevailing conditions in the reactor thermodynamically favor the oxidized phase $(Mn_{0.75}Fe_{0.25})_2O_3$. Subsequently, the O_2 concentration declines to the lowest level within the first 90 s after initiation of the oxidation, indicating the occurrence of the highest reaction rate in every experiment at this point. At 10 NL/min and 15 NL/min all bed temperatures – indicated by ϑ_1 and ϑ_3 – show an instantaneous increase due to the release of the heat of reaction, causing a self-heating effect of the material. The presence of a strong driving force owing to the high degree of undercooling of the granular particles becomes evident, when the gas flow is switched to air. Remarkably, 50 % conversion has already been attained after ≈4.2 min (15 NL/min) and ≈5 min (10 NL/min), with the largest part of the released heat of reaction reflected in the sensible heating of the packed bed.

In accordance with the variation of air mass flow rates in the reduction step (see also Fig. 4.6a) similar results regarding heat transfer effects could be observed. Higher gas velocities due to rising gas flow rates generally lead to increased heat transfer coefficients between the solid particles and the gas phase. Moreover, higher mass flow rates imply enhanced heat capacity rates C_{HTF}, enabling the absorption of a larger amount of thermal energy. This can be recognized by an acceleration of the reaction progress with higher air flow rates, as transfer of thermal energy from the reacting solid to the HTF is enhanced. At 15 NL/min the period of O_2 release is already over after ≈48.2 min, whereas in the case of 5 NL/min the reaction proceeds only very slowly towards the end, eventually reached at roughly 69.5 min. The maximum reaction rate, which can be derived from the O_2 concentration depicted in Fig. 4.7a, decreases significantly with smaller flow rates. The overall discharging stage is completed, once the O_2 concentration at the outlet has reached a stable level – indicating the presence of pure air – and the initial thermal equilibrium within the packed bed has been resumed shortly after.

In all three cases the lowest temperature increase along with the fastest extraction of thermal energy via the HTF was registered by the sensor ϑ_1 for the material close to the inlet of the packed bed, where the granular material initially experiences the strongest cooling effect due to the HTF entering the reactor at 825 °C. As expected, the experiment at 15 NL/min accounts for the most intense cooling effect. The conclusion may be drawn that in the case of 10 and 15 NL/min the

reaction rate constitutes the limiting factor for a further rise in temperature in the lower part of the bed, as the available chemical energy of the reaction has already been consumed within the first 3 min in this section, respectively.

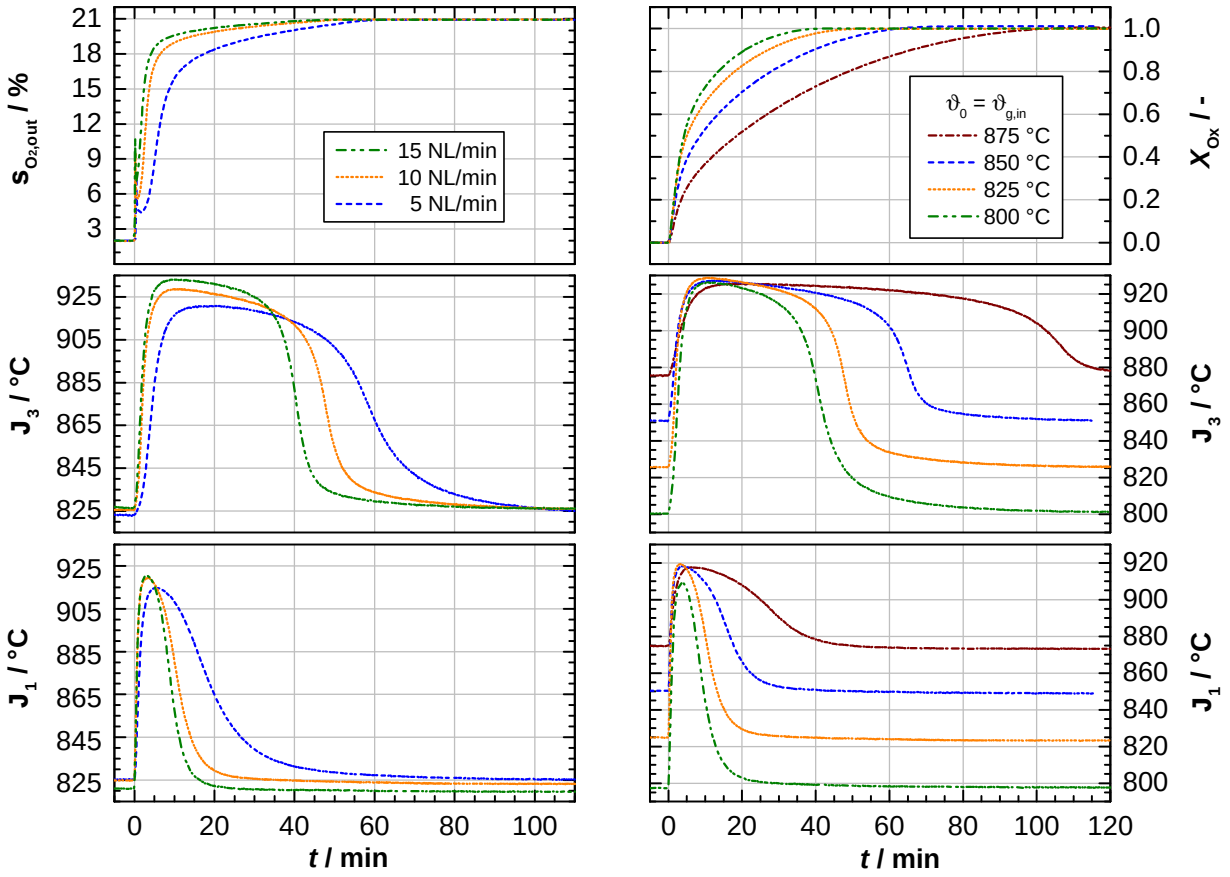

(a) Flow rate variation with initial bed and constant air inlet temperature $\vartheta_0 = \vartheta_{g,in}$ of 825 °C: 5 NL/min, 10 NL/min and 15 NL/min air.

(b) Temperature variation at 10 NL/min air: Initial bed and constant air inlet temperatures $\vartheta_0 = \vartheta_{g,in}$ of 800 °C, 825 °C, 850 °C and 875 °C.

Figure 4.7: Storage discharging step 4 $(Mn_{0.75}Fe_{0.25})_3O_4 + O_2 \rightarrow 6\ (Mn_{0.75}Fe_{0.25})_2O_3$ at constant air inlet temperature $\vartheta_{g,in}$.

Temperatures in the middle and upper part of the bed reveal larger temperature rises, reaching levels closer to the equilibrium, where the reaction rate decreases enormously. Maximum temperatures could always be observed for ϑ_2 (not shown in diagram) in the lower/middle part of the packed bed within the initial 10–15 min of the reaction. It can be assumed that up to the area of the sensor ϑ_2 the HTF has already been heated up to its maximum possible temperature during the initial phase of the discharging step, which is why no more thermal energy can be transferred to and dissipated by the HTF in this case. After this initial temperature increase along the entire bed height, the reaction mainly proceeds in those regions, where the material experiences sufficient cooling by the HTF and hence extraction of the released thermal energy. The end of the reaction at a certain height is marked by the dissipation of sensible heat, reflected in the propagation of a temperature front from the bottom to the top (cooling down to initial bed temperature).

For the experiment at 15 NL/min a maximum bed temperature of ≈934 °C was registered for ϑ_2. In comparison, the technically relevant pO_2-T correlation for the oxidation onset – experimentally derived by means of STA measurements in the cooling phase of the reduced material (see Section 3.4.1) – gives a temperature threshold of ≈920 °C at a pO_2 of 21.2 kPa (air). Moreover, the "self-adjusted" temperature plateaus in the dynamic discharging mode described above (see Fig. 4.6b) turn out to be lower as well (maximum of ≈923.5 °C for ϑ_3 at 15 NL/min). As a particular degree of undercooling needs to be attained to initiate the reaction by thermal activation of nucleation, which degree is particularly pronounced with manganese-based oxides, the oxidation reaction is generally subject to severe kinetic restrictions in the dynamic mode of continuous cooling down under air. Once the oxidation reaction has set in, the solid does not experience a significant temperatures rise (only by ≈1.5–4 °C) further towards the equilibrium, as the present reaction rates turn out to be very slow in this temperature region (see Figs. 3.11 and 3.18b).

In contrast, there seem to be no apparent limitations in the case of the highly undercooled state of the reduced phase at 825 °C in the current runs (presence of a strong thermodynamic driving force). This is why upon switching the gas flow to air the reaction is able to reach temperatures closer to the equilibrium, therefore leading to packed bed temperatures somewhat higher than the temperatures calculated from the experimentally derived pO_2-T dependence of the oxidation onset. This elucidated phenomenon can be considered independently of the locally lower O_2 concentration due to the O_2 uptake in the bed on the one hand as well as the increased local pO_2 due to the pressure drop over the experimental setup on the other hand, both influencing the reaction temperature in accordance with the pO_2-T dependence. For the pressure drop across the entire experimental setup average values of 17.0 kPa at 15 NL/min, 10.2 kPa at 10 NL/min and 4.5 kPa at 5 NL/min could be determined over a period of 20 min after the end of the O_2 uptake (period chosen for a suitable comparison), respectively.

It is particularly exceptional in this measurement series that the highest bed temperatures are reached for 15 NL/min, the experiment with the highest cooling capacity of the HTF. This occurrence can be directly ascribed to the open-loop storage operation with air as HTF, supplying the reactant O_2: In general, the local minimum of the recorded O_2 concentration shortly after the initiation of the reaction denotes the point, where the highest reaction rate and thus the highest rate of heat release occurs, respectively. In the experiment applying a gas flow rate of 15 NL/min, providing the highest molar amount of O_2 for the reaction, the O_2 concentration shortly drops down to 7.1 % due to the uptake of O_2. A value of 5.6 % O_2 is reached for 10 NL/min. At a flow rate of 5 NL/min, however, the O_2 concentration even drops down to 4.4 %, held for the longest time in comparison to the experiments at higher flow rates. In this case the O_2 concentration in the bulk phase is not sufficient for the oxidation reaction to proceed with higher reaction rates. Thus, at a flow rate of 5 NL/min a spreading of the temperatures at different levels as well as different temperature maxima can be found along the bed height. Moreover, the reaction does not take place immediately over the entire height of the packed bed, which becomes apparent in Fig. 4.7a (see ϑ_1

versus ϑ_3 within the initial 15 min).

On the one hand, ϑ_1 close to the reactor inlet shows an abrupt increase, while on the other hand, temperature ϑ_3 towards the upper part exhibits a delayed temperature rise. This is attributed to an O_2 depletion in the initial phase of the reaction (see Fig. 4.7a, top), since a large fraction of the available O_2 is taken up in the bottom part of the packed bed, leading to the presence of a lower O_2 concentration in the upper regions. As a result, at 5 NL/min a reduced O_2 availability implies a reduced local pO_2 and thus a decrease of the particle reaction rate according to the effective oxidation rate in Eq. (3.9). This effect can be even more pronounced with reactors of greater height on a technical scale. It must be taken into consideration that – depending on the storage application – certain modes of operation could be conceivable, where the O_2 concentration in the storage reactor tends to zero and the reaction progress is hindered.

Generally, the decrease of O_2 concentration due to the oxidation implies a reduced pO_2, decrementing the pressure driving force $pO_{2,\mathrm{local}} - pO_{2,\mathrm{eqI}}(T_{\mathrm{Ox,local}})$ for the reaction. This, in turn, is associated with a lower equilibrium temperature of the oxidation. Consequently, the corresponding lower temperature driving force $T_{\mathrm{eqI}}(pO_{2,\mathrm{local}}) - T_{\mathrm{Ox,local}}$ also leads to a decrease of the reaction rate. This thermodynamic effect can be explained by the dependence of the pO_2 on the temperature at thermodynamic equilibrium according to the van't Hoff equation (compare Fig. 3.10 or Fig. 4.3).

In summary, the discharging performance at the lowest flow rate of 5 NL/min is mainly dominated by a decreased reaction rate due to a shortened availability of O_2 as well as by diminished heat transfer and heat transport capabilities, both effects eventually accounting for an elongated cooling process and longer reaction times at fairly constant temperature levels (see ϑ_3 from minute 15 to minute 25) compared to the experiments at higher flow rates. In contrast, higher thermal power output owing to the highest reaction performance can be accomplished in the experiment at 15 NL/min air (Fig. 4.7a), exhibiting the highest O_2 availability (see Fig. 4.7a, top). Hence, at higher gas flow rates of 10 and 15 NL/min the oxidation reaction is mainly determined by heat transfer between the solid particles and the gas phase. Heat transport by means of the HTF – more specifically the maximum possible enthalpy change of the gas – poses the limiting factor in this case. As the HTF has already been heated up by the lower section of the bed, only a smaller ΔT is available for heat transfer in the upper section.

Generally, defining the HTF mass flow rate allows to effectively control the attainable thermal power output during the exothermic reaction in the discharging mode.

Variation of Air Inlet and Initial Bed Temperature

A variation of the gas inlet temperature also represents a practical method to study the reaction performance in the discharging step, directly affecting heat transfer and the maximum possible enthalpy change of the HTF flow from the inlet to the outlet of the packed bed. All experiments are performed under air at ≈21.2 kPa (referred to ambient conditions) with a constant flow rate of

10 NL/min, keeping the O_2 concentration and thus O_2 availability at the inlet of the reactor constant in this measurement series. Four cycles at different air inlet $\vartheta_{g,in}$ and initial bed temperatures ϑ_0 are carried out, adjusting values between 800 °C and 875 °C in a step size of 25 °C. In the case of 800 °C a cooling atmosphere of 1 % O_2 (pO_2 of 1.0 kPa) ensures the prevention of a premature re-oxidation prior to the initiation of the oxidation by means of switching to air. A cooling atmosphere of 2 % O_2 (pO_2 of 2.0 kPa) has been chosen for 825 °C, 850 °C and 875 °C (see also Fig. C.1 in Appendix C.3). All temperatures can be assigned to the range closer to the equilibrium in air, which is characterized by decreasing reaction rates with rising temperature (see Fig. 3.18b in Section 3.4.3). As soon as thermal equilibrium has been kept up for at least 20 min, the reactions are initiated by means of an increase of the pO_2 to ≈21.2 kPa (referred to ambient conditions at the gas outlet).

Figure 4.7b displays the experimental results in terms of reaction conversion and temperatures. Rapid sensible heating of the packed bed indicates a fast self-heating effect ascribed to the release of chemically stored energy. During the initial phase a large part of released thermal energy is absorbed by the material itself, owing to the limitation by the present heat capacity rate C_{HTF}, respectively.

In all cases the most intense convective cooling could be observed in the bottom part of the packed bed close to the gas inlet, as ϑ_1 (Fig. 4.7b, bottom) shows the lowest temperature rise. This clarifies the influence of direct heat transfer from the solid particles to the HTF to dissipate the released heat of reaction. The evolution of the bed temperatures in the proximity to the gas inlet illustrates effectively, that higher temperatures closer to the equilibrium condition cannot emerge, if the rate of heat removal by the HTF is larger than the rate of heat release due to the chemical reaction (see experiment at $\vartheta_{g,in} = 800$ °C in particular). Consequently, the lowest maximum temperature of ϑ_1 – moreover kept up for the shortest period – was recorded for a gas inlet temperature of 800 °C, as the corresponding gas flow exhibits the highest possible cooling capacity in this test series. Furthermore, the lowest O_2 concentration of 5.1 % (not shown) was registered at the experiment with $\vartheta_{g,in} = 800$ °C, which corresponds to the highest reaction rate achieved within this series of measurement. It can be stated that for this comparatively more intense cooling conditions in the bottom area of the packed bed the reaction has already been completed and the available chemical energy thus been consumed within the first few minutes of the discharging step.

Due to the initially high reaction rates at an air inlet temperature of 800 °C the released thermal energy primarily leads to the sensible heating of the particles within the initial phase of the experiment. Higher reaction conversion was observed in this phase compared to experiments at elevated temperatures. Figure 4.7b (top) discloses that 50 % conversion has already been reached after ≈4.2 min in the case of 800 °C, in contrast to a reaction period of 18.7 min in the case of 875 °C. The end of the O_2 uptake is thereby registered after about 46.7 min at 800 °C, which marks the shortest period within all experimental runs conducted in this thesis. Overall, full conversion has been reached in all cases. For comparison, the total reaction time of the experiment

at $\vartheta_{g,in} = 875\,°C$, characterized by the lowest maximum possible enthalpy change of the HTF, amounts to about 117.9 min. Owing to the small ΔT available for heat transfer in the scope of this run, the heat of reaction can be extracted only slowly. Consequently, the reaction can only proceed gradually, resulting in the elongated temperature plateaus observed (see ϑ_3 in Fig. 4.7b, middle).

In summary, a decrease of the air inlet temperature (and initial bed temperature) in the investigated range yields an accelerated reaction process owing to higher reaction rates of Mn-Fe oxide as well as an enhanced cooling effect, which leads to a higher dissipation of the released heat of reaction by the HTF and therefore higher discharging performance. On this account the maximum possible enthalpy change of the adjusted gas flow between the inlet and outlet of the packed bed constitutes the limiting factor in the examined temperature operating range.

It is particularly important to note, though, that there is a lower temperature limit for the increase of the reaction rate and thus shortening of the discharging period with decreasing air inlet and initial bed temperature (see TGA results: highest effective reaction rate in air reached between 750 °C and 800 °C, as indicated in Fig. 3.17b and Fig. 3.18b as well as Fig. B.10). Below this temperature range (750–800 °C) the reaction rate becomes the main restricting factor. In this case a self-accelerating effect owing to the release of the heat of reaction would be suppressed by the enhanced maximum possible cooling capacity of the HTF.

4.3.3 Energy Balance Estimations – Heat Dissipation and Thermal Power Output

Dynamic, temperature driven thermal charging and discharging experiments are strongly influenced by the tube furnace operated in parallel to the gas heater, which makes it difficult to separate the respective share in heat input and output by means of the HTF and across the tube wall. This is why heat balance calculations are solely carried out for the discharging step at constant gas inlet and initial bed temperatures, which experiments provide controlled boundary conditions at the reactor inlet and at the surroundings (tube furnace chamber). The determination of the thermal power output P_{HTF} as well as the quantification of the amount of thermal energy Q_{HTF} extracted from the packed bed storage by the HTF constitute only estimations, though, which can be used appropriately to compare experiments at different operating parameters.

Figure 4.8a and Fig. 4.8b display the calculated mean reaction power output $P_{rxn,av}$ (Eq. (C.13)) as well as the mean thermal discharging power $P_{HTF,av}$ (Eq. (C.20)) of the TCS reactor over the reaction time for each experimental run. As expected, values of $P_{rxn,av}$ and $P_{HTF,av}$ are rising both with enhanced heat capacity rates (increase of HTF flow rate in Fig. 4.8a) and with enhanced cooling capacities of the HTF owing to higher possible temperature gradients between the HTF and the storage material (decrease of air inlet temperature in Fig. 4.8b). Consequently, the thermal power output can generally be controlled by defining the HTF mass flow rate and inlet temperature.

A detailed overview of the progress of calculated reaction power output P_{rxn} and thermal discharging power P_{HTF} over time, along with the decline of the current mass flow rate $\dot{m}_{g,out}$

owing to O_2 uptake (Eq. (C.5)) as well as the measured temperature increase $\Delta T_{g,std}$ (Eq. (C.15)) of the gas outlet temperature $\vartheta_{g,out,av}$ is provided in Fig. C.4 (Appendix C.6).

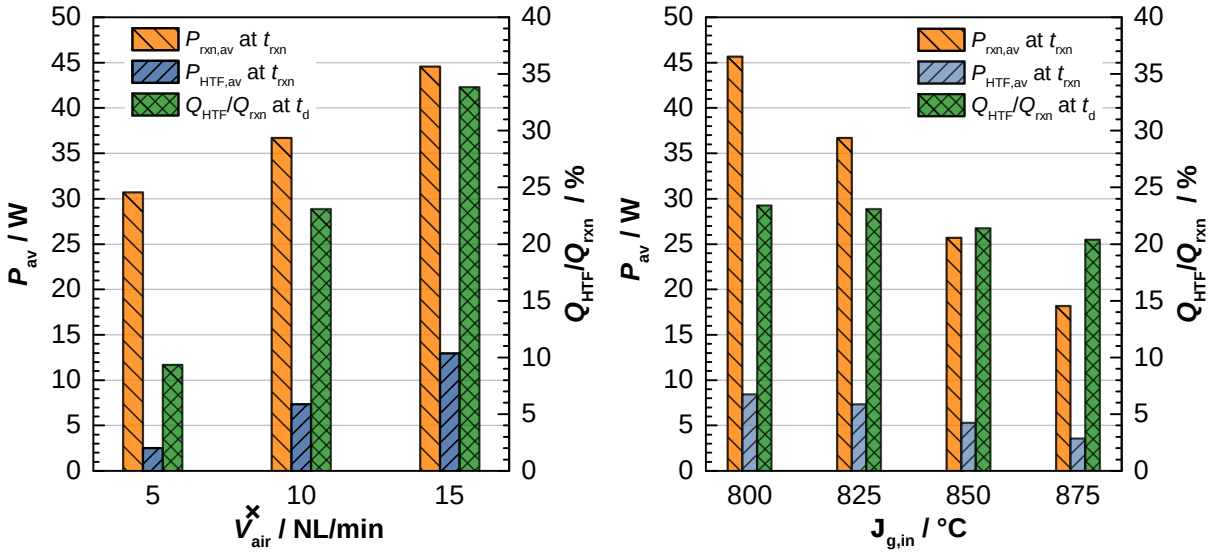

(a) Flow rate variation with initial bed and constant air inlet temperature $\vartheta_0 = \vartheta_{g,in}$ of 825 °C.

(b) Variation of initial bed and constant air inlet temperatures $\vartheta_0 = \vartheta_{g,in}$ at 10 NL/min air.

Figure 4.8: Storage discharging step 4 $(Mn_{0.75}Fe_{0.25})_3O_4 + O_2 \rightarrow 6\ (Mn_{0.75}Fe_{0.25})_2O_3$ at constant air inlet temperature $\vartheta_{g,in}$: Comparison of mean reaction power output P_{rxn} and mean thermal power output P_{HTF} achieved by the HTF; share of released thermal energy (equals chemical storage capacity) which has actually been extracted from the packed bed by the HTF (heat losses account for the remaining share).

Moreover, the ratio of Q_{HTF} (Eq. (C.19)) to Q_{rxn} (Eq. (C.12)) in Fig. 4.8 at the discharging time t_d represents the calculated proportion of stored thermal energy, which has been dissipated by the HTF (estimated calculation based on the registered temperature rise ΔT_g of the HTF according to Eq. (C.15)). The highest fraction of extracted energy has been achieved at 15 NL/min, giving a value of 33.9 %.

It has to be noted that owing to the small-scale experimental setup with the tube furnace evenly controlled at the initial packed bed temperature conditions throughout each experiment, boundary effects exerted a strong influence on the storage operation. Large heat losses across the reactor tube wall to the surroundings (tube furnace) occurred (see Fig. C.3), which losses are generally difficult to assess and can therefore not be directly quantified though. Moreover, the gas outlet temperature $\vartheta_{g,out,av}$ measured in the head space directly above the packed bed (e.g., see Fig. C.2) is strongly influenced by the non-uniform temperature profile in the upper part of the reactor tube towards the gas cooler (operated with cooling water), which is integrated into the casing tube (see Fig. 4.2). Thus, $\vartheta_{g,out,av}$ is similarly subjected to high heat losses and turned out to be significantly too low compared to the measured bed temperatures (see also remarks in Appendices C.4.2 and C.6.1).

The applied experimental conditions in the lab-scale reactor account for laminar flow conditions with low values for the tube Reynolds numbers in the order of 110 (at an average temperature of ≈865 °C). The heat transfer coefficients $h_{s\text{-}g}$ between the particles and the fluid phase in the

packed bed can be estimated based on the Nusselt correlation by Gnielinski [67], described in Appendix C.5. The calculated values for $h_{s\text{-}g}$ are in the range of 200...300 W/(m^2·K), which can be considered sufficiently high. In view of the fairly low bed porosity ε_{bed} of 34 % (Section 4.1.3) as well as the small mean particle diameter $d_{p,m}$ of about 2.4 mm (Section 3.4.4), resulting in a high surface area available for heat transfer, similar temperatures of the solid particles and the gaseous fluid can be expected.

However, as the *thermal capacity rate* of the adjusted HTF flow in the experiments is rather low, the HTF cannot supply and absorb sufficient thermal energy to accelerate the respective redox reaction and hence the charging/discharging process as a whole. In addition, the thermal conductivity of metal oxides is intrinsically low, which factor is slowing down radial heat input across the tube wall during charging. During discharging it can be assumed, that the entering HTF is heated up to the maximum possible temperature, such that the maximum thermal capacity of the HTF to transport thermal energy is exploited. On that account heat input via the HTF and the tube furnace as well as heat output by means of the HTF pose the limiting factors in the lab-scale reactor. On a technical scale the HTF mass flow rate would be adjusted in such a way to reach the targeted thermal power levels for storage charging and discharging.

4.4 Cycling Test – Characterization of Packed Bed and Storage Material

In general, a thermochemical storage material can only be implemented on a larger scale, if it exhibits the ability to maintain its integrity over repeated cycling, both physically and chemically. Cycling stability is considered a key feature of a TCS material, implying the progress of a reversible redox reaction over innumerous cycles without degradation of the material reactivity owing to microstructural changes, which could be caused by phase changes or sintering effects. Furthermore, the mechanical stability of the particles – characterized by low particle attrition and high crushing strength – should be sustained. Especially sintering effects can be more pronounced in larger sample masses and may influence the performance of a packed bed. Macroscopic effects, such as potential channeling, might also impair the redox behavior of the packed bed on the whole.

However, cycling data on the basis of a packed bed of ≈471 g granular $(Mn_{0.75}Fe_{0.25})_2O_3$ material has not been available so far. For that purpose a reference redox cycle (see Section 4.2 and Appendix C.6 for a detailed description of the charging and discharging step) was repeated four times (2nd, 6th, 9th and 17th cycle) under identical experimental conditions in between the execution of different parameter studies, most of which have been presented above (see Section 4.3). Within the scope of the parametric studies this approach allows to verify the comparability of the experiments among each other. Additionally, the cycled material – a total of 17 redox cycles have been performed – can be further analyzed and compared to the original material.

The results of the temperature driven charging step are displayed in Fig. 4.9a. It can be asserted

that the heating-up period of the material – prior to the reaction onset – remained constant for all cycles, demonstrating stable repeatability. During the course of the endothermic reaction a value of ≈982 °C could be observed for the level of the temperature plateau ϑ_3 in the 2nd cycle, whereas the temperature dropped to ≈979 °C in the 9th and to ≈976 °C in the 17th cycle, closer to the equilibrium temperature. Temperature ϑ_1 indicates the same trend. Accordingly, the O_2 evolution onset was registered somewhat earlier in the 17th cycle. The progress of the O_2 evolution curves in the 9th and 17th cycle reveals a slight tendency towards faster reaction rates and somewhat shorter reaction times, also indicated by the conversion curves in Fig. 4.9a. The overall reaction time t_{rxn} (O_2 release) took ≈122.5 min in the 2nd cycle, whereas a duration of ≈118.5 min could be determined for the 17th cycle.

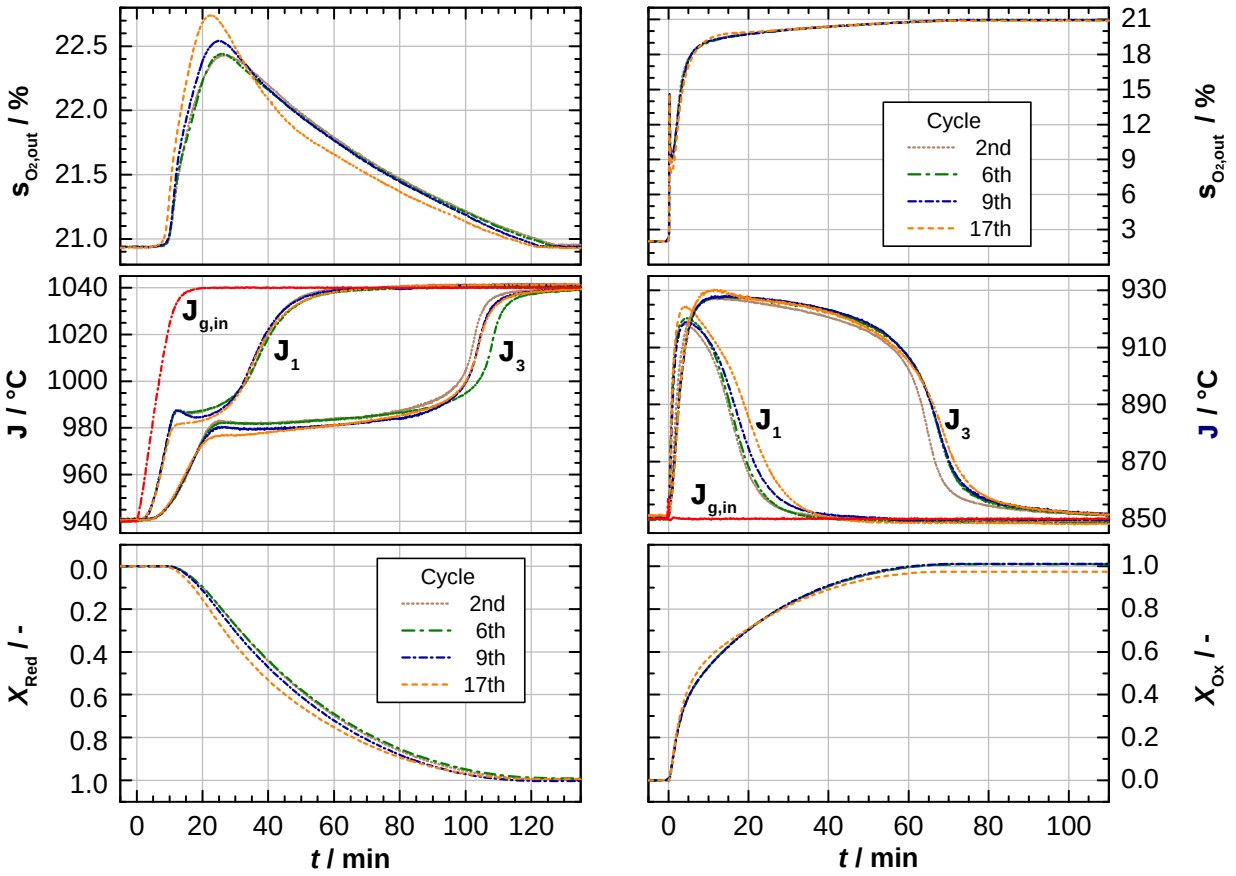

(a) Thermal charging step 6 $(Mn_{0.75}Fe_{0.25})_2O_3 \rightarrow$ 4 $(Mn_{0.75}Fe_{0.25})_3O_4 + O_2$ conducted by means of an increase of the air inlet $\vartheta_{g,in}$ and tube furnace temperature $\vartheta_{furnace}$ from 940 °C to 1040 °C.

(b) Thermal discharging step 4 $(Mn_{0.75}Fe_{0.25})_3O_4$ + $O_2 \rightarrow$ 6 $(Mn_{0.75}Fe_{0.25})_2O_3$ conducted at a constant air inlet $\vartheta_{g,in}$ and tube furnace temperature $\vartheta_{furnace}$ of 850 °C.

Figure 4.9: Test of cycling stability over 17 redox cycles at 10 NL/min air.

In all reference charging experiments complete conversion has been achieved within the possible accuracy of the evaluation. Overall, the packed bed did not exhibit any reactivity deterioration during the reduction step, which is why the diffusion of O_2 out of the material during the phase

transition does not seem to become a limiting factor.

Figure 4.9b illustrates the experimental results of the subsequent discharging step at a constant air inlet and initial bed temperature of 850 °C, assigning a change of the pO_2 to initiate the reaction. For simplification the preceding cooling phase in 2 % O_2 atmosphere is not depicted. The highest O_2 uptake rate in the initial phase of the reaction was observed for the 17th cycle, which also yielded the highest temperature values in the packed bed (Fig. 4.9b, middle). ϑ_1 close to the gas inlet was about 6 °C and ϑ_3 in the middle of the packed bed about 3 °C higher compared to the fresh material in the 2nd cycle.

Analogous to the reduction step the temperature profiles occur to be slightly different in the last cycle, indicating potential changes in the packed bed behavior. The overall reaction time t_{rxn} (O_2 uptake) amounts to ≈78 min on average. As the reaction proceeds only very slowly towards the end, 95 % conversion has already been reached approximately ≈49 min after initiation of the reaction, respectively. Within the accuracy of the evaluation complete conversion has been obtained throughout all reference discharging experiments. The low conversion of 97.5 % calculated for the 17th cycle is considered a runaway value, since the storage material was recovered in the fully oxidized state upon emptying the reaction chamber.

In summary, a continuance of the redox reactivity over several cycles can be verified for the packed of granular Mn-Fe oxide. A redox cycle of the raw and cycled material conducted by TGA is depicted for comparison in Fig. C.5 in the appendix, confirming the observations of the lab-scale cycling test. It is important to note, that the experiments do not allow conclusions to be drawn about the intrinsic cycling stability of the storage material though, owing to this relatively small number of total cycles conducted as well as the scale of ≈500 g of storage material.

When the reaction chamber was opened after 17 cycles, indications of channeling effects were not observed. For illustration purposes the view onto the loose packed bed of granulate just after filling of the reactor tube is presented in Fig. 4.10a, the view onto the bed after cycling looks alike.

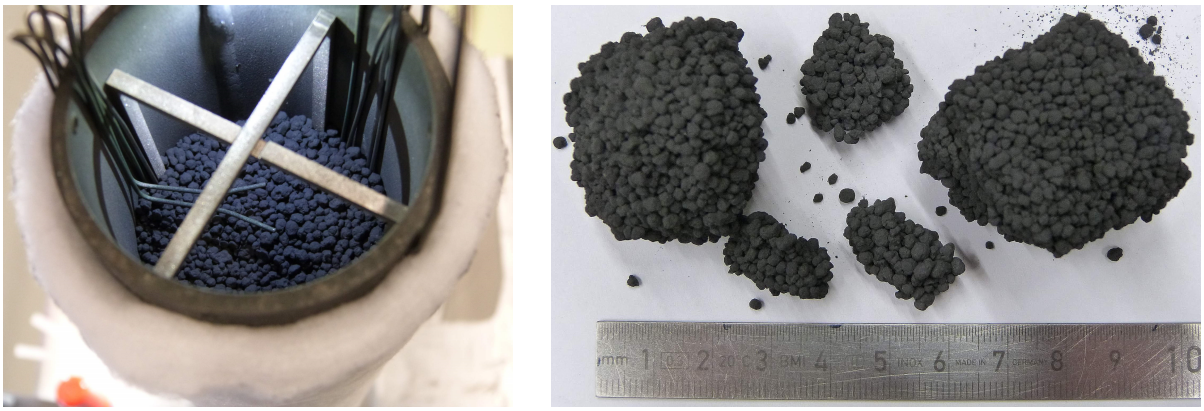

(a) Granulate before cycling. **(b)** Granulate after cycling.

Figure 4.10: View of Mn-Fe oxide granulate in the reaction chamber prior to cycling, along with arrangement of thermocouples measuring the gas temperature above the packed bed (a); agglomerated material after cycling in air (17 redox cycles) upon cleanout of the reactor tube (b).

However, only granules in the upper part of the packed bed showed free outflow upon turning the opened reactor tube. Material in the lower part of the bed formed larger agglomerates embedding the sheath thermocouples. Hence, the granular material still tends to agglomerate due to occurring sintering effects. Agglomerated granules after redox cycling for 17 times are depicted in Fig. 4.10b.

The agglomerates are not hard and can thus easily be broken apart into single granules with exertion of low force. In consequence of these sintering processes the gas flow behavior and present flow distribution within the packed bed cannot be precisely predicted. That is why a reasonably homogeneous gas flow through the packed bed might not have been thoroughly ensured throughout the series of experiments.

The mean equivalent particle diameter $\bar{d}_{\mathrm{p,pr}}$ decreased to 1.74±0.51 mm (≈5900 particles analyzed by means of image analysis based on ImageJ) compared to a mean value of 2.13±0.56 mm identified for the raw material ($d_{\mathrm{p,pr}}$ of single particles calculated according to Eq. (3.11) in Section 3.4.4). Correspondingly, the particle size distribution of the cycled material, depicted in Fig. C.6, demonstrates a slight shift to smaller mean equivalent particle sizes in comparison to the raw material. This observation corroborates the physical impression of the granular particles, which seem to have turned considerably more brittle and fracturable upon cycling. Only single granules – no agglomerates – have been taken into account for the determination of the mean equivalent particle diameter $\bar{d}_{\mathrm{p,pr}}$. Therefor the existing agglomerates had to be broken apart. The slight change in granule size might be attributed to an alteration of the physical material characteristics caused by the high temperature exposition on the one hand, or might even be provoked by the chemical stress due to cycling on the other hand. A spalling of material has been observed, causing increased powder formation, which can be seen in the top right corner of Fig. 4.10b. The granules also experienced slight mechanical impacts during the emptying process of the reactor tube, which might have led to particle breakage as well. Consequently, it cannot be completely excluded, that the slight reduction in mean granule size might also be attributed to the emptying of the reactor tube or the breakup of the agglomerates.

Examinations of granular $(Mn_{0.7}Fe_{0.3})_2O_3$ over 30 redox cycles in air conducted in a quartz tube packed bed reactor (21 g) by Preisner *et al.* have confirmed the current observations. Granules tended towards the formation of agglomerates and exhibited a low particle stability, eventually leading to a reduced expected lifetime of the material. The authors have demonstrated that the addition of inert additives (20 wt-% CeO_2 and especially ZrO_2, respectively) lowered the tendency towards particle agglomeration and improved the particle strength immensely. ZrO_2 has been identified to be the most promising additive in terms of improved resistance to abrasion and attrition [116].

Prior to cycling, the pressure drop solely over the packed bed amounted to ≈1.5 kPa, calculated from measurements at a flow rate of 30 NL/min air at ambient temperature.[3] However, after 17 redox cycles an air flow rate of 30 NL/min at RT yields a calculated total pressure drop of ≈4.0 kPa over the bed (typical accuracy of pressure transducer ±0.625 kPa). From the slight increase in pressure drop noted upon cycling can be deduced that the corresponding increase in pO_2 enhances the reaction temperature by approximately 1 K according to the pO_2-T dependence of the reaction (Table 3.4), which is in agreement with the observations made in the oxidation step of the last cycle (Fig. 4.9b). An explanation for the increased pressure drop might be the observed sintering effects (see Fig. 4.10b) as well as the above-mentioned appearance of some smaller particles, blocking open pathways for the fluid flow and eventually increasing the pressure drop across the packed bed. Consequently, a modification of the granular particle arrangement and especially its interaction forces can be affirmed by means of the pressure drop measurements.

The morphology and shape of the particles before and after thermal cycling in the lab-scale storage reactor are of particular interest. Figure 4.11 shows representative SEM images comparing the microstructure of the raw material (a and b) with the microstructure of the material cycled 17 times in the scope of the experimental study (c and d), both materials being in the oxidized state.

On the one hand, the performed redox cycles did not disclose a significant macroscopic effect on the cycling stability in terms of the reactivity of the material in the lab-scale reactor (see Fig. 4.9). On the other hand, a comparison of the micrograph of the starting material (a) with the micrograph of the cycled material (c) in Fig. 4.11, showing the topview of the granulate surface respectively, reveals a considerable change of the microstructural morphology over the course of the redox cycles.

While the raw material features a finer structure with irregularly shaped individual grains (a), the material cycled 17 times exhibits clearly larger, coherent bulk structures (c). Those can directly be attributed to strong sintering effects induced by the long exposition to HT conditions up to 1040 °C during cycling. The formation of larger bulk structures and sintering necks in the course of cycling might have caused a more homogeneous temperature distribution inside the packed bed, eventually leading to the observed slight change in the reactivity of the packed bed (bulk reactivity), as discussed above.

Moreover, Fig. 4.11 illustrates polished granule cross sections of the raw material (b) and cycled material (d). The granular particles were infiltrated with epoxy glue to stabilize the structure. Dark areas (epoxy glue) represent the voidage of the granules. The image of the cycled material corroborates the formation of larger bulk structures over cycling. As the voidage fraction (dark

[3] Owing to the chosen experimental setup illustrated in Fig. 4.1 (middle), a direct measurement of the pressure drop over the packed bed has not been feasible throughout the experiments. Instead, the pressure drop over the bed was estimated from two pressure drop measurements conducted over the entire reactor tube setup, once with granulate filling and once without, subtracting the Δp of the setup without filling from the Δp of the former. With 30 NL/min, a higher air flow rate was chosen for the pressure drop measurements at RT compared to the actual storage measurements at HT. In this way a higher superficial gas velocity could be simulated at RT, corresponding to the superficial air velocity at a flow rate of 10 NL/min and a temperature of about 625 °C.

areas) per image section is similar in both cases, ≈55 % for raw material and ≈59 % for cycled material (average values of four images, respectively, estimated based on a comparison of the fraction of black pixels), the granulate porosity appears to be essentially unchanged after 17 redox cycles. Overall, the microstructural alterations seem to have an impact on the mechanical properties and integrity of the material, which supports the above-described indications of material embrittlement upon cycling in the reactor. Based on those findings, a preconditioning procedure in the form of repetitive thermal cycling of the storage material in a furnace is advisable prior to use in lab-scale experiments, in order to reach stable conditions with regard to microstructure and reactivity.

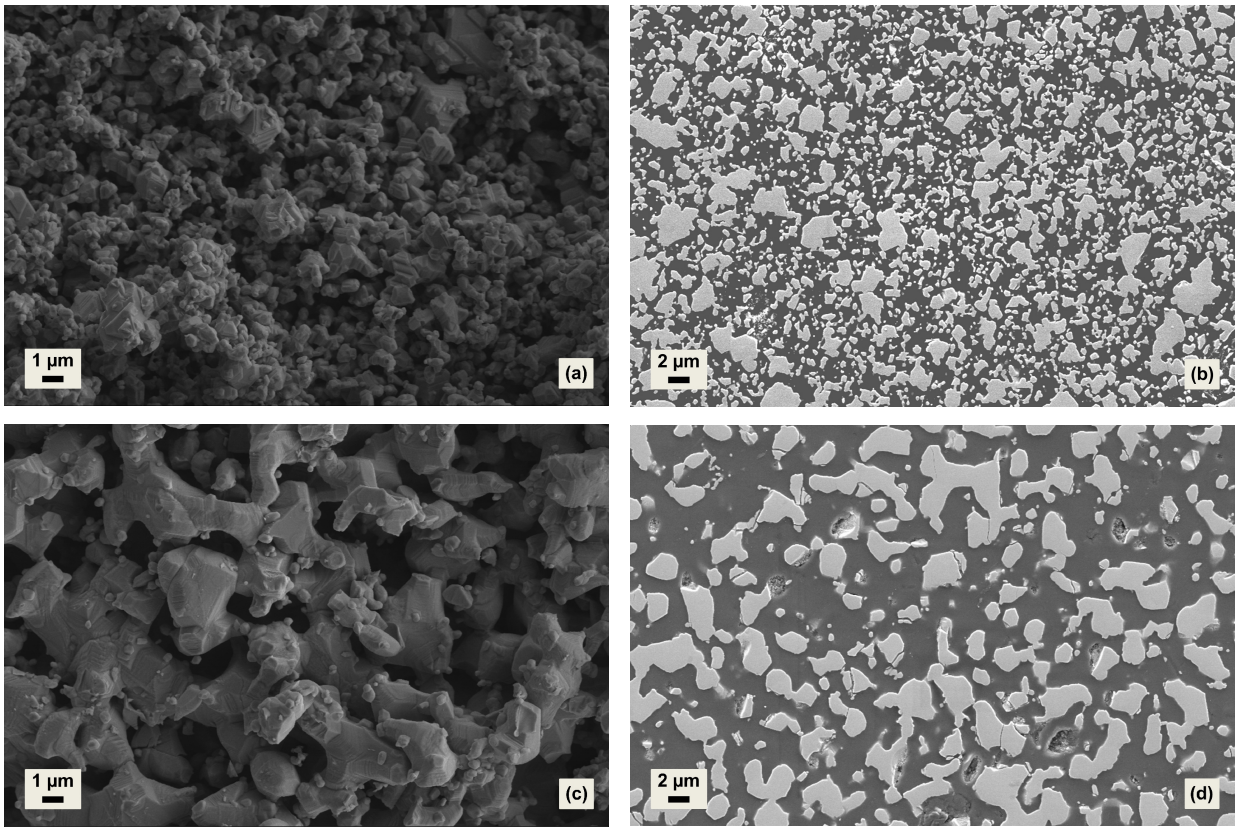

Figure 4.11: Scanning electron micrographs: Granulate surface and microsection of Mn-Fe oxide as prepared (a and b) as well as after 17 cycles conducted in the lab-scale storage reactor (c and d), both samples being in the oxidized state; SEM images (b) and (d) show polished cross sections of granules with epoxy glue (dark areas) and solid particle fraction (grey areas); conditions of SEM measurements: magnification images (a) and (c) 10.000 x, images (b) and (d) 5.000 x; working distances of 7.9 mm (a), 8.0 mm (b and c) and 7.8 mm (d); acceleration voltage of 5.0 kV; SEM images recorded by Institute of Materials Research, DLR.

4.5 Findings Derived from Experimental Investigation of the Granular Packed Bed

The experimental results of the charging and discharging process of a packed bed tube reactor on lab-scale (total chemical storage capacity Q_{chem} of 35.5 Wh) demonstrate the general feasibility of the redox reaction based storage concept with direct contact heat transfer and open-loop operation using air as HTF. The main attention is centered on the influence of essential operating parameters on the storage characteristics, which has been analyzed by means of several parametric studies, arriving at the following conclusions:

- The proceeding redox reactions disclosed the development of distinct temperature profiles with the formation of temperature plateaus and a temperature front traveling in flow direction through the packed bed, characteristic for exploiting the heat effect of reversible reactions for TCS, respectively. The experiments revealed that the advancing reactions are mainly limited due to the respective rate of heat input (thermal charging) and rate of heat dissipation (thermal discharging) by the HTF under the applied operating conditions in the lab-scale reactor. Thus it was concluded, that heat transport poses the most essential factor for storage operation under the applied conditions in contrast to the reaction rate.
- Thermal charging/discharging investigations under constantly increasing/decreasing air inlet temperature demonstrated the feasibility to stabilize bed temperatures due to the proceeding redox reaction with absorption/release of thermal energy. This characteristic TCS behavior leads to an extended charging/discharging period in contrast to established sensible TES systems and thus allows the perpetuation of a, to a certain extent, steady storage discharging temperature over a prolonged period of time. The observed temperature plateaus proved to be highly dependent on the thermodynamic properties of the redox reaction (closely analyzed in Section 3.4.1).
- The dual function of air as HTF and O_2-carrier, removing or supplying the reactant O_2 respectively, has a direct impact on the prevailing O_2 concentration and therefore the pO_2 in the reactor. Changes of the O_2 concentration due to the proceeding reaction both influence the pO_2-dependent reaction rate as well as reaction temperature, and affect the heat capacity rate C_{HTF} of the HTF. Those phenomena need to be taken into account in the future design and operation of redox reaction based TCS reactors with direct contact heat transfer using air as HTF.
- The performance of the discharging process at constant air inlet temperature, inducing the reaction by means of a sudden change of the pO_2, constitutes an alternative operating method, which could be individually adapted to the corresponding process boundary conditions of the envisaged technical application. Moreover, the preceding charging process could also be conducted under an atmosphere of reduced total pressure, implying a lowered pO_2 and thereby lower charging temperature. Cooling the reduced oxide under a reduced total

pressure or inert atmosphere allows to exploit a temperature uplift along with a high reactivity and consequently higher thermal power density in the subsequent discharging step of the storage reactor in air. High oxidation rates could be demonstrated under the applied operating conditions (at air flow rates of 10 NL/min and 15 NL/min) in the scope of the conducted parametric studies (see Figs. 4.7 and C.4).

- The forward and reverse reaction has been examined by means of a reference cycle performed in between the outlined parametric studies, yielding no degradation of the material reactivity over 17 cycles. Hence, the material exhibits practical cycling stability, which has been considered sufficient for the comparability of the experimental results obtained from the conducted parametric studies. On a microstructural level, though, sintering phenomena resulted in an alteration of the microstructure, in turn leading to a lack of mechanical strength of the granules upon cycling.

5 Technological Classification

Fundamental examinations of metal oxide redox reactions to exploit reaction enthalpies for TCS in this thesis have unfolded various benefits but also drawbacks of this concept. On the one hand, HT-TCS potentially facilitates higher energetic storage densities compared to merely sensible TES. On the other hand, reactive metal oxides are costlier than inert ceramics or natural rocks used for sensible-only TES up to date. Some metal oxides may also be harmful to health.

In general, working temperatures of metal oxides have been shown to have an upper temperature limit, mainly due to an intensification of sintering effects with higher temperatures. Those effects could in turn constitute a hindrance of oxygen diffusion, slowing down the oxidation rate. This is an important issue, as the energy to drive the reduction reaction ($\Delta_R H$) has to be supplied by means of a temperature difference between the HTF (air) charging temperature and the reaction temperature. Although thermodynamically favored, the oxidation reaction is confined by a lower temperature limit, as input of thermal energy at an adequate temperature level is initially required to overcome the high activation energy barrier and initiate the reaction, such that the oxidation proceeds at a sufficient rate.

It has been disclosed in Section 4.2, that – in addition to the heat of reaction – a large portion of thermal energy is stored as sensible energy due to the high operating temperatures of a redox reaction based TCS reactor (see Fig. 4.5). This matter of fact equally necessitates the utilization of the sensible thermal energy in the overall storage concept, in order to increase the total storage capacity and exploit the energy storage system efficiently. A brief review on hybrid sensible-thermochemical energy storage concepts suggested in the literature has been given in Section 2.3.5.

In the following, promising concepts for potential technical applications of redox reaction based TCS systems are proposed, deduced from experimental results and theoretical considerations in this work. For instance, the presence of a thermal hysteresis due to the occurrence of kinetic limitations under technically relevant operating conditions only plays a minor role, if the reactive metal oxide particles simultaneously serve as heat transfer medium and storage medium (see Section 5.2) or if the heat of the reaction is alternatively used for temperature buffering purposes (see Section 5.3).

5.1 Regenerator-type Storage with TCS-Topping

Significance of Additional Exploitation of the Sensible Thermal Energy in TCS Storage Concept The operation of a HT-TCS reactor by solely exploiting the reaction enthalpy for thermal energy storage is accompanied by the drawback, that only the ΔT between the HTF and the equilibrium temperature can be used, as the equilibrium temperature is fixed at a constant pO_2 of the HTF. The utilization of atmospheric air as gaseous working fluid brings about only

low heat transport capabilities owing to the inherently low density of air at standard pressure of 1.01325 bar (≈1.18 kg/m^3 at 25 °C, ≈0.28 kg/m^3 at 1000 °C), which is why high HTF flow rates (at ideally elevated gas pressure) – and consequently large pipe diameters to minimize parasitic losses (reduction of pressure loss) – are necessary to achieve high heat capacity rates $C_{\mathrm{HTF}} = c_{p,\mathrm{g}} \cdot \mathrm{d}m_{\mathrm{g}}/\mathrm{d}t$ of the HTF air and therefore the required thermal ratings of the storage system.

Up to date regenerator-type storage systems, sometimes also referred to as *thermocline TES systems*, using a gaseous heat transfer medium and a stationary, inert solid storage medium such as ceramics or natural rocks, constitute established HT storage systems, which are solely based on the storage of sensible thermal energy. Consequently, the achievable energy storage density of the storage system is depending on the temperature increase, generally defined by the temperature boundary conditions at the inlet and outlet of the storage. High temperature waste heat recovery and subsequent preheating of combustion media accounts for one of the main applications of such regenerators on an industrial scale (e.g., at heating and melting furnaces in the metal, ceramic, chemical and glass industry; in particular a so-called *Cowper* in a blast furnace process) [72]. However, regenerators with a fixed storage medium have the disadvantage of a decreasing HTF outlet temperature during discharging, as the storage material cools down [72, 66].

Based on the general operation principle of a HT regenerator-type storage system (see Section 2.1.2) and the lab-scale examinations of a redox reaction using metal oxide particles in a tubular packed bed configuration in this work, a hybrid regenerator-type storage combining inert storage material with a reactive metal oxide topping can be envisaged for a potential application on an industrial scale. The storage has to be operated with ambient air as HTF to provide oxygen for the oxidation to take place.

Hybrid Sensible-Thermochemical Energy Storage System Based on Example of a CSP-Plant

Figure 5.1 illustrates the characteristic operation mode of such a hybrid storage system, which is comparable to the operation of a HT regenerator-type storage system. As an example, the potential storage application in a solar tower power plant with central air receiver is considered.

During the charging stage the HTF from the solar tower field – hot air from the solar receiver – enters the storage tank at the top and flows downward (a), forming a characteristic transient temperature profile along the axis of the solid inventory. The direction of the flow is reversed in the subsequent discharging stage, cold air entering at the bottom of the regenerator storage (b). This reverse-flow mode of operation provides for the perpetuation of an axial thermal stratification inside the packed bed, when thermal energy is transferred to and extracted from the storage [163, 167]. As a result of this cyclic reversal of the gas flow between the charging and the discharging phase, the temperature of the storage mass varies downward and upward periodically, the storage material absorbing a certain amount of thermal energy during charging and releasing it to the colder HTF again during discharging [72]. This periodical temperature change along the bed height owing to the heat transfer between the fluid and the solid storage material is also referred to as the *temperature front*, an *axial thermal gradient* or a *thermocline* [97].

It is therefore self-evident, that the positioning of the reactive TCS material is only reasonable in the HT upper part of the packed bed storage tank, where HTF operating temperatures during the charging phase allow the reduction to take place. The metal oxide can be employed either as solid material or as a reactive coating on a ceramic substrate. Below the reactive TCS zone – where solid temperatures are simply too low and do not exceed the equilibrium temperature of the reaction – the storage unit can be equipped with inert, low-cost storage material (e.g., ceramic refractory bricks or natural stones). This non-reactive lower section is merely used for sensible thermal energy storage, cooling the HTF further down during charging as well as heating up the HTF until the reaction is triggered during discharging, respectively.

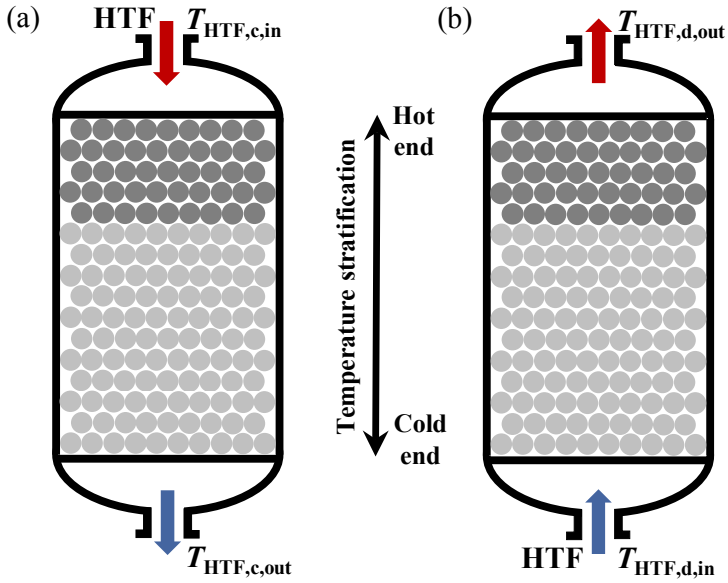

Figure 5.1: Schematic description of a potential regenerator-type storage with a thermochemical storage material topping, allowing the exploitation of the sensible heat and the heat of reaction due to a temperature stratification along the bed height: Thermal charging (a) and thermal discharging (b). The potential dimensions of the TCS zone in the top part (dark gray) and the non-reactive zone with inert material in the lower part (light gray) are marked for exemplification. The dimensions are highly dependent on the operating conditions, material properties as well as the overall reactor design.

The proceeding redox reaction in the TCS zone at the upper end of the regenerator causes a buffer effect, temporarily stabilizing the solid temperatures to a certain extent and therefore shifting the temperature profile in comparison to an operation mode with sensible storage only (see Figs. 4.4 and 4.6b in Chapter 4). Those findings clearly emphasize the intrinsic advantage of sensible and thermochemical energy storage combined in one storage unit, as the attainable gravimetric energy storage density can be enhanced by exploiting the reaction enthalpy of the redox reaction of the TCS-topping in addition to the sensible energy stored by the solid.

The buffering effect of the HTF outflow temperature entails elongated charging and discharging durations, as the attainment of the defined limits for the HTF outflow conditions are deferred, respectively. For a regenerator those limits may be defined as follows: Specification of a maximum HTF outlet temperature ($T_{HTF,c,out,max}$) at the bottom end of the storage during charging (e.g.,

as predetermined by the charging rate of the storage, which is proportional to the temperature difference $T_{\mathrm{HTF,c,in}} - T_{\mathrm{HTF,c,out}}$), and a minimum HTF outlet temperature ($T_{\mathrm{HTF,d,out,min}}$) at the top end of the storage during discharging, as required by the connected process. However, it has to be mentioned that in the operation of a regenerator-type storage with TCS-topping the ΔT between the HTF inlet temperature and the reaction temperature in the charging step cannot be fully recovered in the discharging step. The HTF outflow temperature during discharging typically has to be as high as the required input temperature of the connected process, to ensure a constant heat transfer performance in a power cycle, for example. Further stabilization of this input temperature can be achieved by bypassing the regenerator with a progressively decreasing fraction of the air flow and eventually mixing this cold stream with the hot air flow exiting the storage (see also [72]).

A detailed knowledge of the reactive temperature range, which can be covered by the redox reaction to exploit the heat of reaction in addition to the sensible heat, is crucial for the envisaged application. The usable temperature range is mainly predetermined by the material characteristics, such as the equilibrium position, temperature- and pressure-dependent reaction rates as well as the potential occurrence of kinetic limitations (see also Section 3.4). It should also be noted that the operating temperature level of the proceeding redox reaction can be adjusted by means of the choice of the corresponding redox couple, partially by material modifications (use of mixed oxides) as well as by means of a variation of the pressure level of the gaseous reactant O_2. As the HTF and source of O_2 are directly coupled in this open operation principle using ambient air, the mutual interaction between the attainable thermal charging/discharging power – controlled by adjusting the HTF mass flow rate passing through the storage – and the particle reaction rate has to be accounted for in future engineering and operation of such a hybrid sensible-thermochemical energy storage system.

In view of a packed bed storage unit, the presented concept would facilitate an increase in volumetric and gravimetric energy storage densities of the solid inventory due to a high temperature TCS zone as well as cost savings due to a low temperature non-reacting cooling section employing low-cost inert materials as sensible storage media, which hybrid storage configuration has also been proposed by Ströhle *et al.* [136].

Furthermore, Ströhle *et al.* identified that the most promising integration feasibility of such a hybrid TES system (in the form of a packed bed storage unit) into a CSP plant, for example, appears to be in a parallel setup of the TES system and the power block, taking advantage of the axial thermal stratification in the packed bed to exploit the stored sensible heat as well [136]. So far only similar combined sensible-latent storage concepts have been examined experimentally [64, 138], the potential of a combined sensible-thermochemical storage system has merely been contemplated in a numerical study by Ströhle *et al.* [136, 137].

Potential Advantage of Varying pO_2 in Charging/Discharging Step The described hybrid storage system could also be applied for regenerative heat recovery to improve the overall energy

efficiency of the corresponding manufacturing process. While both charging and discharging of the storage can be performed using air as HTF, the charging step could also be carried out by means of an oxygen-poor or even oxygen-free off-gas of the associated technical process. The occurrence of different oxygen partial pressures between the exhaust gas and the supply air would also allow the attenuation of a prevalent thermal hysteresis or could even realize a thermochemical heat transformation in the sector of industrial waste heat storage, applying alternately operated storage units. Oxygen-deficient exhaust gas could be used for the reduction of the storage material, re-oxidation could be achieved at higher pO_2 using air. Potential charging of the storage reactor with exhaust gas of industrial processes, however, would also necessitate investigations into the sensitivity of the corresponding redox reaction to a variety of reactive gaseous impurities.

5.2 Reactive Metal Oxide Particles as Heat Transfer Medium

Considering an application in the field of CSP for example, several constraints are associated with a potential implementation of an indirect storage concept into a solar tower power plant with central air receiver, such as in the form of a regenerative packed bed storage system applying a TCS material in the upper part of the bed and air as HTF as described in Section 5.1.

Drawbacks of Indirect Storage Concept Applying Air as HTF and MeOs as Storage Medium
The utilization of an air receiver technology implicates that the transfer of large heat flow rates from air to the storage material (storage of sensible heat and reduction of the storage material) as well as to the heat exchanger system of the steam cycle (superheater, evaporator, economizer) requires high temperature differences ΔT and/or large volume flow rates of the HTF air, conditioned by the poor heat transport properties of air used as gaseous working fluid (due to low gas density of air at high temperatures, especially at atmospheric pressure). However, the air outlet temperature of the receiver cannot be effectively increased at will, as the combined efficiency (system efficiency) of the solar receiver coupled to a heat engine system (power cycle) decreases at absorber temperatures being too high, which can be attributed to enhanced thermal radiative and convective losses of the receiver at higher temperatures [77, 115].

Generally, HTF discharging temperatures are intrinsically lower than charging temperatures, simply owing to a temperature gradient essential for heat transfer, which results in a loss of exergy. Utilization of a reactive metal oxide topping with an existing thermal hysteresis, which is the case for Mn-Fe oxide investigated in this work, turns out to be even more unfavorable. The hysteresis effect leads to even lower discharging temperatures. Moreover, with a stationary storage concept the feasible energy storage capacity is limited by the dimensions of the storage tank, as the chosen operating conditions and characteristic material properties offer only little scope for optimization in this respect. Last but not least, in a regenerator-type storage system transient temperature profiles with a moving reaction zone are formed, which are more complex to control than a steady-state

reaction zone in prospective continuous reactor concepts. Consequently, a regenerator-type storage as described in Section 5.1 does not represent the concept of choice for CSP plants. In order to overcome the described challenges associated with a packed bed storage concept, the development of an improved reactor concept for an industrial scale implementation is indispensable.

In view of advanced reactor concepts continuous TCS reactors have the potential to facilitate an enhancement of the gravimetric energy storage density of the TES system in comparison to batch reactors with a stationary storage material, since continuous concepts allow a larger amount of storage material to fully react. A moving bed reactor operated in a counter-current flow of the metal oxide storage material and the HTF air represents a promising concept (see also [136]), which will be elaborated in detail below.

Advantages of a Direct Storage Concept with MeOs as HTM for Thermal Charging In the following, a novel HT reactor concept for continuous charging and discharging is introduced, which constitutes an approach to solving the described challenges with regard to a future upscaling. Figure 5.2 depicts the potential integration of a redox material based storage system into a CSP plant to yield higher plant efficiency and dispatchability of electricity generation.

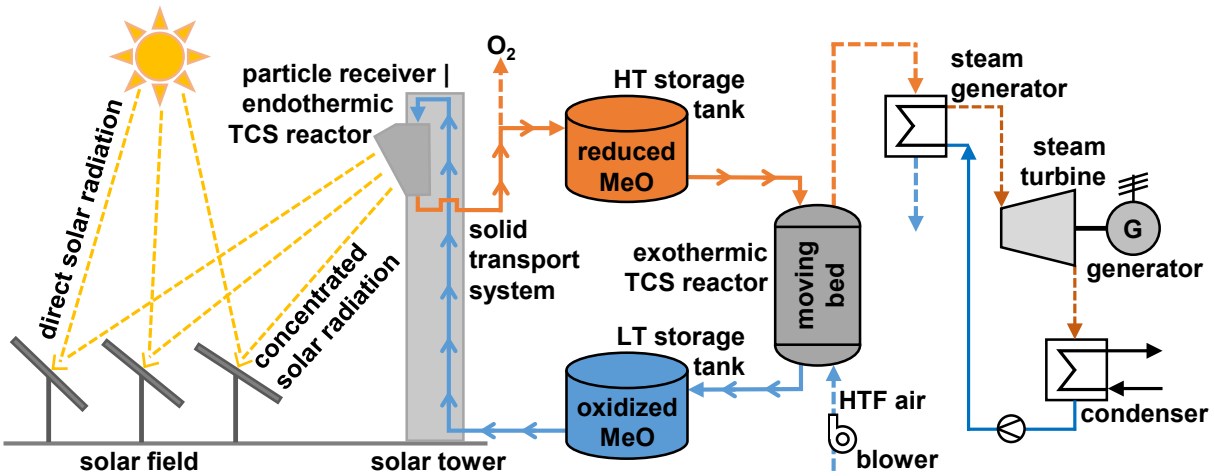

Figure 5.2: Novel storage concept partly using reactive metal oxides as HTM: Direct absorbing particle receiver (TCS reactor) for thermal charging and moving bed reactor for thermal discharging using air as HTF and supplier of the reactant O_2.

The implementation of a direct absorbing particle receiver/reactor into a CSP plant seems to be a promising way to conduct the thermal charging process directly under concentrated solar radiation and overcome the discussed challenges for indirect storage systems working with air as HTF by minimizing energy-conversion losses. In this concept, the granulate is directed through the receiver to absorb solar energy on the oxide surface, so that the particles are heated up (sensible heat storage) and the reduction reaction is driven forward. Thus the metal oxide serves both as reactive storage material (sensible/thermochemical) and heat transfer medium (HTM), which concurrent use is highly beneficial, eliminating the need for additional heat exchangers. This direct storage concept necessitates the movement of the particles, which is easier to manage with material in the

form of granular particles instead of fine powder. It must be taken into account, that the residence time in the aperture of the receiver cavity needs to be sufficient in order to facilitate both heating and complete reduction of the metal oxide particles. Furthermore, the novel thermochemical particle receiver needs to be designed with a greater capacity compared to the continuous moving bed reactor, to enable a buildup of the storage inventory for electricity generation during periods without direct sunlight and after sunset. Upon charging, the "hot" reduced particles are stored in a well insulated tank (HT) at high temperature (approx. reduction temperature) to reserve the redox material until electricity is needed, which allows a round-the-clock operation of the CSP plant for supply of base load power.

As an example, current research on solar particle receiver development includes both falling particle receivers as well as centrifugal particle receivers [76, 161, 46, 77]. The latter type is especially interesting for charging reactive particles, as the residence time of the particles can be adjusted by controlling the rotation speed and mass flow rate. Only few concepts applying metal oxides as HTM and reactive storage media have already been proposed up to date, where a solar particle receiver simultaneously serves as a thermochemical reactor to directly heat up and reduce metal oxide particles with concentrated solar irradiation [55, 129].

Moving Bed Reactor for Storage Discharging The development of a moving bed reactor concept seems to be a reasonable approach for the more critical discharging step, in order to overcome the drawbacks of a concept with a stationary material inventory. Since O_2 is needed for re-oxidation, air serves as secondary HTF to supply O_2, exploit the benefits of direct contact heat transfer between solid and gas and eventually deliver the thermal energy to the heat exchanger network of the power cycle. The reactor would be operated in the form of a counter-current flow of metal oxide particles (moving from top to bottom) and air (flowing vice versa). The idea is aimed at stabilizing a reaction zone to reach a stationary state of continuous oxidation (heat release), which leads to the formation of a stable HTF outlet temperature favored to drive the power block. The sensible heat stored above the reaction zone (range between receiver outlet/reduction temperature and oxidation temperature) and below the reaction zone (range between oxidation temperature and HTF inlet temperature) can be extracted in addition to the chemical energy, increasing the overall energy storage density of the storage system. The oxidized solid can be stocked in a cost-efficient "cold" storage tank (LT) at low temperature until a new storage cycle is started. During sunshine hours a part of the particles are continuously circulated between the irradiated solar particle receiver/reactor, the HT storage tank, the discharging reactor to drive the power cycle, and the LT storage tank. Another part of the storage material, which was charged in the particle receiver, is stocked in the HT storage tank to hold available for the operating period after sunset or during transient cloud coverage.

Besides the receiver/reactors and storage tanks, the concept in Fig. 5.2 comprises other major components such as feeding and collection hoppers as well as a particle conveying system to transport the "hot" and "cold" particles, respectively. The elevation of the particles could be

realized by a particle lift, for which, e.g., the application of an *Olds Elevator*™ seems suitable [46]. However, as the storage material has to withstand increased mechanical stress induced by the required transport of the particles, the preparation of mechanically more stable granules needs to be achieved. First steps in this direction have already been taken recently, as modification of Mn-Fe oxides yielded somewhat more stable granules, which are potentially applicable in continuously operated TCS reactors [116].

A significantly increased gravimetric energy storage density compared to a stationary packed bed reactor can be achieved, as the reaction enthalpy of the entire amount of employed storage material can be exploited. Moreover, a moving bed reactor offers further advantages in terms of a potentially better controllability as well as more flexible operating possibilities. Overall, great importance is attached to this method of storage operation, as the potential of HT-TCS based on metal oxides highly depends on the exploitation of the sensible heat in addition to the heat of reaction. From a technical point of view (upscaling) there is a demand to achieve high thermal power levels, which requires high volumetric HTF flow rates. Therefore, the focus of future work will be on the feasibility to sustain high oxidation rates and prevent the extinction of the reaction in view of a predominant cooling effect exerted by the HTF. Although high oxidation rates have been achieved under the applied operating conditions of the experimental studies described in Section 4.3.2 (see also Figs. 4.7 and C.4), the results obtained in the present thesis need to be verified experimentally on a larger scale (with higher HTF flow rates). A moving bed discharging reactor with a continuous thermal power output of 3 kW over a discharging period of 30 min, applying air as HTF, will be constructed and investigated on the basis of Mn-Fe oxide storage material (storage capacity of about 1.5 kWh) in a follow-up project at the DLR in Cologne.

The elaborated continuous storage operation of the charging and discharging reactor allows a decoupling of the envisaged thermal power level – determined by the size and operating conditions of the solar receiver and discharging reactor – from the energy storage capacity (amount of storage material). This approach would be essential for an efficient upscaling to industrial scale. On the one hand, the dimensioning of the rather costly TCS discharging reactor, which also functions as the heat exchanger to extract the sensible thermal energy, is defined by the thermal power output required at maximum load conditions according to the design data. On the other hand, the size of the rather simple and economic storage tanks accounts for the actual energy storage capacity and thus envisaged duration of charging and discharging. Thus, the illustrated concept facilitates the construction of a smaller, modular TCS reactor, that can be adapted to the respective needs.

5.3 Thermochemical Protection Layer for Temperature Stabilization

Exploitation of the Temperature Stabilization Effect Other than thermal energy storage the observed temperature stabilization effect described in this study could also be exploited for different

scopes of application. Although the investigated Mn-Fe oxide exhibits only a comparatively low energetic storage density (compared to other metal oxide redox couples, e.g., see Table 3.1), the thermal hysteresis of the redox reaction along with a high reactivity of the material in the forward and reverse direction disclose the general potential of metal oxides to be applied for dynamic buffering of technical processes or component parts, which are sensitive to frequent changes in temperature. Especially temperature sensitive metallic component parts which encounter alternating severe thermal stress at high temperatures suffer from so-called *thermal fatigue* and tend to break.

Concept of a Thermochemical Protection Layer Thermal fatigue could be avoided or at least retarded by coating metal components with metal oxides to form a "reactive ceramic coating", functioning as a reactive thermal protection layer in a self-regulating mode to extenuate variations in temperature [157]. The presence of a temperature hysteresis would imply a "passive, non-reactive" temperature range, which even represents a beneficial behavior for this kind of application owing to its buffer effect. Relevant metal oxides have to be modulated in such a way, that the hysteresis arises in the designed operating range of the application system. As soon as the temperature of the off-gas leaves this operating range, the buffer action of this thermochemical protection layer is launched to mitigate either an excess temperature via the process of the reduction step, absorbing thermal energy, or an insufficient temperature via the process of the oxidation step, releasing thermal energy. In this way the temperature of the metallic material can be stabilized in both directions, which in turn reduces thermal fatigue problems of the material.

However, in combustion processes the realization and operational reliability of such a protection layer seems to be challenging, as the layer may not be arranged on the side of the exhaust gas flow, which does not provide O_2 for the reverse oxidation step in case of a drop in the exhaust gas temperature (step corresponds to the regeneration of the oxide material at the same time). Instead the layer needs to be coated on the side exposed to the ambience or an O_2 containing atmosphere in general, which allows an exchange of the reaction gas O_2.

The mechanism of a thermochemical protection layer, solely based on the intrinsic material properties of the applied metal oxide, is schematically illustrated in Fig. 5.3.

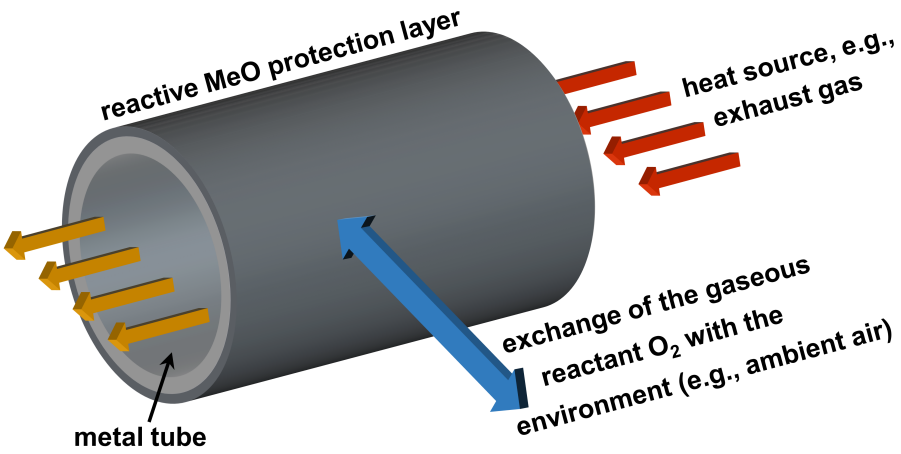

Figure 5.3: Scheme of the operation principle of a potential thermochemical protection layer for temperature stabilization of a flow through metal tube: Illustrated mode of buffering a pending overheating, which would be highly detrimental for the durability of the tube.

Potential Coating Technologies The development of such thermochemical protection layers represents a novel field of research, which can build on substantial experience made in the processing of inert ceramic materials as coating for temperature sensitive metal components over several decades. Those coatings, which are also known as *thermal barrier coatings* (TBC), function as insulation of the metal surface from hot gas streams and therefore effect a reduction of the actual temperature of the metal [47, 61]. This in turn allows to reach higher operating temperatures in the corresponding field of application. A variety of coating technologies are available, among those are *air plasma spray coating* (APS), *electron beam physical vapor deposition* (EBPVD), *high-velocity oxy-fuel deposition* (HVOF) and *direct vapor deposition* (DVD) [61, 51]. Conventional sintering methods are also conceivable.

Metal oxide materials with high energetic storage densities are advantageous, since the manageable thickness of the applied metal oxide layer and thus the attainable storage/buffering capacity is only limited. It has to be noted for this specific application of a reactive TC protection layer, that higher-priced cobalt oxide based materials might be considered interesting (redox couple Co_3O_4/CoO exhibits a thermal hysteresis in a narrower temperature range between reduction and oxidation onset compared to the Mn-Fe oxide investigated in this work, though; see also [28, 37]). However, in view of long-term applicability as well as health and safety issues, a possible spalling of the layer has to be eliminated in any case in advance.

Potential Application Cases Various potential areas of application in the high temperature range can be envisaged for the proposed thermochemical protective layer, in particular where HT materials face thermal fatigue due to the exposure to alternating temperature loadings, e.g.:

- Exhaust manifolds installed downstream of internal combustion engines (e.g., in cars, motorcycles, power saws), as the continuous improvement of combustion engine performance imposes higher requirements on the thermal and mechanical stability of employed metallic

materials (see, e.g., [124, 132]); the application of a reactive TC protection layer would be aimed at enhancing the thermal durability of such exhaust manifolds, typically subjected to severe temperature conditions.

- Components for the construction of industrial furnaces as well as for heating engineering (e.g., temperature stabilization of gas jets).
- Components of solar receivers subjected to high temperatures, e.g., similar to the effect of the proposed thermal protection storage concept for a pressurized air solar receiver using a PCM [143].
- High temperature reversible *solid oxide electrolyzer and fuel cells* (SOEC/SOFC) [125], for which the integration of a HT thermal energy storage system would be advantageous with regard to temperature stabilization and thermal management.

6 Summary and Outlook

The concept of TCS applying gas-solid reactions to exploit reaction enthalpies for the storage of thermal energy offers the potential to achieve enhanced energy storage densities compared to established sensible and latent TES systems. Reversible redox reactions of metal oxides are predestined for TCS in high temperature processes above 500 °C. The application of those storage materials has the significant advantage that ambient air can be simultaneously used as HTF and source of the reaction gas O_2 (HTF as O_2-carrier), which allows an open-loop storage operation with direct contact heat exchange between gas and solid.

Prior to this thesis little work has been done on a comprehensive, systematic examination of metal oxide redox cycles for TCS to concentrate qualitative and quantitative material properties data with respect to the thermodynamic, kinetic and cycling stability behavior. Therefore, this thesis has been targeted on the identification of determining aspects for the metal oxide based TCS technology on an appropriate scale, in order to gain a fundamental understanding of the reaction behavior and derive process technological directions for further TCS material and storage system development in the operating temperature range up to ≈1100 °C. The investigations comprise the selection and characterization of a suitable material as well as the experimental examination and demonstration of the storage concept on lab-scale.

An overall assessment of relevant pure metal oxides has been conducted based on a literature study with regard to thermodynamic equilibrium, energy storage density, reactivity as well as material availability and a general health & safety rating, classifying manganese-based oxides as promising TCS materials. As iron-doped manganese oxides exhibit improved TCS properties in contrast to pure manganese oxide, manganese-iron oxide with a Fe/Mn molar ratio of 1:3 has been selected as reference material for the fundamental examinations in this thesis, applying granules in a size range of about 1 mm to 3.5 mm. Pure manganese oxide served as underlying base material, which measurements were used for experimental comparison of the storage materials in terms of reactive temperature range, reaction enthalpy and cycling stability over 100 cycles.

The binary oxide features fast reaction rates for the forward and reverse reaction as well as a beneficial decrement of the thermal hysteresis between the reduction and oxidation onset temperature as compared to manganese oxide. The specific reaction enthalpy amounts to ≈271 J/g $(Mn_{0.75}Fe_{0.25})_2O_3$, corresponding to about 273 kJ/mol O_2, which is higher than the value measured for the reduction of Mn_2O_3 (≈ 201 J/g). While the Mn_2O_3/Mn_3O_4 transition suffers from a lack of cycling stability, showing a degradation of the oxidation rate over consecutive cycles, the $(Mn_{0.75}Fe_{0.25})_2O_3/(Mn_{0.75}Fe_{0.25})_3O_4$ transformation revealed a significantly improved cycling stability behavior. Besides the criteria evaluated experimentally, the high availability and low cost of the nonhazardous, technical grade raw materials Mn_3O_4 and Fe_2O_3 and therefore a facile, uncritical preparation and application of granular particles count to the key benefits of this storage material. Thereupon, the reaction of the redox couple $(Mn_{0.75}Fe_{0.25})_2O_3/(Mn_{0.75}Fe_{0.25})_3O_4$ was

characterized in detail with regard to thermodynamics, reaction kinetics as well as physical and thermophysical properties, to provide the process parameters essential for the controlled operation of a redox reaction based TCS reactor.

In this context, the corresponding pO_2-T correlations for the reduction and oxidation step have been determined by means of thermoanalytical measurements for a pO_2 range between ≈5 kPa and ≈70 kPa. Those correlations specify technically relevant temperature threshold conditions for the actually prevailing reactivity range of the storage material (reduction at $T >$ ≈982 °C and oxidation at $T <$ ≈920 °C in atmospheric air). Owing to an inhibition of the oxidation reaction in the temperature range nearby equilibrium, which can be attributed partly to thermodynamic but essentially to kinetic limitations, the oxidation step constitutes the critical reaction step within the redox cycle.

Dynamic and isothermal thermogravimetric measurements were conducted to better understand the forward and reverse reaction step, and to derive mathematical models for the effective reaction rate in the relevant temperature- and pO_2-range of each reaction step, respectively. The models describe the dependence of the reaction rate on the temperature, the kinetic model representing the reaction mechanism and on the prevalent pO_2 as well as corresponding partial pressure $pO_{2,eq}$ in equilibrium state. Furthermore, all necessary physical and thermophysical parameters for future modeling and numerical simulation of a TCS reactor have either been experimentally determined or compiled from literature references. With a loose bed of granular $(Mn_{0.75}Fe_{0.25})_2O_3$ studied in this work an energetic storage density of 102 kWh/m^3 is achieved (total packed bed porosity of 73.6 %).

Systematic experimental examinations of the storage charging and discharging process were performed by means of a granular packed bed in a lab-scale tube reactor specifically designed for the described studies. The TCS reactor – filled with ≈470 g of technical grade $(Mn_{0.75}Fe_{0.25})_2O_3$ – exhibits a total chemical storage capacity of 128 kJ (0.0355 kWh). Observed temperature plateaus proved to be highly dependent on the thermodynamic properties as well as kinetic behavior of the redox reaction. Hence, those temperature plateaus reflected the occurrence of the thermal hysteresis, which has been expected according to the pO_2-T correlations for the reduction and oxidation onset determined by thermal analysis. The stabilization of the bed temperatures in the course of the proceeding reaction allows for an extended charging/discharging period in comparison to established HT-TES systems solely based on sensible thermal energy storage. Thereby, it could be verified that the heat of reaction can be exploited in addition to the sensible heat of the storage material, enhancing the overall storage capacity. Overall, the principle of an open-loop storage operation with direct contact heat transfer using air as HTF was demonstrated on lab-scale.

Two different modes of storage operation have been applied in this work to analyze different operating parameters: A temperature driven operation mode for thermal charging and discharging in air, increasing and decreasing the temperature of the packed bed at a defined air flow rate, respectively; and a pressure driven operation mode with constant boundary conditions at the inlet

of the storage reactor to study different influencing factors on thermal discharging, inducing the oxidation reaction by a sudden raise of the oxygen partial pressure (switch from atmosphere at reduced oxygen partial pressure to ambient air).

Parametric studies served to identify the influence of essential operating parameters on the reactor performance, varying the HTF mass flow rate in the range from 5 NL/min to 15 NL/min air (in charging and discharging step) as well as the gas inlet and initial bed temperature ranging from 800 °C to 875 °C at an air flow rate of 10 NL/min (in discharging step). On the one hand, an increase of the heat capacity rate of the HTF air accelerated the charging and discharging progress, which trend accentuated the limitation by heat transport (rate of heat input/dissipation) under the applied operating conditions, respectively. On the other hand, the application of a low heat capacity rate of the HTF air (air flow rate of 5 NL/min at experiment with constant gas inlet and initial bed temperature of 825 °C) revealed the significant peculiarity of this storage concept: The direct coupling of the HTF and the source of O_2 for the reaction has a direct impact on the prevailing O_2 concentration and therefore O_2 partial pressure in the reactor, influencing the O_2 availability (mass transport) and therefore the reaction rates along with the reaction temperatures which can be achieved. Thus, the discharging performance at low HTF mass flow rates is dominated by a reduced particle reaction rate due to a shortened availability of O_2, accompanied by diminished heat transfer and heat transport capabilities. Those interrelationships need to be taken into account in the future design engineering and eventually operation of TCS reactors.

A cycling test based on a reference cycle revealed no degradation of the packed bed reactivity over the course of 17 redox cycles. On a microstructural level, though, sintering phenomena caused an alteration of the microstructure, which in turn led to an enhanced agglomeration of granules and gave indications of a lack of mechanical particle stability.

Based on the comprehensive experimental findings obtained in this work several conclusions have been drawn, which favor three novel application options for reversible redox reactions of metal oxides:

(1) The installation of a reactive metal oxide topping in established industrial scale regenerator-type storage systems for HT operations would offer the benefit to enhance the gravimetric energy storage density by exploiting both the sensible thermal energy of the inert storage material (e.g., ceramics or natural stones) in the lower LT cooling section and the reaction enthalpy of the reversible redox reaction in the upper HT-TCS section, which facilitates a stabilization of the bed temperatures and therefore HTF outflow temperature to a certain extent during discharging of the storage unit.

(2) To overcome inherent drawbacks of a stationary regenerator-type storage concept with air as HTF, such as a limited attainable gravimetric energy storage density and the necessity of high volumetric HTF flow rates at high temperatures to charge the storage and drive the reduction reaction, metal oxides can be employed simultaneously as storage material (sensible/thermochemical) and HTM in the field of CSP, directly heating and reducing metal oxide particles by means of direct solar radiation in a novel generation of particle receivers/reactors. Subsequent discharging can be

conducted on demand by means of a moving bed reactor operated in the form of a counter-current flow of metal oxide particles and air as second HTM, which reactor concept enables the material to react completely. Moreover, the approach allows a decoupling of thermal power input/output and storage capacity.

(3) Metal oxides could also be applied as a coating for temperature sensitive metallic component parts subjected to fluctuating operating temperatures of the medium passing through or by the parts. The oxide coating, which needs to be exposed to an O_2 containing atmosphere (e.g., ambient air) for regeneration of the protective effect (via oxidation), functions as a thermochemical protection layer to stabilize the metal temperatures in case of frequent temperature changes by means of the redox reaction taking place, and therefore prevents thermal fatigue. Temperature stabilization of metallic component parts constitutes a specific case of application for which the presence of a temperature hysteresis between the reduction and oxidation onset can be explicitly taken advantage of.

Future studies need to focus on further modifications of promising metal oxide storage materials, to overcome the drawbacks disclosed for granular Mn-Fe oxide in this work, such as the presence of a thermal hysteresis, occurrence of a particle “swelling effect” in the course of 100 redox cycles, as well as the emergence of particle agglomeration and the lack of mechanical stability over the course of progressive cycling in a packed bed. For example, this could be achieved by means of combining metal oxides with inert compounds to stabilize the microstructure, attenuate particle agglomeration and improve the mechanical stability, which characteristics are essential for the potentially required particle movement in future reactor concepts. From a process engineering point of view the achievement of long-term cyclability along with mechanical stability of metal oxide granules is crucial for the acceptance and large-scale implementation of redox reaction based TCS. On this account, the durability of advanced storage materials needs to be demonstrated under technical scale operating conditions to facilitate the breakthrough of this storage technology.

Overall, the fundamental results on the redox characteristics of the reference material Mn-Fe oxide and its TCS performance on an appropriate scale in the present work lay the foundation for continuing development of metal oxide storage materials, the design of scaled-up continuous reactor concepts (e.g., combined particle receiver/charging reactor, moving bed discharging reactor, etc.), overall system integration concepts as well as diverse application options to further drive this redox reaction based storage technology forward.

A Appendix: Thermodynamic Calculation

Kirchhoff's Law The standard reaction enthalpy $\Delta_R H^{\ominus}$ and reaction entropy $\Delta_R S^{\ominus}$ are temperature dependent. Thereby, a change in reaction enthalpy reflects the difference in the enthalpy changes of the products and educts when increasing the temperature [16].

Standard enthalpies and entropies of reaction at increased temperature can be calculated from heat capacities and the reaction enthalpy at some other temperature. This approach is more accurate than the direct measurement of the reaction enthalpy at a certain temperature, given that sufficient thermodynamic data is available [16]. The standard reaction enthalpy and standard reaction entropy change from $\Delta_R H^{\ominus}(T_1)$ and $\Delta_R S^{\ominus}(T_1)$ to

$$\Delta_R H^{\ominus}(T_2) = \Delta_R H^{\ominus}(T_1) + \int_{T_1}^{T_2} \Delta_R C_p^{\ominus} \mathrm{d}T \tag{A.1}$$

and

$$\Delta_R S^{\ominus}(T_2) = \Delta_R S^{\ominus}(T_1) + \int_{T_1}^{T_2} \frac{\Delta_R C_p^{\ominus}}{T} \mathrm{d}T \tag{A.2}$$

where $\Delta_R C_p^{\ominus}$ represents the difference of the molar heat capacities between the products and educts under standard conditions [16], respectively, weighted by the stoichiometric coefficients of the chemical equation:

$$\Delta_R C_p^{\ominus} = \sum_{\mathrm{j\,products}} \nu_\mathrm{j} C_{p,\mathrm{m,j}}^{\ominus} - \sum_{\mathrm{i\,educts}} \nu_\mathrm{i} C_{p,\mathrm{m,i}}^{\ominus} \tag{A.3}$$

Although the temperature dependence of the individual molar heat capacities of the products and educts can be taken into account, the difference of the heat capacities $\Delta_R C_p$ generally varies only insignificantly over a reasonably limited temperature range. Thus, neglecting the temperature dependence can be considered as a practical approximation [16].

B Appendix: Storage Material Preparation and Characterization

B.1 Physical and Thermophysical Characterization Methods

Metal oxide material properties as well as packed bed properties are determined based on the following physical and thermophysical methods of analysis.

X-Ray Powder Diffractometry (XRD) is performed on a Bruker D8 Advance instrument using Cu-K$\alpha_{1,2}$ radiation to determine the crystalline phase composition of the examined metal oxides.

Scanning Electron Microscopy (SEM) images are taken with a Zeiss Ultra 55 scanning electron microscope in order to analyze the microstructure of the material. An acceleration voltage of 5.0 kV and working distances between 7.8 and 8.0 mm are used for secondary electron imaging.

X-Ray Fluorescence Spectroscopy (XRF) is applied to reveal the average elemental composition of the granules and thereby allows to accurately determine the cation ratio in the sample.

Helium Pycnometry (He Pycnometry): The true or absolute density of $(Mn_{0.75}Fe_{0.25})_2O_3$ is measured by means of a helium pycnometer (AccuPyc 1330) from Micromeritics.

Mercury Intrusion Porosimetry (Hg Porosimetry) is carried out using the instrument Auto Pore IV 9500 Series from Micromeritics to identify the total pore volume and the medium pore diameter of the granular material.

Image Analysis: The equivalent particle diameter $d_{\mathrm{p,pr}}$ and corresponding particle size distribution (PSD) are evaluated by means of an image analysis based on the open source image processing program ImageJ[1]. In the process two-dimensional particle images are recorded to determine the projected areas of the particles for further analyses.

Specific Heat Capacity measurements are performed with the STA instrument 449 *F3 Jupiter*® from NETZSCH Gerätebau GmbH, equipped with a platinum furnace and a TG-DSC sensor (Pt/Rh) specifically designed for c_p-determinations to reach a higher measurement accuracy.

[1] ImageJ 1.48 developed at the National Institutes of Health, USA.

B.2 Hazard Statements and Pictograms for Metal Oxides

Table B.1: Hazard statements and pictograms for metal oxides potentially applicable as TCS materials. The statements are part of the *Globally Harmonized System of Classification and Labeling of Chemicals* (GHS).

Co_3O_4 H317: May cause an allergic skin reaction. H351: Suspected of causing cancer. H410: Very toxic to aquatic life with long lasting effects. 	**CoO** H301: Toxic if swallowed. H330: Fatal if inhaled. H317: May cause an allergic skin reaction. H334: May cause allergy or asthma symptoms orbreathing difficulties if inhaled. H410: Very toxic to aquatic life with long lasting effects. 
CuO H302: Harmful if swallowed. H410: Very toxic to aquatic life with long lasting effects. 	**Cu_2O** H302: Harmful if swallowed. H332: Harmful if inhaled. H318: Causes serious eye damage. H410: Very toxic to aquatic life with long lasting effects. 
Mn_2O_3 H302: Harmful if swallowed. H332: Harmful if inhaled. H315: Causes skin irritation. H319: Causes serious eye irritation. H335: May cause respiratory irritation. 	**Mn_3O_4** H315: Causes skin irritation. H319: Causes serious eye irritation. H335: May cause respiratory irritation. 
Fe_2O_3 Not a dangerous substance according to GHS.	**Fe_3O_4** Not a dangerous substance according to GHS.

B.3 Thermal Analysis: Experimental Procedure and Data Analysis

B.3.1 Determination of the Oxygen Partial Pressure

The oxygen partial pressure, applied in the thermodynamic and kinetic investigations throughout this work, is calculated as follows:

$$pO_2 = y_{O_2} \cdot p_{\text{ambient}} \tag{B.1}$$

The adjusted oxygen volume fraction within the scope of the conducted TG-DSC measurements is equal to the molar fraction of oxygen (y_{O_2}) in the gas flow, assuming ideal gas law conditions.

B.3.2 Determination of Extrapolated Peak Onset Temperatures

As the peak maximum of the DSC signal occurs to coincide with the inflection point of the mass change (see Fig. B.1), extrapolated peak onset temperatures determined by means of the DSC signal are per se closer to the beginning of the reaction than extrapolated onset temperatures of the corresponding TG signal, thus constituting a better indicator for the beginning of the respective redox reaction. The extrapolated peak onset temperature of the DSC peak is determined for the reduction and oxidation reaction based on the common procedure, using the intersection of the extrapolated initial baseline and the tangent through the inflection point of the linear part of the ascending (reduction step) or descending (oxidation step) DSC peak [34], respectively. This data analysis is conducted with the aid of the software *Proteus*® from NETZSCH.

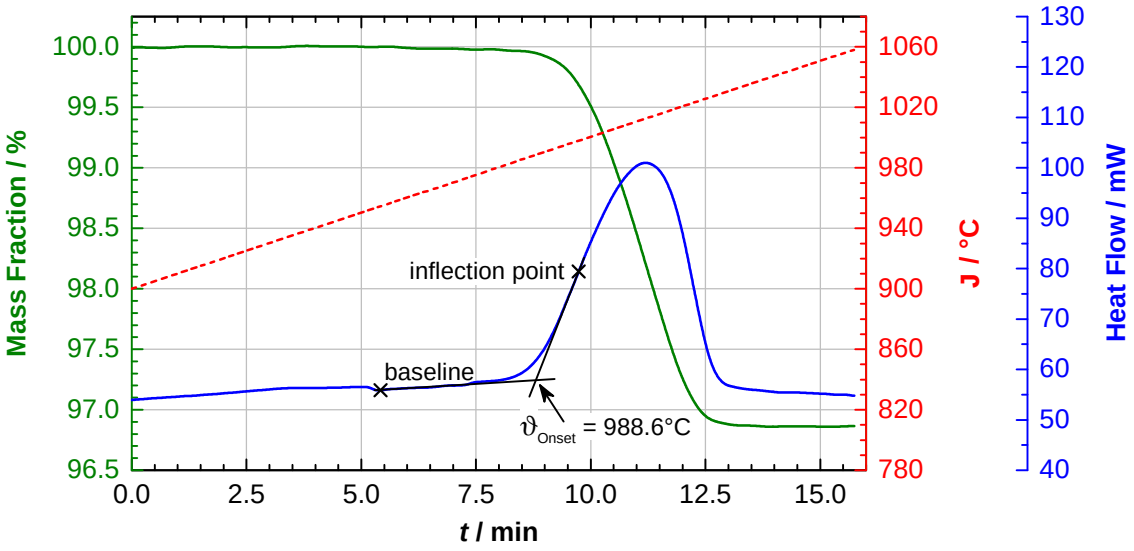

Figure B.1: Exemplification of the extrapolated peak onset temperature determination based on the reduction of Mn-Fe oxide (measurement conditions: $\beta = 10$ K/min, $pO_2 = 19.9$ kPa).

B.3.3 Determination of the Relative Theoretical Mass Change

The relative theoretical mass loss $\Delta m_{\mathrm{theo,Red}}$ (in %) for the reduction step of the stoichiometric redox reactions Mn_2O_3/Mn_3O_4 and $(Mn_{0.75}Fe_{0.25})_2O_3/(Mn_{0.75}Fe_{0.25})_3O_4$ can be calculated in a general way based on the stoichiometric coefficients (ν_{ox} and ν_{red}, see Eqs. (3.4) and (3.5)) and respective molecular weights (M_{ox} and M_{red}) $Mn_2O_3 = 157.87$ g/mol, $Mn_3O_4 = 228.81$ g/mol, $(Mn_{0.75}Fe_{0.25})_2O_3 = 158.33$ g/mol, $(Mn_{0.75}Fe_{0.25})_3O_4 = 229.49$ g/mol:

$$\Delta m_{\mathrm{theo,Red}} = 100 \left(1 - \frac{\nu_{\mathrm{red}} M_{\mathrm{red}}}{\nu_{\mathrm{ox}} M_{\mathrm{ox}}} \right) \tag{B.2}$$

The relative theoretical mass gain $\Delta m_{\mathrm{theo,Ox}}$ (in %) in the course of the oxidation step can be determined likewise:

$$\Delta m_{\mathrm{theo,Ox}} = 100 \left(\frac{\nu_{\mathrm{ox}} M_{\mathrm{ox}}}{\nu_{\mathrm{red}} M_{\mathrm{red}}} - 1 \right) \tag{B.3}$$

B.3.4 Temperature Programs for TG-DSC Measurements

Table B.2: Temperature programs for reference and measuring cycles of metal oxides examined in Section 3.3 and Appendix B.6.

	Reference Cycle			Measuring Cycle	
Metal Oxide	**Drying**	**Heating**	**Cooling**	**Heating**	**Cooling**
Manganese oxide	10 K/min → 200 °C, 30 min	10 K/min → 1000 °C	10 K/min → 550 °C, 30 min	10 K/min → 1000 °C	10 K/min → 550 °C
Manganese-iron oxide	10 K/min → 200 °C, 30 min	10 K/min → 1060 °C	10 K/min → 750 °C, 30 min	10 K/min → 1060 °C	10 K/min → 750 °C

B.4 Phase Diagram of Manganese-Iron Oxide in Air

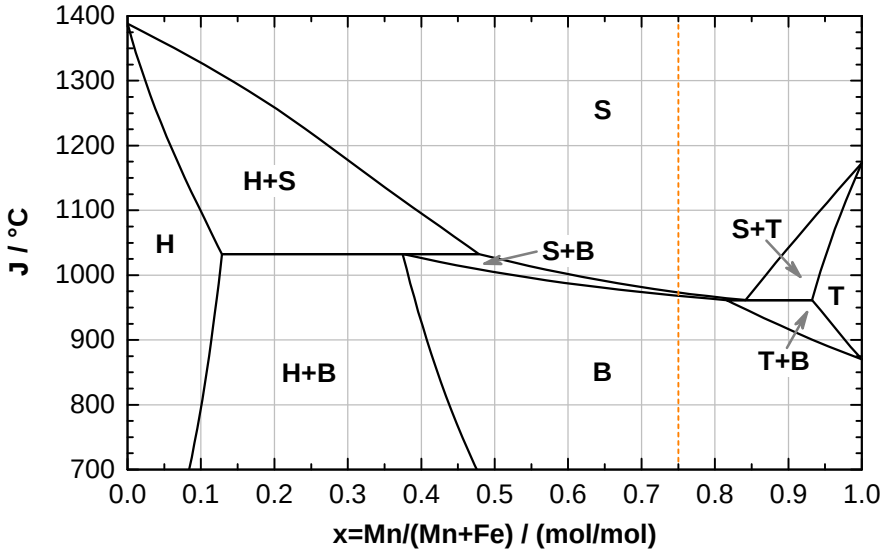

Figure B.2: Binary phase diagram of Mn-Fe oxide calculated with FactSage™ for a fixed oxygen partial pressure of 0.2095 bar; the different phases are denoted by the following symbols: "H" = hematite $(Fe,Mn)_2O_3$, "S" = spinel $(Mn,Fe)_3O_4$, "B" = bixbyite $(Mn,Fe)_2O_3$, "T" = tetragonal spinel $(Mn,Fe)_3O_4$ (hausmannite), and two-phase mixtures of those; the composition with a Fe/Mn molar ratio of 1:3 investigated in this work is highlighted by the orange dashed line.

B.5 $(Mn_{0.75}Fe_{0.25})_2O_3$ Granules – Preparation, XRF spectroscopy & TGA of Varied Sizes

Preparation Procedure For the preparation of the Mn-Fe oxide granules technical grade powders of Fe_2O_3 (CAS No. 1309-37-1, iron(III) oxide, 98 % metals basis from Alfa Aesar) and Mn_3O_4 (TRIMANOX® electronic grade, supplied by Chemalloy) are mixed with a Fe/Mn molar ratio of 1:3, which corresponds to a Fe_2O_3/Mn_3O_4 mass ratio of 25.9:74.1. An Eirich intensive mixer with a capacity of 5 L (Fig. B.3, left) is used for the granulation of the TCS material, a special procedure based on the principle of intensive mixing by rotation of an inclined mixing pan and application of a rotating micro-granulator mixing tool (Fig. B.3, middle).

The powders are combined in the dry state and immediately treated in the Eirich mixer. A total mass fraction of ≈18 % deionized water is added to the dry components to obtain an optimal granulated material in a narrow size range. This is done by adding a mass fraction of ≈12.5 % deionized water at the start and additional ≈1.25 % every 5 min. The rotating speed of the pan, which is an important parameter to receive relatively spherical granules, has been set to 42 rpm. The rotor speed of the mixing tool influencing the granule size (along with the residence time) has been set to 283 rpm over a period of 5 min after each addition of water.

The strength of the granulated material after 1 h of drying at 105 °C is high enough for sieving.

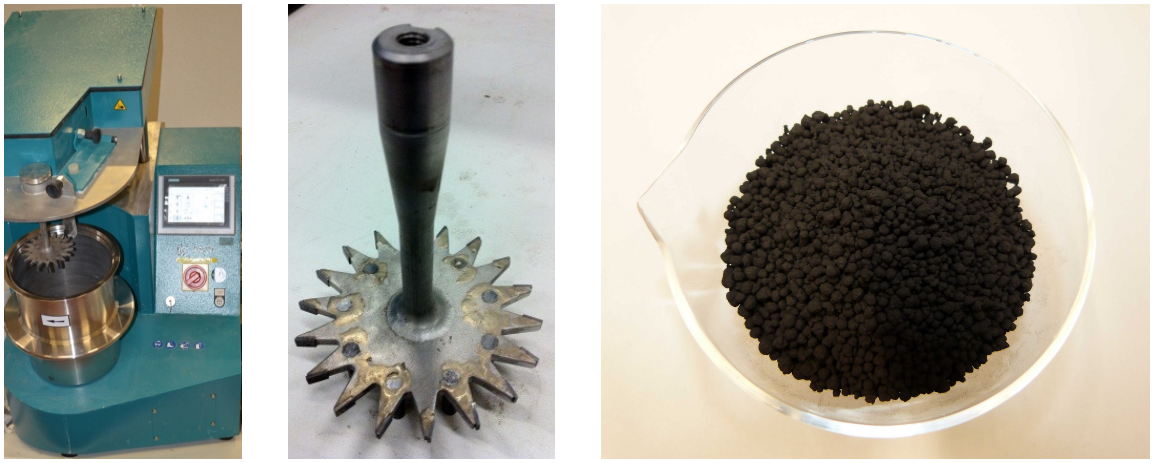

Figure B.3: Eirich Mixer (left) and micro-granulator rotor type (middle) used for the build-up granulation of the storage material (material preparation has been performed by VITO in Mol, Belgium); prepared Mn-Fe oxide granulate after heat treatment in air (right).

Taking the estimated shrinkage of the granules upon heat treatment into account, the mixed material is at first sieved in the dry state to separate a particle size fraction from 1.15 mm to 3.15 mm prior to calcination. This fraction of green bodies is placed in aluminum oxide crucibles and calcined for 4 h at 1025 °C and 4 h at 1050 °C in air, yielding the targeted combined Mn-Fe oxide (solid state reaction) in the form of stable granules, which oxidized to $(Mn_{0.75}Fe_{0.25})_2O_3$ during cooling. Although particle sizes in the order of 1 mm to 3 mm were originally envisaged, a particle size range of approximately 1.0 mm to 3.5 mm has been obtained for experimental studies in this work (Fig. B.3, right). The resulting particle size distribution calculated by means of image analysis is presented in Fig. 3.19a (see Section 3.4.4).

Reactivity of Different Granule Sizes Figure B.4 illustrates a comparison of the oxidation reactivity of three samples with different granule sizes (one, two and eight granules placed in the crucible, having a similar total sample weight of ≈30 mg) at an oxidation isotherm of 855.8 °C in air, conducted by means of thermogravimetric analysis, respectively.

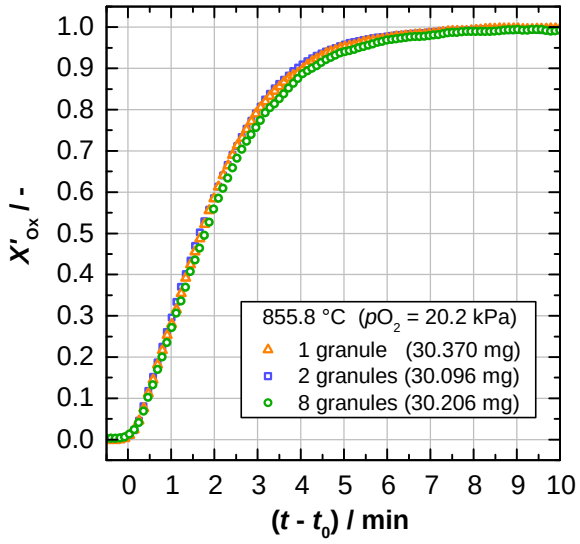

Figure B.4: Comparison of different $(Mn_{0.75}Fe_{0.25})_3O_4$ granule sizes regarding their oxidation reactivity at an isotherm of 855.8 °C in air (TGA).

X-Ray Fluorescence Analysis A chemical analysis performed by means of X-ray fluorescence spectroscopy revealed the total average elemental composition of the Mn-Fe oxide granules used throughout this thesis, yielding the mass fractions and molar fractions shown in Table B.3. Thus, a Fe/Mn molar ratio of 1:3 could be verified.

Table B.3: Chemical analysis of $(Mn_{0.75}Fe_{0.25})_2O_3$ granulate composition by means of XRF spectroscopy, $(Mn_{0.75}Fe_{0.25})_2O_3$ granulate selected for characterization in this work. The XRF measurement was carried out by the Research Institute for Inorganic Materials - Glass/Ceramics - GmbH (FGK) in Höhr-Grenzhausen, Germany.

Element	Mass Fraction / %	Molar Fraction / %
Mn	52.0	30.13
Fe	17.7	10.09
Al	0.31	0.37
Si	0.32	0.36
Mg	0.05	0.07
Ca	0.04	0.03
Na	< 0.02	< 0.03
K	< 0.02	< 0.02
Ti	< 0.02	< 0.01
Cr	< 0.02	< 0.01
O	29.6	58.89
Sum	100.1	100.01

B.6 Characterization of Technical Grade Mn_2O_3/Mn_3O_4

B.6.1 X-Ray Powder Diffractogram of Mn_2O_3

The powder diffractogram of the Mn_2O_3 raw material in Fig. B.5 shows a cubic bixbyite structure (β-Mn_2O_3), crystallizing in the space group $Ia\bar{3}$ with a lattice parameter a = 9.4091.

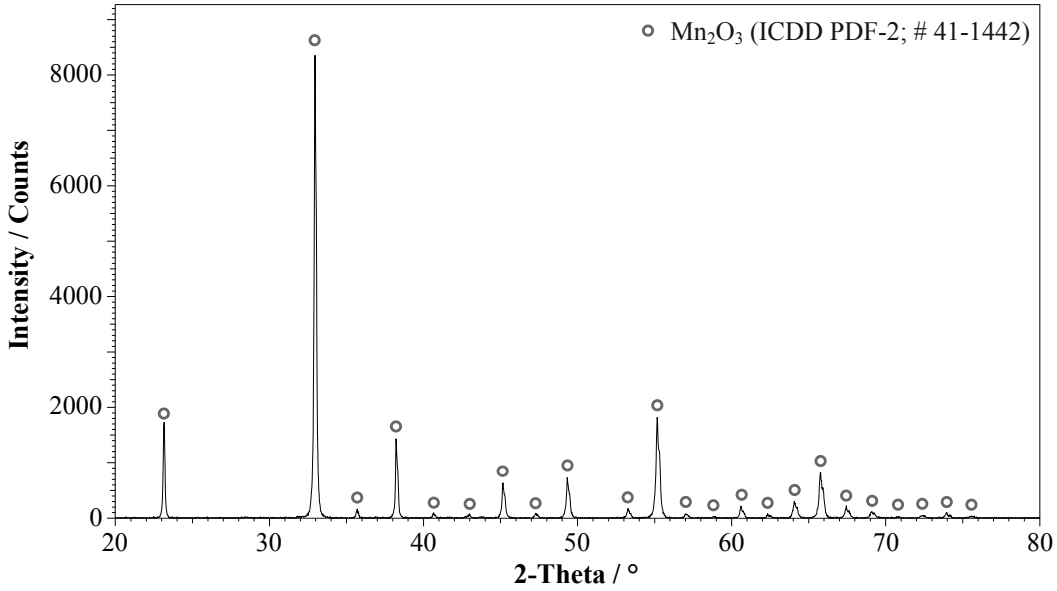

Figure B.5: X-ray diffraction pattern of manganese oxide raw material in the oxidized state (XRD analysis performed by Institute of Materials Research, DLR).

B.6.2 Dynamic Redox Cycle and Specific Reaction Enthalpy

A standard redox cycle of pure manganese oxide in air is shown in Fig. B.6. The observed mass change over the course of the redox reaction (weight loss of 3.36 %, calculated according to Eq. (3.1)) complies with the stoichiometrically expected value of 3.38 %. The drift of the baseline of the DSC signal can be attributed to the measurement conditions, as crucibles have been utilized without a covering lid.

The cycle accentuates the major drawbacks of the redox couple Mn_2O_3/Mn_3O_4. Own preliminary studies as well as literature data have shown, that pure manganese oxide may only be exposed to a maximum restrictive temperature of 1000 °C, since increased material sintering phenomena are critical for the re-oxidation of Mn_3O_4 [155, 40]. While the onset of the reduction during the heating phase is determined at ≈941.4 °C, which is consistent with results in the literature [29, 5, 40], the onset of the oxidation during the cooling phase is identified at merely ≈772.7 °C. This onset temperature highly depends on the history of the material, as synthesis conditions and heat treatment affect the initial particle size and morphology of the raw material, which in turn are reported to affect the re-oxidation reactivity decisively [39, 15]. Moreover, the re-oxidation rate turns out to be comparatively slow [39, 29, 5], turning the oxidation into the limiting step of the redox process.

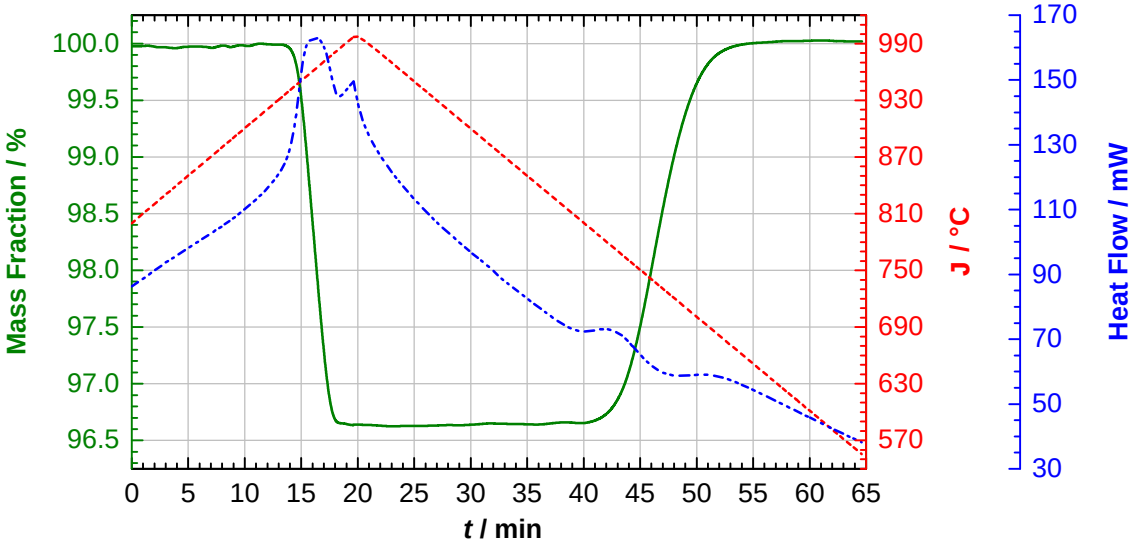

Figure B.6: Excerpt of a dynamic redox cycle of manganese oxide, applying a heating rate of 10 K/min up to 1000 °C and a cooling rate of 10 K/min down to 550 °C in air (TG-DSC measurement).

A reaction time of 17.7 min has been noted down to reach complete conversion (reaction time of the reduction step amounts to 6.2 min).

As the reduction and oxidation step set in at entirely different temperature levels, the presence of a large thermal hysteresis becomes apparent, decoupling the two redox reactions. Generally, a pronounced hysteresis is unfavorable for a TCS system, where it is crucial to release thermal energy at a temperature level as high as possible. This characteristic behavior of materials – based on manganese oxide in particular – eventually implicates a loss of the charge-discharge energy efficiency [40]. The DSC measurement shown in Fig. B.7 reveals a pronounced peak due to the reduction from Mn_2O_3 to Mn_3O_4 (2^{nd} cycle analyzed).

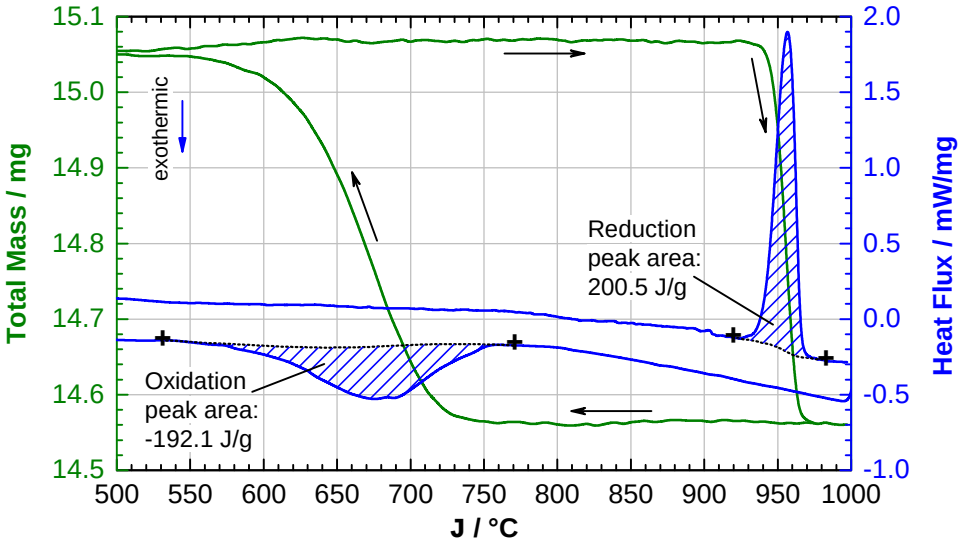

Figure B.7: DSC measurement (excerpt): Evaluation of the specific reaction enthalpy of the Mn_2O_3/Mn_3O_4 transformation in air (20 mL/min O_2, 80 mL/min N_2), applying a heating and cooling rate of 10 K/min (crucible covered with a pierced lid); 2^{nd} cycle taken for analysis of Mn_2O_3 reduction, 1^{st} cycle taken for analysis of Mn_3O_4 oxidation owing to the decline of oxidation reactivity with progressive cycling in this case.

Integration of the peak area for the determination of the specific reaction enthalpy yields a value of ≈200.5 J/g. This enthalpy of reduction is in accordance with values reported in the literature, ranging between 184 J/g [40] and 231 J/g [29]. Owing to a limited gas transport through the pinhole of the pierced lid the re-oxidation of Mn_3O_4 has not been completed over the course of the cooling phase, giving an enthalpy of oxidation of only –192.1 J/g (1st cycle analyzed). Complete re-oxidation has eventually been reached during the subsequent heating phase of the 2nd cycle.

Table B.4 summarizes the evaluated data for the redox transition Mn_2O_3/Mn_3O_4 of pure manganese oxide.

Table B.4: Thermal analysis of the redox couple Mn_2O_3/Mn_3O_4: Onset temperatures (determined on the basis of the DSC signal), reaction times, mass changes (assessed by TG) and specific reaction enthalpies (assessed by DSC) of the reduction and oxidation step.

Crucible	Reduction						Oxidation						Hyst.
	ϑ_{Onset} °C	t_{oo} min	t_{rxn} min	Δm_{exp} %	Δm_{theo} %	Δh J/g	ϑ_{Onset} °C	t_{oo} min	t_{rxn} min	Δm_{exp} %	Δm_{theo} %	Δh J/g	ΔT K
w/o lid [a]	941.4	4.1	6.2	–3.36	–3.38	-	772.7	9.4	17.7	+3.50	+3.49	-	168.7
w/ lid [b]	941.1	-	-	-	-	201.1	740.4	-	-	-	-	–191.8[c]	200.7

[a] Weighted sample of ≈30 mg Mn_2O_3 for the measurement without lid.

[b] Weighted sample of ≈15 mg Mn_2O_3 for the measurement with covering lid (determination of the specific reaction enthalpy Δh by DSC).

[c] Incomplete re-oxidation of Mn_3O_4 over the course of the cooling phase, re-oxidation was completed during the subsequent heating phase instead (see Fig. B.7).

The onset temperatures and specific reaction enthalpies determined by means of the DSC measurements using pierced lids for the sample and reference crucible, listed in Table B.4, represent the average of two individual measurements, respectively. The 2nd cycle has been considered for the data evaluation of the reduction step. However, the oxidation step has been evaluated based on the 1st cycle, owing to a decline in oxidation reactivity with further cycles (see also Fig. 3.6b). A significant shift of the onset temperature of the oxidation step can be observed for the measurements using pierced lids compared to measurements using open crucibles, which can primarily be attributed to an oxygen transport resistance evoked by using pierced lids for the caloric measurements.

B.6.3 Oxidation of Pure Mn_3O_4 at Different Isothermal Temperatures

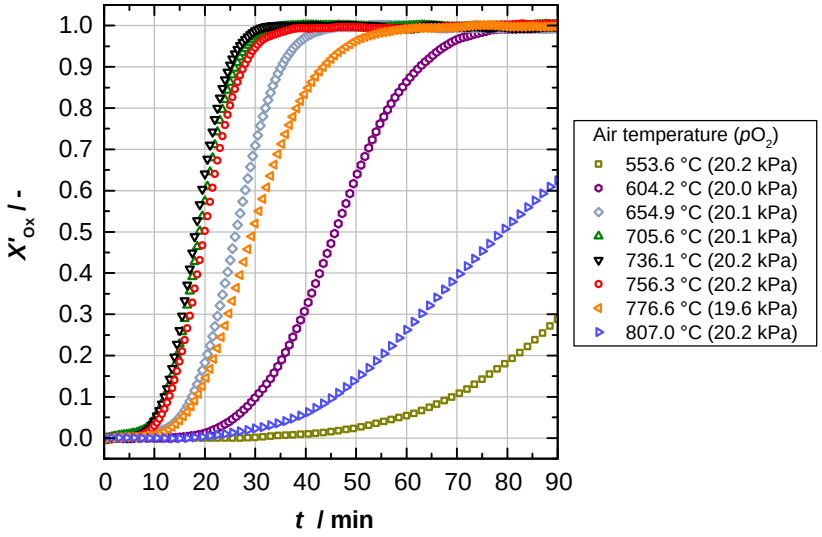

Figure B.8: Oxidation of Mn_3O_4 at different isothermal temperatures in air (TGA): Preceding reduction step has been performed at 10 K/min up to 1000 °C in air, followed by cooling process at 10 K/min under N_2; oxidation step has been initiated by switching from N_2 to air atmosphere (2^{nd} cycles are shown, respectively).

B.6.4 Scanning Electron Micrographs of Manganese Oxide

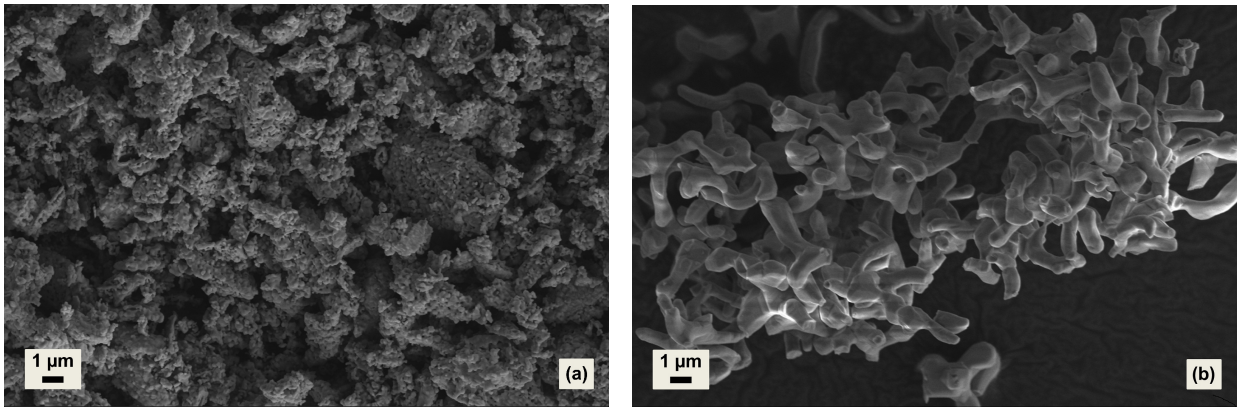

Figure B.9: Scanning electron micrographs: Manganese oxide raw material (a) and material after 100 redox cycles in air conducted by means of TGA (b); conditions of SEM measurements: magnification 10.000 x, working distances of 8.0 mm (a) and 7.9 mm (b), acceleration voltage of 5.0 kV; SEM images recorded by Institute of Materials Research, DLR.

B.7 Extrapolated Onset Temperatures of $(Mn_{0.75}Fe_{0.25})_2O_3/(Mn_{0.75}Fe_{0.25})_3O_4$ Transition

Table B.5: Onset temperature values obtained by extrapolation of the experimentally determined peak onset temperatures for a number of temperature ramps to a heating and cooling rate of 0 K/min at different average prevalent oxygen partial pressures, respectively; in this work the listed onset temperatures of the redox reaction were defined as technically relevant temperature threshold values for the $(Mn_{0.75}Fe_{0.25})_2O_3$ reduction and $(Mn_{0.75}Fe_{0.25})_3O_4$ oxidation onset (see Section 3.4.1).

	Reduction: B → S [a]	**Oxidation: S → B**	
pO_2 / kPa	$\vartheta_{Onset,DSC}$ / °C	$\vartheta_{Onset,DSC}$ / °C	$\Delta T_{Hysteresis}$ / K
5.1	925.8	848.4	77.4
10.1	949.6	883.5	66.1
20.4	976.5	919.3	57.2
40.4	1010.9	956.4	54.5
71.1	1036.9	985.3	51.6

[a] with "B" = bixbyite $(Mn,Fe)_2O_3$ and "S" = spinel $(Mn,Fe)_3O_4$

B.8 Time-Temperature-Transformation Diagram for $(Mn_{0.75}Fe_{0.25})_3O_4$ Oxidation

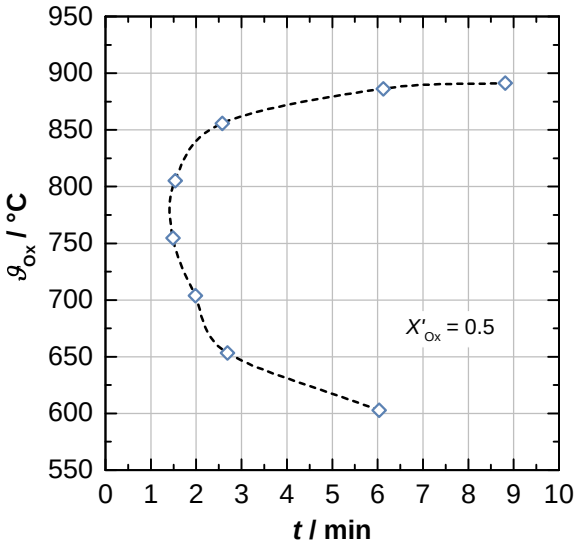

Figure B.10: Time-Temperature-Transformation (TTT) diagram of isothermal $(Mn_{0.75}Fe_{0.25})_3O_4$ oxidation at different temperatures in air ($X'_{Ox} = 0.5$).

B.9 Kinetic Models used in Kinetic Modeling of Gas-Solid Reactions

Table B.6: Selection of common kinetic models (reaction mechanisms) typically applied in kinetic modeling of gas-solid reactions: Differential functions $f(X)$ and integral functions $g(X)$ [63, 145, 33].

Code	Reaction Model	$f(X)$ $= 1/k(T) \cdot 1/[h(p,p_{eq}(T))] \cdot dX/dt$	$g(X)$ $= k(T) \cdot h(p,p_{eq}(T)) \cdot t$
	Accelerating models		
P2	Power law	$2X^{1/2}$	$X^{1/2}$
P3	Power law	$3X^{2/3}$	$X^{1/3}$
P4	Power law	$4X^{3/4}$	$X^{1/4}$
Pn	Power law	$nX^{(n-1)/n}$	$X^{1/n}$
E1	Exponential law	X	$\ln X$
	Sigmoidal models		
A2	Avrami-Erofeev	$2(1-X)[-\ln(1-X)]^{1/2}$	$[-\ln(1-X)]^{1/2}$
A3	Avrami-Erofeev	$3(1-X)[-\ln(1-X)]^{2/3}$	$[-\ln(1-X)]^{1/3}$
A4	Avrami-Erofeev	$4(1-X)[-\ln(1-X)]^{3/4}$	$[-\ln(1-X)]^{1/4}$
An	Avrami-Erofeev	$n(1-X)[-\ln(1-X)]^{(n-1)/n}$	$[-\ln(1-X)]^{1/n}$
B1	Prout-Tompkins	$X(1-X)$	$\ln[X/(1-X)]$
	Decelerating models		
	Geometrical models		
R2	Contracting area	$2(1-X)^{1/2}$	$1-(1-X)^{1/2}$
R3	Contracting volume	$3(1-X)^{2/3}$	$1-(1-X)^{1/3}$
	Diffusion models		
D1	1D diffusion	$1/(2X)$	X^2
D2	2D diffusion	$[-\ln(1-X)]^{-1}$	$(1-X)\ln(1-X)+X$
D3	3D diffusion (Jander equation)	$3/2(1-X)^{2/3}[1-(1-X)^{1/3}]^{-1}$	$[1-(1-X)^{1/3}]^2$
D4	Ginstling-Brounshtein equation	$3/2[(1-X)^{-1/3}-1]^{-1}$	$1-(2X/3)-(1-X)^{2/3}$
	"Order of reaction" models		
F0	zero order	1	X
F1	first order	$1-X$	$-\ln(1-X)$
F2	second order	$(1-X)^2$	$[1/(1-X)]-1$
F3	third order	$(1-X)^3$	$1/2[(1/(1-X)^2)-1]$
Fn	n-th order	$(1-X)^n$	$1/(n-1)[(1/(1-X)^{n-1})-1]$
	Empirical models		
Bn	Extended Prout-Tompkins [33]	$X^m(1-X)^n$	
Sn	Šesták-Berggren [33]	$X^m(1-X)^n[-\ln(1-X)]^p$	
Rn	Extended geometrical model	$n(1-X)^{(n-1)/n}$	$1-(1-X)^{1/n}$

C Appendix: Lab-Scale Test Rig and Experiments

C.1 Overview of Conducted Measurements in Lab-Scale Storage Reactor

Table C.1: Measuring plan for thermal charging step (reduction) and discharging step (oxidation) both performed in air atmosphere.

Cycle [a] No.	$\dot{V}_{Air}$ / NL/min	Reduction $\vartheta_{g,in} = \vartheta_{furnace}$ / °C	Oxidation Initiation	Oxidation $\vartheta_{g,in} = \vartheta_{furnace}$ / °C
(1)	10	940 → 1040	2 % O_2 → Air	$\vartheta_0 = \vartheta_{g,in} = 850$
2	10	940 → 1040	2 % O_2 → Air	$\vartheta_0 = \vartheta_{g,in} = 850$
3	10	940 → 1040	2 % O_2 → Air	$\vartheta_0 = \vartheta_{g,in} = 825$
4	10	940 → 1040	1 % O_2 → Air	$\vartheta_0 = \vartheta_{g,in} = 800$
5	10	940 → 1040	2 % O_2 → Air	$\vartheta_0 = \vartheta_{g,in} = 875$
6	10	940 → 1040	2 % O_2 → Air	$\vartheta_0 = \vartheta_{g,in} = 850$
7	15	940 → 1040	2 % O_2 → Air	$\vartheta_0 = \vartheta_{g,in} = 825$
8	5	940 → 1040	2 % O_2 → Air	$\vartheta_0 = \vartheta_{g,in} = 825$
9	10	940 → 1040	2 % O_2 → Air	$\vartheta_0 = \vartheta_{g,in} = 850$
(10)	10	940 → 1040	-	–5.0 K/min: 1040 → 400 [b]
11	10	940 → 1040	-	–5.0 K/min: 1040 → 400
12	10	940 → 1040	-	–3.5 K/min: 1040 → 400
13	5	940 → 1040	-	–3.5 K/min: 1040 → 400
14	15	940 → 1040	-	–3.5 K/min: 1040 → 400
(15)	10	940 → 1040	-	–2.0 K/min: 1040 → 400
(16)	10	940 → 1040	-	–2.0 K/min: 1040 → 400
17	10	940 → 1040	2 % O_2 → Air	$\vartheta_0 = \vartheta_{g,in} = 850$

[a] Cycles in brackets are not displayed and discussed in this thesis.

[b] Tube furnace turned off during cooling process.

C.2 Calculation of Reaction Conversion

The measured oxygen concentration downstream the gas cooler is used for the calculation of the molar rate of O_2 released and taken up in the process of the reaction, respectively. Moreover, the

reaction progress and the overall conversion of the reaction can be determined.

Table C.2 specifies the main components of dry air. The average molecular weights of N_2, O_2 and Ar follow from the standard atomic weights of the elements N, O and Ar [99].

Table C.2: Composition of air: Overview of main gas species.

Gas Species	Molecular Weight / kg/mol	Molar Fraction y_i / – [134]	Mass Fraction w_i / –
N_2	0.02801371	0.7812	0.75571
O_2	0.03199880	0.2096	0.23160
Ar	0.03994800	0.0092	0.01269

The molar fraction of CO_2 of 0.00038 in air can be readily neglected, as resulting deviations always remain smaller than the uncertainty of the equations used to calculate the material properties of air [134]. Furthermore, the same thought does also apply to the calculation of the reaction conversion, for which only the difference of the molar flow rate of O_2 between the reactor inlet and outlet is of interest anyway. Although the volume concentration of Ar in air amounts to roughly 1 % (see Table C.2), air is – in a simplified but legitimate manner – only regarded as a two-component system in this work, composed of O_2 (which concentration is experimentally measured) and N_2 (which concentration accounts for the base component of air). In this way the amount of N_2 comprises all remaining constituents of air (Ar, CO_2 and minor components), even though those are not considered individually on the basis of their thermophysical properties.

Assuming ideal gas law conditions the measured volume concentrations σ_i of the species in % are equal to the molar fractions y_i ($i = O_2$ or N_2):

$$\sigma_i = \frac{V_i}{V_{tot}} = \frac{V_i}{\sum V_i} = \frac{\frac{V_i}{V_m}}{\sum \frac{V_i}{V_m}} = \frac{n_i}{\sum n_i} = y_i \tag{C.1}$$

The molar flow rate of nitrogen $\dot{n}_{N_2}$ is constant throughout the experiments. According to *Dalton's law* the partial pressure of nitrogen p_{N_2} can be defined as the product of the molar fraction of nitrogen y_{N_2} and the total pressure p. y_{N_2} can be assessed based on the summation criterion $y_{N_2} + y_{O_2} = 1$, with y_{O_2} being the constant molar fraction of oxygen in air measured either before or after the process of the redox reaction. Under the assumption that each gas component obeys the ideal gas law, the molar flow rate of nitrogen can be calculated as follows:

$$\dot{n}_{N_2} = \dot{n}_{N_2,in} = \dot{n}_{N_2,out} = \frac{pN_2}{\mathbb{R} \cdot T} \cdot \dot{V}_{air,in} = y_{N_2} \cdot \frac{p}{\mathbb{R} \cdot T} \cdot \dot{V}_{air,in} = \left(1 - y_{O_2}\right) \cdot \frac{p}{\mathbb{R} \cdot T} \cdot \dot{V}_{air,in} \tag{C.2}$$

The adjusted overall air flow rate $\dot{V}_{air,in}$ at the inlet of the packed bed reactor is given in NL/min at standard conditions of $T = 273.15$ K and total pressure $p = 101325$ Pa (**S**tandard **T**emperature and **P**ressure = STP).

Different periods are used for the calculation of the O_2 baseline level in air (constant, average y_{O_2}), depending on the mode of operation:

- Temperature driven thermal charging: Average value over 10 min prior to the temperature increase of the gas inlet temperature (and tube furnace temperature)
- Temperature driven thermal discharging: Average value over 10 min prior to the onset of the oxygen uptake
- Thermal discharging at constant initial bed and gas inlet temperature $\vartheta_0 = \vartheta_{g,in}$: Average value over 20 min after the end of the oxygen uptake

Subsequently, according to the equation $\dot{n}_{O_2} = y_{O_2} \cdot \dot{n}_{tot} = y_{O_2}(\dot{n}_{N_2} + \dot{n}_{O_2})$ the molar flow rate of oxygen $\dot{n}_{O_2}$ at the reactor inlet and outlet can be obtained for each reading point (measuring interval of 1 s) based on the measured molar fraction of oxygen y_{O_2}, respectively (see also [104]):

$$\dot{n}_{O_2} = \dot{n}_{N_2} \cdot \frac{y_{O_2}}{1 - y_{O_2}} \tag{C.3}$$

Thereupon the molar reaction rate of the material in the reactor – expressed in terms of the rate of oxygen release or uptake $\dot{n}_{O_2,rxn}$ in mol/s – is determined by the absolute value of the difference between the molar O_2 flow rate at the reactor outlet $\dot{n}_{O_2,out}$ and the molar O_2 flow rate at the reactor inlet $\dot{n}_{O_2,in}$ for each measuring point. The latter denotes the baseline level of the molar O_2 flow rate according to the adjusted overall air flow rate.

$$\dot{n}_{O_2,rxn} = \left|\dot{n}_{O_2,out} - \dot{n}_{O_2,in}\right| \tag{C.4}$$

The resulting HTF mass flow rate at the outlet of the reactor, which is particularly important for the estimation of the heat capacity rate of the HTF and therefore the achievable thermal output (see Eq. (C.14)), can be determined by means of subtracting the mass flow rate of reacted oxygen from the mass flow rate of air at the reactor inlet:

$$\dot{m}_{g,out} = \dot{m}_{air,in} - \dot{m}_{O_2,rxn} = (\dot{V}_{air,in} \cdot \rho_{air}) - (\dot{n}_{O_2,rxn} \cdot M_{O_2}) \tag{C.5}$$

Integration of the molar rate of reacted oxygen $\dot{n}_{O_2,rxn}$ over the reaction time t_{rxn} yields the total amount of oxygen $n_{O_2,rxn}$, which was released during the reduction step and taken up during the oxidation step, respectively.

$$n_{O_2,rxn} = \int_{rxn\,begin}^{rxn\,end} \dot{n}_{O_2,rxn}\,\mathrm{d}t. \tag{C.6}$$

The determination of the beginning of the reaction, used for the summation of the molar O_2 flow rate, is dependent on the selected experimental procedure (dynamic mode or constant boundary conditions at the reactor inlet):

- In experiments applying a temperature change for the initiation of the reaction the onset of the oxygen release or uptake is defined at the point, where the oxygen concentration starts to deviate from the baseline level. Accordingly, the end of the oxygen release or uptake is defined at the point, where the current oxygen concentration returns to the baseline level.
- The procedure is different in the case of an oxidation, induced by a sudden increase of the pO_2 by means of an exchange of the gas atmosphere. There the beginning of the reaction is defined at the point, where the maximum O_2 concentration is reached (within the first 25 s after the gas switch) prior to the registered drop of concentration due to the oxygen uptake.

The lab-scale storage reactor has been charged with 471.2 g granular Mn-Fe oxide material in the oxidized state (see Section 4.1.3). According to the stoichiometry of the reaction Eq. (3.5) a weight loss of 3.368 % referred to $(Mn_{0.75}Fe_{0.25})_2O_3$ is expected in the reduction step. However, in the case of the Mn-Fe oxide – prepared with technical grade raw materials – the amount of oxygen converted in practice differs from the stoichiometric value (see Section 3.3). The average weight loss in the reduction step amounts to about 3.181 % throughout the thermogravimetric measurements carried out in this work. From this follows an average experimental mass gain of about 3.292 % compared to the stoichiometric value of 3.486 %. In the lab-scale reactor a weight loss of 3.181 % corresponds to an amount of 14.989 g ($m_{O_2,max}$) or 0.468420 mol O_2 ($n_{O_2,max} = m_{O_2,max}/M_{O_2}$), which can be maximally released and taken up by the metal oxide in the course of the redox cycle.

Referring the experimental amount of oxygen $n_{O_2,rxn}$ released in the reduction step to the maximum amount of oxygen $n_{O_2,max}$ which can be converted corresponding to a weight loss of 3.181 %, the degree of chemical conversion of the reduction step X_{Red} can be evaluated according to:

$$X_{Red} = \frac{n_{O_2,rxn,released}}{n_{O_2,max}} \tag{C.7}$$

The conversion of the reverse reaction step X_{Ox} can be calculated likewise, dividing the accumulative amount of oxygen taken up in the oxidation by $n_{O_2,max}$:

$$X_{Ox} = \frac{n_{O_2,rxn,uptake}}{n_{O_2,max}} \tag{C.8}$$

As the precise initial state of the material prior to the performance of each reaction step is not known, the reaction conversion of each step is calculated independently from the other. The released or absorbed amount of O_2 is generally referred to the maximum possible amount of reacting molar O_2 according to a weight loss of 3.181 %.

The approximated value of the oxygen partial pressure pO_2 is determined by the product of the molar fraction of O_2, which is equal to the recorded volume concentration of O_2 (σ_{O_2}), and the measured atmospheric pressure.

$$pO_2 = y_{O_2} \cdot p_{ambient} \tag{C.9}$$

C.3 TGA: Variation of Isothermal Temperature in Atmosphere of 2 % O_2

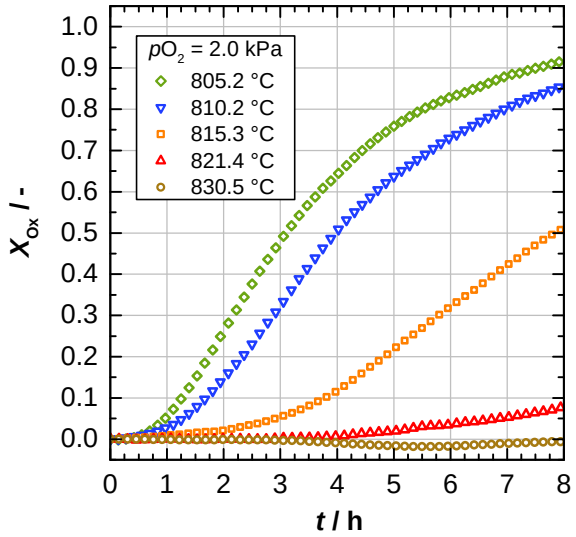

Figure C.1: Isothermal oxidation of $(Mn_{0.75}Fe_{0.25})_3O_4$ in 2 % O_2 atmosphere over a period of 8 h at different temperatures within the thermal hysteresis range experimentally determined in Section 3.4.1 (apart from the measurement at 805.2 °C). Measurement conditions of TG-DSC analyses: Reduction of $(Mn_{0.75}Fe_{0.25})_2O_3$ at a heating rate of 10 K/min up to 1060 °C in air; switch of gas flow from 20 NmL/min O_2 and 80 NmL/min N_2 to 2 NmL/min O_2 and 98 NmL/min N_2 at 1060 °C; cooling down of reduced sample at a rate of 10 K/min to the desired temperature level for isothermal analysis, followed by isothermal period over 8 h.

C.4 Heat Balance – Basic Calculations for Estimation of Heat Effects

The chemical storage capacity Q_{chem} of the reactor is calculated based on the product of the weighted sample and the specific reaction enthalpy $\Delta_R h$ of the redox reaction of 271.4 J/g $(Mn_{0.75}Fe_{0.25})_2O_3$ measured by DSC in Section 3.3.3 (energy density of the storage material):

$$Q_{chem} = m_{(Mn_{0.75}Fe_{0.25})_2O_3} \cdot \Delta_R h \tag{C.10}$$

The chemical storage capacity of the reactor filled with 471.2 g $(Mn_{0.75}Fe_{0.25})_2O_3$ (see Section 4.1.3) amounts to ≈35.5 Wh (≈127.7 kJ), which can theoretically be achieved if full conversion is reached.

C.4.1 Release of Thermal Energy by the Redox Reaction

1. Reaction power output: The specific reaction enthalpy $\Delta_R h$ is converted to the molar value $\Delta_R H$ giving approximately 273.0 kJ/mol O_2, which can be applied to calculate the reaction power

output in terms of a heat release rate of the chemical reaction in (mol·J)/(s·mol) = W:

$$P_{\mathrm{rxn}} = \dot{Q}_{\mathrm{rxn}} = \dot{n}_{\mathrm{O_2,rxn}} \cdot \Delta_{\mathrm{R}} H \tag{C.11}$$

2. Chemical/Thermal storage capacity: Integration of the reaction power output over time gives the storage capacity in Wh (quantity of thermal energy released per unit of time) actually achieved in the discharging step:

$$Q_{\mathrm{rxn}} = \int_{rxn\,begin}^{rxn\,end} P_{\mathrm{rxn}}\,\mathrm{d}t = X_{\mathrm{Ox}} \cdot Q_{\mathrm{chem}} \tag{C.12}$$

3. Mean reaction power output: A mean reaction power output in W can be obtained by referring the chemical/thermal storage capacity Q_{rxn} to the total reaction time t_{rxn}:

$$P_{\mathrm{rxn,av}} = \frac{Q_{\mathrm{rxn}}}{t_{\mathrm{rxn}}} = \frac{X_{\mathrm{Ox}} \cdot Q_{\mathrm{chem}}}{t_{\mathrm{rxn}}} \tag{C.13}$$

C.4.2 Dissipation of Thermal Energy by the Heat Transfer Fluid

1. HTF thermal power output: The time-dependent thermal discharging power P_{HTF} of the lab-scale storage reactor in terms of a heat dissipation rate can be calculated according to:

$$P_{\mathrm{HTF}} = \dot{Q}_{\mathrm{HTF}} = \dot{m}_{\mathrm{g,out}} \cdot c_{p,\mathrm{g}}(T) \cdot \Delta T_{\mathrm{g}} = \dot{m}_{\mathrm{g,out}} \cdot c_{p,\mathrm{g}}(T) \cdot (T_{\mathrm{g,out,av}} - T_{\mathrm{g,in}}) \tag{C.14}$$

taking the current mass flow rate $\dot{m}_{\mathrm{g,out}}$ at the reactor outlet, the average specific heat capacity $c_{p,\mathrm{g}}(T)$ of the HTF and the registered HTF temperature rise ΔT_{g} into account.

However, at steady-state conditions prior to the initiation of the discharging step (experiments at a constant air inlet temperature $\vartheta_{\mathrm{g,in}}$) the gas outlet temperature $\vartheta_{\mathrm{g,out,av}}$ generally turns out to be lower than the gas inlet temperature $\vartheta_{\mathrm{g,in}}$ (e.g., see Fig. C.2). This temperature offset can be attributed to a non-uniform temperature profile of the reactor tube showing lower temperatures towards the water cooler, which is integrated into the casing tube. Thus increased heat losses from the top layer of the packed particle bed towards the filter and the tube wall lead to lower gas outlet temperatures. To allow a better comparison between different experiments, a standardized temperature difference $\Delta T_{\mathrm{g,std}}$ adjusted by the offset between the gas outlet and inlet temperature is introduced for the determination of the rise of the gas temperature ΔT_{g} in Eq. (C.14).

$$\Delta T_{\mathrm{g,std}} = [T_{\mathrm{g,out,av}}(t) - T_{\mathrm{g,in}}(t)] - [T_{\mathrm{g,out,av}}(0) - T_{\mathrm{g,in}}(0)] \tag{C.15}$$

with $T_{\mathrm{g,in}}(t) = T_{\mathrm{g,in}}(0)$ being the controlled gas/air inlet temperature.

The specific heat capacity of the gas phase $c_{p,\mathrm{g}}(T)$ can be determined from the values of the pure components (i = O_2 or N_2) by means of the thermodynamically exact mixing rule for mixtures of ideal gases [88]:

$$c_{p,\mathrm{g}}(T) = \sum_i w_{\mathrm{i}} \cdot c_{p,\mathrm{i}}(T) \tag{C.16}$$

The molar fractions of oxygen and nitrogen y_i ($i = O_2$ or N_2) at the outlet of the reactor – which equal the measured volume concentrations σ_i in the gas mixture – have to be converted into the corresponding mass fractions w_i according to:

$$w_i = \frac{y_i M_i}{y_{O_2} M_{O_2} + y_{N_2} M_{N_2}} \tag{C.17}$$

The *PPDS Equation (**P**hysical **P**roperty **D**ata **S**ervice)* for the specific heat capacity of ideal gases can be used to calculate $c_{p,i}(T)$ for O_2 and N_2, respectively [89]:

$$c_{p,i}(T) = R\left\{B + (C-B)\left(\frac{T}{A+T}\right)^2\left[1 - \frac{A}{A+T}\left(D + E\frac{T}{A+T} + F\left(\frac{T}{A+T}\right)^2 + G\left(\frac{T}{A+T}\right)^3\right)\right]\right\} \tag{C.18}$$

The corresponding coefficients for O_2 and N_2 are listed in Table C.3.

Table C.3: Coefficients for gas species O_2 and N_2 in the PPDS Equation (C.18) for the calculation of the specific heat capacities of ideal gases.

Gas Species	R / J/(kg · K)	A	B	C	D	E	F	G
N_2	296.8039	432.2027	3.516	2.8021	–4.1924	42.0153	–114.25	111.1019
O_2	259.8329	2122.2098	3.5302	–7.1076	–1.4542	30.6057	–83.6696	79.4375

For each data point the average specific heat capacity (according to Eq. (C.18)) is referred to the mean temperature value $T = [T_{g,out,av}(t) + T_{g,out,av}(0)]/2$ of the temperature increase.

2. Thermal energy extracted by the HTF: Integration of the thermal power output P_{HTF} over the discharging time t_d provides a rough estimation of the accumulated amount of thermal energy Q_{HTF} extracted from the packed bed storage by the HTF at any given time during the discharging period:

$$Q_{HTF} = \int_{d,begin}^{d,end} P_{HTF}\,\mathrm{d}t \tag{C.19}$$

The discharging time t_d defines the period from the point of gas switching (initiation of the reaction) to the point at which the gas outlet temperature $\vartheta_{g,out,av}$ reaches its baseline level. In cases where the experiment is terminated, but the baseline level of $\vartheta_{g,out,av}$ has not yet been reached, t_d has to be approximated by extrapolation of the gas outlet temperature profile.

3. Mean HTF thermal power output: Referring the extracted amount of thermal energy Q_{HTF} at the end of the actual oxidation period to the total reaction time t_{rxn} gives a mean thermal power output in W, which can be compared to $P_{rxn,av}$:

$$P_{HTF,av} = \frac{Q_{HTF}}{t_{rxn}} \tag{C.20}$$

C.5 Thermal Packed Bed Parameter: Solid-Gas Heat Transfer Coefficient

The interface heat flux – expressed in terms of a Nusselt number for fluid-to-particle heat transfer – couples the energy balance equations of the solid and gas phase with each other. In this work

the heat transfer coefficient $h_{\text{s-g}}$ between the granular particles and the gas phase can be predicted based on the Nusselt correlation of Gnielinski [67]:

$$\mathrm{Nu} = \frac{h_{\text{s-g}} \cdot d_{\text{p,m}}}{\lambda_{\text{g}}} = f_{\text{a}}\,\mathrm{Nu}_{\text{sphere}} = \left[1 + 1.5(1-\varepsilon_{\text{bed}})\right]\left(2 + \sqrt{\mathrm{Nu}_{\text{lam}}^2 + \mathrm{Nu}_{\text{turb}}^2}\right) \tag{C.21}$$

$$\mathrm{Nu}_{\text{lam}} = 0.664\sqrt{\mathrm{Re}_{\text{p},\varepsilon_{\text{bed}}}}\sqrt[3]{\mathrm{Pr}} \tag{C.22}$$

$$\mathrm{Nu}_{\text{turb}} = \frac{0.037\,\mathrm{Re}_{\text{p},\varepsilon_{\text{bed}}}^{0.8}\,\mathrm{Pr}}{1 + 2.433\,\mathrm{Re}_{\text{p},\varepsilon_{\text{bed}}}^{-0.1}\left(\mathrm{Pr}^{2/3} - 1\right)} \tag{C.23}$$

λ_{g} being the continuum thermal conductivity of the pure gas phase.

For the calculation of the particle Reynolds number $\mathrm{Re}_{\text{p},\varepsilon_{\text{bed}}}$ used in this Nusselt correlation the interstitial velocity $\vec{u}_{\text{g}} = \vec{u}/\varepsilon_{\text{bed}}$ has to be chosen instead of the superficial gas velocity. The form factor $f_{\text{a}} = 1 + 1.5(1-\varepsilon_{\text{bed}})$ for a bed consisting of spheres of the same size is used as an assumption in this thesis. Equation (C.21) is valid for a particle Reynolds number range of $10^{-1} < \mathrm{Re}_{\text{p},\varepsilon_{\text{bed}}} < 10^4$ and Prandtl numbers between 0.6 and 10^3.

C.6 Experimental Results of Lab-Scale Examinations

C.6.1 Reference Experiment: Thermal Discharging at a Constant Gas Inlet Temperature of 850 °C

Once the reduction step – performed in the way as described in Section 4.2 – has been completed, the packed bed of granular $(Mn_{0.75}Fe_{0.25})_3O_4$ is cooled down to 850 °C under a flow of 2 % O_2 in N_2 at a total flow rate of 10 NL/min, as the atmosphere with reduced O_2 concentration inhibits the initiation of the oxidation reaction. This procedure simulates a cooling process at reduced total pressure, more precisely 10 % of atmospheric pressure. The temperature of 850 °C was selected as a reference case for measurements at different constant gas inlet and initial bed temperatures (see Section 4.3.2).

Based on preliminary studies it was found that the procedure yields higher reaction rates along with shorter reaction times in the subsequent oxidation step in air, when cooling has been performed under a gas flow of 2 % O_2 in contrast to pure N_2. This observation might be explained by early nuclei formation of the oxidized phase, induced by thermal fluctuations due to the presence of O_2 during the cooling process (see also presence of thermal hysteresis in Fig. 4.3). However, it has been verified by thermogravimetric measurements over isothermal periods of 8 h, that – within this time period – an oxidation at 2 % O_2 does not take place even down to temperatures of 825 °C (Fig. C.1). From a technical point of view higher thermal power densities of the storage reactor can be achieved by means of this operating procedure, which is why a pure N_2 atmosphere has thus been excluded throughout the experimental campaign in this work (see Table C.1).

Once thermal equilibrium in the packed bed has been reached and maintained over a period of at least 20 min, the gas flow is switched to air, abruptly increasing the pO_2 from ≈2.0 kPa to

≈21.1 kPa, measured at the gas outlet at ambient conditions. The air inlet as well as tube furnace temperature are kept at 850 °C throughout the entire period of the experiment. Figure C.2 shows the thermal discharging of the storage with a constant gas inlet temperature ($\vartheta_{g,in}$). The gas change is indicated by the point of origin ($t = 0$ min).

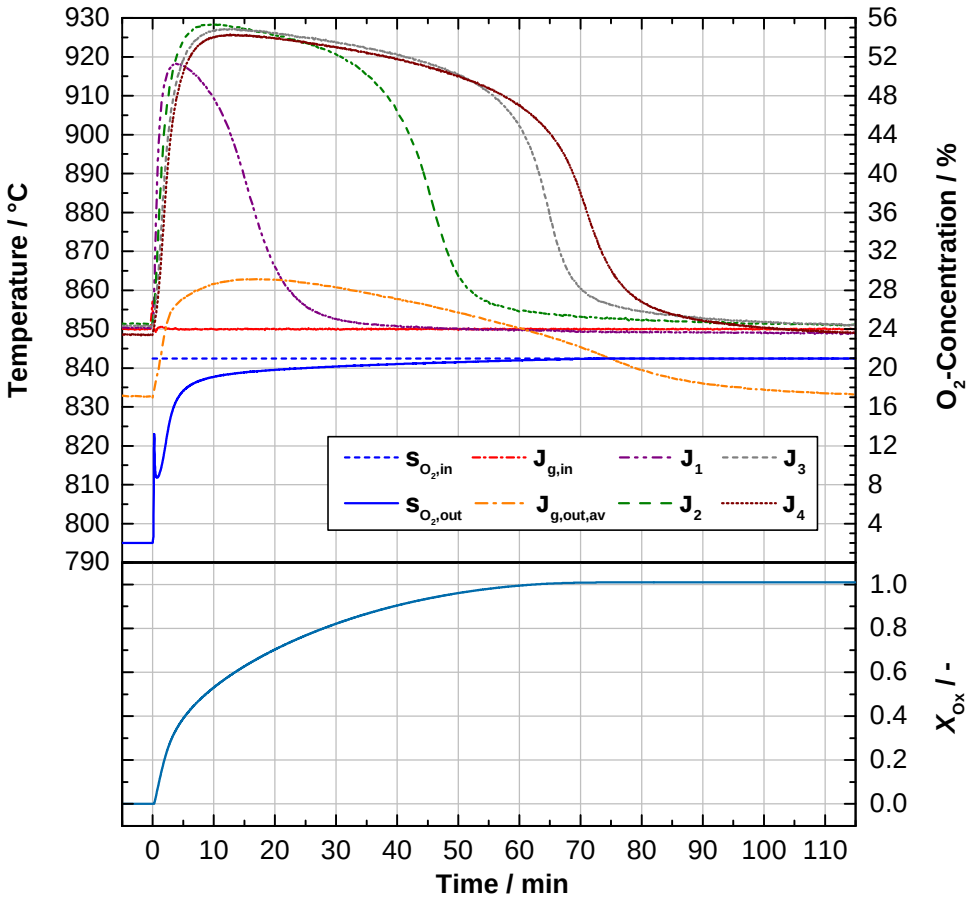

Figure C.2: Reaction progress of the discharging stage 4 $(Mn_{0.75}Fe_{0.25})_3O_4 + O_2 \rightarrow 6\ (Mn_{0.75}Fe_{0.25})_2O_3$ at a constant air inlet $\vartheta_{g,in}$ and tube furnace temperature $\vartheta_{furnace}$ of 850 °C, and at an air flow rate of 10 NL/min (2nd redox cycle, reference experiment).

When switching the gas atmosphere the O_2 concentration at the outlet rises (see peak in Fig. C.2 at $t = 0$ min), which indicates the flushing of the reaction chamber superimposed by the abrupt initiation of the oxidation reaction. The prevailing reactor conditions thermodynamically favor the oxidized phase. After 14 s a drop of the O_2 concentration (down to 8.7 % for a short time) follows due to the uptake of O_2.

The release of the heat of reaction leads to an instantaneous increase of all bed temperatures. This observation indicates high initial reaction rates in combination with excess of oxygen available over the entire bed height. The presence of a strong driving force due to the high degree of undercooling becomes evident upon switching the gas flow to air. 50 % conversion is already reached after ≈8.7 min, with the largest part of the released heat of reaction reflected in the sensible heating of the packed bed (self-heating of the material). The material in the bottom region exhibits the lowest temperature increase, attributed to the initially highest cooling capacity of the HTF entering the

reactor at 850 °C. This is why a maximum temperature of only ≈918.5 °C – further away from the equilibrium – was registered by the sensor ϑ_1 close to the inlet of the packed bed, denoting the fastest extraction of thermal energy via the HTF in this region. Temperatures ϑ_2, ϑ_3 and ϑ_4 in the middle and upper part of the bed reveal the largest temperature rise, reaching levels closer to the equilibrium, where the reaction rate decreases enormously. At this point the reaction mainly proceeds, once the material experiences cooling by the HTF, slowly extracting the released heat of reaction. Based on those observations the oxidation reaction is mainly limited due to the rate of heat dissipation by the HTF.

A pronounced temperature front moving through the reactor from the bottom to the top owing to the extraction of thermal energy could be observed. The position of the temperature front in the packed bed clearly indicates the time, when the reaction has been completed and the entire heat of reaction has been released in the part below the considered temperature sensor position. From that point on, only sensible heat is transferred to the HTF, causing the bed to cool down to the initial temperature.

It has to be mentioned, that the reactor tube is also heated up in the course of the reaction process, as the tube furnace temperature is maintained at the same value as the gas inlet temperature and initial bed temperature ($\vartheta_{\text{furnace}}$ and $\vartheta_{\text{g,in}}$ both at 850 °C in the reference experiment). Hence, large heat losses in the radial direction across the reactor tube and casing tube wall towards the surroundings (tube furnace) emerge. The temporal course of the temperatures in the radial direction from the axial measurement position inside the packed bed (ϑ_2 and ϑ_4) to the outer wall temperature of the casing tube ($\vartheta_{2,\text{w2}}$ and $\vartheta_{4,\text{w2}}$) is presented in Fig. C.3, respectively.

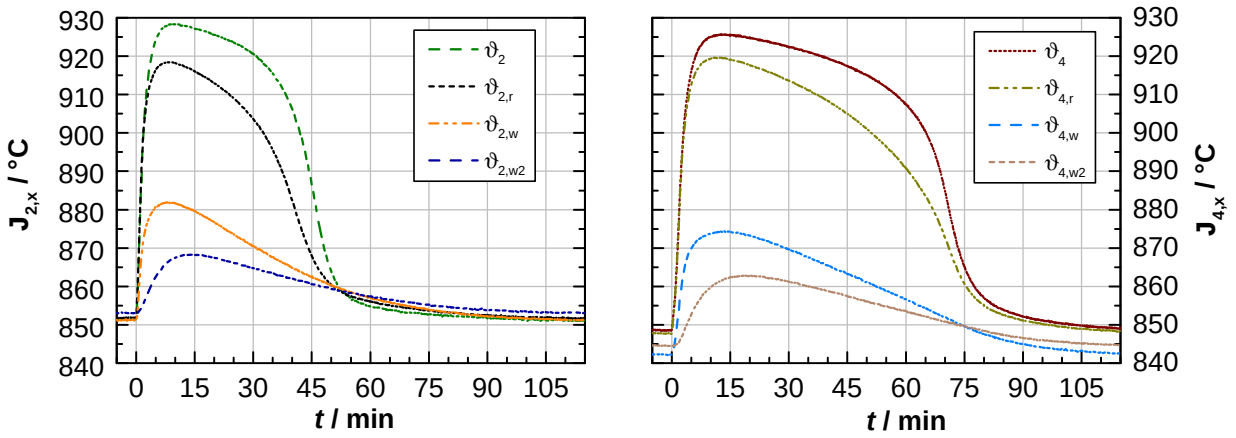

(a) Position #2 at a bed height of 50 mm.

(b) Position #4 at a bed height of 130 mm.

Figure C.3: Radial temperature distribution at different bed heights above the gas distribution disc, exemplarily illustrated for the discharging experiment 4 $(Mn_{0.75}Fe_{0.25})_3O_4 + O_2 \rightarrow 6\ (Mn_{0.75}Fe_{0.25})_2O_3$ at a constant air inlet $\vartheta_{\text{g,in}}$ and tube furnace temperature $\vartheta_{\text{furnace}}$ of 850 °C, and at an air flow rate of 10 NL/min (2^{nd} redox cycle, reference experiment).

The profiles in both section planes clearly disclose the strong cooling effect which the packed bed experiences by the reactor tube wall. However, this matter of fact is not relevant for the

lab-scale experiments to identify the determining factors of influence on the performance of a redox reaction based TCS reactor (Section 4.3).

Similar temperatures for the gas outlet temperature $\vartheta_{g,out,av}$ (measured directly above the packed bed) and the reactor tube wall $\vartheta_{g,out,w}$ at the same height ($\vartheta_{g,out,w}$ not shown in Fig. C.2) could be monitored, indicating the typically low thermal storage capability of the gaseous fluid (high gas flow rates at ideally elevated pressure necessary for high thermal energy transport). At the outlet of the packed bed thermal energy is transferred from the HTF to the metallic tube wall, which in turn features a high thermal storage capability owing to its high thermal mass (see material properties in Appendix C.7).

The end of the storage discharging period can be identified, once the O_2 concentration has reached the stationary O_2 level in air (end of the redox reaction) and steady state conditions have been attained again. A value of ≈101.0 % has been calculated for the oxidation conversion within the limits of the measurement accuracy (Fig. C.2, bottom). The total reaction time t_{rxn} (period of O_2 uptake in the reactor) amounts to ≈83.8 min. The duration of the oxidation step is shorter compared to the reduction step (see for example reduction in Section 4.2), which is based on the initial high degree of undercooling as well as the generally larger ΔT between the reaction temperature and the temperature of the incoming air in the presented operating method for discharging.

C.6.2 Thermal Discharging at Constant Gas Inlet Temperature – Heat Dissipation and Thermal Power Output

For the parametric studies of different air flow rates at 825 °C and varied temperatures at 10 NL/min air, described respectively in Section 4.3.2, Fig. C.4 provides an overview of the progress of calculated reaction power output P_{rxn} and thermal discharging power P_{HTF} over time, along with the measured temperature increase $\Delta T_{g,std}$ (see Eq. (C.15)) of the gas outlet temperature $\vartheta_{g,out,av}$.

The diagrams clearly demonstrate, that the influence of the O_2 uptake on the overall HTF mass flow rate $\dot{m}_{g,out}$ at the outlet of the reactor (Eq. (C.5)) cannot be neglected. The maximum O_2 changes were observed in the runs at $\vartheta_{g,in} = 825$ °C and 5 NL/min as well as $\vartheta_{g,in} = 800$ °C and 10 NL/min, leading to a short-time drop of the HTF mass flow rate by 19.1 % and 18.4 % within the first 1.5 min upon switching to air atmosphere, respectively. For comparison, in the dynamic discharging experiment at an air flow rate of 10 NL/min and a constant cooling rate of the gas inlet temperature of 5 K/min (see Fig. 4.4) the HTF mass flow rate $\dot{m}_{g,out}$ shortly declined by 3.5 % due to the uptake of O_2.

On this account, the present heat capacity rate $C_{HTF} = \dot{m}_{g,out} \cdot c_{p,g}(T)$ of the N_2/O_2 mixture, which is crucial for the attainable thermal power output of the TCS reactor according to Eq. (C.14), is attenuated correspondingly. The estimated HTF thermal power output achieved throughout the experimental series turned out to be generally low ($P_{HTF} << P_{rxn}$). In the experiment with the highest heat capacity rate (run at 15 NL/min and $\vartheta_{g,in} = 825$ °C) a maximum value of 15.9 W has

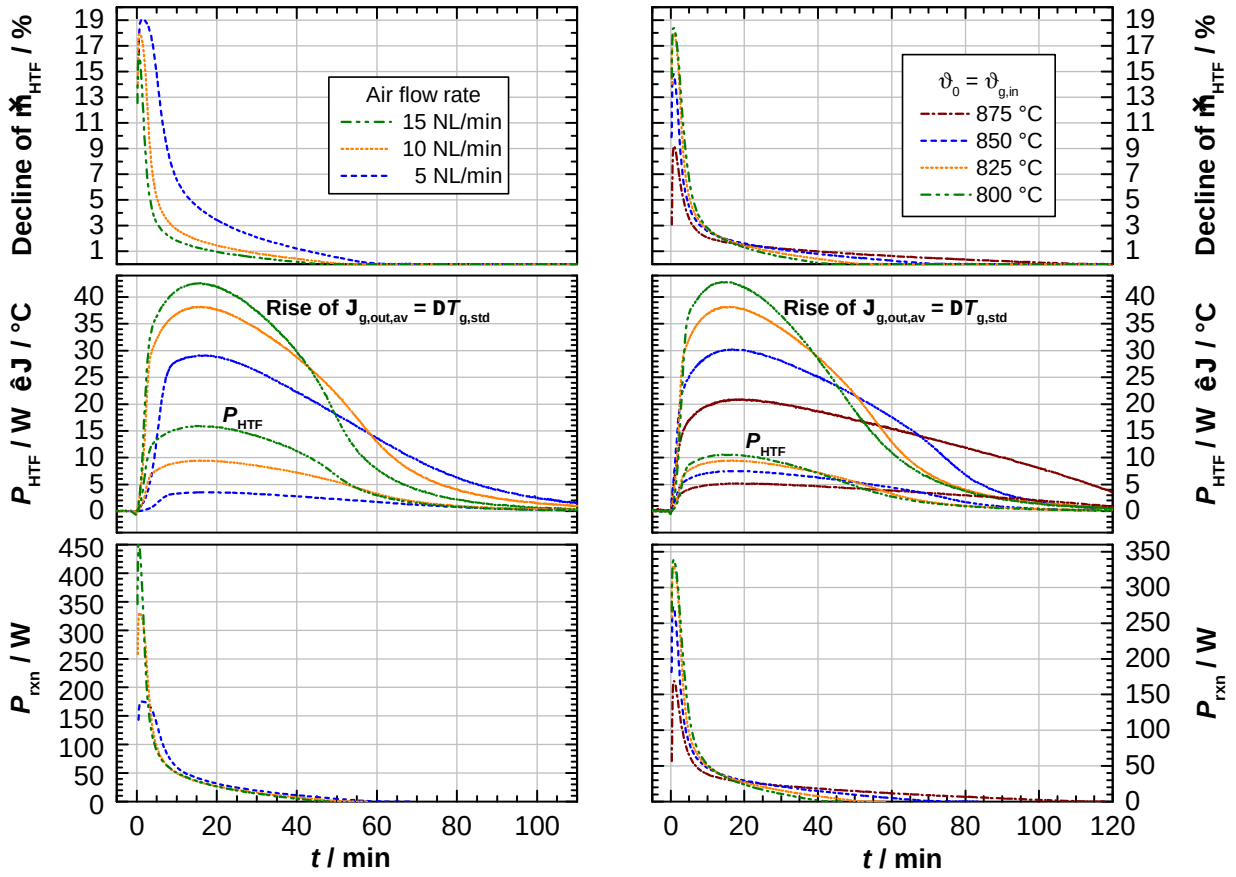

(a) Flow rate variation with initial bed and constant air inlet temperature $\vartheta_0 = \vartheta_{g,in}$ of 825 °C: 5 NL/min, 10 NL/min and 15 NL/min air.

(b) Temperature variation at 10 NL/min air: Initial bed and constant air inlet temperatures $\vartheta_0 = \vartheta_{g,in}$ of 800 °C, 825 °C, 850 °C and 875 °C.

Figure C.4: Storage discharging step 4 $(Mn_{0.75}Fe_{0.25})_3O_4 + O_2 \rightarrow 6\ (Mn_{0.75}Fe_{0.25})_2O_3$ at constant air inlet temperature $\vartheta_{g,in}$: Progress of calculated reaction power output P_{rxn} and thermal discharging power P_{HTF} of the HTF.

been reached for P_{HTF}.

C.6.3 Material Cycled 17 Times in Lab-Scale Storage Reactor – Thermogravimetric Analysis and Particle Size Distribution

To verify the reactivity of the Mn-Fe oxide material after cycling in the reactor, a sample is analyzed by means of TGA, largely eliminating heat and mass transport effects during the redox reaction. Prior to the measuring cycle shown in Fig. C.5, a typical reference cycle is carried out according to the program described for Mn-Fe oxide in Table B.2. After reduction of the oxide at a heating rate of 3 K/min in air the material is cooled down under an atmosphere of 2 % O_2, followed by an isothermal oxidation period at 850 °C in air. Figure C.5 presents the comparison between the redox cycle of the raw material and cycled material (17 cycles performed in lab-scale storage reactor).

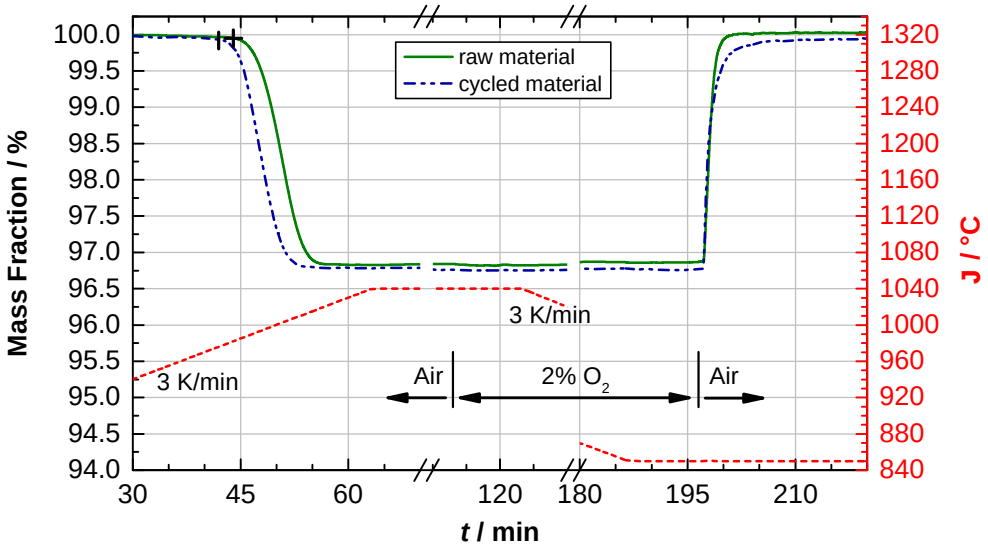

Figure C.5: Thermogravimetric analysis of the Mn-Fe oxide raw material and a sample of the material cycled 17 times in the lab-scale storage reactor: Reduction of $(Mn_{0.75}Fe_{0.25})_2O_3$ with a heating rate of 3 K/min up to 1040 °C in air and subsequent oxidation of $(Mn_{0.75}Fe_{0.25})_3O_4$ at 850 °C in air, after a cooling period at 3 K/min under 2 % O_2; "|" corresponds to 976 °C and "+" to 982 °C (ϑ_3 plateau temperatures of 2nd cycle and 17th cycle in lab-scale experiment, see Fig. 4.9a).

The observed shift in the onset temperature of the reduction in Fig. 4.9a (middle) could be confirmed by thermal analysis. The lowest temperature values measured for ϑ_3 in the course of the temperature plateau formation in the packed bed (see Fig. 4.9a, middle) are indicated in Fig. C.5 by "+" for the 2nd cycle (982 °C) and "|" for the 17th cycle (976 °C). Correspondingly, the beginning of the mass loss shows a similar shift to lower temperatures for the cycled material in comparison to the raw material, whereas the reaction time remains nearly the same. The oxidation of the cycled material at 850 °C in air initially started more rapidly compared to the raw material. At a conversion of roughly 50 %, though, the reaction rate of the cycled material slowed down to such an extent, that eventually a longer reaction time was registered.

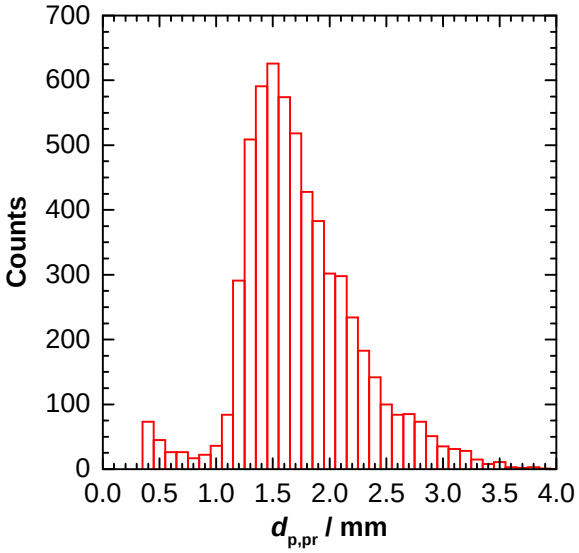

Figure C.6: Particle size distribution showing the calculated equivalent particle diameter $d_{\mathrm{p,pr}}$ (see Eq. (3.11)) of $(Mn_{0.75}Fe_{0.25})_2O_3$ after 17 redox cycles in the lab-scale storage reactor.

C.7 Material Properties of Insulation Materials and Nickel-Based Metal Alloys

The material properties of the fiber mat insulation material Contherm BTM 1300 (Co. Morgan Ceramics) are listed in Table C.4.

Table C.4: Physical material properties of the employed fiber mat insulation material Contherm BTM 1300 (Co. Morgan Ceramics | Contherm Wärmedämmsysteme GmbH); material specification data taken from corresponding data sheets.

	Employed position			
	Between reactor and casing tube	**Attached around the casing tube**	ϑ **°C**	T **K**
t_{insu} **/ mm**	6	9		
ρ_{app} **/ kg/m^3**	96	160		
λ_{insu} **/ W/(m · K)**	0.05	0.05	200	473.15
	0.10	0.08	400	673.15
	0.19	0.12	600	873.15
	0.32	0.19	800	1073.15
	0.48	0.28	1000	1273.15
	0.69		1200	1473.15

The material properties of the reactor tube made of *Alloy 625* ($\rho_{\text{Alloy 625}} = 8.47\,\text{g/cm}^3$) and the casing tube made of *Alloy 602 CA* ($\rho_{\text{Alloy 602 CA}} = 7.93\,\text{g/cm}^3$) are listed in Table C.5.

Table C.5: Physical material properties of nickel-based Alloy 625 (Nicrofer® 6020 hMo, 2.4856) and Alloy 602 CA (Nicrofer® 6025 HT, 2.4633), material specification data taken from VDM Metals International GmbH (Data Sheets No. 4118 and No. 4137).

		Alloy 625		Alloy 602 CA	
ϑ	T	$c_{p,\text{w}}$	λ_{w}	$c_{p,\text{w2}}$	λ_{w2}
°C	K	J/(kg·K)	W/(m·K)	J/(kg·K)	W/(m·K)
20	293.15	-	-	447	10.4
100	373.15	496	12.4	465	12.3
200	473.15	521	14.2	488	14.0
300	573.15	538	16.0	501	15.5
400	673.15	555	17.7	514	16.9
500	773.15	573	19.3	516	18.4
600	873.15	620	21.5	517	20.1
700	973.15	654	-	550	22.0
800	1073.15	663	-	583	24.1
900	1173.15	677	26.7	603	26.2
1000	1273.15	684	28.2	626	28.2
1100	1373.15	695	29.6	631	29.7
1200	1473.15	705	31.1	636	30.6

Bibliography

[1] S. Abanades, P. Charvin, G. Flamant, and P. Neveu. Screening of water-splitting thermochemical cycles potentially attractive for hydrogen production by concentrated solar energy. *Energy*, 31(14):2805–2822, 2006.

[2] A. H. Abedin and M. A. Rosen. A Critical Review of Thermochemical Energy Storage Systems. *The Open Renewable Energy Journal*, 4:42–46, 2011.

[3] C. Agrafiotis, A. Becker, M. Roeb, and C. Sattler. Exploitation of thermochemical cycles based on solid oxide redox systems for thermochemical storage of solar heat. Part 5: Testing of porous ceramic honeycomb and foam cascades based on cobalt and manganese oxides for hybrid sensible/thermochemical heat storage. *Solar Energy*, 139:676–694, 2016.

[4] C. Agrafiotis, T. Block, M. Senholdt, S. Tescari, M. Roeb, and C. Sattler. Exploitation of thermochemical cycles based on solid oxide redox systems for thermochemical storage of solar heat. Part 6: Testing of Mn-based combined oxides and porous structures. *Solar Energy*, 149:227–244, 2017.

[5] C. Agrafiotis, M. Roeb, and C. Sattler. Exploitation of thermochemical cycles based on solid oxide redox systems for thermochemical storage of solar heat. Part 4: Screening of oxides for use in cascaded thermochemical storage concepts. *Solar Energy*, 139:695–710, 2016.

[6] C. Agrafiotis, M. Roeb, M. Schmücker, and C. Sattler. Exploitation of thermochemical cycles based on solid oxide redox systems for thermochemical storage of solar heat. Part 1: Testing of cobalt oxide-based powders. *Solar Energy*, 102:189–211, 2014.

[7] C. Agrafiotis, M. Roeb, M. Schmücker, and C. Sattler. Exploitation of thermochemical cycles based on solid oxide redox systems for thermochemical storage of solar heat. Part 2: Redox oxide-coated porous ceramic structures as integrated thermochemical reactors/heat exchangers. *Solar Energy*, 114:440–458, 2015.

[8] I. A. Al-Shankiti, B. D. Ehrhart, B. J. Ward, A. Bayon, M. A. Wallace, R. Bader, P. Kreider, and A. W. Weimer. Particle design and oxidation kinetics of iron-manganese oxide redox materials for thermochemical energy storage. *Solar Energy*, 183:17–29, 2019.

[9] E. Alonso, C. Hutter, M. Romero, A. Steinfeld, and J. Gonzalez-Aguilar. Kinetics of Mn2O3-Mn3O4 and Mn3O4-MnO Redox Reactions Performed under Concentrated Thermal Radiative Flux. *Energy & Fuels*, 27(8):4884–4890, 2013.

[10] E. Alonso, C. Pérez-Rábago, J. Licurgo, E. Fuentealba, and C. A. Estrada. First experimental studies of solar redox reactions of copper oxides for thermochemical energy storage. *Solar Energy*, 115:297–305, 2015.

[11] L. André, S. Abanades, and L. Cassayre. Experimental and Thermodynamic Study of Co-Fe and Mn-Fe Based Mixed Metal Oxides for Thermochemical Energy Storage Application. *AIP Conference Proceedings*, 1850(1):0900021–0900029, 2017.

[12] L. André, S. Abanades, and L. Cassayre. High-temperature thermochemical energy storage based on redox reactions using Co-Fe and Mn-Fe mixed metal oxides. *Journal of Solid State Chemistry*, 253:6–14, 2017.

[13] L. André, S. Abanades, and L. Cassayre. Experimental Investigation of Co-Cu, Mn-Co, and Mn-Cu Redox Materials Applied to Solar Thermochemical Energy Storage. *ACS Applied Energy Materials*, 1(7):3385–3395, 2018.

[14] L. André, S. Abanades, and L. Cassayre. Mixed Metal Oxide Systems Applied to Thermochemical Storage of Solar Energy: Benefits of Secondary Metal Addition in Co and Mn Oxides and Contribution of Thermodynamics. *Applied Sciences*, 8(12):1–20, 2018.

[15] L. André, S. Abanades, and G. Flamant. Screening of thermochemical systems based on solid-gas reversible reactions for high temperature solar thermal energy storage. *Renewable and Sustainable Energy Reviews*, 64:703–715, 2016.

[16] P. Atkins and J. de Paula. *Atkin's Physical Chemistry*. Oxford University Press, Oxford, 9th edition, 2010.

[17] F. Ausfelder, C. Beilmann, M. Bertau, S. Bräuninger, A. Heinzel, R. Hoer, W. Koch, F. Mahlendorf, A. Metzelthin, M. Peuckert, L. Plass, K. Räuchle, M. Reuter, G. Schaub, S. Schiebahn, E. Schwab, F. Schüth, D. Stolten, G. Teßmer, K. Wagemann, and K.-F. Ziegahn. Energy Storage as Part of a Secure Energy Supply. *ChemBioEng Reviews*, 4(3):144–210, 2017.

[18] M. Avrami. Kinetics of Phase Change. I General Theory. *The Journal of Chemical Physics*, 7(12):1103–1112, 1939.

[19] M. Avrami. Kinetics of Phase Change. II Transformation–Time Relations for Random Distribution of Nuclei. *The Journal of Chemical Physics*, 8(2):212–224, 1940.

[20] M. Avrami. Kinetics of Phase Change. III Granulation, Phase Change, and Microstructure. *The Journal of Chemical Physics*, 9(2):177–184, 1941.

[21] G. Azimi, H. Leion, T. Mattisson, M. Rydén, F. Snijkers, and A. Lyngfelt. Mn-Fe Oxides with Support of MgAl2O4, CeO2, ZrO2 and Y2O3-ZrO2 for Chemical-Looping Combustion and Chemical-Looping with Oxygen Uncoupling. *Industrial & Engineering Chemistry Research*, 53(25):10358–10365, 2014.

[22] G. Azimi, H. Leion, M. Rydén, T. Mattisson, and A. Lyngfelt. Investigation of Different Mn-Fe Oxides as Oxygen Carrier for Chemical-Looping with Oxygen Uncoupling (CLOU). *Energy & Fuels*, 27(1):367–377, 2013.

[23] S. M. Babiniec, E. N. Coker, J. E. Miller, and A. Ambrosini. Investigation of LaxSr1-xCoyM1-yO3-delta (M = Mn, Fe) perovskite materials as thermochemical energy storage media. *Solar Energy*, 118:451–459, 2015.

[24] S. M. Babiniec, E. N. Coker, J. E. Miller, and A. Ambrosini. Doped calcium manganites for advanced high-temperature thermochemical energy storage. *International Journal of Energy Research*, 40(2):280–284, 2016.

[25] C. W. Bale, E. Bélisle, P. Chartrand, S. A. Decterov, G. Eriksson, A. E. Gheribi, K. Hack, I. H. Jung, Y. B. Kang, J. Melançon, A. D. Pelton, S. Petersen, C. Robelin, J. Sangster, P. Spencer, and M. A. Van Ende. FactSage thermochemical software and databases, 2010–2016. *Calphad*, 54:35–53, 2016.

[26] E. Barbour, D. Mignard, Y. Ding, and Y. Li. Adiabatic Compressed Air Energy Storage with packed bed thermal energy storage. *Applied Energy*, 155:804–815, 2015.

[27] I. Barin and G. Platzki. *Thermochemical Data of Pure Substances*, volume 2. VCH Verlagsgesellschaft mbH, Weinheim, 3rd edition, 1995.

[28] T. Block, N. Knoblauch, and M. Schmücker. The cobalt-oxide/iron-oxide binary system for use as high temperature thermochemical energy storage material. *Thermochimica Acta*, 577:25–32, 2014.

[29] T. Block and M. Schmücker. Metal oxides for thermochemical energy storage: A comparison of several metal oxide systems. *Solar Energy*, 126:195–207, 2016.

[30] J. A. Botas, J. Marugán, R. Molina, and C. Herradón. Kinetic modelling of the first step of Mn2O3/MnO thermochemical cycle for solar hydrogen production. *International Journal of Hydrogen Energy*, 37(24):18661–18671, 2012.

[31] R. G. Bowrey and J. Jutsen. Energy storage using the reversible oxidation of barium oxide. *Solar Energy*, 21(6):523–525, 1978.

[32] A. Brüggemann. The energy transition will not work without a heating transition. *KfW Research - Focus on Economics*, 129:1–3, 2016.

[33] M. E. Brown. The Prout-Tompkins rate equation in solid-state kinetics. *Thermochimica Acta*, 300(1):93–106, 1997.

[34] M. E. Brown. *Handbook of Thermal Analysis and Calorimetry*, volume 1 Principles and Practice. Elsevier Science B.V., Amsterdam, 1st edition, 1998.

[35] T. A. Brown, F. Scala, S. A. Scott, J. S. Dennis, and P. Salatino. The attrition behaviour of oxygen-carriers under inert and reacting conditions. *Chemical Engineering Science*, 71:449–467, 2012.

[36] M. Buck, A. Graf, and P. Graichen. *European Energy Transition 2030: The Big Picture. Ten Priorities for the next European Commission to meet the EU's 2030 targets and accelerate towards 2050.* Agora Energiewende, Berlin, Germany, 1st edition, 2019.

[37] A. J. Carrillo, J. Moya, A. Bayón, P. Jana, V. A. de la Peña O'Shea, M. Romero, J. Gonzalez-Aguilar, D. P. Serrano, P. Pizarro, and J. M. Coronado. Thermochemical energy storage at high temperature via redox cycles of Mn and Co oxides: Pure oxides versus mixed ones. *Solar Energy Materials and Solar Cells*, 123:47–57, 2014.

[38] A. J. Carrillo, D. Sastre, D. P. Serrano, P. Pizarro, and J. M. Coronado. Revisiting the BaO2/BaO redox cycle for solar thermochemical energy storage. *Physical Chemistry Chemical Physics*, 18(11):8039–8048, 2016.

[39] A. J. Carrillo, D. P. Serrano, P. Pizarro, and J. M. Coronado. Thermochemical heat storage based on the Mn2O3/Mn3O4 redox couple: Influence of the initial particle size on the morphological evolution and cyclability. *Journal of Materials Chemistry A*, 2(45):19435–19443, 2014.

[40] A. J. Carrillo, D. P. Serrano, P. Pizarro, and J. M. Coronado. Improving the Thermochemical Energy Storage Performance of the Mn2O3/Mn3O4 Redox Couple by the Incorporation of Iron. *ChemSusChem*, 8(11):1947–1954, 2015.

[41] A. J. Carrillo, D. P. Serrano, P. Pizarro, and J. M. Coronado. Thermochemical heat storage at high temperatures using Mn2O3/Mn3O4 system: Narrowing the redox hysteresis by metal co-doping. *Energy Procedia*, 73:263–271, 2015.

[42] A. J. Carrillo, D. P. Serrano, P. Pizarro, and J. M. Coronado. Manganese oxide-based thermochemical energy storage: Modulating temperatures of redox cycles by Fe-Cu co-doping. *Journal of Energy Storage*, 5:169–176, 2016.

[43] A. J. Carrillo, D. P. Serrano, P. Pizarro, and J. M. Coronado. Understanding Redox Kinetics of Iron-Doped Manganese Oxides for High Temperature Thermochemical Energy Storage. *The Journal of Physical Chemistry C*, 120(49):27800–27812, 2016.

[44] D. Chadda, J. D. Ford, and M. A. Fahim. Chemical Energy Storage by the Reaction Cycle CuO/Cu2O. *International Journal of Energy Research*, 13(1):63–73, 1989.

[45] H. N. Ch'ng and J. Pan. Sintering of particles of different sizes. *Acta Materialia*, 55(3):813–824, 2007.

[46] J. Christian and C. Ho. System design of a 1 MW north-facing, solid particle receiver. *Energy Procedia*, 69:340–349, 2015.

[47] D. R. Clarke and S. R. Phillpot. Thermal barrier coating materials. *Materials Today*, 8(6):22–29, 2005.

[48] C. K. Clayton, H. Y. Sohn, and K. J. Whitty. Oxidation Kinetics of Cu2O in Oxygen Carriers for Chemical Looping with Oxygen Uncoupling. *Industrial & Engineering Chemistry Research*, 53(8):2976–2986, 2014.

[49] J. Cot-Gores, A. Castell, and L. F. Cabeza. Thermochemical energy storage and conversion: A-state-of-the-art review of the experimental research under practical conditions. *Renewable and Sustainable Energy Reviews*, 16(7):5207–5224, 2012.

[50] J. V. Crum, B. J. Riley, and J. D. Vienna. Binary Phase Diagram of the Manganese Oxide-Iron Oxide System. *Journal of the American Ceramic Society*, 92(10):2378–2384, 2009.

[51] R. Darolia. Thermal barrier coatings technology: Critical review, progress update, remaining challenges and prospects. *International Materials Reviews*, 58(6):315–348, 2013.

[52] M. Deutsch, F. Horvath, C. Knoll, D. Lager, C. Gierl-Mayer, P. Weinberger, and F. Winter. High-Temperature Energy Storage: Kinetic Investigations of the CuO/Cu2O Reaction Cycle. *Energy & Fuels*, 31(3):2324–2334, 2017.

[53] J. D. Donaldson and D. Beyersmann. *Cobalt and Cobalt Compounds*. Ullmann's Encyclopedia of Industrial Chemistry, pages 429-465. Wiley-VCH Verlag GmbH & Co. KGaA, 2005.

[54] P. Dorogokupets, T. Sokolova, A. Dymshits, and K. Litasov. Thermodynamic Properties of Rock-Forming Oxides, alpha-Al2O3, Cr2O3, alpha-Fe2O3, and Fe3O4 at High Temperatures and Pressures. *Geodynamics & Tectonophysics*, 7(3):459–476, 2016.

[55] B. Ehrhart, E. Coker, N. Siegel, and A. Weimer. Thermochemical cycle of a mixed metal oxide for augmentation of thermal energy storage in solid particles. *Energy Procedia*, 49:762–771, 2014.

[56] G. Ervin. Solar Heat Storage Using Chemical Reactions. *Journal of Solid State Chemistry*, 22(1):51–61, 1977.

[57] A. Eschner. *Industrial Refractories (D6.4)*. VDI Heat Atlas. Springer-Verlag Berlin Heidelberg, Düsseldorf, 2nd edition, 2010.

[58] M. A. Fahim and J. D. Ford. Energy Storage Using the BaO2-BaO Reaction Cycle. *The Chemical Engineering Journal*, 27(1):21–28, 1983.

[59] M. Felderhoff, R. Urbanczyk, and S. Peil. Thermochemical Heat Storage for High Temperature Applications – A Review. *Green*, 3(2):113–123, 2013.

[60] V. B. Fetisov, N. V. Korchemkina, G. A. Kozhina, S. A. Petrova, R. G. Zakharov, E. A. Pastukhov, A. V. Fetisov, A. N. Ermakov, and K. S. Mitrofanov. Kinetics of Redox Processes in Manganese Oxides. *Inorganic Materials*, 42(4):374–376, 2006.

[61] A. Feuerstein, J. Knapp, T. Taylor, A. Ashary, A. Bolcavage, and N. Hitchman. Technical and Economical Aspects of Current Thermal Barrier Coating Systems for Gas Turbine Engines by Thermal Spray and EBPVD: A Review. *Journal of Thermal Spray Technology*, 17(2):199–213, 2008.

[62] H. L. Friedman. Kinetics of Thermal Degradation of Char-Forming Plastics from Thermogravimetry. Application to a Phenolic Plastic. *Journal of Polymer Science Part C: Polymer Symposia*, 6(1):183–195, 1964.

[63] A. Galwey and M. Brown. *Thermal Decomposition of Ionic Solids*, volume 86 of *Studies in Physical and Theoretical Chemistry*. Elsevier Science B.V., Amsterdam, 1st edition, 1999.

[64] L. Geissbühler, M. Kolman, G. Zanganeh, A. Haselbacher, and A. Steinfeld. Analysis of industrial-scale high-temperature combined sensible/latent thermal energy storage. *Applied Thermal Engineering*, 101:657–668, 2016.

[65] D. Geldart. Types of Gas Fluidization. *Powder Technology*, 7(5):285–292, 1973.

[66] A. Gil, M. Medrano, I. Martorell, A. Lazaro, P. Dolado, B. Zalba, and L. F. Cabeza. State of the art on high temperature thermal energy storage for power generation. Part 1 - Concepts, materials and modellization. *Renewable & Sustainable Energy Reviews*, 14(1):31–55, 2010.

[67] V. Gnielinski. *Fluid-Particle Heat Transfer in Flow Through Packed Beds of Solids (G9)*. VDI Heat Atlas. Springer-Verlag Berlin Heidelberg, Düsseldorf, 2nd edition, 2010.

[68] F. J. Gotor, J. M. Criado, J. Malek, and N. Koga. Kinetic Analysis of Solid-State Reactions: The Universality of Master Plots for Analyzing Isothermal and Nonisothermal Experiments. *The Journal of Physical Chemistry A*, 104(46):10777–10782, 2000.

[69] A. N. Grundy, B. Hallstedt, and L. J. Gauckler. Assessment of the Mn-O System. *Journal of Phase Equilibria*, 24(1):21–39, 2003.

[70] P. J. Haines, G. R. Heal, P. G. Laye, D. M. Price, S. B. Warrington, and R. J. Wilson. *Principles of Thermal Analysis and Calorimetry*. The Royal Society of Chemistry, Cambridge, UK, 1st edition, 2002.

[71] M. Hamidi, A. Bayon, V. M. Wheeler, P. Kreider, M. A. Wallace, T. Tsuzuki, K. Catchpole, and A. W. Weimer. Reduction kinetics for large spherical 2:1 iron-manganese oxide redox materials for thermochemical energy storage. *Chemical Engineering Science*, 201:74–81, 2019.

[72] H. Hausen. *Heat Transfer in Regenerators (N1)*. VDI Heat Atlas. Springer-Verlag Berlin Heidelberg, Düsseldorf, 2nd edition, 2010.

[73] W. F. Hemminger and H. K. Cammenga. *Methoden der Thermischen Analyse*, volume 24 of *Anleitung für die chemische Laboratoriumspraxis*. Springer-Verlag Berlin, Heidelberg, 1989.

[74] G. W. H. Höhne, H. K. Cammenga, W. Eysel, E. Gmelin, and W. Hemminger. The Temperature Calibration of Scanning Calorimeters. *Thermochimica Acta*, 160(1):1–12, 1990.

[75] M. Hänchen, A. Stiel, Z. R. Jovanovic, and A. Steinfeld. Thermally Driven Copper Oxide Redox Cycle for the Separation of Oxygen from Gases. *Industrial & Engineering Chemistry Research*, 51(20):7013–7021, 2012.

[76] C. Ho, J. Christian, D. Gill, A. Moya, S. Jeter, S. Abdel-Khalik, D. Sadowski, N. Siegel, H. Al-Ansary, L. Amsbeck, B. Gobereit, and R. Buck. Technology Advancements for Next Generation Falling Particle Receivers. *Energy Procedia*, 49:398–407, 2014.

[77] C. K. Ho. Advances in central receivers for concentrating solar applications. *Solar Energy*, 152:38–56, 2017.

[78] K. N. Hutchings, M. Wilson, P. A. Larsen, and R. A. Cutler. Kinetic and thermodynamic considerations for oxygen absorption/desorption using cobalt oxide. *Solid State Ionics*, 177(1-2):45–51, 2006.

[79] C. Igathinathane, L. O. Pordesimo, E. P. Columbus, W. D. Batchelor, and S. R. Methuku. Shape identification and particles size distribution from basic shape parameters using ImageJ. *Computers and Electronics in Agriculture*, 63(2):168–182, 2008.

[80] Q. Imtiaz, D. Hosseini, and C. R. Müller. Review of Oxygen Carriers for Chemical Looping with Oxygen Uncoupling (CLOU): Thermodynamics, Material Development, and Synthesis. *Energy Technology*, 1(11):633–647, 2013.

[81] K. T. Jacob, A. Kumar, G. Rajitha, and Y. Waseda. Thermodynamic Data for Mn3O4, Mn2O3 and MnO2. *High Temperature Materials and Processes*, 30(4-5):459–472, 2011.

[82] S. Jahromy, F. Birkelbach, C. Jordan, C. Huber, M. Harasek, A. Werner, and F. Winter. Impact of Partial Pressure, Conversion, and Temperature on the Oxidation Reaction Kinetics of Cu2O to CuO in Thermochemical Energy Storage. *Energies*, 12(3):1–16, 2019.

[83] W. B. Jensen. The Origin of the Brin Process. *Journal of Chemical Education*, 86(11):1266–1267, 2009.

[84] C. Jin, T. Suehiro, A. Kodama, M. Goto, and T. Hirose. Equilibrium and Reaction Rate of Reversible BaO-BaO2 Reaction for Oxygen Production. *Journal of Chemical Engineering of Japan*, 34(2):279–282, 2001.

[85] G. Karagiannakis, C. Pagkoura, E. Halevas, P. Baltzopoulou, and A. G. Konstandopoulos. Cobalt/cobaltous oxide based honeycombs for thermochemical heat storage in future concentrated solar power installations: Multi-cyclic assessment and semi-quantitative heat effects estimations. *Solar Energy*, 133:394–407, 2016.

[86] G. Karagiannakis, C. Pagkoura, A. Zygogianni, S. Lorentzou, and A. G. Konstandopoulos. Monolithic ceramic redox materials for thermochemical heat storage applications in CSP plants. *Energy Procedia*, 49:820–829, 2014.

[87] L. Kjellqvist and M. Selleby. Thermodynamic Assessment of the Fe-Mn-O System. *Journal of Phase Equilibria and Diffusion*, 31(2):113–134, 2010.

[88] M. Kleiber and R. Joh. *Calculation Methods for Thermophysical Properties (D1)*. VDI Heat Atlas. Springer-Verlag Berlin Heidelberg, Düsseldorf, 2nd edition, 2010.

[89] M. Kleiber and R. Joh. *Properties of Pure Fluid Substances: Liquids and Gases (D3.1)*. VDI Heat Atlas. Springer-Verlag Berlin Heidelberg, Düsseldorf, 2nd edition, 2010.

[90] S. Kuravi, J. Trahan, D. Y. Goswami, M. M. Rahman, and E. K. Stefanakos. Thermal energy storage technologies and systems for concentrating solar power plants. *Progress in Energy and Combustion Science*, 39(4):285–319, 2013.

[91] D. Laing and S. Zunft. *4 - Using concrete and other solid storage media in thermal energy storage (TES) systems*. Advances in Thermal Energy Storage Systems. Woodhead Publishing, Cambridge, 2015.

[92] M. Liu, N. H. Steven Tay, S. Bell, M. Belusko, R. Jacob, G. Will, W. Saman, and F. Bruno. Review on concentrating solar power plants and new developments in high temperature thermal energy storage technologies. *Renewable and Sustainable Energy Reviews*, 53:1411–1432, 2016.

[93] S. Álvarez de Miguel, S. Bellan, J. M. García de María, J. González-Aguilar, and M. Romero. Numerical Modelling of a 100-Wh Lab-Scale Thermochemical Heat Storage System for Concentrating Solar Power Plants. *AIP Conference Proceedings*, 1734(1):0500051–0500058, 2016.

[94] S. Álvarez de Miguel, J. Gonzalez-Aguilar, and M. Romero. 100-Wh multi-purpose particle reactor for thermochemical heat storage in concentrating solar power plants. *Energy Procedia*, 49:676–683, 2014.

[95] J. Marugán, J. A. Botas, M. Martín, R. Molina, and C. Herradón. Study of the first step of the Mn2O3/MnO thermochemical cycle for solar hydrogen production. *International Journal of Hydrogen Energy*, 37(8):7017–7025, 2012.

[96] T. Mattisson. Review Article: Materials for Chemical-Looping with Oxygen Uncoupling. *ISRN Chemical Engineering*, 2013:1–19, 2013.

[97] J. D. McTigue, C. N. Markides, and A. J. White. Performance response of packed-bed thermal storage to cycle duration perturbations. *Journal of Energy Storage*, 19:379–392, 2018.

[98] A. Meier, C. Winkler, and D. Wuillemin. Experiment for modelling high temperature rock bed storage. *Solar Energy Materials*, 24(1):255–264, 1991.

[99] J. Meija, B. Coplen Tyler, M. Berglund, A. Brand Willi, P. De Bièvre, M. Gröning, E. Holden Norman, J. Irrgeher, D. Loss Robert, T. Walczyk, and T. Prohaska. Atomic weights of the elements 2013 (IUPAC Technical Report). *Pure and Applied Chemistry*, 88(3):265–291, 2016.

[100] B. Moghtaderi. Review of the Recent Chemical Looping Process Developments for Novel Energy and Fuel Applications. *Energy & Fuels*, 26(1):15–40, 2012.

[101] M. Molenda, J. Stengler, M. Linder, and A. Wörner. Reversible hydration behavior of CaCl2 at high H2O partial pressures for thermochemical energy storage. *Thermochimica Acta*, 560:76–81, 2013.

[102] A. Muan and S. Somiya. The System Iron Oxide-Manganese Oxide in Air. *American Journal of Science*, 260(3):230–240, 1962.

[103] A. P. Muroyama, A. J. Schrader, and P. G. Loutzenhiser. Solar electricity via an Air Brayton cycle with an integrated two-step thermochemical cycle for heat storage based on Co3O4/CoO redox reactions II: Kinetic analyses. *Solar Energy*, 122:409–418, 2015.

[104] M. Neises, S. Tescari, L. de Oliveira, M. Roeb, C. Sattler, and B. Wong. Solar-heated rotary kiln for thermochemical energy storage. *Solar Energy*, 86(10):3040–3048, 2012.

[105] NETZSCH. *Manufacturer Specifications - The DSC 404/STA 449 Platform: High Flexibility and Performance in Thermal Analysis*. NETZSCH-Gerätebau GmbH, Selb, Germany, 2016.

[106] J. Obermeier, K. Müller, and W. Arlt. Thermodynamic analysis of chemical heat pumps. *Energy*, 88:489–496, 2015.

[107] F. Oeters, M. Ottow, D. Senk, A. Beyzavi, J. Güntner, H. B. Lüngen, M. Koltermann, A. Buhr, J. Yagi, L. Formanek, F. Rose, J. Flickenschild, R. Hauk, R. Steffen, R. Skroch, G. Mayer-Schwinning, H. Bünnagel, and H. Hoff. *Iron*. Ullmann's Encyclopedia of Industrial Chemistry. Wiley-VCH Verlag GmbH & Co. KGaA, 2008.

[108] A. Ortega. A Simulation of the Mass-Transfer Effects on the Kinetics of Solid-Gas Reactions. *International Journal of Chemical Kinetics*, 40(4):217–222, 2008.

[109] C. Pagkoura, G. Karagiannakis, A. Zygogianni, S. Lorentzou, and A. G. Konstandopoulos. Cobalt oxide based honeycombs as reactors/heat exchangers for redox thermochemical heat storage in future CSP plants. *Energy Procedia*, 69:978–987, 2015.

[110] C. Pagkoura, G. Karagiannakis, A. Zygogianni, S. Lorentzou, M. Kostoglou, A. G. Konstandopoulos, M. Rattenburry, and J. W. Woodhead. Cobalt oxide based structured bodies as redox thermochemical heat storage medium for future CSP plants. *Solar Energy*, 108:146–163, 2014.

[111] P. Pardo, A. Deydier, Z. Anxionnaz-Minvielle, S. Rougé, M. Cabassud, and P. Cognet. A review on high temperature thermochemical heat energy storage. *Renewable and Sustainable Energy Reviews*, 32:591–610, 2014.

[112] F. Pestalozzi. *Experimental Investigation of Mn-Based Redox Reaction Kinetics for Thermochemical Energy Storage*. Master Thesis, Department of Mechanical and Process Engineering, ETH Zurich, 2013.

[113] S. Pfenninger, P. Gauche, J. Lilliestam, K. Damerau, F. Wagner, and A. Patt. Potential for concentrating solar power to provide baseload and dispatchable power. *Nature Climate Change*, 4(8):689–692, 2014.

[114] M. Pijolat, L. Favergeon, and M. Soustelle. From the drawbacks of the Arrhenius-f(X) rate equation towards a more general formalism and new models for the kinetic analysis of solid-gas reactions. *Thermochimica Acta*, 525(1-2):93–102, 2011.

[115] R. Pitz-Paal. Concentrating Solar Power Systems. *EPJ Web of Conferences*, 148(8):1–19, 2017.

[116] N. C. Preisner, T. Block, M. Linder, and H. Leion. Stabilizing Particles of Manganese-Iron Oxide with Additives for Thermochemical Energy Storage. *Energy Technology*, 6(11):2154–2165, 2018.

[117] C. Prieto, P. Cooper, A. I. Fernández, and L. F. Cabeza. Review of technology: Thermochemical energy storage for concentrated solar power plants. *Renewable and Sustainable Energy Reviews*, 60:909–929, 2016.

[118] C. Reichl, M. Schatz, and G. Zsak. *World-Mining-Data*, volume 31 of *Minerals Production Report*. International Organizing Committee for the World Mining Congresses, Vienna, 2016.

[119] A. H. Reidies. *Manganese Compounds*. Ullmann's Encyclopedia of Industrial Chemistry, pages 1-22. Wiley-VCH Verlag GmbH & Co. KGaA, 2005.

[120] H. W. Richardson. *Copper Compounds*. Ullmann's Encyclopedia of Industrial Chemistry, pages 273-301. Wiley-VCH Verlag GmbH & Co. KGaA, 2005.

[121] C. Roßkopf, M. Haas, A. Faik, M. Linder, and A. Wörner. Improving powder bed properties for thermochemical storage by adding nanoparticles. *Energy Conversion and Management*, 86:93–98, 2014.

[122] M. Ron. The normalized pressure dependence method for the evaluation of kinetic rates of metal hydride formation/decomposition. *Journal of Alloys and Compounds*, 283(1–2):178–191, 1999.

[123] M. Rydén, H. Leion, T. Mattisson, and A. Lyngfelt. Combined oxides as oxygen-carrier material for chemical-looping with oxygen uncoupling. *Applied Energy*, 113:1924–1932, 2014.

[124] P. O. Santacreu, L. Bucher, A. Koster, and L. Remy. Thermomechanical fatigue of stainless steels for automotive exhaust systems. *Revue de Métallurgie*, 103(1):37–42, 2006.

[125] S. Santhanam, M. P. Heddrich, M. Riedel, and K. A. Friedrich. Theoretical and experimental study of Reversible Solid Oxide Cell (r-SOC) systems for energy storage. *Energy*, 141:202–214, 2017.

[126] F. Schaube, L. Koch, A. Wörner, and H. Müller-Steinhagen. A thermodynamic and kinetic study of the de- and rehydration of Ca(OH)2 at high H2O partial pressures for thermo-chemical heat storage. *Thermochimica Acta*, 538:9–20, 2012.

[127] F. Schaube, A. Kohzer, J. Schütz, A. Wörner, and H. Müller-Steinhagen. De- and rehydration of Ca(OH)2 in a reactor with direct heat transfer for thermo-chemical heat storage. Part A: Experimental results. *Chemical Engineering Research & Design*, 91(5):856–864, 2013.

[128] C. A. Schneider, W. S. Rasband, and K. W. Eliceiri. NIH Image to ImageJ: 25 years of image analysis. *Nature Methods*, 9(7):671–675, 2012.

[129] A. J. Schrader, A. P. Muroyama, and P. G. Loutzenhiser. Solar electricity via an Air Brayton cycle with an integrated two-step thermochemical cycle for heat storage based on Co3O4/CoO redox reactions I: Thermodynamic analysis. *Solar Energy*, 118:485–495, 2015.

[130] A. Shulman, E. Cleverstam, T. Mattisson, and A. Lyngfelt. Manganese/Iron, Manganese/Nickel, and Manganese/Silicon Oxides Used in Chemical-Looping With Oxygen Uncoupling (CLOU) for Combustion of Methane. *Energy & Fuels*, 23(10):5269–5275, 2009.

[131] J. A. Simmons. Reversible oxidation of metal oxides for thermal energy storage. *Proceedings of the ISES Meeting*, 8:219–225, 1976.

[132] S. Sissa, M. Giacopini, and R. Rosi. Low-cycle Thermal Fatigue and High-cycle Vibration Fatigue Life Estimation of a Diesel Engine Exhaust Manifold. *Procedia Engineering*, 74:105–112, 2014.

[133] H. Song, K. Shah, E. Doroodchi, and B. Moghtaderi. Development of a Cu-Mg-Based Oxygen Carrier with SiO2 as a Support for Chemical Looping Air Separation. *Energy & Fuels*, 28(1):163–172, 2014.

[134] R. Span and R. Krauss. *Properties of Dry Air, Nitrogen and Oxygen (D2.2, D2.3, D2.5)*. VDI Heat Atlas. Springer-Verlag Berlin Heidelberg, Düsseldorf, 2nd edition, 2010.

[135] M. Stieß. *Mechanische Verfahrenstechnik - Partikeltechnologie 1*. Springer-Lehrbuch. Springer-Verlag Berlin Heidelberg, 3rd edition, 2009.

[136] S. Ströhle, A. Haselbacher, Z. R. Jovanovic, and A. Steinfeld. The Effect of the Gas-Solid Contacting Pattern in a High-Temperature Thermochemical Energy Storage on the Performance of a Concentrated Solar Power Plant. *Energy & Environmental Science*, 9(4):1375–1389, 2016.

[137] S. Ströhle, A. Haselbacher, Z. R. Jovanovic, and A. Steinfeld. Upgrading sensible-heat storage with a thermochemical storage section operated at variable pressure: An effective way toward active control of the heat-transfer fluid outflow temperature. *Applied Energy*, 196:51–61, 2017.

[138] U. Taut. *Speicherung thermischer Energie im Temperaturbereich bis 1000°C mit Salz/Keramik als Speichermaterial*. Doctoral Thesis, Faculty of Energy-Engineering, University of Stuttgart, 1997.

[139] S. Tescari, C. Agrafiotis, S. Breuer, L. de Oliveira, M. Neises-von Puttkamer, M. Roeb, and C. Sattler. Thermochemical solar energy storage via redox oxides: Materials and reactor/heat exchanger concepts. *Energy Procedia*, 49:1034–1043, 2014.

[140] S. Tescari, A. Singh, C. Agrafiotis, L. de Oliveira, S. Breuer, B. Schlögl-Knothe, M. Roeb, and C. Sattler. Experimental evaluation of a pilot-scale thermochemical storage system for a concentrated solar power plant. *Applied Energy*, 189:66–75, 2017.

[141] M. Timm. *Definition des Begriffs "Energiespeicher"*. BDEW German Association of Energy and Water Industries, Berlin, 2014.

[142] E. Tsotsas. *Thermal Conductivity of Packed Beds (D6.3)*. VDI Heat Atlas. Springer-Verlag Berlin Heidelberg, Düsseldorf, 2nd edition, 2010.

[143] D. Verdier, Q. Falcoz, and A. Ferrière. Design of a Protection Thermal Energy Storage Using Phase Change Material Coupled to a Solar Receiver. *High Temperature Materials and Processes*, 33(6):509–523, 2014.

[144] A. L. Ávila Marín. Volumetric Receivers in Solar Thermal Power Plants with Central Receiver System Technology: A review. *Solar Energy*, 85(5):891–910, 2011.

[145] S. Vyazovkin, A. K. Burnham, J. M. Criado, L. A. Pérez-Maqueda, C. Popescu, and N. Sbirrazzuoli. ICTAC Kinetics Committee recommendations for performing kinetic computations on thermal analysis data. *Thermochimica Acta*, 520(1-2):1–19, 2011.

[146] S. Vyazovkin, K. Chrissafis, M. L. Di Lorenzo, N. Koga, M. Pijolat, B. Roduit, N. Sbirrazzuoli, and J. J. Suñol. ICTAC Kinetics Committee recommendations for collecting experimental thermal analysis data for kinetic computations. *Thermochimica Acta*, 590:1–23, 2014.

[147] G. Wedler and H.-J. Freund. *Lehrbuch der Physikalischen Chemie*, volume 6. Wiley-VCH, Weinheim, 2012.

[148] R. Weiland. *Untersuchung zur Thermodynamik oxidischer Lösungsphasen im System Co-Fe-Mn-O*. Doctoral Thesis, Faculty of Chemistry, University of Stuttgart, 2002.

[149] W. E. Wentworth and E. Chen. Simple Thermal Decomposition Reactions for Storage of Solar Thermal Energy. *Solar Energy*, 18(3):205–214, 1976.

[150] D. G. Wickham. The Chemical Composition of Spinels in the System Fe3O4-Mn3O4. *Journal of Inorganic and Nuclear Chemistry*, 31(2):313–320, 1969.

[151] O. M. Williams and P. O. Carden. Screening reversible reactions for thermochemical energy transfer. *Solar Energy*, 22(2):191–193, 1979.

[152] K.-E. Wirth. *Pressure Drop in Fixed Beds (L1.6)*. VDI Heat Atlas. Springer-Verlag Berlin Heidelberg, Düsseldorf, 2nd edition, 2010.

[153] M. Wokon, T. Bauer, and M. Linder. Investigations on thermochemical energy storage based on manganese-iron oxide in a lab-scale reactor. *AIP Conference Proceedings*, 1850(1):0900081–0900089, 2017.

[154] M. Wokon, T. Block, S. Nicolai, M. Linder, and M. Schmücker. Thermodynamic and kinetic investigation of a technical grade manganese-iron binary oxide for thermochemical energy storage. *Solar Energy*, 153:471–485, 2017.

[155] M. Wokon, A. Kohzer, A. Benzarti, T. Bauer, M. Linder, A. Wörner, and A. Thess. *Thermochemical energy storage based on the reversible reaction of metal oxides*. 3rd International Conference on Chemical Looping, Gothenburg, Sweden, September 9-11, 2014.

[156] M. Wokon, A. Kohzer, and M. Linder. Investigations on thermochemical energy storage based on technical grade manganese-iron oxide in a lab-scale packed bed reactor. *Solar Energy*, 153:200–214, 2017.

[157] M. Wokon, M. Linder, and T. Bauer. *Metallic component with a reactive thermal protective layer, its use and process for its production*. Patent specification DE 10 2013 214 396 B4 2020.03.26, German Aerospace Center e.V. (DLR), Cologne, Germany, 2020.

[158] B. Wong. *Thermochemical Heat Storage for Concentrated Solar Power*. Phase II Final Report, GA-C27137, General Atomics, San Diego, USA, October 2011.

[159] B. Wong, L. Brown, F. Schaube, R. Tamme, and C. Sattler. *Oxide Based Thermochemical Heat Storage*. 16th SolarPACES Conference, Perpignan, France, September 21-24, 2010.

[160] C.-Y. Wu, S. M. Best, A. C. Bentham, B. C. Hancock, and W. Bonfield. Predicting the Tensile Strength of Compacted Multi-Component Mixtures of Pharmaceutical Powders. *Pharmaceutical Research*, 23(8):1898–1905, 2006.

[161] W. Wu, L. Amsbeck, R. Buck, R. Uhlig, and R. Ritz-Paal. Proof of concept test of a centrifugal particle receiver. *Energy Procedia*, 49:560–568, 2014.

[162] T. Yan, R. Z. Wang, T. X. Li, L. W. Wang, and I. T. Fred. A review of promising candidate reactions for chemical heat storage. *Renewable and Sustainable Energy Reviews*, 43:13–31, 2015.

[163] G. Zanganeh, A. Pedretti, S. Zavattoni, M. Barbato, and A. Steinfeld. Packed-bed thermal storage for concentrated solar power – Pilot-scale demonstration and industrial-scale design. *Solar Energy*, 86(10):3084–3098, 2012.

[164] H. Zhang, J. Baeyens, G. Cáceres, J. Degrève, and Y. Lv. Thermal energy storage: Recent developments and practical aspects. *Progress in Energy and Combustion Science*, 53:1–40, 2016.

[165] Z. Zhang, L. André, and S. Abanades. Experimental assessment of oxygen exchange capacity and thermochemical redox cycle behavior of Ba and Sr series perovskites for solar energy storage. *Solar Energy*, 134:494–502, 2016.

[166] S. Zunft, M. Hänel, M. Krüger, and V. Dreißigacker. A design study for regenerator-type heat storage in solar tower plants – Results and conclusions of the HOTSPOT project. *Energy Procedia*, 49:1088–1096, 2014.

[167] S. Zunft, M. Hänel, M. Krüger, V. Dreißigacker, F. Göhring, and E. Wahl. Jülich Solar Power Tower – Experimental Evaluation of the Storage Subsystem and Performance Calculation. *Journal of Solar Energy Engineering*, 133(3):0310191–0310195, 2011.